Near-Capacity Multi-Functional MIMO Systems:

Sphere-Packing, Iterative Detection and Cooperation

by

L. Hanzo, O. R. Alamri, M. El-Hajjar, N. Wu

We dedicate this monograph to the numerous contributors of this field, many of whom are listed in the Author Index

The classic Shannon-Hartley law suggests that the achievable channel capacity increases logarithmically with the transmit power. By contrast, the MIMO capacity increases linearly with the number of transmit antennas, provided that the number of receive antennas is equal to the number of transmit antennas. With the further proviso that the total transmit power is increased proportionately to the number of transmit antennas, a linear capacity increase is achieved upon increasing the transmit power, which justifies the spectacular success of MIMOs...

School of Electronics and Computer Science
University of Southampton
Southampton SO17 1BJ
United Kingdom

Contents

About the Authors

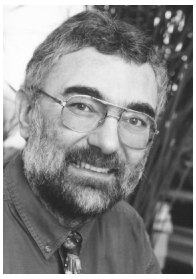

Lajos Hanzo (http://www-mobile.ecs.soton.ac.uk) FREng, FIEEE, FIET, DSc received his degree in electronics in 1976 and his doctorate in 1983. During his 31-year career in telecommunications he has held various research and academic posts in Hungary, Germany and the UK. Since 1986 he has been with the School of Electronics and Computer Science, University of Southampton, UK, where he holds the chair in telecommunications. He has co-authored 17 books on mobile radio communications totalling in excess of 10 000, published in excess of 800 research papers, acted as TPC Chair of IEEE conferences, presented keynote lectures and been awarded a number of distinctions. Currently he is directing an academic research team, working on a range of research projects in the field of wireless multimedia communications sponsored by industry, the Engineering and Physical Sciences Research Council (EPSRC) UK, the European IST Programme and the Mobile Virtual Centre of Excellence (VCE), UK. He is an enthusiastic supporter of industrial and academic liaison and he offers a range of industrial courses. He is also an IEEE Distinguished Lecturer as well as a Governor of both the IEEE ComSoc and the VTS. He is the acting Editor-in-Chief of the IEEE Press. For further information on research in progress and associated publications please refer to http://www-mobile.ecs.soton.ac.uk

Osamah Rashed Alamri received his B.S. degree with first class honours in electrical engineering from King Fahd University of Petroleum and Minerals (KFUPM), Dhahran, Saudi Arabia, in 1997, where he was ranked first with a 4.0 GPA. In 2002, he received his M.S. degree in electrical engineering from Stanford University, California, USA. Mr. Alamri submitted his PhD thesis in October 2006 and published in excess of 20 research papers while working towards his PhD degree with the Communications Group, Shool of Electronics and Computer Science, University of Southampton, UK. His research interests include sphere packing modulation, space-time coding, turbo coding and detection, multidimensional mapping and MIMO systems. At the time of writing he is continuing his investigations as a post-doctoral researcher.

Mohammed El-Hajjar received the B.Eng. degree (with Distinction) in Electrical Engineering from the American University of Beirut (AUB), Lebanon, and the M.Sc. degree (with Distinction) in Radio Frequency Communication Systems from the University of Southampton, UK. Since October 2005, he has been working towards his Ph.D. degree with the Communications Group, School of Electronics and Computer Science, University of Southampton, U.K. Mohammed is the recepient of several academic awards from the AUB as well as the University of Southampton. His research interests include sphere packing modulation, space-time coding, differential space-time spreading, adaptive transceiver design and cooperative communications. In 2008 he completed his PhD thesis and joined Ensigma in Chepstow, Wales, UK as wireless system architect.

Nan Wu received his B.Eng in Electronics Engineering in 2003 from Dalian University of Technology, China. He then moved to the UK and received his M.Sc degree (with Distinction) and PhD from the University of Southampton, UK in 2004 and 2008, respectively. His research interests are in the areas of wireless communications, including space-time coding, channel coding and cooperative MIMO systems. In September 2008 he joined the National Institute of Standards and Technology (NIST) in the USA as a guest researcher working on cross-layer designs.

Other Wiley and IEEE Press Books on Related Topics [1]

- R. Steele, L. Hanzo (Ed): *Mobile Radio Communications: Second and Third Generation Cellular and WATM Systems*, John Wiley and IEEE Press, 2nd edition, 1999, ISBN 07 273-1406-8, 1064 pages
- L. Hanzo, T.H. Liew, B.L. Yeap: *Turbo Coding, Turbo Equalisation and Space-Time Coding*, John Wiley and IEEE Press, 2002, 751 pages
- L. Hanzo, C.H. Wong, M.S. Yee: *Adaptive Wireless Transceivers: Turbo-Coded, Turbo-Equalised and Space-Time Coded TDMA, CDMA and OFDM Systems*, John Wiley and IEEE Press, 2002, 737 pages
- L. Hanzo, L-L. Yang, E-L. Kuan, K. Yen: *Single- and Multi-Carrier CDMA: Multi-User Detection, Space-Time Spreading, Synchronisation, Networking and Standards*, John Wiley and IEEE Press, June 2003, 1060 pages
- L. Hanzo, M. Münster, T. Keller, B-J. Choi, *OFDM and MC-CDMA for Broadband Multi-User Communications, WLANs and Broadcasting*, John-Wiley and IEEE Press, 2003, 978 pages
- L. Hanzo, S-X. Ng, T. Keller and W.T. Webb, *Quadrature Amplitude Modulation: From Basics to Adaptive Trellis-Coded, Turbo-Equalised and Space-Time Coded OFDM, CDMA and MC-CDMA Systems*, John Wiley and IEEE Press, 2004, 1105 pages
- L. Hanzo, T. Keller: *An OFDM and MC-CDMA Primer*, John Wiley and IEEE Press, 2006, 430 pages
- L. Hanzo, F.C.A. Somerville, J.P. Woodard: *Voice and Audio Compression for Wireless Communications*, John Wiley and IEEE Press, 2007, 858 pages
- L. Hanzo, P.J. Cherriman, J. Streit: *Video Compression and Communications: H.261, H.263, H.264, MPEG4 and HSDPA-Style Adaptive Turbo-Transceivers* John Wiley and IEEE Press, 2007, 680 pages
- L. Hanzo, J.S. Blogh, S. Ni: *3G, HSDPA, HSUPA and FDD Versus TDD Networking: Smart Antennas and Adaptive Modulation* John Wiley and IEEE Press, 2008, 564 pages

[1] For detailed contents and sample chapters please refer to http://www-mobile.ecs.soton.ac.uk

Preface

The family of recent wireless standards included the optional employment of MIMO tyechniques. This was motivated by the observation according to the classic Shannon-Hartley law the achievable channel capacity increases logarithmically with the transmit power. By contrast, the MIMO capacity increases linearly with the number of transmit antennas, provided that the number of receive antennas is equal to the number of transmit antennas. With the further proviso that the total transmit power is increased proportionately to the number of transmit antennas, a linear capacity increase is achieved upon increasing the transmit power, which justifies the spectacular success of MIMOs...

Hence this volume explores recent research advances in MIMO techniques as well as their limitations. The basic types of multiple antenna-aided wireless systems are classified and their benefits are characterised. We also argue that under realistic propagation conditions, when for example the signals associated with the MIMO elements become correlated owing to shadow fading, the predicted performance gains may substantially erode. Furthermore, owing to the limited dimensions of shirt-pocket-sized handsets the employment of multiple antenna elements at the mobile station is impractical. In this scenario only the family of distributed MIMO elements relying on the cooperation of potentially single-element mobile stations is capable of eliminating the correlation of the signals impinging on the MIMO elements, as it will be discussed in the book. The book also reports on a variety of avantgarde hybrid MIMO designs to set out promising future research directions.

Our intention with the book is:

1. First, to pay tribute to all researchers, colleagues and valued friends, who contributed to the field. Hence this book is dedicated to them, since without their quest for better MIMO solutions for wireless communications this monograph could not have been conceived. They are too numerous to name here, hence they appear in the author index of the book. Our hope is that the conception of this monograph on the topic will provide an adequate portrayal of the community's research and will further fuel this innovation process.

2. We expect to stimulate further research by exposing open research problems and by collating a range of practical problems and design issues for the practitioners. The coherent further efforts of the wireless research community is expected to lead to the solution of the range of outstanding problems, ultimately providing us with flexible MIMO-aided wireless transceivers exhibiting a performance close to information theoretical limits.

Chapter 1

Problem Formulation, Objectives and Benefits

The objective of this light-hearted introductory chapter is to provide a brief rudimentary exposure of the pivotal aspects of the book. Our treatment in this chapter is conceptual, rather than mathematically motivated, with the objective of characterizing the attainable diversity gains, multiplexing gains and beamforming gains. All issues touched upon in this chapter will be revisited in a more rigorous mathematical approach in the remaining chapters.

Digital communication exploiting multiple-input multiple-output (MIMO) wireless channels has recently attracted considerable attention as one of the most significant technical breakthroughs in modern communications. Soon after its invention, the technology seems to have the potential to be part of large-scale standards-driven commercial wireless products and networks such as broadband wireless access systems, wireless local area networks (WLAN), third-generation (3G) networks and beyond [1]. The 3G systems are expected to have the capability to support circuit and packet data at high bit rates. Rates of 144 kilobits/second or higher in high mobility (vehicular) traffic, 384 Kbits/second for pedestrian traffic, and 2 Megabits/second or higher for indoor traffic are targeted [2]. Wireless systems that employ multiple antennas provide a promising platform for achieving such high rates because of the improved bit/symbol capacity compared to the single-input single-output systems [3].

As shown in Figure 1.1, MIMO systems can be defined as wireless communication systems for which the transmitting end as well as the receiving end is equipped with multiple antenna elements. The basic concept of MIMO is that the transmitted signals from all transmit antennas are *combined* at each receive antenna element in such a way to improve the Bit Error Rate (BER) performance or the data rate (bits/sec) of the transmission. Both the network's quality of service and the operator's revenues can be increased significantly because of this advantage of MIMO systems. One can think of MIMO systems as an extension to smart antennas. However, the idea of using antenna arrays for improving the wireless transmission was introduced several decades ago.

Space-time processing (STP) is the core concept of MIMO systems. Time is the natural dimension of digital communication data. Space refers to the spatial dimension inherent in the use of multiple spatially distributed antennas. Most of the current interest in space-time coding (STC) is driven by discoveries in the late 1980s and early 1990s that multiple antennas can exploit a rich wireless scattering environment and benefit from the multi-path fading nature of the wireless channel. Current research mostly focuses on channel modelling and measurement, and on the design of modulation and coding techniques that take into consideration the two-dimensional nature of STP (i.e. the space and time dimensions) [4].

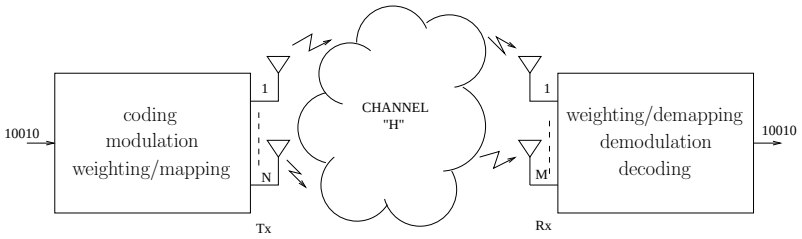

Figure 1.1: MIMO wireless transmission system

1.1 The Wireless Channel and the Concept of Diversity

The key characteristics of the mobile radio channel in contrast to the Gaussian channel are small-scale fading and multipath propagation [5]. Small-scale fading, which is usually simply called fading, refers to the rapid fluctuation of signal strength over a short travel distance or period of time. Fading is primarily caused by multipath propagation of the transmitted signal, which creates replicas of the transmitted signal that arrive at the receiver with different delays. These versions of the transmitted signal combine either constructively or destructively at the receiver resulting in fluctuation in amplitude and phase of the resultant signal. Other factors that influence the small-scale fading include speed of the mobile, speed of the surrounding objects and the transmission bandwidth of the signal [5]. During severe fading, the transmitted signal cannot be determined by the receiver unless some less attenuated version of it is available at the receiver. This usually can be achieved by introducing some sort of diversity in the transmitted signal. The three most common diversity techniques are [6]:

- **Temporal Diversity**: An example of temporal diversity is channel coding with time interleaving. The receiver is provided with several versions of the transmitted signal as redundancy in the temporal domain.

- **Frequency Diversity**: This type of diversity is based on the phenomenon that the structure of multipath propagation depends on the frequency of the transmitted wave. Thus redundancy in the frequency domain provides the receiver with several replicas of the transmitted signal that experience different fading at any particular time instance.

- **Antenna or Space Diversity**: In order to create space diversity, several spatially separated or differentially polarised antennas are employed. This would generate redundancy of the transmitted signal in the spatial domain, where each replica would undergo different propagation path. In this context, diversity order refers to the number of decorrelated spatial branches available at the transmitter or receiver, where the probability of losing a signal decreases exponentially with increasing diversity order.

It is always desirable to employ all forms of diversity in order to combat the adverse effects of the wireless channel [7]. However, it becomes sometimes impractical to employ a particular type of diversity in a specific situation [8]. For example, temporal diversity is ineffective in slow fading channels especially for delay-sensitive applications. In addition, antenna diversity at the mobile unit induces design impracticality. The most common systems that employ different types of diversity techniques for the sake of improving the performance of wireless transmission/reception are STC and MIMO schemes. Next, a brief historical overview on space-time coding and MIMO systems will be presented summarising the main contributions in this field.

1.2 Diversity and Multiplexing Tradeoffs in Multi-functional MIMO Systems

1.2.1 Classification of Multiple-Input Multiple-Output Systems

Again, our objective in this light-hearted section is to provide a brief conceptual overview of the material discussed in significantly more detail in Parts I and III of the book. More specifically, we will briefly consider the design alternatives of different Multiple-Input Multiple-Output (MIMO) schemes, while considering the attainable diversity gains, multiplexing gains and beamforming gains. Our easy-reading conceptual treatment in this section aims for avoiding the rigor of mathematics, which is left for the detailed approach of the remaining chapters.

Here we would like to commence with a brief classification of different MIMO schemes, which are categorised as *diversity techniques, multiplexing schemes, multiple access arrangements and beamforming techniques*. We then introduce two *multi-functional MIMO families*. These multi-functional MIMOs are capable of combining the benefits of several MIMO schemes and hence they attain an improved performance in terms of both their Bit Error Ratio (BER) as well as throughput. The first multi-functional MIMO family represents the recently proposed Layered Steered Space-Time Codes (LSSTC), which combines the triple benefits of Space-Time Block Codes (STBC), Vertical Bell Labs Layered Space-Time (V-BLAST) schemes and beamforming. The other multi-functional MIMO scheme is referred to as Layered Steered Space-Time Spreading (LSSTS) that combines the benefits of Space-Time Spreading (STS), V-BLAST and beamforming with those of the generalised Multi-Carrier Direct Sequence Code Division Multiple Access (MC DS-CDMA). We also compare the attainable diversity, multiplexing and beamforming gains of the different MIMO schemes in order to document the advantages of the multi-functional MIMOs over conventional MIMO schemes.

Recently, there has been an urging demand for flexible and bandwidth-efficient transceivers capable of supporting the explosive expansion of the Internet and the continued dramatic increase in demand for high-speed multimedia wireless services. Advances in channel coding made it feasible to approach Shannon's capacity limit in systems equipped with a single antenna [9], but fortunately these capacity limits can be further extended with the aid of multiple antennas. Recently, Multiple-Input Multiple-Output (MIMO) systems have attracted considerable research attention and it is considered as one of the most significant technical breakthroughs in contemporary communications.

Explicitly, the MIMO schemes can be categorised as diversity techniques, multiplexing schemes, multiple access methods, beamforming as well as multi-functional MIMO arrangements, as shown in Figure 1.2. Spatial diversity can be attained by employing multiple antennas at the transmitter or the receiver. Multiple antennas can be used to transmit and receive appropriately encoded replicas of the same information sequence in order to achieve diversity and hence to obtain an improved BER performance. In the context of diversity techniques, the antennas are spaced as far apart as possible, so that the signals transmitted to or received by the different antennas experience independent fading and hence we attain the highest possible diversity gain.

A simple spatial diversity technique, which does not involve any loss of bandwidth, is constituted by the employment of multiple antennas at the receiver, where several techniques can be employed for combining the independently fading signal replicas, including Maximum Ratio Combining (MRC), Equal Gain Combining (EGC) and Selection Combining (SC), as shown in Figure 1.2. Several transmit - rather than receive - diversity techniques have also been proposed in the literature [10–13], as shown in Figure 1.2. In [10] Alamouti proposed a witty transmit diversity technique using two transmit antennas, whose key advantage was the employment of low-complexity single-receive-antenna-based detection, which avoids the more complex joint detection of multiple symbols. The decoding algorithm proposed in [10] can be generalised to an arbitrary number of receive antennas using MRC, EGC or SC. Alamouti's achievement inspired Tarokh *et*

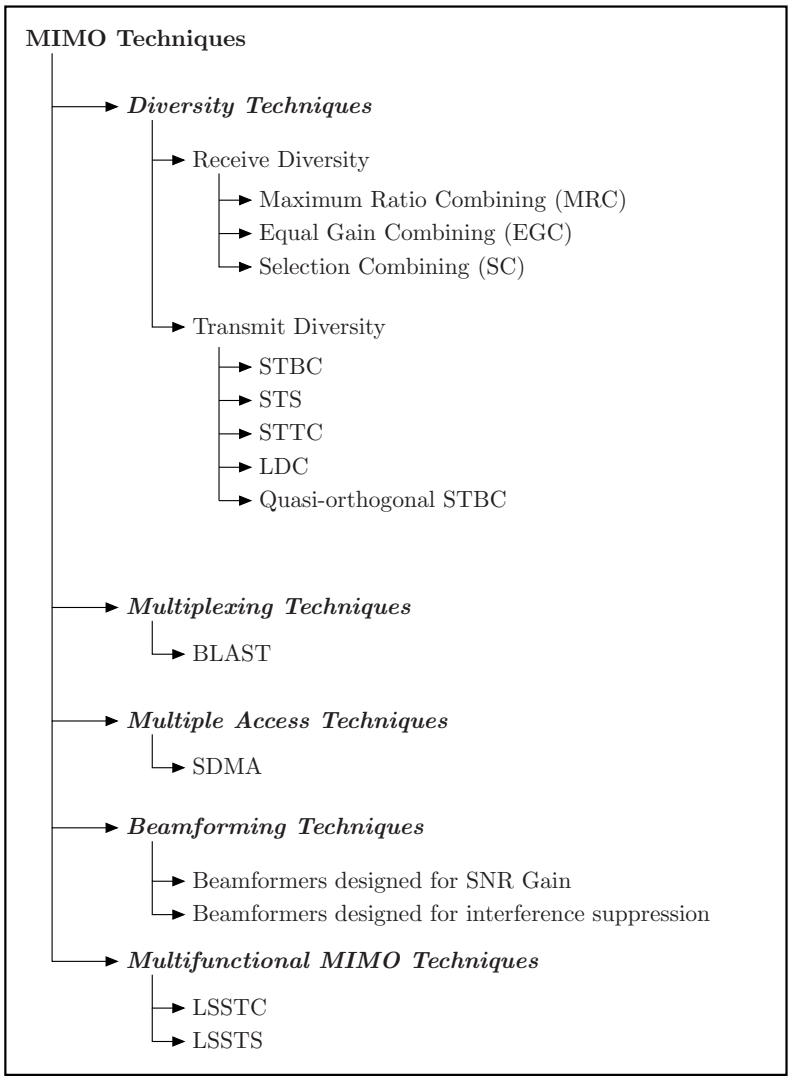

Figure 1.2: Classification of MIMO Techniques.

al. [11] to generalise the concept of transmit diversity schemes to more than two transmit antennas, contriving the generalised concept of Space-Time Block Codes (STBC). The family of STBCs is capable of attaining the same diversity gain as Space-Time Trellis Codes (STTC) [12] at a lower decoding complexity, when employing the same number of transmit antennas. However, a disadvantage of STBCs when compared to STTCs is that they employ unsophisticated repetition-coding and hence provide no coding gain. Furthermore, inspired by the philosophy of STBCs, Hochwald *et al*. [14] proposed the transmit diversity concept known as Space-Time Spreading (STS) for the downlink of Wideband Code Division Multiple Access (WCDMA) that is capable of achieving the highest possible transmit diversity gain.

Regretfully, the STBC and STS designs of [11,14] contrived for more than two transmit antennas result in a reduction of the achievable throughput per channel use. An alternative idea invoked for constructing full-rate STBCs for complex-valued modulation schemes and more than two antennas was suggested in [15]. Here the strict constraint of perfect orthogonality was relaxed in favour of achieving a higher data rate. The resultant STBCs were referred to as quasi-orthogonal STBCs [15].

The STBC and STS designs offer - at best - the same data rate as an uncoded single-antenna

system, but they provide an improved BER performance compared to the family of single-antenna-aided systems by providing diversity gains. In contrast to this, several high-rate space-time transmission schemes having a normalised rate higher than unity have been proposed in the literature. For example, high-rate space-time codes that are linear both in space and time, namely the family of the so-called Linear Dispersion Codes (LDC), was proposed in [13]. LDCs provide a flexible trade-off between emulating space-time coding and/or spatial multiplexing.

STBCs and STTCs are capable of providing diversity gains for the sake of improving the achievable system performance. However, this BER performance improvement is often achieved at the expense of a rate-loss, since STBCs and STTCs may result in a throughput-loss compared to single-antenna-aided systems. As a design alternative, a specific class of MIMO systems was designed for improving the attainable spectral efficiency of the system by transmitting different signal streams independently over each of the transmit antennas, hence resulting in a multiplexing gain. This class of MIMOs subsumes Bell Labs' Layered Space-Time (BLAST) scheme and its relatives [16]. The BLAST scheme aims for increasing the system throughput in terms of the number of bits per symbol that can be transmitted in a given bandwidth at a given integrity.

In contrast to the family of BLAST schemes, where multiple antennas are activated by a single user for increasing the user's throughput, Space Division Multiple Access (SDMA) [17] employs multiple antennas for the sake of supporting multiple users. SDMA exploits the unique user-specific Channel Impulse Response (CIR) of the different users for separating their received signals. On the other hand, in beamforming arrangements [17] typically $\lambda/2$-spaced antenna elements are used for the sake of creating a spatially selective transmitter/receiver beam, where λ represents the carrier's wavelength. Beamforming is employed for providing a beamforming gain by mitigating the effects of various interfering signals, provided that they arrive from sufficiently different directions. Additionally, beamforming is capable of suppressing the effects of co-channel interference, hence allowing the system to support multiple users by angularly separating them. Again, this angular separation becomes feasible only on condition, if the corresponding users are separable in terms of the angle of arrival of their beams.

Finally, multi-functional MIMOs, as the terminology suggests, combine the benefits of several MIMO schemes including diversity gains, multiplexing gains as well as beamforming gains. As mentioned earlier, V-BLAST is capable of achieving the maximum attainable multiplexing gain, while STBC can achieve the full achievable antenna diversity gain facilitated by the number of independently fading diversity channels. Hence, it was proposed in [18] to combine these two techniques in order to provide both antenna diversity and spectral efficiency gains. Furthermore, the combined array processing proposed in [18] was improved in [19] by optimising the decoding order of the different antenna layers. An iterative decoding algorithm was proposed in [19] that results in achieving the full receive diversity gain for the combined V-BLAST STBC system facilitated by the number of independently fading diversity channels. On the other hand, in [20] the authors presented a transmission scheme referred to as Double Space-Time Transmit Diversity (D-STTD), which consists of two STBC layers at the transmitter that is equipped with four transmit antennas, while the receiver is equipped with two antennas. Furthermore, in order to achieve additional performance gains, beamforming has been combined both with spatial diversity as well as spatial multiplexing techniques. STBC has been combined with beamforming in order to attain an improved SNR gain in addition to the diversity gain [21].

This contribution provides a light-hearted perspective on further research advances in the field of multi-functional MIMO systems and demonstrates how diversity, multiplexing and beamforming gains are achieved by multi-functional MIMOs. More explicitly, in Section 1.2.2 we elaborate on the design of two novel multi-functional MIMOs, that are characterised by diversity gain, multiplexing gain as well as beamforming gain. In Section 1.2.3 we quantify the achievable performance of the different MIMO schemes. A comparison of the different MIMO schemes expressed in terms of their diversity, multiplexing and beamforming gains is presented in Section 1.2.4, followed by our brief conclusions.

1.2.2 Multi-functional MIMO Systems

Space-time codes have been designed for the sake of attaining the highest possible diversity gain, where the diversity order of STBC schemes is $(N_t \times N_r)$, where N_t is the number of transmit antennas and N_r represents the number of receive antennas. However, the STBC schemes were not designed for attaining any multiplexing gain; quite the contrary, in some STBC designs there is a rate loss, which results in a reduced throughput in comparison to Single-Input Single-Output (SISO) systems. On the other hand, the V-BLAST scheme was designed for attaining the maximum achievable multiplexing gain equal to the number of transmit antennas, although it does not attain a high diversity gain. Therefore, the appealing concept of multi-functional MIMO schemes designed for combining the benefits of STBC and BLAST schemes arises, in order to provide both diversity and multiplexing gains. Below we describe two novel multi-functional MIMO schemes that can attain diversity gain, multiplexing gain and beamforming gain, while employing low-complexity linear receivers.

1.2.2.1 Layered Steered Space-Time Codes

The first multi-functional MIMO scheme combines the benefits of the V-BLAST scheme, of STBCs as well as of beamforming. Thus, the proposed system benefits from the multiplexing gain of V-BLAST, from the diversity gain of STBCs and from the SNR gain of the beamformer. This multi-functional MIMO scheme was referred to as a Layered Steered Space-Time Code (LSSTC) [22].

A block diagram of the proposed LSSTC scheme is illustrated in Figure 1.3. The system's architecture in Figure 1.3 has N_t transmit Antenna Arrays (AA) spaced sufficiently far apart in order to experience independent fading and hence to achieve transmit diversity. The L_{AA} number of elements of each of the AAs are spaced at a distance of $\lambda/2$ for the sake of achieving a beamforming gain. Furthermore, the receiver is equipped with $N_r \geqslant N_t$ antennas. According to Figure 1.3, a block of B input information symbols is serial-to-parallel converted to K groups of symbol streams of length B_1, B_2, $\cdots$, B_K, where $B_1 + B_2 + \cdots + B_K = B$. Each group of B_k symbols, $k \in [1, K]$, is then encoded by a component space-time code STC_k associated with m_k transmit AAs, where $m_1 + m_2 + \cdots + m_K = N_t$.

The L_{AA}-dimensional spatio-temporal CIR vector spanning the mth transmitter AA, $m \in [1, \cdots, N_t]$, and the nth receiver antenna, $n \in [1, \cdots, N_r]$, can be expressed as $\mathbf{h}_{nm}(t) = \mathbf{a}_{nm}(t)\delta(t - \tau_k)$, where τ_k is the signal's delay and $\mathbf{a}_{nm}(t)$ is the CIR of the mnth link between the mth AA and the nth receive antenna. Based on the assumption that the array elements are separated by half a wavelength, we have $\mathbf{a}_{nm}(t) = \alpha_{nm}(t) \cdot \mathbf{d}_{nm}$, where $\alpha_{nm}(t)$ is a Rayleigh faded envelope and $\mathbf{d}_{nm}$ is an L_{AA}-dimensional vector, whose elements are based on the Direction Of Arrival (DOA) of the signal to the receiver. As for the AA-specific DOA, we consider a scenario where the distance between the transmitter and the receiver is significantly higher than that between the AAs and thus we can assume that the signals arrive at the different AAs in parallel, i.e. the DOA at the different AAs is the same. In this scenario, the MRC-criterion based transmit beamformer, which constitutes an effective solution to maximising the antenna gain, is the optimum beamformer.

The decoder applies Group Successive Interference Cancellation (GSIC) based on the Zero Forcing (ZF) algorithm [18] for decoding the received signal. The most beneficial decoding order of the STC layers is determined on the basis of detecting the highest-power layer first for the sake of a high correct detection probability. For simplicity, let us consider the case of $K = 2$ STBC layers, where layer 1 is detected first, which allows us to eliminate the interference caused by the signal of layer 2. However, the proposed concept is applicable to arbitrary STCs and to an arbitrary number of layers K. For this reason, the decoder of layer 1 has to compute a matrix $\mathbf{Q}$, so that we have $\mathbf{Q} \cdot \widehat{\mathbf{H}}_2 = 0$, where $\widehat{\mathbf{H}}_2$ represents the channel matrix of the second STBC layer whose nmth element is α_{nm}. Therefore, the decoder computes an orthonormal basis for the left null space of $\widehat{\mathbf{H}}_2$ and assigns the vectors of the basis to the rows of $\mathbf{Q}$. Multiplying $\mathbf{Q}$ by the received signal matrix

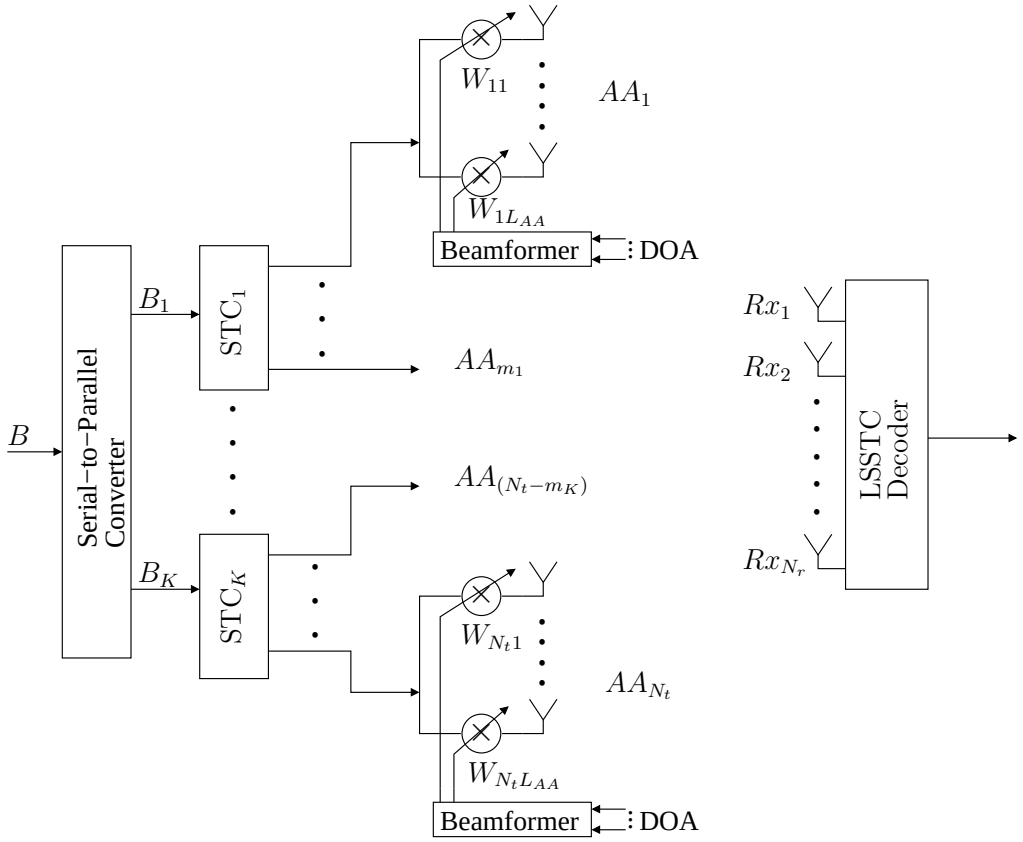

Figure 1.3: Layered steered space-time code system block diagram.

$\mathbf{Y}$ suppresses the interference of layer 2 originally imposed on layer 1 and generates a signal which can be decoded using Maximum Likelihood (ML) STBC detection. Then, the decoder subtracts the remodulated contribution of the decoded symbols of layer 1 from the composite twin-layer received signal $\mathbf{Y}$. Finally, the decoder applies direct STBC decoding to the second layer, since the interference imposed by the first layer has been eliminated. This group-interference cancellation procedure can be generalised to arbitrary N_t and K values.

1.2.2.2 Layered Steered Space-Time Spreading

The LSSTC scheme of Section 1.2.2.1 combines the benefits of V-BLAST, STBC and beamforming and hence is characterised by a diversity gain, a multiplexing gain as well as a beamforming gain. However, a drawback of the LSSTC scheme is the fact that the number of receive antennas N_r should be at least equal to the number of transmit antennas N_t. This condition is not very practical for employing shirt-pocket sized Mobile Stations (MS) that are limited in size and complexity. The LSSTC scheme can be applied in a scenario where two Base Stations (BS) cooperate or a BS is communicating with a MIMO-aided laptop. Therefore, in order to allow communication between a BS and a MS accommodating less antennas than the transmitting BS while employing simple linear receivers, the Layered Steered Space-Time Spreading (LSSTS) scheme described below can be employed.

A block diagram of the LSSTS scheme is shown in Figure 1.4. The LSSTS scheme combines the benefits of V-BLAST, STS and beamforming with generalised MC DS-CDMA [23] for the sake of achieving a multiplexing gain, a spatial and frequency diversity gain as well as a beamforming

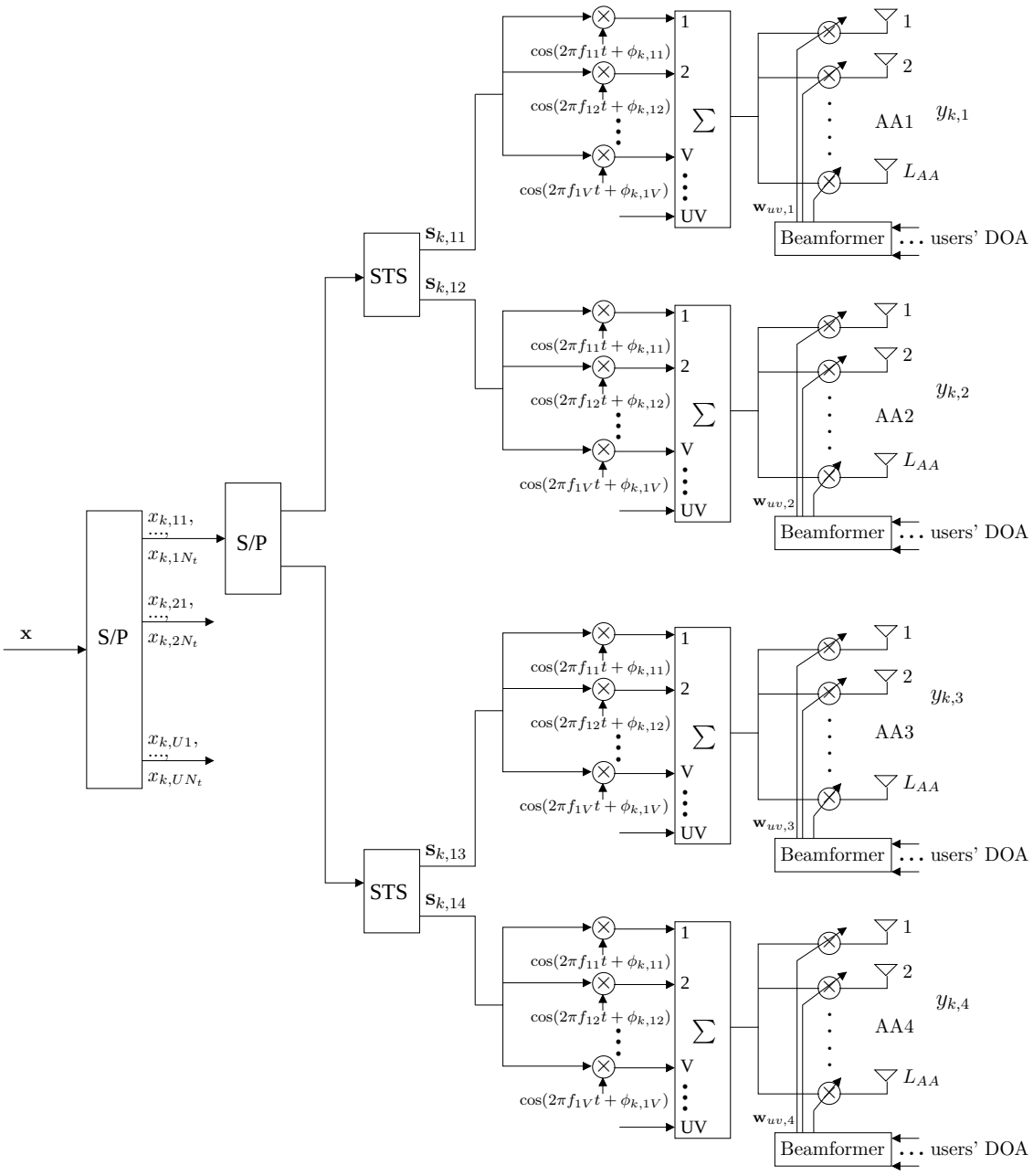

Figure 1.4: The k_{th} user's LSSTS aided Generalised MC DS-CDMA transmitter model.

gain. The LSSTS scheme described in this section employs N_t=4 transmit antennas and N_r=2 receive antennas and employs a linear receiver to decode the received signal.

The system architecture employed in Figure 1.4 for the proposed scheme is equipped with N_t=4 transmit AAs spaced sufficiently far apart in order to experience independent fading. The L_{AA} number of elements of each of the AAs are spaced at a distance of $\lambda/2$ for the sake of achieving beamforming. The system can support K users transmitting at the same time and using the same carrier frequencies, while they can be differentiated by the user-specific spreading code $\bar{\mathbf{c}}_k$, where $k \in [1, K]$. Additionally, in the generalised MC DS-CDMA system considered, the subcarrier frequencies are arranged in a way that guarantees that the same STS signal is spread to and hence transmitted by the specific V number of subcarriers having the maximum possible frequency separation, so that they experience independent fading and achieve the maximum attainable frequency diversity.

The system considered employs the generalised MC DS-CDMA scheme of [23] using UV number of subcarriers. The transmitter schematic of the kth user is shown in Figure 1.3, where a block of UN_t data symbols $\mathbf{x}$ is Serial-to-Parallel (S/P) converted to U parallel sub-blocks. Afterwards, each set of N_t symbols is S/P converted to G=2 groups, where each group is encoded using the N_{tg}=2 antenna-aided STS procedure of [14], where the transmitted signal is spread to N_{tg} transmit antennas with the aid of the orthogonal spreading codes of $\{\bar{\mathbf{c}}_{k,1}, \bar{\mathbf{c}}_{k,2}, \cdots, \bar{\mathbf{c}}_{k,N_tg}\}$, k=1, 2, ..., K. The spreading codes $\bar{\mathbf{c}}_{k,1}$ and $\bar{\mathbf{c}}_{k,2}$ are generated from the same user-specific spreading code $\bar{\mathbf{c}}_k$ as in [14]. The discrete symbol duration of the orthogonal STS codes is $N_{tg}N_e$, where N_e represents the kth user's TD spreading factor.

The UN_t outputs of the UG number of STS blocks modulate a group of subcarrier frequencies $\{f_{u,1}, f_{u,2}, ..., f_{u,V}\}$. Since each of the U sub-blocks is spread to and hence conveyed with the aid of V subcarriers, a total of UV number of subcarriers are required in the MC DS-CDMA system considered. The UV number of subcarrier signals are superimposed on each other in order to form the complex-valued modulated signal for transmission. Finally, according to the kth user's channel information, the UVN_t signals of the kth user are weighted by the transmit weight vector $\mathbf{w}_{uv,n}^{(k)}$ determined for the uvth subcarrier of the kth user, which is generated for the nth AA. Assuming that the system employs a modulation scheme transmitting D bits-per-symbol, then the bandwidth efficiency of the LSSTS aided Generalised MC DS-CDMA system is given by $2UD$ bits-per-channel-use.

The uvth CIR considered in the case of LSSTS is the same as that considered in the previous section for LSSTC. Assuming that the K users' data are transmitted synchronously over a dispersive Rayleigh fading channel, decoding is carried out in two steps, first SIC is performed according to [20], followed by the STS decoding procedure of [14].

Finally, after combining the k=1st user's identical replicas of the same signal transmitted by spreading over V number of subcarriers, the decision variables corresponding to the symbols transmitted in the uth sub-block can be expressed as $\widetilde{x}_{1,u} = \sum_{v=1}^{V} \widetilde{x}_{1,uv}$. Therefore, the decoded signal has a diversity order of $2V$. More explicitly, second order spatial diversity is attained from the STS operation and a diversity order of V is achieved as a benefit of spreading by the generalised MC DS-CDMA scheme, where the subcarrier frequencies are arranged in a way that guarantees that the same STS signal is spread to and hence transmitted by the specific V number of subcarriers having the maximum possible frequency separation, so that they experience as independent fading as possible.

1.2.3 Expected Performance and Discussions

In this section we compare the BER performance of the different MIMO schemes to that of the SISO system. We compare BPSK modulated systems, while considering transmissions over correlated Rayleigh fading channels associated with a normalised Doppler frequency of 0.01.

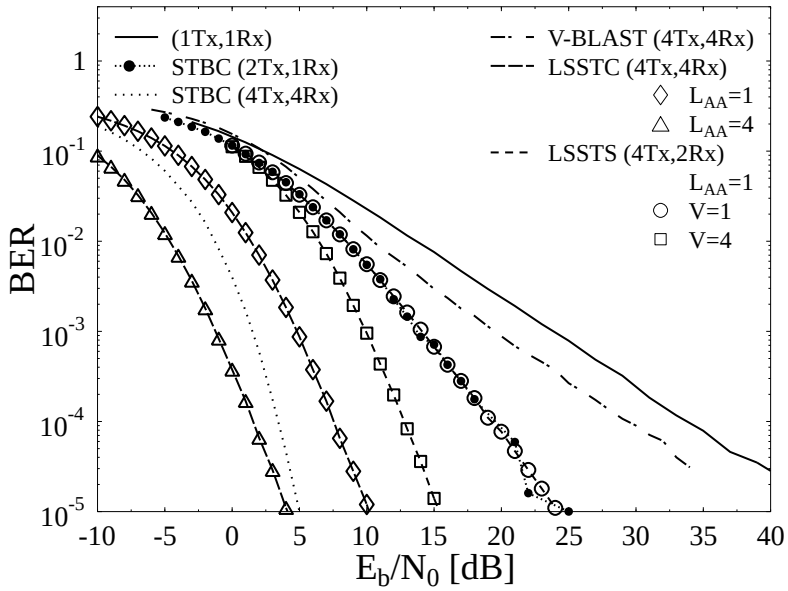

Figure 1.5: BER performance comparison of the SISO, STBC, V-BLAST, LSSTC and LSSTS schemes, while communicating over a correlated Rayleigh fading channel associated with a normalised Doppler frequency of f_d=0.01.

Table 1.1: Comparison of the gains achieved by various MIMO schemes.

	N_t	N_r	L_{AA}	V	Number of Layers	Diversity Order	Multiplexing Order	Beamforming Order
STBC	2	N_r	1	1	1	$2 \times N_r$	1	1
	4	N_r	1	1	1	$4 \times N_r$	1/2	1
	8	N_r	1	1	1	$8 \times N_r$	1/2	1
V-BLAST ZF-SIC	2	2	1	1	2	1	2	1
	4	4	1	1	4	1	4	1
	8	8	1	1	8	1	8	1
LSSTC	4	4	L_{AA}	1	2	4	2	L_{AA}
	8	8	L_{AA}	1	2	16	1	L_{AA}
	8	8	L_{AA}	1	4	4	4	L_{AA}
LSSTS	4	2	L_{AA}	V	2	$2 \times V$	2	L_{AA}

According to Figure 1.5, the V-BLAST system employing $(N_t, N_r)=(4,4)$ antennas has a slightly better BER performance than the SISO system, despite its quadrupled throughput. Also observe in Figure 1.5 that the slope of the BER curves of both the V-BLAST and of the SISO system is similar, which suggests that V-BLAST does not attain a high diversity gain, but it is capable of attaining a high multiplexing gain. Additionally, Figure 1.5 shows that the STBC system employing $(N_t, N_r)=(2,1)$ attains a better BER performance than the SISO and V-BLAST schemes due to the diversity gain attained by the STBC. Further diversity gain can be attained by the four-antenna aided STBC employing four receive antennas, which results in a diversity order of 16. As shown in Figure 1.5 the four-antenna-aided STBC scheme employing four receive antennas is capable of attaining around 15 dB gain at a BER of 10^{-5} over the twin-transmit-antenna aided STBC system using N_r=1. However, a drawback of the four-antenna aided system is that it results in a throughput loss, where four symbols are transmitted in eight time slots, resulting in a rate of 1/2.

Observe in Figure 1.5 that the LSSTS scheme employing $(N_t, N_r)=(4,2)$ and V=1 attains an identical BER performance to that of the twin-transmit-antenna aided STBC system. This means that the LSSTS scheme employing V=1 has a diversity order of 2 similar to the twin-antenna aided STBC. On the other hand, the LSSTS scheme attains twice the throughput of the twin-transmit-antenna aided STBC scheme. Additionally, when V is increased from 1 to 4, the achievable BER performance improves due to the additional frequency diversity gain attained.

A further performance improvement is attained by the LSSTC scheme in conjunction with $(N_t, N_r)=(4,4)$ compared to the LSSTS scheme. The LSSTC scheme employs more antennas than the LSSTS scheme and hence attains both a higher diversity order as well as a better BER performance. Furthermore, Figure 1.5 shows the performance improvements attained by beamforming, where the LSSTC scheme employing L_{AA}=4 attains around 6 dB performance improvement at a BER of 10^{-5} over its counterpart employing L_{AA}=1, provided that the DOA is perfectly known. Finally, a comparison between the STBC and LSSTC schemes using $(N_t, N_r)=(4,4)$ reveals that the STBC arrangement attains a better performance than the LSSTC scheme employing L_{AA}=1. This is due to the fact that the STBC scheme has a higher diversity gain, while the LSSTC scheme attains a throughput that is 4 times that of its STBC counterpart.

1.2.4 Diversity versus Multiplexing Tradeoffs in MIMO Systems

According to our previous discussions, different MIMO schemes have different structures and hence a different BER as well as throughput performance. Explicitly, the STBC scheme is capable of attaining the highest possible spatial diversity gain, while having no multiplexing gain, in fact, some STBC structures result in a throughput loss. On the other hand, the V-BLAST scheme is capable of achieving the maximum possible multiplexing gain, while attaining a low diversity gain, depending on the choice of the V-BLAST decoder employed. Furthermore, we have introduced the LSSTC and LSSTS multi-functional MIMO designs that are capable of attaining diversity, multiplexing as well as beamforming gains.

Table 1.1 compares the diversity, multiplexing and beamforming gains of the different MIMO schemes for different configurations. In Table 1.1, N_t and N_r stand for the number of transmit and receive antennas, respectively, while L_{AA} represents the number of elements per transmit AA and V denotes the number of subcarriers employed by the generalised MC DS-CDMA system. Additionally, the number of layers represents the number of antenna layers that is used for transmitting different data symbols at the same time, for the sake of attaining a multiplexing gain.

As shown in Table 1.1, the STBC schemes are capable of attaining a full diversity order of $(N_t \times N_r)$, while achieving no multiplexing or beamforming gain. By contrast, in the case of four-antenna and eight-antenna aided STBC schemes, the multiplexing gain is 1/2, resulting in half the throughput of the SISO scheme. For example, in the four-antenna aided STBC scheme, four symbols are transmitted in eight time slots and similarly for the eight-antenna aided STBC

scheme, eight complex-valued symbols are transmitted in 16 time slots. On the other hand, as shown in Table 1.1, the V-BLAST scheme can attain a multiplexing gain of N_t, since the different antennas transmit different symbols in the same time slot. For example, for the V-BLAST scheme employing $(N_t, N_r)=(4, 4)$, the transmitter transmits four different symbols from the four different antennas in the same time slot, which results in a quadrupled multiplexing gain in comparison to that of the SISO scheme. Observe in Table 1.1 that the diversity order of V-BLAST employing the ZF-SIC is 1 for different (N_t, N_r) configurations. The diversity order of the V-BLAST scheme employing ZF-SIC is $(N_r - N_t + 1)$.

The LSSTC scheme combines the benefits of STBC, V-BLAST as well as of beamforming, as discussed earlier. This becomes clear in Table 1.1, where it is shown that the LSSTC scheme attains a diversity gain, a multiplexing gain as well as a beamforming gain. In the case of the $(N_t, N_r)=(4, 4)$ configuration, two twin-antenna STBC layers are implemented, which results in a diversity order of 4 and a multiplexing order of 2. This is due to the fact that four symbols are transmitted from the four transmit antennas in two time slots. Additionally, when L_{AA} elements are used per AA, then a beamforming gain can be attained. In the $(N_t, N_r)=(8, 8)$ configuration, two different schemes can be implemented. The first scheme is a two-layer one with each layer constituted of a four-antenna STBC scheme. The other configuration employs four layers of the twin-antenna STBC scheme. The two configurations result in the different diversity and multiplexing gains shown in Table 1.1.

Finally, in the LSSTS scheme four transmit and two receive antennas are employed, where the transmit antennas are separated into two STS layers. The diversity order achieved by the LSSTS scheme is $(2 \times V)$ as discussed in Section 1.2.2.2. The multiplexing order of the LSSTS scheme is 2, since four symbols are transmitted in two time slots. Moreover, the LSSTS scheme is capable of attaining a beamforming gain, when $L_{AA} > 1$ elements per AA are used.

In this section a brief classification of MIMO schemes was presented based on their attainable diversity, multiplexing or beamforming gains. We also investigated the design of multi-functional MIMO schemes that are capable of combining the benefits of several MIMO schemes and hence attaining diversity, multiplexing as well as beamforming gains. More explicitly, we introduced two multi-functional MIMO schemes: LSSTC and LSSTS. The LSSTC combines the benefits of STBC, V-BLAST as well as beamforming, while the LSSTS combines the advantages of STS, V-BLAST and beamforming with those of generalised MC DS-CDMA, while supporting multiple users. Finally, a comparison between the BER performance as well as the diversity, multiplexing and beamforming gains of the different MIMO schemes reveals that multi-functional MIMOs are capable of attaining an improved performance over STBC and V-BLAST schemes.

1.3 Coherent vs. Non-Coherent Detection for STBCs Using Co-located and Cooperative Antenna Elements

1.3.1 Motivation

Again, our objective in this conceptually motivated section is to provide a brief overview of the material discussed in intricate detail in Part II of the monograph. More specifically, we will briefly consider the design alternatives of various STBCs documented in the open literature, focussing our attention on the so-called orthogonal design approach and on the layered method. We introduce the generalized concept of the linear dispersion space-time coding architecture, which allows us to strike a compromise between the above-mentioned two approches. We will also demonstrate that the powerful linear dispersion structure is capable of unifying the entire suite of existing schemes. As a further benefit, it offers extra design flexibility so that diverse system requirements can be satisfied. Furthermore, after characterizing the fundamental relationship between STBCs and Differential STBCs (DSTBCs), we highlight the benefits of non-coherently detected schemes, which

are capable of exploiting the advantages of multiple antennas, while circumventing the potentially excessive burden of multi-antenna channel estimation. Additionally, we will demonstrate that the linear dispersion structure can also be applied in systems, where the multiple-antenna array is formed in a distributed fashion by multiple single-antenna-aided cooperating mobile stations. Hence, the design of co-located and cooperative MIMO systems aiming for achieving diversity is linked from a linear dispersion perspective.

As argued above, apart from employing multiple antennas at the transmitter and receiver in a 'co-located' fashion, a Virtual Antenna Array (VAA) may also be formed by a group of cooperating single-antenna-aided mobile stations. The resultant cooperative MIMO system is capable of offering similar degrees of freedom to those of a co-located MIMO system having independently fading signal impinging on the antenna elements. In other words, the distributed MIMO elements are capable of mimicking the functionality of the co-located MIMO elements.

The advantage of a MIMO system can be exploited in two ways: to increase the reliability of the system by providing a diversity gain [24] and/or to increase the data rate by providing multiplexing gain [24]. In fact, it has been shown that there is a fundamental tradeoff between the achievable diversity gain and the attainable multiplexing gain for a given MIMO system [24]. The term spatial multiplexing gain refers to the fact that one can use multiple antennas to achieve a higher throughput at the cost of an increased SNR requirement. On the other hand, the concept of spatial diversity is to provide multiple independently fading replicas of the transmitted signal for the receiver with the aid of the MIMO channel. If indeed these replicas are faded independently, it is unlikely that all copies of the transmitted signal are in a deep fade simultaneously. Therefore, the receiver is expected to reliably decode the transmitted signal using these independently faded received signals. Finally, apart from the 'spatial' dimension, diversity can also be achieved in both the temporal as well as the frequency domains.

In many practical scenarios, reliable wireless communications may not be guaranteed, even when multiple antennas have been employed. For example, when large-scale shadow fading contaminates the wireless links, all the channels tend to fade together rather than independently, hence eroding the achievable diversity gain. Therefore, the concept of 'cooperative diversity' [25] has been proposed in the literature, which is a technique designed for providing diversity using the single antennas of other nodes in the cellular network as 'virtual' antennas.

In this section the design philosophies of spatial-diversity-oriented Space-Time Block Codes (STBCs) designed for open-loop MIMO systems are presented from a unique linear dispersion perspective. More explicitly, Section 1.3.2 demonstrates various design guidelines of STBCs and presents a general framework to unify all the existing coherently detected STBCs found in the open literature. Section 1.3.3 exploits the linkage between coherently detected STBCs and non-coherently detected STBCs having no Channel State Information (CSI), which enables our general framework to incorporate the subclass of differential encoding/decoding techniques. Similarly, Section 1.3.4 examines the fundamental linkage between co-located and cooperative MIMO systems. Hence, cooperative STBCs can be created by applying the general linear dispersion framework. The expected performance is illustrated in Section 1.3.5, along with the related brief conclusions.

1.3.2 Evolution of Space-Time Block Codes

In order to exploit both the spatial as well as temporal domains offered by a MIMO system, STBCs transmit a signal matrix $\mathbf{S}$ conveying the source information. For a MIMO system having M transmit and N receive antennas, a STBC scheme can be designed to transmit Q symbols using T channel slots. The STBC scheme may be described by the parameter combination $(MNTQ)$ having the normalized throughput of $R = Q/T$. In other words, the concept of STBCs is to design a set of matrices $\mathbf{S}$ satisfying both the throughput as well as diversity order requirements under certain complexity constraints. However, the number of matrices to be designed may become excessive, when the system is operating at a high normalized throughput facilitated by a high number of

antennas. This challenge was mainly addressed from two perspectives in the open literature, namely from the orthogonal and the layered approaches, both of which will be highlighted below.

1.3.2.1 Orthogonal Approach

The 'orthogonal' approach was first proposed in [10], which was later generalized in [26]. The philosophy behind Orthogonal STBCs (OSTBCs) is that the space-time signal matrix $\mathbf{S}$ has to be an orthogonal/unitary matrix, where the orthogonality embedded in $\mathbf{S}$ is capable of decoupling the transmitted multi-antenna-coded symbol streams into independent single-antenna symbols. For example, Alamouti's scheme [10] can be characterized as follows:

$$\mathbf{G}_2 = \begin{pmatrix} s_1 & s_2 \\ -s_2^* & s_1^* \end{pmatrix}. \tag{1.1}$$

Although the associated single-stream decoding procedure is appealing, the orthogonality of the multi-antenna streams limits the choice of modulation schemes and restricts the antenna configurations supported. Hence, the OSTBCs are unable to reach a high normalized throughput. On the other hand, when relaxing the above-mentioned orthogonality of the OSTBCs, a potentially higher normalized throughput can be achieved, as exemplified by the family of Quasi-Orthogonal STBCs (QOSTBCs) [15].

Furthermore, the design of OSTBCs involves the inevitable throughput versus diversity gain tradeoff characterized in [27]. This is because each spatial and temporal slot is used to convey either a new symbol to increase the throughput or a redundant symbol to attain diversity. However, with the aid of the recent advances in high-throughput full-diversity [1] STBCs [28], it has been shown that it is not necessary to sacrifice the throughput in favor of achieving diversity or vice versa. The philosophy of these schemes is that they impose redundancy on the space-time codeword, but additional diversity gain can be achieved by spreading the information across both the spatial and temporal domains. We will elaborate on this idea in more detail using Linear Dispersion Codes (LDCs) [28] [29] in Section 1.3.2.3.

1.3.2.2 Layered Approach

The motivation of introducing a 'layered' structure into the STBCs is that of supporting high-throughput communications, as exemplified by schemes such as Bell Labs' Layered-Space-Time (BLAST) architecture [16]. Although conventional BLAST-type schemes were not designed for achieving diversity, they provide a new insightful angle for STBC designs. For example, the $\mathbf{G}_2$ STBC of Equation (1.1) can be considered as a scheme consisting two layers. The first layer only conveys the information symbol s_1, which is 'repetition-coded' and mapped to one of the diagonals of Equation (1.1). The second layer contains the symbol s_2, which is mapped to the other diagonal of Equation (1.1). Each layer occupies half of the four spatial and temporal slots and the inherent orthogonality enables the receiver to separate the two layers to facilitate simple single-layer decoding. Since having more layers has the promise of an increased normalized throughput, the question of how many layers can a STBC codeword accommodate arises. In the literature, the authors of [30] proposed a class of STBCs employing a unitary Time Variant Linear Transformation (TVLT), which is capable of transmitting using T layers, while maintaining a normalized throughput of $R = M$. Furthermore, high-throughput Threaded Algebraic Space-Time Block Codes (TASTBCs) [31] were proposed in order to support up to M number of adaptively reconfigurable layers. One of the intriguing features of both TVLTs and TASTBCs is that both of them are capable of achieving the full attainable spatial diversity order of MN, while maintaining a high throughput. This is guaranteed by mapping the signals of each layer across all the antennas,

[1] Using the average pairwise symbol error probability analysis technique [26], it follows that the maximum attainable diversity order of a STBC scheme designed for an $(M \times N)$-element MIMO system is $D_{full} = MN$.

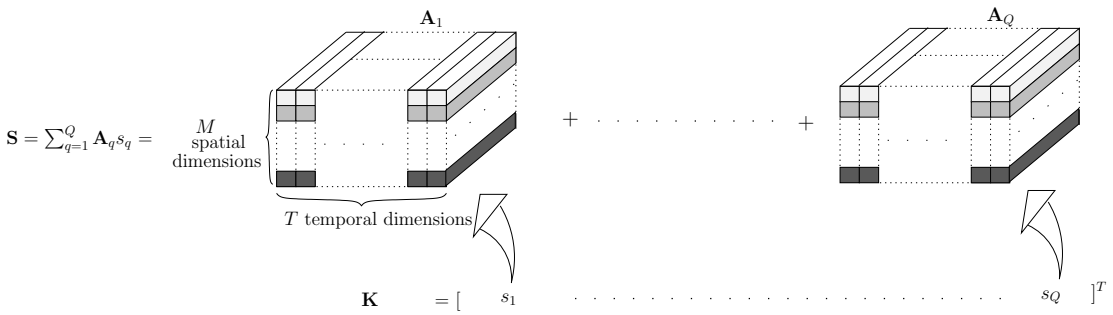

Figure 1.6: The space-time codeword $\mathbf{S}$ employing the linear dispersion structure.

in order to achieve spatial diversity, as exemplified in Equation (1.1). Again, this philosophy will be further augmented using the linear dispersion structure below.

1.3.2.3 Linear Dispersion Codes

At this stage of our discussions, the challenge of STBC design becomes that of finding an appropriate way of relaxing the orthogonality, while maintaining the maximum diversity order of MN. Alternatively, we may cast this design dilemma as contriving a 'layered' structure capable of exploiting all the spatial and temporal diversity resources available for a single layer, while supporting multiple layers. Remarkably, these design objectives may be satisfied by the family of LDCs proposed by Hochwald and Hassibi [29]. The revolutionary concept of LDCs [28] [29] invokes a matrix-based linear modulation framework, where each space-time transmission matrix $\mathbf{S}$ is generated by a linear combination of so-called dispersion matrices and the weights of the components are determined by the associated transmitted symbol vector. More explicitly, given an information symbol vector $\mathbf{K} = [s_1, s_2, \ldots, s_Q]^T$ constituted by symbols of an arbitrary modulation constellation, the transmitted space-time matrix $\mathbf{S}$ may be defined as [28] $\mathbf{S} = \sum_{q=1}^{Q} \mathbf{A}_q s_q$, where each symbol s_q is dispersed to the M spatial- and T temporal dimensions using a specific dispersion matrix $\mathbf{A}_q \in \zeta^{M \times T}$ and $\mathbf{S}$ is attained by the linear combination of all the weighted dispersion matrices. The schematic of the LDCs is specifically visualized in Figure 7.4.

Hence, it is beneficial to revisit the OSTBCs of Section 1.3.2.1 using the linear dispersion structure of Figure 1.6. More explicitly, if each individual dispersion matrix $\mathbf{A}_q$ is an orthogonal matrix and the set of dispersion matrices are orthogonal to each other, the resultant space-time codeword $\mathbf{S}$ has to be an orthogonal/unitary matrix achieving full diversity [32]. This design philosophy is that of the family of Linear STBCs (LSTBCs) [32]. Furthermore, by appropriately choosing the set of dispersion matrices depicted in Figure 1.6, the degree of orthogonality can be adjusted, leading to an increased design flexibility.

When compared to the layered STBCs discussed in Section 1.3.2.2, the LDCs of Figure 1.6 consist of Q layers corresponding to the number of symbols transmitted per space-time block. Since the parameter Q is unrestricted, LDCs are capable of supporting an arbitrary number of layers. Furthermore, rather than using only some of the $(M \times T)$ slots available, each layer of the LDCs spans all the dimensions available, resulting in a high number of legitimate dispersion matrices. However, it may not be feasible to perfectly separate the high number of superimposed layers, unless sophisticated multi-stream receivers are used.

In summary, the LDCs of Figure 1.6 subsume all the above-mentioned space-time block codes exhibiting diverse characteristics by simply employing different sets of dispersion matrices. Hence, the LDCs provide a natural framework for satisfying diverse design criteria. Below, we offer a range of further remarks concerning LDCs.

- LDCs are suitable for arbitrary transmit and receive antenna configurations, combined with arbitrary modulation schemes;
- The maximum achievable diversity order of an LDC scheme is $N \cdot \min(M, T)$. This implies that increasing T beyond M does not provide any further advantage in terms of an increased diversity, whereas having $T < M$ could decrease the maximum achievable spatial diversity order. As expected, the receive diversity order is determined by the number of receive antennas N alone. For the proof of the theorem please refer to [28].
- Every transmitted signal launched from each antenna is the linear combination of all the information symbols weighted by a set of dispersion matrices of Figure 1.6, which ensures that different replicas of the same information symbol are attainable. In other words, LDCs demonstrate that spatial diversity can also be achieved without transmitting redundant information at the cost of reducing the normalized throughput R.
- All the dispersion matrices $\mathbf{A}_q$ of Figure 1.6 can be described with the aid of the a single Dispersion Character Matrix (DCM) χ specified by $\chi = [vec(\mathbf{A}_1), vec(\mathbf{A}_2), \ldots, vec(\mathbf{A}_Q)]$, where the $vec()$ operation represents the vertical stacking of the columns of an arbitrary matrix. The benefit of using a single DCM is that there is no need to design Q number of separate dispersion matrices.
- The linear nature of Figure 1.6 enables the receiver to recover the source information, provided that the CSI is perfectly known at the receiver.

As far as the design of the set of dispersion matrices or the DCM is concerned, in their original form, the LDCs [29] were optimized to maximize the ergodic capacity. In practice, the channel's input is constituted by non-Gaussian symbols, such as discrete-amplitude PSK and QAM signals, where a Discrete-input Continuous-output Memoryless Channel (DCMC) is encountered. Therefore, the more pertinent DCMC capacity is employed to optimize the LDCs [33]. Naturally, other optimization criteria can also be imposed on the DCM. For example, the authors of [28] specifically designed the LDCs to maximize the ergodic capacity, while maintaining a low BER. On the other hand, LDCs can also be optimized using the so-called determinant criterion [26], where having a non-vanishing determinant is guaranteed.

1.3.3 Differential STBCs Using Colocated Antenna Elements

The primary focus of the codes discussed in Section 1.3.2 has been the case, where the receiver has the knowledge of the CSI. In practice, the knowledge of the CSI is typically acquired using a channel sounding sequence, which has an exponentially increasing complexity as a function of the number of antennas. Furthermore, the relative frequency of estimating the channel has to be increased proportionately to the Doppler frequency. Finally, an excessive number of training symbols may be required. Hence, precious transmit power as well as valuable bandwidth are wasted. Therefore, differentially encoded low-complexity schemes, dispensing with pilot-based channel estimation and invoking non-coherent detection became attractive.

The conventional Differential PSK (DPSK) designed for single antenna aided systems differentially encodes the information between successive transmission symbols, thus the information can be recovered without the knowledge of the CSI, provided that the CSI does not change substantially between them. A DPSK scheme is constituted by the serial concatenation of a PSK modulator and a differential encoder. Here, we extend this philosophy to multiple antenna aided systems and the schematic of the resultant Differential STBC (DSTBC) system is portrayed in Figure 1.7.

More explicitly, the 'space-time mapper' of Figure 1.7 maps the n-th differentially encoded transmission matrix $\mathbf{S}_n$ to all the spatial and temporal slots, whereas the 'differential encoder' of Figure 1.7 correlates the consecutive transmission matrices by $\mathbf{S}_n = \mathbf{S}_{n-1} \cdot \mathbf{X}_n$, where $\mathbf{X}_n$ is the

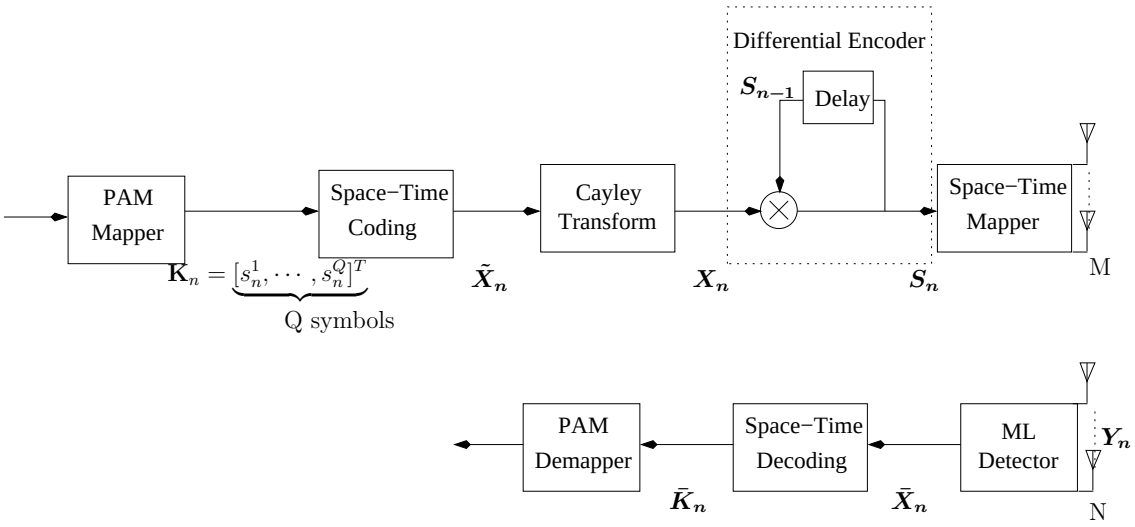

Figure 1.7: Schematic of a DLDC($MNTQ$) scheme equipped with M transmit and N receive antennas and employing the Cayley transform, while transmitting Q symbols over T time slots using $\mathbf{S}_n$.

space-time coded information matrix. Furthermore, this differential encoding process restricts the set of matrices $\mathbf{X}_n$ to be unitary, otherwise, the product $\mathbf{S}_n = \mathbf{X}_n\mathbf{X}_{n-1}\cdots\mathbf{X}_1$ may become zero, infinity, or both in different spatial and temporal directions. **In other words, the challenge of designing DSTBCs can be described as that of designing a family of STBCs, where all the space-time matrices $\mathbf{X}_n$ are unitary.**

Recall that the OSTBCs detailed in Section 1.3.2.1 generate orthogonal/unitary matrices by default, hence they become natural candidates for employment in DSTBC designs. Since the LDCs exhibit a high design flexibility as demonstrated in Section 1.3.2.3, it is desirable to retain the linear dispersion architecture in the differential design. Hence, the 'space-time encoding' block of Figure 1.7 is configured to generate space-time codewords $\tilde{\mathbf{X}}_n$ obeying the linear dispersion structure of Figure (1.6). However, even if each individual dispersion matrix is a unitary matrix, there is no guarantee that their weighted sum $\tilde{\mathbf{X}}_n$ will automatically become a unitary matrix. Hence, the 'Cayley transform' [13] block of Figure 1.7 is introduced in order to provide an efficient way of projecting the linearly-structured matrix $\tilde{\mathbf{X}}_n$ into a unique unitary matrix $\mathbf{X}_n$, which potentially facilitates the differential encoding of Figure 1.7. Apart from its additional computational complexity, the Cayley transform requires the employment of real-valued modulation schemes in order to generate the unitary matrices. Also note that the DSTBCs typically suffer from a 3dB penalty in comparison to the STBCs having perfect CSI, owing to the doubled equivalent channel noise encountered during the detection.

In summary, the design of DSTBCs based on coherently detected STBCs is facilitated by the 'unitary' constraint. Furthermore, the philosophy of LDCs may be extended to the differential encoding domain and the resultant Differential Linear Dispersion Codes (DLDCs) based on the Cayley transform [34] provide a general framework for DSTBCs. Consequently, DLDCs are capable of supporting arbitrary antenna configurations as well as a dynamically reconfigurable throughput. Similarly to LDCs, all the dispersion matrices of a DLDC scheme can be characterized by a single DCM. On the other hand, the performance of DLDCs is affected by the rate of Doppler-induced channel fluctuations.

1.3.4 Cooperative STBCs Using Distributed Antenna Elements

The STBC techniques detailed in Sections 1.3.2 and 1.3.3 provide promising solutions in the context of co-located MIMO systems requiring reliable wireless communications at high rates. However, it may not always be practical to accommodate multiple antennas at the mobile stations, owing to cost, size and other hardware limitations. A further limitation of having co-located MIMO elements is that even at relatively large element separations their elements may not benefit from independent fading, when subjected to shadow-fading imposed for example by large-bodied vehicles or other shadowing local paraphernalia. As a remedy, the concept of cooperative MIMOs have been proposed for cellular systems as an attempt to attain a better communication efficiency beyond that permitted by a single node's resources. More specifically, a group of mobile nodes, known as relays, 'shares' their antennas with other users to create a VAA to provide spatial diversity gain.

Owing to the philosophical similarities between the cooperative MIMO and the co-located MIMO systems, numerous space-time block coding techniques have been 'transplanted' into relay-aided schemes in order to achieve cooperative diversity, based on either Amplify-and-Forward (AF) strategies or Decode-and-Forward (DF) arrangements. It was Laneman and Wornell [25] who first proposed to employ OSTBCs for cooperative MIMO systems, where each relay transmits according to a different column of the orthogonal STBC matrix. In this section, we focus our attention on the employment of the LDC structure in the context of cooperative MIMO systems, namely in twin-layer Cooperative LDCs (CLDCs).

Figure 1.8 portrays the schematic of the cooperation-aided UpLink (UL) system using the above-mentioned twin-layer CLDC. As seen in Figure 1.8, each transmission block consists of two intervals, namely the broadcast interval of duration T_1 and the cooperation interval of length T_2. This scheme supports the cooperation of M number of relays transmitting Q information symbols per block to the base station equipped with N receive antennas, provided that the total number of channel uses T obeys $T = T_1 + T_2$.

The assumptions and the rationale of this model are summarized as follows:

- All the relays of Figure 1.8 are assumed to transmit synchronously. Quasi-synchronous transmissions can be accomplished, when the relative delays between the relays are significantly shorter than the symbol duration;
- All the nodes of Figure 1.8 are assumed to have a single antenna and hence operate in half-duplex mode, i.e. at any point of time, a node can either transmit or receive. This constraint is imposed, in order to prevent the high-power transmit signal from contaminating the low-power received signal, for example, by the non-linear distortion-induced out-of-bound emissions routinely encountered at the transmitter.
- All the relays of Figure 1.8 transmit and receive on the same frequency as the source node, in order to avoid wasting or occupying additional bandwidth;
- No communication is permitted between the relays, in an effort to minimize the total network traffic. The relays may use the same previously unallocated time-slot for their reception and transmission;
- Since the simple AF strategy is adopted, only linear combination operations are performed at the relays before retransmitting the signals dispersed to the cooperating MIMO elements to the BS;
- We confine the total number of channel uses of the twin-layer CLDC scheme of Figure 1.8 to T. Hence, by appropriately adjusting the parameters T_1 or T_2, different degrees of freedom can be provided for the broadcast interval as well as for the cooperation interval;
- At any given time, the total transmit power of the twin-layer CLDC scheme of Figure 1.8 is normalized to unity.

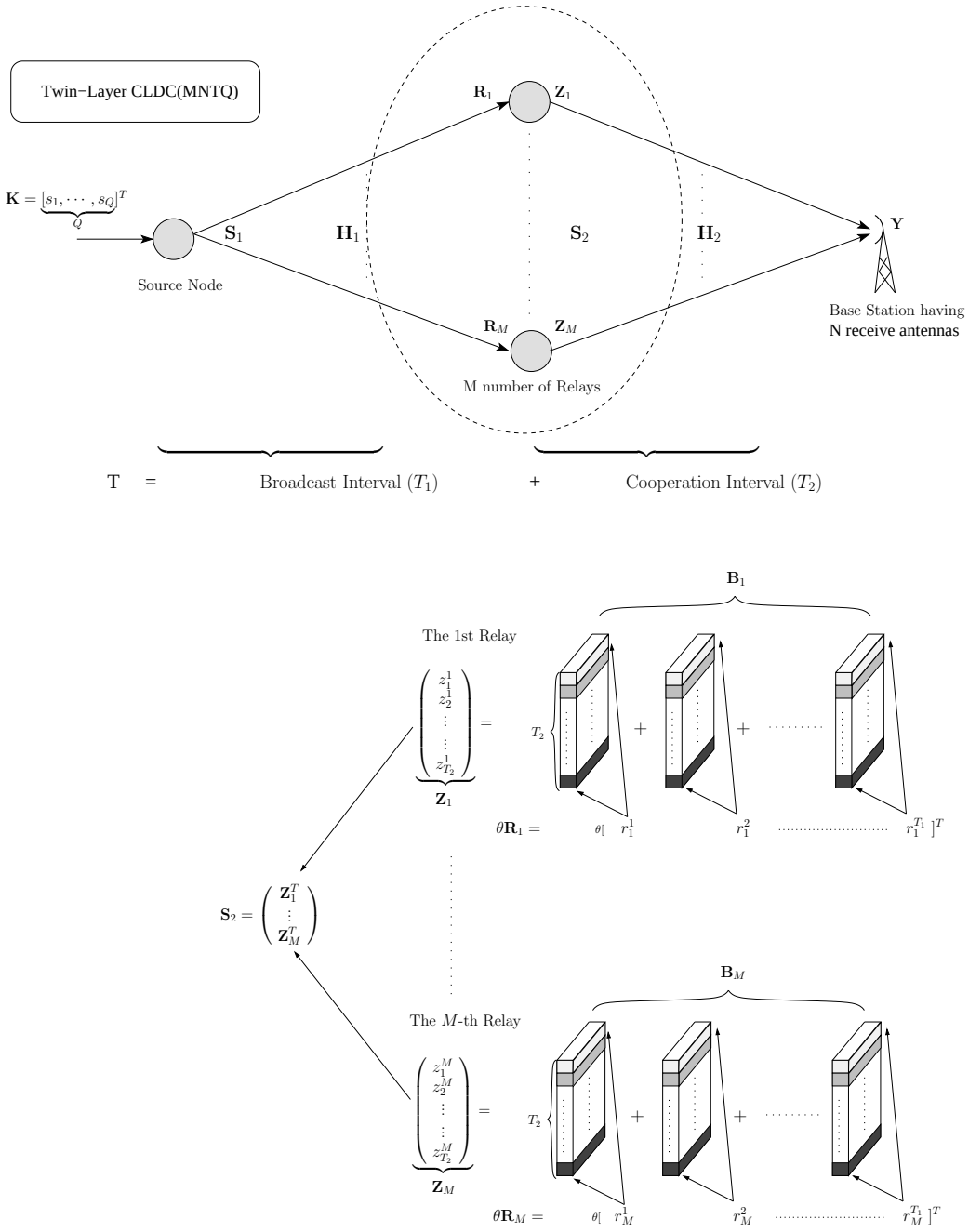

Figure 1.8: Schematic of the cooperation-aided uplink system employing twin-layer Cooperative Linear Dispersion Codes (CLDCs).

During the broadcast interval T_1, the first-layer dispersion matrix χ_1 is responsible for dispersing the source information vector $\mathbf{K} = [s_1, \ldots, s_Q]^T$ to all the T_1 temporal slots. The resultant space-time codeword $\mathbf{S}_1$ of Figure 1.8 is transmitted through independent source-to-relay Rayleigh fading channels. The received signal vector of the m-th relay is $\mathbf{R}_m$. During the cooperation interval T_2, the relays form a VAA and cooperatively transmit the space-time codeword $\mathbf{S}_2$ of Figure 1.8 to the BS based on CLDC's second-layer dispersion matrix. More explicitly, the process of forming the cooperative space-time codeword $\mathbf{S}_2$ for the cooperation interval is also visualized in Figure 1.8. Each relay contributes one row of the cooperative space-time codeword $\mathbf{S}_2$ by dispersing the corresponding normalized received signal vector $\theta\mathbf{R}_m = \theta[r_m^1, \ldots, r_m^{T_1}]^T$ to the available T_2 temporal slots using the pre-assigned dispersion matrix. Again, the dispersion matrices from all the relays can be characterized by a single DCM χ_2. Hence, the receiver can recover the source information by exploiting the linearity of the CLDCs, provided that the CSI as well as the dispersion matrices χ_1 and χ_2 are known at the receiver. Since only T_2 time slots are used for achieving cooperative diversity and the relays only have access to the noisy version of the transmitted information, the maximum achievable diversity order of the CLDCs becomes $D \approx N \cdot \min(M, T_2)$.

Hence, we conclude that the fundamental difference between cooperative and co-located MIMO systems is the existence of the broadcast interval, which is used by the relays to attain preferably perfect but typically imperfect source information, depending on the specific cooperation strategy employed. As a result, instead of employing a single DCM as in the LDC scheme, the CLDC scheme requires a pair of DCMs (χ_1, χ_2) in order to characterize the transmission regime of both the broadcast interval and of the cooperation interval, respectively.

1.3.5 Performance for Imperfect Channel Estimates and Shadow-Fading

In this section, we provide a set of comparisons between the family of LDCs, DLDCs and CLDCs in order to evaluate their advantages as well as limitations, when communicating in *small*-scale or *large*-scale fading scenarios as well as when having *perfect* or *imperfect* CSI at the receiver. All the simulation parameters were listed in Table 1.2. Observe in Table 1.2 that we set $M = T$ and assume that the channels were subjected to Rayleigh fading having $f_d = 10^{-2}$ in order to enable the adequate operation of the DLDCs based on the Cayley transform. Hence, the group of LDCs and DLDCs have the potential to achieve the full attainable diversity order of $D = N \cdot \min(M, T)$ [28] in comparison to the reduced maximum diversity order $D \approx N \cdot \min(M, T_2)$ of the CLDCs.

For Comparison A of Table 1.2, Figure 1.9 characterizes the achievable throughput of the group of LDCs, DLDCs and CLDCs recorded at BER=10^{-4}, when the wireless channels were subjected to *small*-scale Rayleigh fading and *perfect* CSI was available at the receiver. Observe in Figure 1.9 that the class of LDCs is capable of operating at the lowest SNR at a certain throughput. The group of DLDCs suffers from the usual 3dB SNR penalty in comparison to that of the LDCs, since no CSI was exploited. The family of CLDCs operates at SNRs further away from that of the LDCs, owing to their reduced achievable diversity order as well as due to having the noisy rather than perfect version of the source information.

For Comparison B of Table 1.2, Figure 1.10 characterizes the effective throughput of the LDCs, the DLDCs and the CLDCs of Table 1.2 recorded at BER=10^{-4}, when the wireless channels were subjected to *small*-scale Rayleigh fading and the receiver has *imperfect* CSI. We assume that the channel estimation errors obey the Gaussian distribution and the degree of the CSI estimation errors is governed by the ratio ω (dB) with respect to the received signal power. Hence, the perfect CSI scenario corresponds to $\omega = -\infty$. Observe in Figure 1.10 that the family of DLDCs demonstrated a significant advantage over the LDCs at a high throughput, even when the channel estimation errors were as low as $\omega = -10$dB. Since the group of CLDCs has an error floor higher than BER=10^{-4}, the associated throughput curve was omitted from Figure 1.10. This phenomenon suggested that the CLDCs are more sensitive to the channel estimation errors than

Table 1.2: Comparison of the LDCs of Section 1.3.2.3, the DLDCs of Section 1.3.3 and the CLDCs of Section 1.3.4, when communicating over small-scale/large-scale fading channels and having perfect/imperfect CSI at the receiver.

	LDC	**DLDC**	**CLDC**
M	3	3	3
N	2	2	2
T	3	3	$T_1 = 1, T_2 = 2$
Q	1,2,3	1,2,3	1,2,3
Modulation	BPSK	BPSK	BPSK
Mapping	Gray mapping	Gray mapping	Gray mapping
Detector	ML	ML	ML
Doppler frequency	$f_d = 10^{-2}$	$f_d = 10^{-2}$	$f_d = 10^{-2}$
Diversity	$D = 6$	$D = 6$	$D \approx 4$
Comparison A	*Small*-scale Rayleigh fading, *perfect* CSI in Figure 1.9		
Comparison B	*Small*-scale Rayleigh fading, *imperfect* CSI in Figure 1.10		
Comparison C	*Large*-scale shadowing, *perfect* CSI in Figure 1.11		

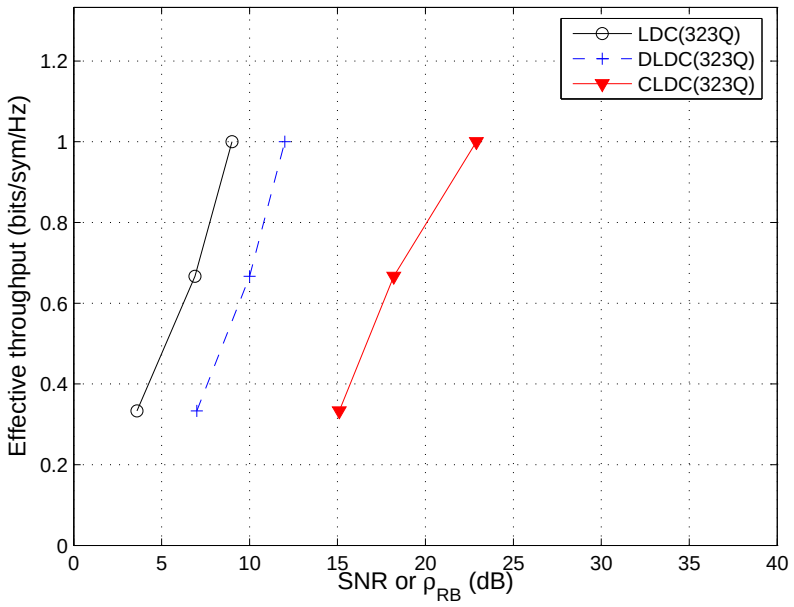

Figure 1.9: Throughput comparison for the LDCs of Section 1.3.2.3, the DLDCs of Section 1.3.3 and the CLDCs of Section 1.3.4 recorded at BER=10^{-4}, when communicating over *small*-scale Rayleigh fading channels and assuming that the *perfect* CSI was known by the receiver. All the system parameters were summarized in Table 1.2.

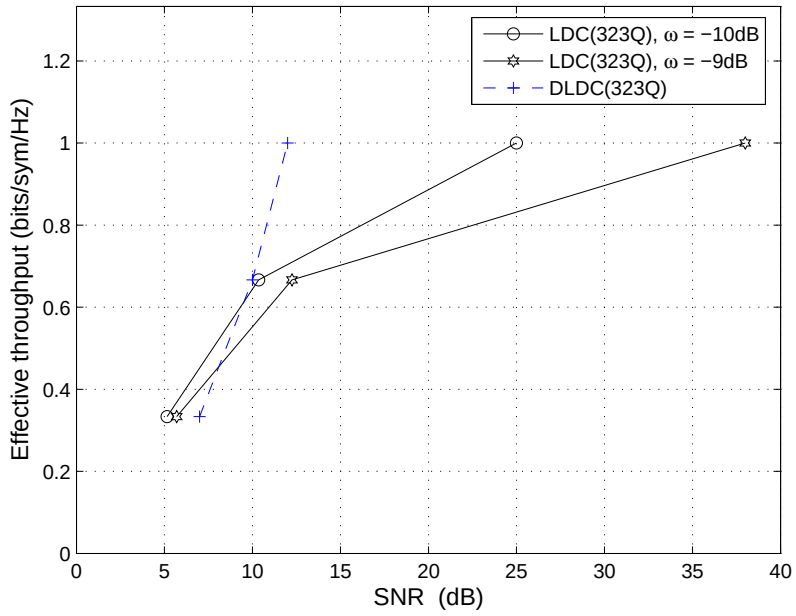

Figure 1.10: Throughput comparison for the LDCs of Section 1.3.2.3, the DLDCs of Section 1.3.3 and the CLDCs of Section 1.3.4 recorded at BER=10^{-4}, when communicating over *small*-scale Rayleigh fading channels and having *imperfect* CSI governed by ω (dB). All the system parameters were summarized in Table 1.2.

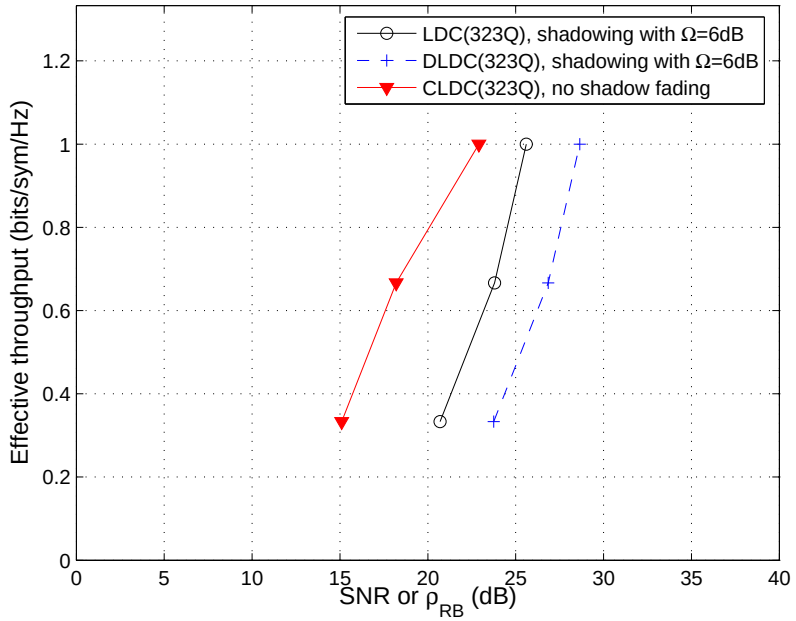

Figure 1.11: Throughput comparison for the LDCs of Section 1.3.2.3, the DLDCs of Section 1.3.3 and the CLDCs of Section 1.3.4 recorded at BER=10^{-4}, when the channels were subjected to *large*-scale shadowing and assuming that the *perfect* CSI was known at the receiver. All the system parameters were summarized in Table 1.2.

the LDCs. This is because the CLDCs require the CSI knowledge of both the source-to-relay and the relay-to-destination channels in comparison to the classic single-phase direct transmission regime of co-located MIMO systems.

Finally, in Comparison C of Table 1.2, Figure 1.11 characterizes the throughput of the LDCs, the DLDCs and the CLDCs of Table 1.2 recorded at BER=10^{-4}, when the communication channels were subjected to *shadowing* and the receiver had access to *perfect* CSI. The shadow fading effect was assumed to have log-normal distribution and was governed by a random Gaussian variable having zero mean and a standard deviation of Ω (dB). Observe in Figure 1.11 that the family of CLDCs designed for the cooperative MIMO systems has the best ability to combat the effect of large-scale shadowing with the aid of relays. Compared to the small-scale Rayleigh fading performance curves of Figure 1.9, the SNR required for the group of LDCs in Table 1.2 to maintain a BER of 10^{-4} increased by about 17dB, even though the receiver had access to perfect CSI.

Again, our investigations indicate that the LDCs obeying the structure of Figure 1.6 are ideal for small-scale fading environments, when near-perfect CSI is available. On the other hand, the DLDCs having the structure of Figure 1.7 constitute the most appropriate solution, when the CSI is unavailable or the channel estimation would impose severe errors. Finally, when large-scale shadowing dominates the achievable performance, the family of CLDCs obeying the structure of Figure 1.8 remains capable of maintaining reliable wireless communications.

In conclusion of this brief section, the design guidelines of diverse STBCs schemes found in the open literature were considered. More explicitly, we demonstrated that the linear dispersion structure unifies the orthogonal approach as well as the layered architecture. The flexibility of the LDCs allows them to be designed according to diverse constraints and to be adopted to various MIMO scenarios. Furthermore, the linkage between STBCs and DSTBCs may be established with the aid of the 'unitary' constraint, which enables us to invoke the LDC structure also in the differential encoding domain. In the case of cooperative MIMO systems, the flexible linear structure remains applicable, but an additional dipersion character matrix is required to characterize the transmissions during the broadcast interval. Finally, the rudimentary performance results provided explicitly demonstrated the suitable application scenarios for the various LDCs, DLDCs and CLDCs considered.

1.4 Historic Perspective and Sate-of-the-art Contributions

1.4.1 Colocated MIMO Techniques

MIMO systems exhibit higher capacity than single-antenna-aided systems. Multiple antennas can be used to provide diversity gains and hence a better BER performance or multiplexing gains, in order to attain a higher throughput. Additionally, multiple antennas can be used at the transmitter or receiver in order to attain a beamforming gain. On the other hand, multiple antennas can be employed in order to attain diversity gains, multiplexing gains as well as beamforming gains as shown in Figure 1.2. The terminology of colocated MIMOs refers to the systems, where the multiple antennas are located at the same transmitter or receiver station. In the sequel, we give an overview of the family of multiple antennas, when used for achieving diversity, multiplexing or beamforming gains.

1.4.1.1 Diversity Techniques

Communication in the presence of channel fading has been one of the grand research challenges in recent times. In a fading channel, the associated severe attenuation often result in decoding errors. A natural way of overcoming this problem is to allow the receiver to have several replicas of the same transmitted signal, while assuming that at least some of them are not severely attenuated.

Year	Author(s)	Contribution
1959	Brennan [35]	introduced and provided analysis for the three combining techniques: selection combining, maximum ratio combining and equal gain combining.
1991	Wittneben [36]	proposed a bandwidth-efficient transmit diversity technique, where different base stations transmit the same signal.
1993	Wittneben [37]	proposed a modulation diversity scheme in a system equipped with multiple transmit antennas.
	Seshadri *et al.* [38]	proposed a transmit diversity scheme that was inspired by the delay diversity design of Wittneben [37].
1994	Winters [39]	proved that the diversity advantage of the scheme proposed in [36] is equal to the number of transmit antennas.
1996	Eng *et al.* [40]	Compared several diversity combining techniques in a Rayleigh fading transmission with coherent detection and proposed a new second order selection combining technique.
1998	Alamouti [10]	discovered a transmit diversity scheme using two transmit antennas with simple linear processing at the receiver.
	Tarokh *et al.* [12]	proposed a complete study of design criteria for maximum diversity and coding gains in addition to the design of space-time trellis codes.
1999	Tarokh *et al.* [11, 26]	generalised Alamouti's diversity scheme [10] to more than two transmit antennas.
	Guey [41]	derived the criterion for designing the maximum transmit diversity gain.
2001	Hochwald *et al.* [14]	proposed the twin-antenna-aided space-time spreading scheme.
	Jafarkhani *et al.* [15]	designed rate-one STBC codes which are quasi-orthogonal and provide partial diversity gain.
2002	Hassibi *et al.* [13]	proposed the LDCs that provide a flexible trade-off between space-time coding and spatial multiplexing.
	Stoica *et al.* [42]	compared the performance of STBC when employing different estimation/detection techniques and proposed a blind detection scheme dispensing with the pilot symbols transmission for channel estimation.

Table 1.3: Major coherent spatial diversity techniques (Part 1).

This technique is referred to as diversity, where it is possible to attain diversity gains by creating independently fading signal replicas in the time, frequency or spatial domain.

Spatial diversity can be attained by employing multiple antennas at the transmitter or the receiver. Multiple antennas can be used to transmit and receive the same information sequence in order to achieve diversity and hence to obtain an improved BER performance. A simple spatial diversity technique, which does not involve any loss of bandwidth, is constituted by the employment of multiple antennas at the receiver. In case of narrowband frequency-flat fading, the optimum combining strategy in terms of maximising the SNR at the combiner output is Maximum Ratio Combining (MRC) [9, 35, 43]. Additionally, other combining techniques have been proposed in the literature, as shown in Figure 1.2, including Equal Gain Combining (EGC) [35] and Selection Combining (SC) [9]. All the three combining techniques are said to achieve full diversity order, which is equal to the number of receive antennas [40].

On the other hand, the idea of transmit diversity corresponds to the transmission of the same signal over multiple transmit antennas at the same time within the same bandwidth. The first

Year	Author(s)	Contribution
2003	Wang *et al.* [44]	derived upper bounds for the rates of complex orthogonal STBCs.
	Su *et al.* [45]	introduced the concept of combining orthogonal STBC designs with the principle of sphere packing.
2005	Zhang *et al.* [46]	derived the capacity and probability of error expressions for PSK/PAM/QAM modulation with STBC for transmission over Rayleigh-, Ricean- and Nakagami-fading channels.
2006	Liew *et al.* [47]	studied the performance of STTC and STBC in the context of wideband channels using adaptive orthogonal frequency division multiplex modulation.
2007	Alamri *et al.* [48]	modified the SP demapper of [45] for the sake of accepting the *a priori* information passed to it from the channel decoder as extrinsic information.
2008	Luo *et al.* [49]	combined orthogonal STBCs with delay diversity and designed special symbol mappings for maximising the coding advantage.

Table 1.4: Major coherent spatial diversity techniques (Part 2).

bandwidth-efficient transmit diversity scheme was proposed in [36] and it was shown that the diversity advantage of this scheme is equal to the number of transmit antennas [39, 50, 51]. In [10] Alamouti discovered a witty transmit diversity technique using two transmit antennas, whose key advantage was the employment of simple linear processing at the receiver, which is based on Maximum-Likelihood (ML) detection. The decoding algorithm proposed in [10] can be generalised to an arbitrary number of receive antennas using MRC, EGC or SC. Alamouti's achievement inspired Tarokh *et al.* [11, 26] to generalise the transmit diversity scheme to more than two transmit antennas, contriving the concept of Space-Time Block Codes (STBC). The family of STBCs is capable of attaining the same diversity gain as Space-Time Trellis Codes (STTC) [12, 52] at lower decoding complexity, when employing the same number of transmit antennas. However, a disadvantage of STBCs when compared to STTCs is that they provide no coding gain [9], as documented for example in [47].

Inspired by the philosophy of STBCs, Hochwald *et al.* [14] proposed the transmit diversity concept known as Space-Time Spreading (STS) for the downlink of Wideband Code Division Multiple Access (WCDMA) [53] that is capable of achieving the highest possible transmit diversity gain. The STBC and STS designs contrived for higher number of transmit antennas results in a reduction of the achievable transmission rate and hence in a reduction of the attainable bandwidth efficiency. An alternative idea for constructing full-rate STBCs for complex modulation schemes and more than two antennas was pursued in [15, 51]. Here the strict constraint of perfect orthogonality was relaxed in favour of a higher data rate. The resultant STBCs were referred to as quasi-orthogonal STBCs [15].

The STBC and STS designs offer at best the same data rate as an uncoded single-antenna system, but they provide an improved BER performance as compared to the family of single-antenna-aided systems by providing diversity gains. In contrast to this, several high-rate space-time transmission schemes having a normalised rate higher than one have been proposed in the literature. For example, high-rate space-time codes that are linear in space and time, namely the so-called Linear Dispersion Codes (LDC), were proposed in [13]. LDCs provide a flexible trade-off between achieving space-time coding and spatial multiplexing.

Additionally, the concept of combining orthogonal transmit diversity designs with the principle of Sphere Packing (SP) was introduced by Su *et al.* [45] in order to maximise the achievable coding advantage, where it was demonstrated that the proposed SP aided STBC scheme was capable of outperforming the conventional orthogonal design based STBC schemes of [10, 11]. A further

Year	Author(s)	Contribution
1998	Tarokh *et al.* [54]	proposed a detection algorithm for the Alamouti scheme [10] dispensing with channel estimation.
1999	Tarokh *et al.* [55]	proposed a differential encoding/decoding of Alamouti's scheme [10] with PSK constellations.
2000	Hochwald *et al.* [56]	proposed a differential modulation scheme for transmit diversity based on unitary space-time codes.
	Hughes [57]	proposed a differential modulation scheme that is based on group codes.
2001	Jafarkhani *et al.* [58]	proposed a differential detection scheme for the multiple antenna STBC [11].
2002	Schober *et al.* [59]	proposed non-coherent receivers for differential space-time modulation (DSTM) that can provide satisfactory performance in fast fading unlike the conventional differential schemes that perform poorly in fast fading.
2003	Hwang *et al.* [60,61]	extended the scheme of [58] to QAM constellations.
2004	Nam *et al.* [62]	extended the scheme of [60, 61] to four transmit antennas and QAM constellations.
2005	Zhu *et al.* [63]	proposed a differential modulation scheme based on quasi-orthogonal STBCs, which when compared with that of [58] results in a lower BER and provides full diversity.
2007	Song *et al.* [64]	proposed a new class of quasi-orthogonal STBCs and presented a simple differential decoding scheme for the proposed structures that avoids signal constellation expansion.

Table 1.5: Major differential spatial diversity techniques.

advance was proposed in [48], where the SP demapper of [45] was modified for the sake of accepting the *a priori* information passed to it from the channel decoder as extrinsic information. The major coherent spatial diversity techniques are summarised in Tables 1.3 and 1.4.

A common feature of all the above-mentioned schemes is that they use coherent detection, which assumes the availability of accurate Channel State Information (CSI) at the receiver. In practice, the CSI of each link between each transmit and each receive antenna pair has to be estimated at the receiver either blindly or using training symbols. However, channel estimation invoked for all the antennas substantially increases both the cost and complexity of the receiver. Furthermore, when the CSI fluctuates dramatically from burst to burst, an increased number of training symbols has to be transmitted, potentially resulting in an undesirably high transmission overhead and wastage of transmission power. Therefore, it is beneficial to develop low-complexity techniques that do not require any channel information and thus are capable of mitigating the complexity of MIMO-channel estimation.

A detection algorithm designed for Alamouti's scheme [10] was proposed in [54], where the channel encountered at time instant t was estimated using the pair of symbols detected at time instant $t-1$. The algorithm, nonetheless, has to estimate the channel during the very first time instant using training symbols and hence is not truly differential. Tarokh and Jafarkhani [55, 65] proposed a differential encoding and decoding algorithm for Alamouti's scheme [10] using real-valued phasor constellations and hence the transmitted signal can be demodulated both with or without CSI at the receiver. The resultant differential decoding aided non-coherent receiver performs within 3 dB from the coherent receiver assuming perfect channel knowledge at the receiver. The differential scheme of [55] was restricted to complex-valued PSK modulation. The twin-antenna-aided differential STBC scheme of [55] was extended to QAM constellations in [60, 61].

Differential STBC (DSTBC) schemes designed for multiple antennas were proposed in [58] for

real-valued constellations. Afterwards, the authors of [60, 62] developed a DSTBC scheme that supports non-constant modulus constellations combined with four transmit antennas. This extension, however, requires the knowledge of the received power in order to appropriately normalise the received signal. The received power was estimated blindly using the received differentially encoded signals without invoking any channel estimation techniques or transmitting any pilot symbols. In [56], a differential modulation scheme was proposed for the sake of attaining transmit diversity based on unitary space-time codes [66]. The proposed scheme can be employed in conjunction with an arbitrary number of transmit antennas. Around the same time, a similar differential scheme was also proposed in [57] based on the employment of group codes.

Zhu *et al.* [63] proposed a differential modulation scheme based on quasi-orthogonal STBCs, which were compared to that of [58] and resulted in a reduced BER as a benefit of providing full diversity. Additionally, a new class of quasi-orthogonal STBCs was proposed in [64], which presented a simple differential decoding scheme that avoids signal constellation expansion. The major contributions on differential spatial diversity techniques are summarised in Table 1.5.

1.4.1.2 Multiplexing Techniques

STBC and STTC are capable of providing diversity gains for the sake of improving the achievable system performance. However, this BER performance improvement is often achieved at the expense of a rate loss since the STBC and STTC may result in a throughput loss compared to single-antenna-aided systems. As a design alternative, a specific class of MIMO systems was designed for improving the attainable spectral efficiency of the system by transmitting the signals independently from each of the transmit antennas, hence resulting in a multiplexing gain.

The basic principle of spatial multiplexing can be summarised as follows. The source bit sequence at the transmitter side is split into N_t sequences, which are modulated and then transmitted simultaneously from the N_t transmit antennas using the same carrier frequency. At the receiver side, interference cancellation is employed in order to separate the different transmitted signals. In the case of narrowband frequency flat fading, there are several decoding algorithms designed for interference cancellation at the receiver side of the spatial multiplexing systems. The different receivers can be characterised by a tradeoff between the achievable performance and the complexity imposed. A low-complexity receiver is constituted by the Zero-Forcing (ZF) or the Minimum Mean Square Error (MMSE) technique [67,68]. However, when we employ the ZF receiver, the attainable BER performance is typically poor in addition to imposing the condition that the number of receive antennas should be at least equal to the number of transmit antennas. The optimum receiver is the Maximum Likelihood (ML) receiver [69], which is capable of achieving full diversity gain, i.e. the same diversity order, as the number of receive antennas. However, a major drawback of the ML receiver is its complexity that grows exponentially with the number of transmit antennas and the number of bits per symbol employed by the modulation scheme. Fortunately, the complexity of the ML decoders can be reduced by employing sphere decoders [70–72] that are capable of achieving a similar performance to the ML decoders at a fraction of their complexity.

In [73] Foschini proposed a multi-layer MIMO structure, known as the Diagonal Bell Labs Layered Space-Time (D-BLAST) scheme[2], which is in principle capable of approaching the substantial capacity of MIMO systems. The D-BLAST signal may be subjected to low-complexity linear processing for decoding the received signals. However, the diagonal approach suffers from a potentially high implementation complexity that led Wolniansky *et al.* to propose another version of BLAST, which is known as Vertical BLAST (V-BLAST) [16]. In V-BLAST, each transmit antenna simultaneously transmits independent data over the same carrier frequency band. At the receiver side, provided that the number of receive antennas is higher than or equal to the number

[2]The diagonal approach implies that the signal mapped to the consecutive antenna elements is delayed in time, which has the potential of subjecting the delayed signal components of a space-time symbol to more independent fading, hence leading to a potential diversity gain.

Year	Author(s)	Contribution
1996	Foschini *et al.* [73]	studied the encoding and decoding of the diagonal BLAST structure.
1998	Wolniansky *et al.* [16]	introduced the vertical BLAST architecture for reducing the implementation complexity of the diagonal approach.
1999	Golden *et al.* [74]	provided the first real-time BLAST demonstrations.
2001	Benjebbour *et al.* [75]	introduced the minimum mean square error receiver for V-BLAST and introduced an ordering scheme for improving the attainable performance.
2002	Sellathurai *et al.* [76]	studied the combination of BLAST architecture with that of a turbo code to improve its performance.
2003	Wubben *et al.* [77]	proposed a detector for improving the attainable performance of V-BLAST.
2004	Zhu *et al.* [78]	proposed a complexity-reduction algorithm for BLAST detectors.
2005	Huang *et al.* [79]	proposed a new detection algorithm for BLAST based on the concept of particle filtering and provided a near ML performance at a reasonable complexity.

Table 1.6: Major spatial multiplexing techniques.

of transmit antennas, a low complexity *serial* decoding algorithm may be applied to detect the transmitted data. The V-BLAST transceiver is capable of providing a substantial increase of a specific user's effective bit-rate without the need for any increase in the transmitted power or the system's bandwidth. However, its impediment is that it was not designed for exploiting transmit diversity. Furthermore, the decision errors of a particular antenna's detector propagate to other bits of the multi-antenna symbol, when erroneously cancelling the effects of the sliced bits from the composite signal. The V-BLAST detector first selects the layer[3] with the largest SNR and estimates the transmitted bits of that layer, while treating the other layers as interference. The detected symbol is then subtracted from the received signal and then the layer with the second highest SNR is selected for decoding. The procedure is repeated for all the layers. The BER performance of each layer is different and it depends on the received SNR of each layer. The first decoded layer has the highest SNR, while the layers detected later have a higher diversity order, since they suffer from less interference.

The BLAST detection algorithm is based on Successive Interference Cancellation (SIC), which was originally proposed for multiuser detection in CDMA systems [80]. Several BLAST detectors have been proposed in the literature for either reducing the complexity [81–86] or for improving the attainable BER performance [77, 87–92]. An alternative design approach contrived for spatial multiplexing using less receive antennas than transmit antennas was proposed in [93] based on group Maximum A Posteriori (MAP) detection. In [76, 94] a spatial multiplexing scheme referred to as Turbo-BLAST was proposed, which uses quasi-random interleaving in conjunction with an iterative receiver structure, in order to separate the individual layers. The major spatial multiplexing techniques are summarised in Table 1.6.

1.4.1.3 Beamforming Techniques

According to Sections 1.4.1.1 and 1.4.1.2, it becomes clear that multiple antennas can be used for the sake of attaining either spatial diversity or spatial multiplexing gains. However, multiple antennas can also be used in order to improve the Signal-to-Noise Ratio (SNR) at the receiver or the Signal-to-Interference-plus-Noise Ratio (SINR) in a multi-user scenario. This can be achieved

[3]The layer in the case of the V-BLAST corresponds to each of the transmit antennas.

by employing beamforming techniques [17, 95]. Beamforming constitutes an effective technique of reducing the multiple access interference, where the antenna gain is increased in the direction of the desired user, whilst reducing the gain towards the interfering users.

In a wireless communications scenario the transmitted signals propagate via several paths and hence are received from different directions/phases at the receiver. If the directions of the different propagation paths are known at the transmitter or the receiver, then beamforming techniques can be employed in order to direct the received beam pattern in the direction of the specified antenna or user [96, 97]. Hence, significant SNR gains can be achieved in comparison to a single antenna system. On the transmitter side, when the Direction of Arrival (DOA) of the dominant paths at the receiver is known for the transmitter, then the transmit power is concentrated in the direction of the target user, where less power is wasted in the other directions.

On the other hand, beamforming can be used in order to reduce the co-channel interference or multiuser interference. When using beamforming, each user adjusts his/her beam pattern to ensure that there are nulls in the directions of the other users, while there is a high directivity in the direction of the desired receiver [17, 98]. Hence, the system attains an SINR gain.

1.4.1.4 Multi-functional MIMO Techniques

V-BLAST is capable of achieving full multiplexing gain, while STBC can achieve full antenna diversity gain. Hence, it was proposed in [18] to combine the two techniques to provide both antenna diversity and spectral efficiency gains. More specifically, it was proposed that the antennas at the transmitter be partitioned into layers, where each layer uses STBC. At the receiver side, successive group interference cancellation can be applied to each layer before decoding the signals using ML STBC decoding. Therefore, by combining V-BLAST and STBC, an improved transmit diversity gain can be achieved as compared to pure V-BLAST, while ensuring that the overall bandwidth efficiency is higher than that of pure STBC due to the independence of the signals transmitted by different STBC layers. Furthermore, the combined array processing proposed in [18] was improved in [19] by optimising the decoding order of the different antenna layers. An iterative decoding algorithm was proposed in [19] that results in a full receive diversity gain for the combined V-BLAST STBC system.

In [20] the authors presented a transmission scheme referred to as Double Space-Time Transmit Diversity (D-STTD), which consists of two STBC layers at the transmitter that is equipped with four transmit antennas, while the receiver is equipped with two antennas. The decoding of D-STTD presented in [20] is based on a linear decoding scheme presented in [110], where the authors provided a broad overview of space-time coding and signal processing designed for high data rate wireless communications. A two-user scheme was presented in [110], where each user is equipped with a twin-antenna-aided STBC scheme transmitting at the same carrier frequency and in the same time slot. A two-antenna-aided receiver was implemented for the sake of decoding the two users' data, while eliminating the interference imposed by the users on each others' data. An extension to the idea of combining interference cancellation with STBC techniques was presented in [100, 102], where the STBC and interference cancellation arrangements were combined with CDMA for the sake of increasing the number of users supported by the system. A zero-forcing decoder designed for the D-STTD was presented in [107] for the sake of reducing the decoding complexity. Finally, the authors of [101, 111] presented further results that compare the performance of STBC versus D-STTD and extended the applicability of the D-STTD scheme to more than two STBC layers.

Furthermore, in order to achieve additional performance gains, beamforming has been combined with spatial diversity as well as spatial multiplexing techniques. STBC has been combined with beamforming in order to attain a higher SNR gain in addition to the diversity gain [21, 104, 105, 112–114]. In [21], the authors combined conventional transmit beamforming with STBC, assuming that the transmitter has partial knowledge of the channel and derived a performance criterion for a frequency-flat fading channel. In addition, a particularly efficient solution was developed in [21]

Year	Author(s)	Contribution
1998	Naguib *et al.* [99]	presented a multi-user scenario where each user employs STBC and the receiver applies interference cancellation for eliminating the co-channel interference and then uses ML decoding for the STBC of each user.
1999	Tarokh *et al.* [18]	proposed to combine STBC with V-BLAST in order to provide both antenna diversity and spectral efficiency gains.
2000	Huang *et al.* [100]	extended the idea of combining interference cancellation with STBC to multiuser scenarios using CDMA.
2001	Stamoulis *et al.* [101]	proposed a simple decoder for the two-user system, where each user employs STBC and showed how the decoder can be extended to more users and then extended the results for frequency-selective channels.
2002	Onggosanusi *et al.* [20]	presented the Double Space-Time Transmit Diversity scheme, which consists of two STBC blocks at the transmitter that is equipped with four antennas, while the receiver is equipped with two antennas.
	Jongren *et al.* [21]	combined conventional transmit beamforming with STBC assuming that the transmitter has partial knowledge of the channel and derived a performance criteria for improving the system performance.
	Huang *et al.* [102]	introduced a transmission scheme that can achieve transmit diversity and spatial separation and proposed a generalisation of the V-BLAST detector for CDMA signals.
	Soni *et al.* [103]	designed a hybrid downlink technique for achieving both transmit diversity and transmit beamforming combined with DS-CDMA.
2003	Liu *et al.* [104]	combined the twin-antenna-aided Alamouti STBC with ideal beamforming in order to show that the system can attain a better performance while keeping full diversity and unity rate.
2004	Tao *et al.* [19]	improved the design of [18] by optimising the decoding order of the different antenna layers. Also proposed an iterative decoder than can achieve full diversity.
	Zhu *et al.* [105]	compared the performance of two systems combining beamforming with STBC, while using a single or two antenna arrays and studied the effect of the DOA on the performance of the two schemes.

Table 1.7: Major multi-functional MIMO techniques (Part 1).

Year	Author(s)	Contribution
2005	Zhao *et al.* [106]	compared the performance of the combined diversity and multiplexing systems while employing ZF, QR and MMSE group interference cancellation techniques.
	Lee *et al.* [107]	proposed a computationally efficient ZF decoder for the double space-time transmit diversity scheme [20] that achieves similar performance to the conventional ZF decoder but with less complexity.
2007	Sellathurai *et al.* [108]	investigated the performance of multi-rate layered space-time coded MIMO systems and proposed a framework where each of the layers is encoded independently with different rates subject to equal per-layer outage probabilities.
2008	Ekbatani *et al.* [109]	combined STBC and transmit beamforming while using limited-rate channel state information at the transmitter. Also proposed a combined coding, beamforming and spatial multiplexing scheme over multiple-antenna multi-user channels that enables a low-complexity joint interference cancellation.
	Luo *et al.* [49]	considered a new class of full-diversity STCs that consist of a combination of delay transmit diversity with orthogonal STBCs and specially designed symbol mappings.

Table 1.8: Major multi-functional MIMO techniques (Part 2).

for the specific case of independently fading channel coefficients. More explicitly, the transmission scheme of [21] combines the benefits of conventional beamforming with those of orthogonal STBC. Furthermore, in [105] the performance of combined beamforming and STBC has been analysed as a function of the number of antenna array groups. Explicitly, Zhu *et al.* [105] compared the performance of the system combining beamforming with STBC, while using either a single or two antenna arrays and studied the effect of the DOA on the attainable system performance. Finally, multiplexing techniques have been combined with beamforming techniques in [115–117]. The major multi-functional MIMO techniques are summarised in Tables 1.7 and 1.8.

1.4.2 Distributed MIMO Techniques

Wireless channels suffer from multipath propagation of the signals that results in channel fading. Employing multiple transmit antennas is a beneficial method that can be used for counteracting the effects of the channel fading by providing diversity gains. Transmit diversity results in a significantly improved BER performance, when the different transmit antennas are spatially located so that the paths arriving from each transmit antenna to the destination experience independent fading, which can be achieved by having a distance between the different antennas, which is significantly higher than the carrier's wavelength. However, considering a handheld mobile phone, it is not a feasible option to position the transmit antennas far enough in order to achieve independent fading. On the other hand, the spatial fading correlation caused by insufficiently high antenna spacing at the transmitter or receiver of a MIMO system results in a degradation of both the achievable capacity and the BER performance of MIMO systems. The problem of correlation of the transmit signals can be circumvented by introducing a new class of MIMOs also referred to as distributed MIMOs or cooperative communications [118, 119].

The basic idea behind cooperative communications can be traced back to the idea of the relay channel which was introduced in 1971 by Van der Meulen [120]. Cover and El Gamal [121] characterised the relay channel from an information theoretic point of view. In [123] Sendonaris *et al.* generalised the conventional relay model, where there is one source, one relay and one

Year	Author(s)	Contribution
1971	Meulen [120]	investigated a simple 3-node relay channel incorporating a transmitter, a relay and a receiver using a time-sharing approach.
1979	Cover *et al.* [121]	characterised the relay channel from an information theoretic point of view.
1983	Willems [122]	introduced a partially cooperative communications scenario where the encoders are connected by communication links with finite capacities, which permit both encoders to communicate with each other. The paper also established the capacity region of the multiple access channel with partially cooperating encoders.
1998	Sendonaris *et al.* [123]	generalised the relay model to multiple nodes that transmit their own data as well as serve as relays for each other.
2001	Laneman *et al.* [124]	built upon the classical relay channel and exploited space diversity available at distributed antennas through coordinated transmission and processing by cooperating radios.
2002	Hunter *et al.* [125]	proposed a user cooperation scheme for wireless communications in which the idea of cooperation was combined with the existing channel coding methods.
	Dohler *et al.* [126]	introduced the concept of virtual antenna arrays that emulates Alamouti's STBC for single-antenna-aided cooperating users.
2003	Sendonaris *et al.* [118, 119]	presented a simple user-cooperation methodology based on a DF signalling scheme using CDMA.
	Laneman *et al.* [25]	developed space-time coded cooperative diversity protocols for exploiting spatial diversity in a cooperation scenario, which can also be used for higher spectral efficiencies than repetition-based schemes.
	Valenti and Zhao [127, 128]	proposed a turbo coding scheme in a relay network.
2004	Laneman *et al.* [129]	developed and analysed cooperative diversity protocols and compared the DF, AF, selection relaying and incremental relaying.
	Nabar *et al.* [130]	analysed the spatial diversity performance of various signalling protocols.
	Janani *et al.* [131]	presented two extensions to the coded cooperation framework [125]: increased the diversity of coded cooperation via ideas borrowed from space-time codes and applied turbo codes in the proposed relay framework.

Table 1.9: Major distributed MIMO techniques (Part 1).

Year	Author(s)	Contribution
2004	Stefanov *et al.* [132]	analysed the performance of channel codes that are capable of achieving the full diversity provided by user cooperation in the presence of noisy interuser channels.
2005	Azarian *et al.* [133]	proposed cooperative signalling protocols that can achieve the diversity-multiplexing tradeoff.
	Sneessens *et al.* [134]	proposed a soft decode-and-forward signalling strategy that can outperform the conventional DF and AF.
	Hu *et al.* [135]	proposed Slepian-Wolf cooperation that exploits distributed source coding technologies in wireless cooperative communication.
	Yu [136]	compared the AF and DF signalling schemes in practical scenarios.
2006	Hunter *et al.* [137, 138]	developed the idea of coded cooperation [125] by computing BER and FER bounds as well as the outage probability of coded cooperation.
	Li *et al.* [139]	employed soft information relaying in a BPSK modulated relay system employing turbo coding.
	Hu *et al.* [140]	proposed Wyner-Ziv cooperation as a generalisation of the Slepian-Wolf cooperation [135] with a compress-and-forward signalling strategy.
	Hϕst-Madsen [141]	derived upper and lower bounds for the capacity of four-node ad hoc networks with two transmitters and two receivers using cooperative diversity.
2007	Bui *et al.* [142]	proposed soft information relaying where the relay LLR values are quantised, encoded and superimposedly modulated before being forwarded to the destination.
	Khormuji *et al.* [143]	improved the performance of the conventional DF strategy by employing constellation rearrangement in the source and the relay.
	Bao *et al.* [144]	combined the benefits of AF and DF and proposed a new signalling strategy referred to as decode-amplify-forward.
	Xiao *et al.* [145]	introduced the concept of network coding in cooperative communications.

Table 1.10: Major distributed MIMO techniques (Part 2).

destination, to multiple nodes that transmit their own data as well as serve as relays for each other. The scheme of [123] was referred to as "user cooperation diversity". Sendonaris *et al.* presented in [118, 119] a simple user-cooperation methodology based on a Decode-and-Forward (DF) signalling scheme using CDMA. In [124] the authors reported data rate gains and a decreased sensitivity to channel variations, where it was concluded that cooperation effectively mimics the multi-antenna scenario with the aid of single-antenna terminals. Dohler *et al.* [126] introduced the concept of Virtual Antenna Arrays (VAA) that emulates Alamouti's STBC for single-antenna-aided cooperating users. Space-time coded cooperative diversity protocols for exploiting spatial diversity in a cooperative scenario was proposed in [25].

Cooperative communications has been shown to offer significant performance gains in terms of various performance metrics, including diversity gains [25, 129, 149] as well as multiplexing gains [133]. Hunter *et al.* [125] proposed the novel philosophy of coded cooperation schemes, which combine the idea of cooperation with the classic channel coding methods. Extension to the framework of coded cooperation was presented in [131], where the diversity gain of coded cooperation was increased with the aid of ideas borrowed from the area of space-time codes. Additionally, a turbo coded scheme was proposed in [131] in the framework of cooperative communications. Furthermore, the analysis of the performance benefits of channel codes in a coded cooperation aided

Year	Author(s)	Contribution
2008	Yue *et al.* [146]	compared the multiplexed coding and superposition coding in the coded cooperation system.
	Zhang *et al.* [147]	proposed a distributed space-frequency coded cooperation scheme for communication over frequency-selective channels.
	Wang *et al.* [148]	introduced the complex field network coding approach that can mitigate the throughput loss in the conventional signalling schemes and attain full diversity gain.

Table 1.11: Major distributed MIMO techniques (Part 3).

scenario was performed in [132]. Laneman *et al.* [129] developed and analysed cooperative diversity protocols and compared the DF, Amplify-and-Forward (AF), selection relaying and incremental relaying signalling strategies.

Recently, there has been substantial research interest in the idea of soft relaying, where the relay passes soft information to the destination. In [134], it was argued that the DF signalling loses soft information and hence, it was proposed to use soft DF signalling, where all operations are performed using the Log-Likelihood Ratio (LLR) based representation of soft information. It was shown in [134] that the soft DF philosophy outperforms the DF and the AF signalling strategies. In [142] soft DF was also used, where the soft information was quantised, encoded and superimposed before transmission to the destination. In [139] soft information based relaying was employed in a turbo coding scheme, where the relay derives parity checking BPSK symbol estimates for the received source information and forwards the symbols to the destination. In [134, 139, 142] soft information relaying has been used, where it was shown that soft DF attains a better performance than hard DF. Furthermore, in [135, 140] distributed source coding techniques have been adopted for employment in wireless cooperative communications in order to improve the attainable performance. The major distributed MIMO techniques are summarised in Tables 1.9, 1.10 and 1.11.

1.5 Iterative Detection Schemes and Their Convergence Analysis

The concept of concatenated codes has been proposed in [150]. However, at the time of its conception it was deemed to have an excessive complexity and hence it failed to initiate immediate research interest. It was not until the discovery of turbo codes [151] that efficient iterative decoding of concatenated codes became a reality at a low complexity by employing simple constituent codes. Since then, the appealing iterative decoding of concatenated codes has inspired numerous researchers to extend the technique to other transmission schemes consisting of a concatenation of two or more constituent decoding stages [152–168].

For example, in [159] iterative decoding was invoked for exchanging extrinsic information between a soft-output symbol detector and an outer channel decoder in order to combat the effect of Inter-Symbol Interference (ISI). In [160] iterative decoding was carried out by exchanging information between an outer convolutional decoder and an inner Trellis Coded Modulation (TCM) decoder. The authors of [161, 162] presented a unified theory of Bit-Interleaved Coded Modulation (BICM). On the other hand, the employment of the iterative detection principle in [163] was considered for iterative soft demapping in the context of BICM, where a soft demapper was used between the multilevel demodulator and the channel decoder. In addition, iterative multiuser detection and channel decoding was proposed in [167] for CDMA schemes. Finally, in [168] an iteratively detected scheme was proposed for the Rayleigh fading MIMO channel, where an orthogonal STBC scheme was considered as the inner code combined with an additional block code

Year	Author(s)	Contribution
1966	Forney [150]	promoted concatenated codes.
1974	Bahl *et al.* [169]	invented the Maximum A-Posteriori (MAP) algorithm.
1993	Berrou *et al.* [151]	invented the turbo codes and showed that the iterative decoding is an efficient way of improving the attainable performance.
1995	Robertson *et al.* [170]	proposed the log-MAP algorithm that results in similar performance to the MAP algorithm but with significantly lower complexity.
	Divsalar *et al.* [152]	extended the turbo principle to multiple parallel concatenated codes.
1996	Benedetto *et al.* [153]	extended the turbo principle to serially concatenated block and convolutional codes.
1997	Benedetto *et al.* [160]	proposed an iterative detection scheme where iterations were carried out between the outer convolutional code and an inner TCM decoders.
	Caire *et al.* [161, 162]	presented the BICM concept with its design rules.
	Li *et al.* [164–166]	presented the BICM with iterative detection scheme.
1998	Benedetto *et al.* [154, 171]	studied the design of multiple serially concatenated codes with interleavers.
	Brink *et al.* [163]	introduced a soft demapper between the multilevel demodulator and the channel decoder in an iteratively detected coded system.
1999	Wang *et al.* [167]	proposed iterative multiuser detection and channel decoding for coded CDMA systems.
2000	Divsalar *et al.* [172, 173]	employed unity-rate inner codes for designing low-complexity iterative detection schemes suitable for bandwidth and power limited systems having stringent BER requirements.
	ten Brink [174]	proposed the employment of EXIT charts for analysing the convergence behaviour of iteratively detected systems.
2001	Lee [175]	studied the effect of precoding on serially concatenated systems with ISI channels.
	ten Brink [176, 177]	extended the employment of EXIT charts to three-stage parallel concatenated codes.
	EL Gamal *et al.* [178]	used SNR measures for studying the convergence behaviour of iterative decoding.

Table 1.12: Major concatenated schemes and iterative detection (Part 1).

Year	Author(s)	Contribution
2002	Tüchler *et al.* [179]	simplified the computation of EXIT charts.
	Tüchler *et al.* [180]	compared several algorithms predicting the decoding convergence of iterative decoding schemes.
	Tüchler *et al.* [181]	extended the EXIT chart analysis to three-stage serially concatenated systems.
2003	Sezgin *et al.* [168]	proposed an iterative detection scheme where a block code was used as an outer code and STBC as an inner code.
2004	Tüchler *et al.* [182]	proposed a design procedure for creating systems exhibiting beneficial decoding convergence depending on the block length.
2005	Lifang *et al.* [183]	showed that non-square QAM can be decomposed into parity-check block encoder having a recursive nature and a memoryless modulator. Iterative decoding was implemented with an outer code for improving the system performance.
	Brännström *et al.* [184]	considered EXIT chart analysis for multiple concatenated codes using 3-dimensional charts and proposed a way for finding the optimal activation order.
2008	Maunder *et al.* [185]	designed irregular variable length codes for the near-capacity design of joint source and channel coding aided systems.

Table 1.13: Major concatenated schemes and iterative detection (Part 2).

as the outer channel code.

It was shown in [186] that a recursive inner code is needed in order to maximise the interleaver gain and to avoid the average BER floor, when employing iterative decoding. This principle has been adopted by several authors designing serially concatenated schemes, where unity-rate inner codes were employed for designing low complexity iterative detection aided schemes suitable for bandwidth- and power-limited systems having stringent BER requirements [172,173,175,183,187].

Semi-analytical tools devised for analysing the convergence behaviour of iteratively decoded systems have attracted considerable research attention [172, 174, 177–180, 184, 188, 189]. In [174], ten Brink proposed the employment of the so-called EXtrinsic Information Transfer (EXIT) characteristics for describing the flow of extrinsic information between the soft-in soft-out constituent decoders. The computation of EXIT charts was further simplified in [179] to a time averaging, when the PDFs of the information communicated between the input and output of the constituent decoders are both symmetric and consistent. A tutorial introduction to EXIT charts can be found in [188]. The concept of EXIT chart analysis has been extended to three-stage concatenated systems in [176,181,184]. The major contributions on iterative detection and its convergence analysis are summarised in Tables 1.12 and 1.13.

1.6 Outline and Novel Aspects of the Monograph

1.6.1 Outline of the Book

Having briefly reviewed the literature of space-time coding, concatenated schemes, iterative decoding and having studied the convergence behaviour of iterative schemes, let us now outline the organisation of the book.

- **Chapter 2: Space-Time Block Code Design using Sphere Packing**
  In this chapter, we consider the theory and design of space-time block codes using sphere packing modulation, referred to here as (STBC-SP). We first summarise the design criteria

of space-time coded communication systems in Section 2.2. In Section 2.3, we emphasise the design criteria relevant for time-correlated fading channels, where both the pairwise error probability as well as the corresponding design criterion are presented in Section 2.3.2. In Section 2.4, orthogonal space-time designs combined with sphere packing modulation are considered for space-time signals, where the motivation behind the adoption of sphere packing modulation in conjunction with orthogonal design is discussed in Section 2.4.2. Section 2.4.4 discusses the problem of constructing a sphere packing constellation having a particular size L. The capacity of STBC-SP schemes employing $N_t = 2$ transmit antennas is derived in Section 2.4.5, demonstrating that STBC-SP schemes exhibit a higher capacity than conventionally modulated STBC schemes. Finally, the performance of STBC-SP schemes is presented in Section 2.5, demonstrating that STBC-SP schemes are capable of outperforming STBC schemes that employ conventional modulation (i.e. PSK, QAM).

- **Chapter 3: Turbo Detection of Channel-Coded STBC-SP Schemes**
  In this chapter, we demonstrate that the performance of STBC-SP systems can be further improved by concatenating sphere packing aided modulation with channel coding and performing demapping as well as channel decoding iteratively. The sphere packing demapper of [190] is further developed for the sake of accepting the *a priori* information passed to it from the channel decoder as extrinsic information. Two realisations of a novel bit-based iterative-detection aided STBC-SP scheme are presented, namely a recursive systematic convolutional (RSC) coded turbo-detected STBC-SP scheme and a binary LDPC-coded turbo-detected STBC-SP arrangement. Our system overview is provided in Section 3.2. In Section 3.3, we show how the STBC-SP demapper is modified for exploiting the *a priori* knowledge provided by the channel decoder, which is essential for the employment of iterative demapping and decoding. EXIT chart analysis is invoked in Section 3.4 in order to study and design the turbo-detected schemes proposed in Section 3.2. We propose 10 different anti-Gray mapping (AGM) schemes that are specifically selected from all the possible mapping schemes for $L = 16$ in order to demonstrate the different extrinsic information transfer characteristics associated with different bit-to-symbol mapping schemes. The slope of the EXIT curves corresponding to the different AGM schemes increases gradually in fine steps. This attractive characteristic is a result of the multi-dimensional constellation mapping and having this property is essential for the sake of designing near-capacity turbo detected systems. The performance of the turbo-detected bit-based STBC-SP schemes is presented in Section 3.5, where we investigate the relation between the achievable BER and the mutual information at the input as well as at the output of the outer decoders. Additionally, the predictions of our EXIT chart analysis are verified by generating the actual decoding trajectories and BER curves. The effect of interleaver depth is also addressed, since matching the predictions of the EXIT chart analysis is only guaranteed, when employing large interleaver depths. The BER performance of the proposed channel-coded STBC-SP scheme is compared to that of an uncoded STBC-SP scheme [190] and to that of a channel-coded conventionally modulated STBC scheme.

- **Chapter 4: Turbo Detection of Channel-Coded DSTBC-SP Schemes**
  In Chapter 2 and Chapter 3, we assume that the channel state information is perfectly known at the receiver. This, however, requires sophisticated channel estimation techniques, which imposes excess cost and complexity. In Chapter 4, we consider the design of novel sphere packing modulated differential STBC schemes, referred to here as DSTBC-SP, that require no channel estimation, where we describe in Section 4.2.1 how DSTBC schemes are constructed using sphere packing modulation. The performance of uncoded DSTBC-SP schemes is considered in Section 4.2.2, where we compare the performance of different DSTBC-SP schemes against equivalent conventional DSTBC schemes under various channel conditions. Simulation results are provided for systems having different BPS rates in conjunction with appropriate conventional and sphere packing modulation schemes. In Section 4.3, we propose

novel bit-based RSC-coded turbo-detected DSTBC-SP schemes. The system's architecture is outlined in Section 4.3.1. The EXIT chart analysis of Section 3.4 is employed in Section 4.3.2 in order to design and analyse the convergence behaviour of the proposed turbo-detected RSC-coded DSTBC-SP schemes. In Section 4.3.3, we investigate the performance of the proposed RSC-coded DSTBC-SP schemes. The actual decoding trajectories and BER performance curves are also provided, when using various interleaver depths.

- **Chapter 5: Three-Stage Turbo-Detected STBC-SP Schemes**
  The conventional two-stage turbo-detected schemes introduced in Chapter 3 suffer from a BER floor, preventing them from achieving infinitesimally low BER values, since the inner coding stage is of non-recursive nature. In Chapter 5, we circumvent this deficiency by proposing a three-stage turbo-detected STBC-SP scheme, where a rate-1 recursive inner precoder is employed to avoid having a BER floor. Section 5.2 provide a brief description of the proposed three-stage system. We consider three different types of channel codes for the outer encoder, namely a repeater, an RSC code and an irregular convolutional code (IRCC). Our 3D EXIT chart analysis is presented in Section 5.3.2, where its simplified 2D projections are provided in Section 5.3.3. In Section 5.3.4, we employ the powerful technique of EXIT tunnel-area minimisation for near-capacity operation. More specifically, we exploit the well-understood properties of conventional 2D EXIT charts that a narrow but nonetheless open EXIT-tunnel represents a near-capacity performance. Consequently, we invoke IRCCs for the sake of appropriately shaping the EXIT curves by minimising the area within the EXIT-tunnel using the procedure of [182, 191]. In Section 5.4, an upper bound on the maximum achievable rate is calculated based on the EXIT chart analysis. More explicitly, a procedure is proposed for calculating a tighter upper bound of the maximum achievable bandwidth efficiency of STBC-SP schemes based on the area property of the EXIT charts discussed in Section 5.3.4. The design procedure is summarised in Algorithm 5.1. The performance of the three-stage turbo-detected STBC-SP schemes is demonstrated and characterised in Section 5.5, where we discuss the actual decoding trajectories, BER performance and the effect of interleaver depth on the achievable performance. We also investigate the E_b/N_0 distance to capacity for the three-stage RSC-coded as well as for the IRCC-coded STBC-SP schemes, when employing various interleaver depths and using different number of three-stage iterations. Finally, in Section 5.5.5, the performance of both the three-stage RSC-coded and IRCC-coded STBC-SP schemes are compared, when employing various interleaver depths, while using different number of three-stage iterations.

- **Chapter 6: Symbol-Based Channel-Coded STBC-SP Schemes**
  In all previous chapters, iterative decoding is employed at the bit-level. By contrast, in this chapter, we explore a range of further design options and propose a purely symbol-based scheme, where symbol-based turbo detection is carried out by exchanging extrinsic information between an outer non-binary LDPC code and a rate-1 non-binary inner precoder. The motivation behind the development of this symbol-based scheme is that a reduced transmit power may be required, when symbol-based rather than bit-based iterative decoding is employed [192]. The system's architectures of the proposed symbol-based and turbo-detected scheme and its equivalent bit-based scheme are presented in Section 6.2. Symbol-based iterative decoding is discussed in Section 6.3, where it is demonstrated how the *a priori* information is removed from the decoded *a posteriori probability* with the aid of symbol-based element-wise division for the sake of generating the *extrinsic probability*. Section 6.4 provides our non-binary EXIT chart analysis. More specifically, in Section 6.4.1 we demonstrate, how non-binary EXIT charts can be generated without generating an L-dimensional histogram [193] since the complexity of this operation may become higher than conducting full-scale BER or SER simulations, when the number of bits per symbol is high. In Section 6.4.2, we address the problem of generating the *a priori* symbol probabilities, when

the binary bits within each non-binary symbol are assumed be either independent or not. Accordingly, a detailed procedure is described in Section 6.4.2.2 for creating the *a priori* symbol probabilities, when the binary bits of each non-binary symbol may no longer be assumed to be independent. The results of our non-binary EXIT chart analysis are provided in Section 6.4.3, where the EXIT charts of both the symbol-based and bit-based schemes are compared demonstrating that the symbol-based schemes require a lower transmit power and a lower number of decoding iterations for achieving a performance comparable to that of their bit-based counterparts. The performance of the symbol-based and bit-based LDPC-coded STBC-SP schemes is investigated in Section 6.5, in terms of the actual decoding trajectories and the attainable BER performance. The effect of employing various interleaver depths or, equivalently, LDPC output block lengths on the achievable performance is also considered in Section 6.5.

- **Chapter 7: IR-PLDCs for Co-located MIMO Antenna Elements**
  The theory and design of LDCs designed for co-located MIMO systems is investigated and a novel irregular near-capacity scheme using LDCs as the *inner* constituent code is proposed. Section 7.2 presents LDC models suitable for describing OSTBCs and for non-orthogonal STBCs. Furthermore, a novel method of optimizing the LDCs according to their DCMC capacities is proposed. In Section 7.3, the relationship between various STBC designs and LDCs is exploited in detail, demonstrating the flexibility of the linear dispersion framework. Table 7.3 specifically characterizes the evolution of STBCs in terms of their rate, diversity and flexibility. As far as channel-coded schemes concerned, Section 7.4 investigates various design issues related to two-stage concatenated convolutional coded LDCs as well as to three-stage precoder-assisted LDCs with the aid of EXIT chart, including their maximum achievable rates and their iteration parameters. Section 7.5 investigates the irregular code design principle originally derived for IRCCs and employ a similar concept to design a family of IrRegular Precoded Linear Dispersion Codes (IR-PLDCs) as the *inner* constituent code of a SCC. In Sections 7.5.1 to 7.5.3, different degrees of irregularity are imposed on both the *inner* IR-PLDCs and the *outer* IRCCs.

- **Chapter 8: IR-PDLDCs for Co-located MIMO Antenna Elements**
  In Chapter 8, we exploit the linear dispersion structure in the context of non-coherently detected MIMO systems as well as characterize the effective throughput achieved by an irregular SCC scheme. In Section 8.2, the multi-antenna aided DSTBC's system architecture is derived from the conventional single-antenna aided Differential Phase Shift Keying (DPSK) scheme, followed by the characterization of the fundamental relationship between STBCs and DSTBCs in Section 8.2.3. After characterizing the performance of DSTBCs based on various orthogonal constraints in Section 8.3, Section 8.4 proposes the family of DLDCs based on the Cayley transform. In Section 8.5, we introduce the concept of Sphere Packing (SP) modulation [194] and jointly design the SP modulation and DSTBCs. The convolutional-coded SP-aided DSTBC scheme of Figure 8.18 is capable of approaching the capacity at a specific SNR. Finally, in Section 8.6 the irregular design philosophy is imposed on both the *inner* and *outer* codes. Again, the resultant IRCC-coded IrRegular Precoded Differential Linear Dispersion Codes (IR-PDLDCs) of Figure 8.25 has the potential of operating near the attainable capacity across a wide range of SNRs.

- **Chapter 9: IR-PCLDCs for Cooperative MIMO Systems**
  In Chapter 9, we apply the linear dispersion structure to the family of relay-aided cooperative schemes and characterize the maximum achievable throughput achieved by the irregular system. More explicitly, Section 9.1 justifies the need for cooperation and portrays the system architecture in Figure 9.2. The mathematical model of the proposed twin-layer CLDCs as well as the rationale of our assumptions are discussed in Sections 9.2.1 to 9.2.3. The fundamental link between LDCs and CLDCs is exploited in Section 9.2.4, followed by their achievable performance recorded in Section 9.2.5. Similarly, we impose the irregular design

philosophy in the context of cooperative MIMO systems in Section 9.3. The resultant IRCC-coded IrRegular Precoded Cooperative Linear Dispersion Codes (IR-PCLDCs) of Figure 9.16 become capable of achieving a flexible effective throughput according to the SNR encountered, while maintaining an infinitesimally low BER.

- **Chapter 10: Differential Space-Time Spreading**
  This chapter introduces the idea of differential space-time spreading and its combination with Sphere-Packing (SP) modulation. The chapter first reviews the concept of differential encoding in Section 10.2. It is shown that differential encoding requires no channel state information at the receiver and thus eliminates the complexity of channel estimation at the expense of a 3 dB performance loss compared to the coherently detected system assuming perfect CIR recovery at the receiver. In Section 10.3, we outline the encoding and decoding processes of the differential space-time spreading scheme, when combined with conventional modulation schemes such as PSK and QAM. In Section 10.3.3, the philosophy of DSTS using sphere packing modulation is introduced based on the fact that the diversity product of the DSTS design is improved by maximising the Minimum Euclidean Distance (MED) of the DSTS symbols, which is motivated by the fact that SP has the best known MED in the real-valued space. Section 10.3.4 discusses the problem of constructing a sphere packing constellation having a particular size L. The capacity of DSTS-SP schemes employing $N_t = 2$ transmit antennas is derived in Section 10.3.6, followed by the performance characterisation of a twin-antenna-aided DSTS scheme in Section 10.3.7, demonstrating that the DSTS scheme is capable of providing full diversity. Our results demonstrate that DSTS-SP schemes are capable of outperforming DSTS schemes dispensing with SP.

  The four-antenna-aided DSTS design is characterised in Section 10.4, where it is demonstrated that the DSTS scheme can be combined with conventional real- and complex-valued constellations as well as with SP modulation. It is also shown that the four-dimensional SP modulation scheme is constructed differently in the case of two transmit antennas than when employing four transmit antennas. The capacity of the four-antenna-aided DSTS-SP scheme is also derived for different spectral efficiency systems, while employing a variable number of receive antennas in Section 10.4.5. Finally, Section 10.4.6 presents the simulation results obtained for the four-antenna-aided DSTS scheme, when combined with conventional as well as SP modulations.

- **Chapter 11: Turbo Detection of Channel-Coded DSTS Schemes**
  In this chapter, two realisations of a novel iterative-detection aided DSTS-SP scheme are presented, namely an iteratively detected RSC-coded DSTS-SP scheme as well as an iteratively detected RSC-coded and URC precoded DSTS-SP arrangement. The iteratively detected RSC-coded DSTS-SP scheme is described in detail in Section 11.2. In Section 11.2.1, we show how the DSTS-SP demapper was modified for exploiting the *a priori* knowledge provided by the channel decoder, which is essential for the employment of iterative detection.

  The concept of EXIT charts is introduced in Section 11.2.2 as a tool designed for studying iterative detection aided schemes. Then, we propose a novel technique for computing the maximum achievable bandwidth efficiency of the system based on EXIT charts in Section 11.2.3, followed by a discussion of the system's performance. Section 11.2.5 presents an application of the iteratively detected RSC-coded DSTS-SP system, where an Adaptive Multi-Rate WideBand (AMR-WB) source codec was employed by the system in order to demonstrate the attainable performance improvements.

  Additionally, in Section 11.3 we propose an iteratively detected RSC-coded and URC-precoded DSTS-SP scheme that is capable of eliminating the error floor exhibited by the system of Section 11.2, which hence performed closer to the system's achievable capacity. In Section 11.3.1 we present an overview of the system operation, followed by a discussion of the results in Section 11.3.2. In Section 11.3.3 we present an application of the proposed system, while employing Irregular Variable Length Codes (IrVLC) as our outer code for the sake of achieving a near-capacity performance.

- **Chapter 12: Adaptive Differential Space-Time-Spreading-Assisted Turbo-Detected Sphere Packing Modulation**
  In this chapter we propose a novel adaptive DSTS aided system that exploits the advantages of differential encoding, iterative decoding, as well as SP modulation, while adapting the system parameters for the sake of achieving the highest possible bandwidth efficiency, as well as maintaining a given target BER. The proposed adaptive DSTS-SP scheme benefits from a substantial diversity gain, while using four transmit antennas without the need for pilot-assisted channel envelope estimation and coherent detection. The proposed scheme reaches the target BER of 10^{-3} at an SNR of about 5 dB and maintains it for SNRs in excess of this value, while increasing the effective throughput. The system's bandwidth efficiency varies from 0.25 bits/sec/Hz to 16 bits/sec/Hz.

- **Chapter 13: Layered Steered Space-Time Codes**
  In this chapter, we propose a multi-functional MIMO scheme, that combines the benefits of Vertical Bell Labs Layered Space-Time (V-BLAST) codes, of space-time codes as well as of beamforming. Thus, the proposed system benefits from the multiplexing gain of the V-BLAST, from the diversity gain of the space-time codes and from the SNR gain of the beamformer. The MIMO scheme is referred to as Layered Steered Space-Time Codes (LSSTC). To further enhance the attainable system performance and to maximise the coding advantage of the proposed transmission scheme, the system is also combined with multi-dimensional SP modulation.

  In Section 13.2 we outline the encoding and decoding processes of this multi-functional MIMO scheme when combined with conventional as well as SP modulation schemes. Then, in Section 13.3 we quantify the capacity of the proposed multi-functional MIMO and present the capacity limits for a system employing $N_t = 4$ transmit antennas, $N_r = 4$ receive antennas and a variable number L_{AA} of elements per Antenna Array (AA). Furthermore, in Section 13.4.3 we quantify the upper bound of the achievable bandwidth efficiency of the system based on the EXIT charts obtained for the iteratively detected system.

  To further enhance the attainable system performance, the proposed MIMO scheme is serially concatenated with both an outer code and a URC, where three different receiver structures are presented by varying the iterative detection configuration of the constituent decoders/demapper. In Section 13.4.1 we provide a brief description of the iteratively detected two-stage RSC-coded LSSTC-SP scheme, where extrinsic information is exchanged between the outer RSC decoder and the inner URC decoder, while no iterations are carried out between the URC decoder and the SP demapper. The convergence behaviour of the iterative-detection-aided system is analysed using EXIT charts in Section 13.4.1.1. In Section 13.4.1.2, we employ the powerful technique of EXIT tunnel-area minimisation, for the sake of achieving a near-capacity operation. Consequently, we invoke IrCCs for the sake of appropriately shaping the EXIT curves by minimising the area within the EXIT-tunnel using the procedure of [179, 182].

  In Section 13.4.2 we present an iteratively detected three-stage RSC-coded LSSTC scheme, where extrinsic information is exchanged between the three constituent decoders, namely the outer RSC decoder, the inner URC decoder as well as the demapper. 3D EXIT charts are presented in Section 13.4.2.1, followed by Section 13.4.2.2, where the simplified 2D projections of the 3D EXIT charts were provided. Finally, in Section 13.5 we discuss our performance results and characterise the three iteratively detected LSSTC schemes proposed. Explicitly, the SP aided system is capable of operating within 0.9 dB, 0.6 dB and 0.4 dB from the maximum achievable rate limit. However, to operate within 0.6 dB from the maximum achievable rate limit, the system imposes twice the complexity compared to a system operating within 0.9 dB from this limit. On the other hand, to operate as close as 0.4 dB from the maximum achievable rate limit, the system imposes 20 times higher complexity in comparison to the one operating within 0.9 dB from the maximum achievable rate limit. The proposed design principles are applicable to an arbitrary number of antennas and diverse antenna configura-

tions as well as modem schemes. By contrast, the QPSK modulated three-stage iteratively detected system is capable of operating within 1.54 dB from the maximum achievable rate limit and thus the SP modulated system outperforms its QPSK aided counterpart by about 1 dB at a BER of 10^{-6}.

- **Chapter 14: Downlink LSSTS Aided Generalised MC DS-CDMA**
  A multi-functional multiuser MIMO scheme that combines the benefits of V-BLAST, of STS, of generalised MC DS-CDMA as well as of beamforming is presented. The proposed system is referred to as Layered Steered Space-Time Spreading (LSSTS) aided generalised MC DS-CDMA, which benefits from a multiplexing gain, a spatial diversity gain, a frequency diversity gain and a beamforming gain.
  In Section 14.2 the proposed LSSTS scheme's transmitter structure is characterised and then the decoding process is illustrated. Afterwards, in order to increase the number of users supported by the system, Frequency Domain (FD) spreading is applied in the generalised MC DS-CDMA in addition to the Time Domain (TD) spreading action of the STS. A user-grouping technique is employed that minimises the FD interference coefficient for the users in the same TD group.

  To further enhance the achievable system's performance, the proposed MIMO scheme is serially concatenated with an outer code combined with a URC, where three different iteratively detected systems are presented in Section 14.4. EXIT charts are used to study the convergence behaviour of the proposed systems and in Section 14.4.1 we propose an LLR post-processing technique for the soft output of the QPSK demapper in order to improve the achievable system performance. In Section 14.5 we discuss our performance results and characterise the three proposed iteratively detected schemes, while employing N_t=4 transmit AAs, N_r=2 receive antennas, L_{AA} number of elements per AA, V number of subcarriers supporting K users.

- **Chapter 15: Distributed Turbo Coding**
  A cooperative communication scheme referred to as Distributed Turbo Coding (DTC) is presented. In the proposed scheme, two users are cooperating, where each user's transmitter is constituted by an RSC code and an interleaver followed by a SP mapper. In Section 15.2 we provide an overview of cooperative communications and the background of the major cooperative signalling strategies including AF, DF and coded cooperation. In Section 15.3 the DTC scheme is presented, where a two-phase cooperation scheme is proposed. In the first phase, the two users exchange their data, while in the second phase the two users simultaneously transmit their data to the base station. In Section 15.4 we characterise the attainable system performance and study the effects of varying the inter-user channel characteristics on the performance of the uplink DTC scheme.

- **Chapter 16: Conclusions and Future Research Ideas**

  This chapter summarises the main findings of the book, giving cognizance to the current trends in the research community and outlines a range of suggestions for future research.

1.6.2 Novel Aspects of the Book

The book is based on a diverse range of publications, which were listed at the back of the book as well as in the Author Index and covers the following novel research aspects:

- The achievable performance of several STBC-SP schemes employing various sphere packing constellation sizes L was investigated, where the constellation points were first chosen based

on a minimum energy criterion. Then, an exhaustive computer search was conducted in order to find the set of L points having the highest MED from the entire set of constellation points satisfying the minimum energy criterion.

- A turbo-detected sphere packing modulation aided STBC scheme was proposed, where the sphere packing demapper was further developed for the sake of accepting the *a priori* information passed to it from the channel decoder as extrinsic information [195, 196].

- In order to portray the different EXIT characteristics associated with different bit-to-SP-symbol mapping schemes, 10 different anti-Gray mapping (AGM) schemes were developed that were specifically selected from all the possible mapping schemes available for $L = 16$. The slope of the EXIT curves corresponding to the different AGM schemes increases gradually in fine steps demonstrating the advantages of multi-dimensional constellation mapping. Exhibiting a gradually increasing EXIT characteristic is essential for the sake of designing near-capacity turbo-detected systems. The proposed turbo-detected STBC-SP scheme was optimised using using EXIT charts [197].

- A differential turbo-detected sphere packing modulation aided STBC scheme that requires no channel state information was proposed and its performance was optimised using EXIT charts [198].

- A three-stage serially concatenated turbo-detected STBC-SP scheme was proposed that is capable of achieving infinitesimally low BER values, where the performance was no longer limited by a BER floor. The convergence behaviour of the three-stage system was analysed and designed with the aid of 3D EXIT charts and their 2D projections, resulting in a near-capacity performance [199, 200].

- A procedure was proposed for calculating a tighter upper bound on the maximum achievable bandwidth efficiency of concatenated schemes based on the so-called 'area property' of the EXIT charts [199, 200].

- A purely symbol-based scheme was proposed, where symbol-based turbo detection was carried out by exchanging extrinsic information between an outer non-binary LDPC code and a rate-1 non-binary inner precoder. The convergence behaviour of the proposed symbol-based scheme was analysed using novel symbol-based EXIT charts [48, 201–203].

- Llinear dispersion codes were used in order to unify the family of orthogonal and non-orthogonal STBC designs. This unified structure enables us to examine existing STBCs from a novel perspective. More explicitly, we characterized the linkage between existing STBCs found in the open literature and LDCs in terms of both their mathematical representations and their design philosophies. Furthermore, we proposed to optimize the LDCs from a capacity maximization perspective, namely by maximizing the LDCs' Discrete-input Continuous-output Memoryless Channel (DCMC) capacity.

- We demonstrated the fundamental relationship between STBCs and DSTBCs, which enables us to extend the STBC design philosophy to DSTBCs. Furthermore, the Cayley transform [13] was introduced as an efficient way of constructing unitary matrices for their description. The resultant Differential Linear Dispersion Codes (DLDCs) based on the Cayley transform exhibited similar characteristics to those of their coherently detected LDC counterparts.

- The fundamental relationship between co-located and cooperative MIMO systems has been investigated, which is facilitated by the establishment of the broadcast interval. In other words, CSTBCs are designed to provide spatial diversity with the aid of a two-phase transmission regime. Hence, we proposed the family of twin-layer Cooperative Linear Dispersion Codes (CLDCs), which inherited the flexible linear dispersion structure and were specifically designed to exploit the above-mentioned two-phase transmission regime.

- A quantitative comparative study of LDCs, DLDCs and CLDCs is conducted, since all of them are based on the linear dispersion structure. Our investigations suggested that the family of LDCs is suitable for co-located MIMO systems employing coherent detection. The class of DLDCs is more applicable, when no CSI is available at the receiver. When relay-aided cooperative transmission is necessary to avoid the performance erosion imposed by shadow fading, our specifically designed twin-layer CLDCs are more beneficial.

- The concept of irregular coding [204] was documented and it was extended to a broad range of systems. More explicitly, the irregular design principle was applied in the context of the inner code of a serial concatenated coding scheme. The resultant inner IrRegular Precoded LDC (IR-PLDC) scheme facilitates the system's near-capacity operation across a wide range of SNRs. Similarly, we proposed the IR-DLDCs for non-coherent MIMO systems and IR-CLDCs for cooperative MIMO systems.

- A Differential Space-Time Spreading (DSTS) scheme is proposed, which is advocated for the sake of achieving a high transmit diversity gain in a multi-user system, while eliminating the complexity of MIMO channel estimation. Additionally, the system is combined with multi-dimensional Sphere Packing (SP) modulation, which is capable of maximising the coding advantage of the transmission scheme by jointly designing and detecting the sphere-packed DSTS symbols. The capacity of the DSTS-SP scheme is quantified analytically, where it is shown that the DSTS-SP system attains a higher capacity than its counterpart dispensing with SP [205–207].

- Iteratively detected DSTS-SP schemes are designed for near-capacity operation, where EXIT charts are used for analysing the convergence behaviour of the iterative detection. The outer code used in the iterative detection aided systems is a Recursive Systematic Convolutional (RSC) code, while the inner code is SP mapper in the first system and a Unity Rate Code (URC) in the second system, where the URC is capable of eliminating the error floor present in the BER performance of the system dispensing with URC [205, 208–210].

- An algorithm is devised for computing the maximum achievable rate of the DSTS system using EXIT charts, where the maximum achievable rate obtained using EXIT charts matches closely with the analytically computed capacity [205].

- An adaptive DSTS-SP scheme is proposed in order to maximise the system's throughput. The adaptive scheme exploits the advantages of differential encoding, iterative decoding as well as SP modulation. The achievable integrity and bit rate enhancements of the system are determined by the following factors: the specific transmission configuration used for transmitting data from the four antennas, the spreading factor used and the RSC encoder's code rate [211].

- The merits of V-BLAST, STC and beamforming are amalgamated in a Layered Steered Space-Time Coded (LSSTC) multi-functional MIMO scheme for the sake of achieving a multiplexing gain, a diversity gain as well as a beamforming gain. Additionally, the capacity of the LSSTC-SP scheme is quantified analytically [212].

- Furthermore, in order to characterise the LSSTC scheme, three iteratively detected LSSTC-SP receiver structures are proposed, where iterative detection is carried out between the outer code's decoder, the intermediate code's decoder and the LSSTC-SP demapper. The three systems are capable of operating within 0.9, 0.4 and 0.6 dB from the maximum achievable rate limit of the system. A comparison between the three iteratively detected schemes reveals that a carefully designed two-stage iterative detection aided scheme is capable of operating sufficiently close to capacity at a lower complexity, when compared to a three-stage system employing RSC or a two-stage system employing an Irregular Convolutional Code (IrCC) as the outer code [22, 213].

- A multi-functional MIMO combining STS, V-BLAST and beamforming with generalised MC DS-CDMA is proposed and referred to as Layered Steered Space-Time Spreading (LSSTS). The LSSTS scheme is capable of achieving a spatial diversity gain, frequency diversity gain, multiplexing gain as well as beamforming gain.The number of users supported can be extended by employing combined time- and frequency-domain spreading [214].
- A novel LLR post-processing technique is devised for improving the iteratively detected LSSTS system's performance [214].
- Finally, ideas from cooperative communications and turbo coding are combined to form a Distributed Turbo Code (DTC), where turbo coding is employed by exchanging extrinsic information between the outer codes' decoders in the two cooperating users' handsets.

Part I

Coherent Versus Differential Turbo-Detection of Sphere-Packing Aided Single-User MIMO Systems

Chapter 2

Space-Time Block Code Design Using Sphere Packing

2.1 Introduction

Most of the schemes outlined in Chapter 1 assumed encountering one of two different idealised channel conditions, namely either quasi-static or rapid fading [8, 215–231]. However, practical wireless communication channels exhibit both spatial and temporal correlation. The space-time codes that have been specifically designed for quasi-static or rapid fading channels may not be optimum when they are employed in practice. Therefore, the specific design criteria adopted should take into account the typical fading rates encountered, which determines the amount of correlation. In this chapter, a general design criterion is considered that takes into account the amount of correlation encountered.

In [190], the design of robust space-time modulation schemes designed for time-correlated Rayleigh fading channels was considered. It was assumed that the wireless channel is only time-correlated. Specific design criteria adopted for the time-correlated Rayleigh fading channel were derived. The design concept of maximising the diversity product [222, 223] was generalised in [190] in order to account of the effects of the temporal correlation. The lower and upper bounds of the general diversity product were also established in order to assist in the development of systematic space-time signal design procedures. In order to maximise the achievable coding advantage for space-time signals that achieve full diversity, a class of space-time block coded signals was constructed by combining orthogonal space-time code design with sphere packing (SP) modulation, which is referred to here as STBC-SP.

The rest of the chapter is organised as follows. First, the design criteria devised for space-time signals are presented in Section 2.2, where the channel model is discussed along with the design criteria invoked for quasi-static and rapid fading channels. Then, the design space-time signals recommended for time-correlated fading channels is reviewed in Section 2.3, where the concept of general diversity product is presented. In Section 2.4, the motivation behind the adoption of sphere packing modulation combined with orthogonal design is discussed, where the specific signal design devised for two transmit antennas is considered in more detail. Finally, the performance of STBC-SP schemes will be presented in Section 2.5, demonstrating that the amalgamated STBC-SP schemes outperform STBC arrangements that employ conventional modulation (i.e. PSK, QAM).

2.2 Design Criteria for Space-Time Signals

2.2.1 Channel Model

A wireless communication system having N_t transmit and N_r receive antennas is considered. The space-time modulator first divides the input information bits into blocks of B bits and maps each block to the appropriate space-time signal selected from the signal set of size $L = 2^B$. The space-time signal is then transmitted over the N_t transmit antennas using T time slots as detailed in [8, 190]. In general terms, each space-time signal can be expressed using the following $(T \times N_t)$-dimensional matrix

$$\mathbf{C} = \begin{bmatrix} c_1^1 & c_1^2 & \cdots & c_1^{N_t} \\ c_2^1 & c_2^2 & \cdots & c_2^{N_t} \\ \vdots & \vdots & \ddots & \vdots \\ c_T^1 & c_T^2 & \cdots & c_T^{N_t} \end{bmatrix}_{T \times N_t}, \tag{2.1}$$

where c_t^i denotes the symbol transmitted by transmit antenna i, for $i = 1, \ldots, N_t$, in time slot t, for $t = 1, \ldots, T$. The above space time signal satisfies the following energy constraint

$$E\left[||\mathbf{C}||_F^2\right] \;=\; N_t T, \tag{2.2}$$

where $E[\cdot]$ refers to the expected value and $||\mathbf{C}||_F$ is the Frobenius norm of $\mathbf{C}$, defined as [232]

$$||\mathbf{C}||_F^2 \;=\; \mathrm{tr}(\mathbf{C}^{\mathcal{H}}\mathbf{C}) \;=\; \mathrm{tr}(\mathbf{C}\mathbf{C}^{\mathcal{H}}) \;=\; \sum_{t=1}^{T}\sum_{i=1}^{N_t} |c_t^i|^2, \tag{2.3}$$

where $\mathrm{tr}(\cdot)$ denotes the trace of a matrix and $(\cdot)^{\mathcal{H}}$ denotes the complex conjugate transpose of a matrix. The signal y_t^j received by antenna j at time t is given by

$$y_t^j \;=\; \sqrt{\frac{\rho}{N_t}} \sum_{i=1}^{N_t} c_t^i h_{i,j}(t) + z_t^j, \qquad t = 1, \ldots, T, \tag{2.4}$$

where z_t^j is the complex AWGN noise encountered at receive antenna j at time t, which has zero mean and unit variance, while $h_{i,j}(t)$ is the channel coefficient characterising the non-dispersive link between transmit antenna i and receive antenna j at time t. The channel coefficients are modelled as zero-mean complex-valued Gaussian random variables having a unit variance and they are assumed to be known at the receiver, but unknown at the transmitter. It is also assumed that the channel has temporal correlation but no spatial correlation. In other words, the channel coefficients $h_{i,j}(t)$ are independent for different indices (i, j), but correlated in the time domain. Furthermore, ρ is defined as the signal to noise ratio per space-time signal at each receive antenna, and it is independent of the number of transmit antennas.

In [233, 234], the received signal of Equation (2.4) was rewritten in a vectorial form as

$$\mathbf{Y} = \sqrt{\frac{\rho}{N_t}}\mathbf{D}\mathbf{H} + \mathbf{Z}, \tag{2.5}$$

where $\mathbf{D}$ is an $(N_r T \times N_t N_r T)$-dimensional matrix constructed from the space-time signal matrix $\mathbf{C}$ as follows

$$\mathbf{D} = \begin{bmatrix} \mathbf{D}_1 & \mathbf{D}_2 & \cdots & \mathbf{D}_{N_t} & 0 & 0 & \cdots & 0 & \cdots & 0 & 0 & \cdots & 0 \\ 0 & 0 & \cdots & 0 & \mathbf{D}_1 & \mathbf{D}_2 & \cdots & \mathbf{D}_{N_t} & \cdots & 0 & 0 & \cdots & 0 \\ & & \vdots & & & & \vdots & & \ddots & & & \vdots & \\ 0 & 0 & \cdots & 0 & 0 & 0 & \cdots & 0 & \cdots & \mathbf{D}_1 & \mathbf{D}_2 & \cdots & \mathbf{D}_{N_t} \end{bmatrix}_{N_rT \times N_tN_rT}, \tag{2.6}$$

where

$$\mathbf{D}_i = \text{diag}(c_1^i, c_2^i, \ldots, c_T^i), \qquad i = 1, \ldots, N_t, \tag{2.7}$$

which corresponds to the i-th column of the space-time signal matrix $\mathbf{C}$. The (N_tN_rT)-dimensional non-dispersive channel coefficient vector $\mathbf{H}$ can be written as

$$\mathbf{H} = \begin{bmatrix} \mathbf{h}_{1,1}^T & \cdots & \mathbf{h}_{N_t,1}^T & \mathbf{h}_{1,2}^T & \cdots & \mathbf{h}_{N_t,2}^T & \cdots & \mathbf{h}_{1,N_r}^T & \cdots & \mathbf{h}_{N_t,N_r}^T \end{bmatrix}^T_{N_tN_rT \times 1}, \tag{2.8}$$

where $(\cdot)^T$ denotes the transpose of a matrix and finally we have

$$\mathbf{h}_{i,j} = \begin{bmatrix} h_{i,j}(1) & h_{i,j}(2) & \cdots & h_{i,j}(T) \end{bmatrix}^T_{T \times 1}. \tag{2.9}$$

The received signal vector $\mathbf{Y}$ is written as

$$\mathbf{Y} = \begin{bmatrix} y_1^1 & \cdots & y_T^1 & y_1^2 & \cdots & y_T^2 & \cdots & y_1^{N_r} & \cdots & y_T^{N_r} \end{bmatrix}^T_{N_rT \times 1}. \tag{2.10}$$

Finally, the noise vector $\mathbf{Z}$ has the form

$$\mathbf{Z} = \begin{bmatrix} z_1^1 & \cdots & z_T^1 & z_1^2 & \cdots & z_T^2 & \cdots & z_1^{N_r} & \cdots & z_T^{N_r} \end{bmatrix}^T_{N_rT \times 1}. \tag{2.11}$$

Example 2.2.1. *(2 × 2) systems:*
In order to illustrate the employment of the vectorial representation of Equation (2.5), we will consider the simple scenario, when we have $N_t = N_r = T = 2$. The matrix $\mathbf{D}$ can be written as follows:

$$\mathbf{D} = \begin{bmatrix} \mathbf{D}_1 & \mathbf{D}_2 & 0 & 0 \\ 0 & 0 & \mathbf{D}_1 & \mathbf{D}_2 \end{bmatrix}_{4 \times 8},$$

where

$$\mathbf{D}_i = \begin{bmatrix} c_1^i & 0 \\ 0 & c_2^i \end{bmatrix}_{2 \times 2},$$

which leads to

$$\mathbf{D} = \begin{bmatrix} c_1^1 & 0 & c_1^2 & 0 & 0 & 0 & 0 & 0 \\ 0 & c_2^1 & 0 & c_2^2 & 0 & 0 & 0 & 0 \\ 0 & 0 & 0 & 0 & c_1^1 & 0 & c_1^2 & 0 \\ 0 & 0 & 0 & 0 & 0 & c_2^1 & 0 & c_2^2 \end{bmatrix}_{4 \times 8}.$$

The non-dispersive channel impulse response (CIR) vector $\mathbf{H}$ *is written as*

$$\mathbf{H} = \left[\begin{array}{cccccccc} h_{1,1}(1) & h_{1,1}(2) & h_{2,1}(1) & h_{2,1}(2) & h_{1,2}(1) & h_{1,2}(2) & h_{2,2}(1) & h_{2,2}(2) \end{array} \right]^T_{8 \times 1} .$$

Accordingly, the received signal $\mathbf{Y}$ *expressed in Equations (2.5) and (2.10) for the* 2×2 *system under consideration is written as*

$$\mathbf{Y} = \left[\begin{array}{c} y_1^1 \\ y_2^1 \\ y_1^2 \\ y_2^2 \end{array} \right] = \left[\begin{array}{c} c_1^1 \cdot h_{1,1}(1) + c_1^2 \cdot h_{2,1}(1) + z_1^1 \\ c_2^1 \cdot h_{1,1}(2) + c_2^2 \cdot h_{2,1}(2) + z_2^1 \\ c_1^1 \cdot h_{1,2}(1) + c_1^2 \cdot h_{2,2}(1) + z_1^2 \\ c_2^1 \cdot h_{1,2}(2) + c_2^2 \cdot h_{2,2}(2) + z_2^2 \end{array} \right].$$

2.2.2 Pairwise Error Probability and Design Criterion

Consider Equation (2.10) and let $\mathbf{D}$ as well as $\tilde{\mathbf{D}}$ be two different matrices corresponding to two different space-time signals $\mathbf{C}$ and $\tilde{\mathbf{C}}$, respectively. According to [233,234], the pairwise error probability between $\mathbf{D}$ and $\tilde{\mathbf{D}}$ can be upper bounded as

$$P(\mathbf{D} \rightarrow \tilde{\mathbf{D}}) \leq \binom{2K-1}{K} \left(\prod_{i=1}^{K} \gamma_i \right)^{-1} \left(\frac{\rho}{N_t} \right)^{-K}, \tag{2.12}$$

where K is the rank of $(\mathbf{D} - \tilde{\mathbf{D}})\mathbf{R}(\mathbf{D} - \tilde{\mathbf{D}})^{\mathcal{H}}$; $\gamma_1, \gamma_2, \ldots, \gamma_K$ are the non-zero eigenvalues of $(\mathbf{D} - \tilde{\mathbf{D}})\mathbf{R}(\mathbf{D} - \tilde{\mathbf{D}})^{\mathcal{H}}$; and $\mathbf{R} = E[\mathbf{H}\mathbf{H}^{\mathcal{H}}]$ is the correlation matrix of $\mathbf{H}$. Maximising the pairwise error probability of Equation (2.12), rather than that between the modulated symbols of the individual time slots implies that the individual space-time (ST) signals have to have the maximum possible Euclidean distance.

The authors of [233, 234] have also proposed a general design criterion based on the upper bound of the pairwise error probability expressed in Equation (2.12) that consists of two parts:

- The minimum rank of $(\mathbf{D} - \tilde{\mathbf{D}})\mathbf{R}(\mathbf{D} - \tilde{\mathbf{D}})^{\mathcal{H}}$ should be maximised.
- The minimum value of the product $\prod_{i=1}^{K} \gamma_i$ should be maximised.

This criterion is consistent with the well-know space-time signal design criteria outlined in [8, 217] for the extreme cases of the quasi-static and the rapid fading channel models, which are reproduced here for completeness:

- **Quasi-static fading channels**: The minimum rank of

$$\mathbf{\Delta} \stackrel{\triangle}{=} (\mathbf{C} - \tilde{\mathbf{C}})(\mathbf{C} - \tilde{\mathbf{C}})^{\mathcal{H}}, \tag{2.13}$$

  over all pairs of distinct ST signals $\mathbf{C}$ and $\tilde{\mathbf{C}}$ should be maximised. According to [222, 223], if $\mathbf{\Delta}$ is of full rank for any pair of distinct signals $\mathbf{C}$ and $\tilde{\mathbf{C}}$, in other words, if columns are independent of each other, then the so-called diversity product is given by [222, 223]

$$\zeta_{\text{static}} = \frac{1}{2\sqrt{N_t}} \min_{\mathbf{C} \neq \tilde{\mathbf{C}}} |det(\mathbf{\Delta})|^{\frac{1}{2T}}, \tag{2.14}$$

where the diversity product or coding advantage is defined as the estimated SNR gain over an uncoded system having the same diversity order as the coded system [8].

- **Rapid fading channels**: The minimum number of non-zero rows of $(\mathbf{C}-\tilde{\mathbf{C}})$ should be maximised for any pair of distinct signals $\mathbf{C}$ and $\tilde{\mathbf{C}}$. If there is no zero row in $(\mathbf{C}-\tilde{\mathbf{C}})$, then the diversity product is given by [8, 217]

$$\zeta_{\text{rapid}} = \frac{1}{2\sqrt{N_t}} \min_{\mathbf{C}\neq\tilde{\mathbf{C}}} \left(\prod_{t=1}^{T} ||\mathbf{c}_t - \tilde{\mathbf{c}}_t||_F^2 \right)^{\frac{1}{2T}}, \tag{2.15}$$

where $\mathbf{c}_t$ and $\tilde{\mathbf{c}}_t$ are the t-th rows of $\mathbf{C}$ and $\tilde{\mathbf{C}}$, respectively.

2.3 Design Criteria for Time-Correlated Fading Channels

In this section, the design criteria devised for time-correlated fading channels in [190] are considered. The pairwise error probability of the ST signals and related design criteria will be presented in Section 2.3.2. The generalised diversity product along with its lower and upper bounds will also be discussed in Sections 2.3.3.1 and 2.3.3.2, respectively.

2.3.1 Preliminaries

The channel's correlation matrix $\mathbf{R}$ can be written as

$$\begin{aligned} \mathbf{R} &= E[\mathbf{H}\mathbf{H}^{\mathcal{H}}] \\ &= \text{diag}\left(\mathbf{R}_{1,1}, \ldots, \mathbf{R}_{N_t,1}, \mathbf{R}_{1,2}, \ldots, \mathbf{R}_{N_t,2}, \ldots\ldots, \mathbf{R}_{1,N_r}, \ldots, \mathbf{R}_{N_t,N_r}\right), \end{aligned} \tag{2.16}$$

where

$$\mathbf{R}_{i,j} = E[\mathbf{h}_{i,j}\mathbf{h}_{i,j}^{\mathcal{H}}] \tag{2.17}$$

corresponds to the time-domain correlation matrix of the channel coefficients describing the link between transmit antenna i and receive antenna j. When using Jakes fading model [235], all of the time-domain correlation matrices $\mathbf{R}_{i,j}$ are the same. In other words, the temporal correlation of the signal transmitted from transmit antenna i to receive antenna j is the same. Hence, the correlation matrix of Equation (2.16) can be written as

$$\mathbf{R} = \mathbf{I}_{N_t N_r} \otimes \breve{\mathbf{R}}, \tag{2.18}$$

where $\otimes$ denotes the tensor product [232], $\mathbf{I}_{N_t N_r}$ is the identity matrix of size $(N_t N_r \times N_t N_r)$ and R is the time correlation matrix of the signal transmitted between antenna i and antenna j, defined as

$$\breve{\mathbf{R}} \triangleq \mathbf{R}_{i,j} = \underbrace{\begin{bmatrix} r_{1,1} & \cdots & r_{1,T} \\ \vdots & \ddots & \vdots \\ r_{T,1} & \cdots & r_{T,T} \end{bmatrix}}_{T \times T}. \tag{2.19}$$

From Equations (2.6), (2.7), and (2.18), one can write [190]

$$
\begin{aligned}
& (\mathbf{D}-\tilde{\mathbf{D}})\mathbf{R}(\mathbf{D}-\tilde{\mathbf{D}})^{\mathcal{H}} \\
= \;& \mathbf{I}_{N_r} \otimes \left[\sum_{i=1}^{N_t}(\mathbf{D}_i-\tilde{\mathbf{D}}_i)\breve{\mathbf{R}}(\mathbf{D}_i-\tilde{\mathbf{D}}_i)^{\mathcal{H}}\right] \\
= \;& \mathbf{I}_{N_r} \\
& \otimes \begin{bmatrix} \sum_{i=1}^{N_t}|c_1^i-\tilde{c}_1^i|^2 r_{1,1} & \sum_{i=1}^{N_t}(c_1^i-\tilde{c}_1^i)(c_2^i-\tilde{c}_2^i)^* r_{1,2} & \cdots & \sum_{i=1}^{N_t}(c_1^i-\tilde{c}_1^i)(c_T^i-\tilde{c}_T^i)^* r_{1,T} \\ \sum_{i=1}^{N_t}(c_2^i-\tilde{c}_2^i)(c_1^i-\tilde{c}_1^i)^* r_{2,1} & \sum_{i=1}^{N_t}|c_2^i-\tilde{c}_2^i|^2 r_{2,2} & \cdots & \sum_{i=1}^{N_t}(c_2^i-\tilde{c}_2^i)(c_T^i-\tilde{c}_T^i)^* r_{2,T} \\ \vdots & \vdots & \ddots & \vdots \\ \sum_{i=1}^{N_t}(c_T^i-\tilde{c}_T^i)(c_1^i-\tilde{c}_1^i)^* r_{T,1} & \sum_{i=1}^{N_t}(c_T^i-\tilde{c}_T^i)(c_2^i-\tilde{c}_2^i)^* r_{T,2} & \cdots & \sum_{i=1}^{N_t}|c_T^i-\tilde{c}_T^i|^2 r_{T,T} \end{bmatrix} \\
= \;& \mathbf{I}_{N_r} \otimes \left\{ \left[(\mathbf{C}-\tilde{\mathbf{C}})(\mathbf{C}-\tilde{\mathbf{C}})^{\mathcal{H}}\right] \circ \breve{\mathbf{R}} \right\} \\
= \;& \mathbf{I}_{N_r} \otimes \left\{ \mathbf{\Delta} \circ \breve{\mathbf{R}} \right\}, \qquad (2.20)
\end{aligned}
$$

where $\mathbf{\Delta}$ is defined in Equation (2.13), and $\circ$ denotes the Hadamard product [232], which is defined as follows

Definition 2.3.1. *Let* $\mathbf{A} = \{a_{i,j}\}$ *and* $\mathbf{B} = \{b_{i,j}\}$ *be two matrices of dimension* $(m \times n)$*. The Hadamard product of* $\mathbf{A}$ *and* $\mathbf{B}$ *is defined as*

$$
\mathbf{A} \circ \mathbf{B} = \begin{bmatrix} a_{1,1}b_{1,1} & \cdots & a_{1,n}b_{1,n} \\ \vdots & \ddots & \vdots \\ a_{m,1}b_{m,1} & \cdots & a_{m,n}b_{m,n} \end{bmatrix}. \qquad (2.21)
$$

2.3.2 Pairwise Error Probability and Design Criterion

Upon combining Equation (2.20) with Equation (2.12), the upper bound of the pairwise ST symbol error probability between $\mathbf{C}$ and $\tilde{\mathbf{C}}$ can be written as [190]

$$
P(\mathbf{C} \to \tilde{\mathbf{C}}) \leq \binom{2rN_r-1}{rN_r} \left(\prod_{i=1}^{r}\lambda_i\right)^{-N_r} \left(\frac{\rho}{N_t}\right)^{-rN_r}, \qquad (2.22)
$$

where r is the rank of $\mathbf{\Delta} \circ \breve{\mathbf{R}}$, and $\lambda_1, \lambda_2, \ldots, \lambda_r$ are the non-zero eigenvalues of $\mathbf{\Delta} \circ \breve{\mathbf{R}}$. According to Equations (2.22), the ST code design criteria devised for time-correlated fading channels can be formulated as follows [190]:

a) Design for diversity advantage: The minimum rank of $\mathbf{\Delta} \circ \breve{\mathbf{R}}$ should be maximised over all pairs of distinct ST signals $\mathbf{C}$ and $\tilde{\mathbf{C}}$.

b) Design for coding advantage: The minimum value of the product $\prod_{i=1}^{r}\lambda_i$ over all pairs of distinct ST signals $\mathbf{C}$ and $\tilde{\mathbf{C}}$ should be maximised.

2.3.3 Coding Advantage

The above-mentioned coding advantage or the diversity product was used in [222, 223] in order to characterise the performance of different space-time coding schemes that achieve an identical diversity advantage. The concept of the diversity product was generalised in [190] to time-correlated fading channels. Undoubtedly, this generalisation renders the evaluation and comparison of different space-time coding schemes more straightforward. Additionally, upper and lower bounds on the generalised diversity product were also developed in [190].

2.3.3.1 Generalised Diversity Product

According to the upper bound of the pairwise ST symbol error probability expressed in Equation (2.22), and assuming that $\mathbf{\Delta} \circ \breve{\mathbf{R}}$ is of full rank, the generalised diversity product can be written as [190]:

$$\zeta_R = \frac{1}{2\sqrt{N_t}} \min_{\mathbf{C} \neq \tilde{\mathbf{C}}} |det\left(\mathbf{\Delta} \circ \breve{\mathbf{R}}\right)|^{\frac{1}{2T}}. \tag{2.23}$$

It may be directly observed that for quasi-static fading channels (i.e. for $\mathbf{\Delta} \circ \breve{\mathbf{R}} = \mathbf{\Delta}$), Equation (2.23) reduces to Equation (2.14), namely to

$$\zeta_{\text{static}} = \frac{1}{2\sqrt{N_t}} \min_{\mathbf{C} \neq \tilde{\mathbf{C}}} |det(\mathbf{\Delta})|^{\frac{1}{2T}}.$$

For rapid fading channels the correlation matrix $\breve{\mathbf{R}}$ indicates that unless the time-lag considered is zero, the corresponding correlation coefficient is also zero, which is expressed as

$$\breve{\mathbf{R}} \;=\; \mathbf{I}_T \;=\; \begin{bmatrix} 1 & 0 & \cdots & 0 \\ 0 & 1 & \cdots & 0 \\ \vdots & \vdots & \ddots & \vdots \\ 0 & 0 & \cdots & 1 \end{bmatrix}_{T \times T}.$$

Additionally, it may be directly observed that for this case $\mathbf{\Delta} \circ \breve{\mathbf{R}}$ is a diagonal matrix whose entries are the diagonal entries of $\mathbf{\Delta}$, namely

$$\left(\mathbf{\Delta} \circ \breve{\mathbf{R}}\right)_{rapid} = \begin{bmatrix} ||\mathbf{c}_1 - \tilde{\mathbf{c}}_1||_F^2 & 0 & \cdots & 0 \\ 0 & ||\mathbf{c}_2 - \tilde{\mathbf{c}}_2||_F^2 & \cdots & 0 \\ \vdots & \vdots & \ddots & \vdots \\ 0 & 0 & \cdots & ||\mathbf{c}_T - \tilde{\mathbf{c}}_T||_F^2 \end{bmatrix}_{T \times T}, \tag{2.24}$$

where $\mathbf{c}_t$ and $\tilde{\mathbf{c}}_t$, $t = 1, \ldots, T$, are the t-th rows of $\mathbf{C}$ and $\tilde{\mathbf{C}}$, respectively. Consequently, Equation (2.23) reduces to Equation (2.15), namely to

$$\zeta_{\text{rapid}} = \frac{1}{2\sqrt{N_t}} min_{\mathbf{C} \neq \tilde{\mathbf{C}}} \left(\prod_{t=1}^{T} ||\mathbf{c}_t - \tilde{\mathbf{c}}_t||_F^2 \right)^{\frac{1}{2T}}.$$

2.3.3.2 Upper and Lower Bounds on the Generalised Diversity Product

It was shown in [190] that the generalised diversity product, ζ_R of Equation (2.23) is lower bounded by ζ_{static} of Equation (2.14) and upper bounded by ζ_{rapid} of Equation (2.15). More specifically, if a set of space-time signals characterised in terms of its dimension $(T \times N_t)$ has L elements and $\mathbf{\Delta} \circ \breve{\mathbf{R}}$ is of full rank for any pair of distinct ST signals $\mathbf{C}$ and $\tilde{\mathbf{C}}$, then the diversity product ζ_R of these signals devised for a fading channel and defined by the time-correlation matrix $\breve{\mathbf{R}}$, satisfies [190]

$$\max\left\{\zeta_{\text{static}}, |\det(\breve{\mathbf{R}})|^{\frac{1}{2T}} \zeta_{\text{rapid}}\right\} \;\leq\; \zeta_R \;\leq\; \zeta_{\text{rapid}} \;\leq\; \sqrt{\frac{L}{2(L-1)}}. \tag{2.25}$$

According to Equation (2.25), the diversity product ζ_R is determined by ζ_{rapid} if the time correlation matrix $\breve{\mathbf{R}}$ is of full rank, since $|\det(\breve{\mathbf{R}})|^{\frac{1}{2T}} \zeta_{\text{rapid}} \leq \zeta_R \leq \zeta_{\text{rapid}}$. By contrast, if $\breve{\mathbf{R}}$

does not have full rank, the diversity product ζ_R is no longer determined by ζ_{rapid}, since we have $\det(\breve{\mathbf{R}}) = 0$, which leads to $0 \leq \zeta_R \leq \zeta_{\text{rapid}}$. Another observation inferred from Equation (2.25) is that we have $\zeta_{\text{static}} \leq \zeta_R \leq \zeta_{\text{rapid}}$, which suggests that the diversity product ζ_R will be independent of the channel's correlation matrix $\breve{\mathbf{R}}$ for all space-time codes having $\zeta_{\text{static}} = \zeta_{\text{rapid}}$. Furthermore, the problem of designing robust space-time signals for time-correlated fading channels can be reduced to that of designing space-time signals for quasi-static fading channels, if ζ_{static} achieves the upper bound of $\sqrt{\frac{L}{2(L-1)}}$ quantified in Equation (2.25) or at least it is close to it, since ζ_R will also achieve or will at least be close to this upper bound for any time-correlated fading channel. Based on these results, all space-time signals designed for quasi-static fading channels, such as cyclic ST codes [222], ST codes derived from orthogonal design [215, 216, 219, 220], parametric ST codes [225], Cayley ST codes [224], etc., can also be used for communication over time-correlated fading channels.

2.4 Orthogonal ST-Code Design Using Sphere Packing

In this section, orthogonal ST-code design using sphere packing modulation is considered. First, a rudimentary introduction to sphere-packing as a geometric problem is provided in Section 2.4.1, followed by the general concept and the motivation of combining orthogonal ST-code design using sphere packing are discussed in Section 2.4.2. Then, the specific signal design proposed for $N_t = 2$ transmit antennas is provided in Section 2.4.3 in order to shed further light on the concept of combining orthogonal design with sphere packing. The sphere packing constellation construction is described in Section 2.4.4. Finally, the capacity of STBC-SP schemes is derived in Section 2.4.5

2.4.1 General Concept of Sphere Packing

In this section we present a brief overview of sphere packing, addressing some of the fundamental issues, such as the problem of packing spheres in a given n-dimensional Euclidean space $\mathbb{R}^n$ and the problem of determining how many spheres can just touch another sphere of the same size in this space. The latter problem is referred to as the 'kissing number problem'. More detailed discussions on these issues may be found in [236].

2.4.1.1 The Sphere Packing Problem

The classic sphere packing problem is to find out how densely identical non-overlapping spheres can be packed in a specific space. For the traditional 3-dimensional space, the sphere packing problem may be exemplified by considering a large storage area, and asking what is the highest number of identical balls that can be packed into this space. The packing problem becomes trivial, if we consider wooden cubes, for example, instead of the balls. The number of wooden cubes that we can pack would be equal to the volume of the storage area divided by the volume of one wooden cube, assuming that no space would be left over. In other words, we can ideally fill one hundred percent of the storage space since the wooden cubes fit together with no space wasted in between. By contrast, there is always some wasted space in between packed spheres.

Generally, the density Δ of a sphere packing is defined as the proportion of a volume occupied by the spheres, which may be defined as [236]:

$$\begin{aligned} \Delta &= \text{proportion of the space that is occupied by the spheres,} \\ &= \frac{\text{volume of one sphere}}{\text{volume of total space}}. \end{aligned} \tag{2.26}$$

The sphere packing problem is concerned with finding the densest packing of equal spheres in a specific n-dimensional space. This geometric problem has numerous practical applications.

2.4.1.2 Representation of n-dimensional Real Euclidean Space $\mathbb{R}^n$

A phasor point in the n-dimensional real-valued Euclidean space $\mathbb{R}^n$ may be represented by a string of n real numbers [236]

$$x = (x_1, x_2, x_3, \ldots, x_n).$$

Accordingly, a sphere in $\mathbb{R}^n$ with a centre $u = (u_1, \ldots, u_n)$ and radius ρ consists of all points $x = (x_1, x_2, x_3, \ldots, x_n)$ that satisfy the following constraint

$$(x_1 - u_1)^2 + (x_2 - u_2)^2 + \cdots + (x_n - u_n)^2 = \rho^2.$$

The graphical representation of the sphere packing problem is only feasible in two or three dimensions. Generally, a sphere packing in $\mathbb{R}^n$ is unambiguously described by specifying the centres u and the radius ρ, where all manipulations are carried out using coordinates. For example, the 4-dimensional real-valued Euclidean space $\mathbb{R}^4$ consists of phasor points having four coordinates instead of the conventional three coordinates that represent the 3-dimensional real Euclidean space $\mathbb{R}^3$. Example phasor points in the 4-dimensional real Euclidean space $\mathbb{R}^4$ include $(1.0, -2.3, 3.4, 0.7)$, $(5.6, 8.0, 14.2, -7.2)$, ...

2.4.1.3 Kepler Conjecture

In the 3-dimensional Euclidean space $\mathbb{R}^3$, the best packing is the one, when the centres of the spheres form a so-called face-entered cubic lattice [236], where the spheres only occupy $\pi/\sqrt{18} \approx 0.7405$ of the total space. Consequently, the density Δ of the face-entered cubic lattice packing is about 0.7405. Johannes Kepler had conjectured in 1611 that this is the maximum attainable density in the 3-dimensional Euclidean space $\mathbb{R}^3$. This has been known as the Kepler conjecture. In 1998, Thomas Hales announced the proof of the Kepler conjecture [237, 238], where he based his proof on the approach suggested by Lszl Fejes Tth in 1953 and employed complex computer calculations in order to check many individual cases. The Kepler conjecture has been extended to dimensions higher than three, where it is still an open mathematical problem.

2.4.1.4 Kissing Numbers

Another important issue, closely related to the sphere packing problem, is known as the kissing number problem. With respect to our 3-dimensional bowling balls example mentioned in Section 2.4.1.1, the kissing number problem asks what is the highest number of balls that can be arranged so that they all touch, or 'kiss', another ball of the same size [236]. Generally, the kissing number problem asks for the highest number of n-dimensional spheres that can kiss another sphere of a similar size.

In the one-dimensional Euclidean space, the answer is 2, while in the 2-dimensional Euclidean space, it is 6, as seen in Figure 2.1. In the 3-dimensional Euclidean space, the answer is now known to be 12. The answer is also known in 8 and 24 dimensions to be 240 and 196 560, respectively. However, in four dimensions the highest kissing number is only known to be either 24 or 25.

2.4.1.5 n-dimensional Packings

The 1-dimensional lattice Z, representing the integers, is the densest packing in one dimension with a density of $\Delta = 1$. In two dimensions, the densest packing is also known with a density

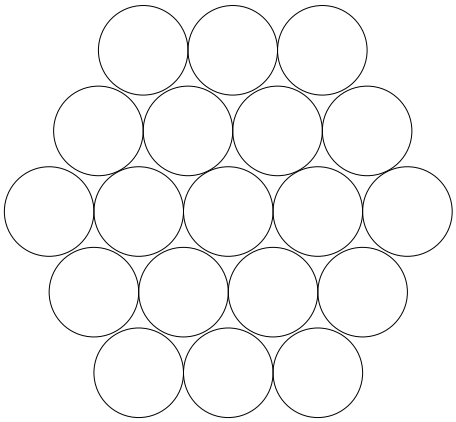

Figure 2.1: Sphere-packing (or circle-packing) in the 2-dimensional Euclidean space.

Dimension	1	2	3	4	5	6	7	8	12	16	24
Densest Packing	**Z**	$\mathbf{A_2}$	$\mathbf{A_3}$	D_4	D_5	E_6	E_7	E_8	K_{12}	Λ_{16}	Λ_{24}
Highest Kissing Number	**2**	**6**	**12**	24	40	72	126	**240**	756 4	320	**196560**

Table 2.1: Sphere packing and kissing number in several dimensions. The bold-faced values refer to those that were proven optimal © [236].

of $\Delta = \pi/\sqrt{12} \approx 0.9069$. Figure 2.1 shows the hexagonal lattice packing, which is the densest in two dimensions. In three dimensions, the face-entered cubic lattice is the densest packing with a density of $\Delta = \pi/\sqrt{18} \approx 0.7405$.

In the 4-dimensional real Euclidean space $\mathbb{R}^4$, the lattice D_4 is deemed to be the densest sphere packing arrangement, although this fact is not yet proven. More specifically, D_4 may be defined as a lattice that consists of all phasor points having integer coordinates (a_1, a_2, a_3, a_4), which are subjected to the sphere packing constraint of $a_1 + a_2 + a_3 + a_4 = k$, where k is an even integer. The sphere centred at $(0, 0, 0, 0)$ has 24 spheres around it, centred at the points $(+/-1, +/-1, 0, 0)$, where any choice of signs and any ordering of the coordinates is legitimate [236].

The densest packing in the 8-dimensional real-valued Euclidean space $\mathbb{R}^8$ is the E_8 lattice, which is a discrete subfield of $\mathbb{R}^8$ that consists of all phasor points having natural or half-natural[1] coordinates $(a_1, \ldots, a_8)$ that are subjected to the sphere packing constraint of $a_1 + \ldots + a_8 = k$, where k is an even integer. The existence of E_8 was proven in 1867 by J. S. Smith [239], but its first quadratic form expression was given in 1873 by A. Korkine and G. Zolotareff [240]. It was proven to be the densest packing in eight dimensions in 1979 [241, 242]. Table 2.1 summarises the sphere packing schemes and the highest kissing numbers in several dimensions.

2.4.1.6 Applications of Sphere Packing

In this section, some example applications will be briefly presented in order to justify our interest in finding dense packings of n-dimensional spheres. These applications include pure geometry, number theory, coding theory and code search as well as approximation problems.

The sphere packing problem originally appeared as an interesting problem in pure geometry, which was mentioned by Hilbert in his list of open problems in 1900 [243, 244]. Several authors demonstrated great interest in the sphere packing problem from the perspective of geometry [245–250]. Moreover, applications of sphere packing in number theory include, for example,

[1] If a is a natural number then $b = a + \frac{1}{2}$ is a half-natural number.

solving the so-called Diophantine equations and the geometry of numbers [251–253]. The sphere packing problem also has a direct connection with the construction of error correction codes. More specifically, the construction of an (n, M, d)-code[2] can be viewed as finding the densest packing of spheres having a radius of $\rho = (d-1)/2$ in n dimensions [236]. Another application of sphere packing is in solving n-dimensional search or approximation problems [254–257]. A recently proposed search method that has attracted considerable attention is sphere decoding [258, 259], which provides an accurate estimation similar to the optimum maximum likelihood solution but with a far lower complexity.

2.4.2 Sphere-Packing Aided STBC Concept

The concept of orthogonal ST signal design has become synonymous to space-time coding, following the remarkable discovery of Alamouti [215]. Since then, it has attracted considerable further attention [260]. The orthogonal ST-code design can be described with the aid of the following recursive procedure [221] as follows. Let $\mathbf{G}_1(x_1) = x_1\mathbf{I}_1$, and

$$\mathbf{G}_{2^k}(x_1, x_2, \ldots, x_{k+1}) = \begin{bmatrix} \mathbf{G}_{2^{k-1}}(x_1, x_2, \ldots, x_k) & x_{k+1}\mathbf{I}_{2^{k-1}} \\ -x_{k+1}^*\mathbf{I}_{2^{k-1}} & \mathbf{G}^{\mathcal{H}}_{2^{k-1}}(x_1, x_2, \ldots, x_k) \end{bmatrix}, \tag{2.27}$$

for $k = 1,\ 2, \ldots$, where x_{k+1}^* is the complex conjugate of x_{k+1}. Then, $\mathbf{G}_{2^k}(x_1, x_2, \ldots, x_{k+1})$ constitutes an orthogonal ST-code generator matrix design of size $(2^k \times 2^k)$, which maps the complex variables representing $(x_1, x_2, \ldots, x_{k+1})$ to $N_t = 2^k$ transmit antennas. In other words, $x_1, x_2, \ldots, x_{k+1}$ represent $(k+1)$ number of complex modulated symbols to be transmitted from $N_t = 2^k$ transmit antennas in $T = 2^k$ time slots. The effective throughput of $\mathbf{G}_{2^k}$ is $(k+1)/2^k$ complex symbols per time slot, which is the maximum throughput that may be achieved by an orthogonal ST-code design having a square-shaped generator matrix [221].

Space-time signals can be constructed directly from the orthogonal ST-code design $\mathbf{G}_{2^k}$ of Equation (2.27) for $N_t = 2^k$, $k = 1,\ 2, \ldots$, transmit antennas as [221]

$$\mathbf{C} = \sqrt{\frac{2^k}{k+1}}\ \mathbf{G}_{2^k}(x_1, x_2, \ldots, x_{k+1}), \tag{2.28}$$

where $x_1, x_2, \ldots, x_{k+1}$ are specifically chosen from a constellation space satisfying the following condition:

$$E\left[|x_1|^2 + |x_2|^2 + \ldots + |x_{k+1}|^2\right] \ = \ k+1.$$

The multiplicative term $\sqrt{2^k/(k+1)}$ in Equation (2.28) is a normalisation factor used for ensuring that the space-time signal $\mathbf{C}$ of Equation (2.28) satisfies the energy constraint of Equation (2.2), which dictates that

$$E\left[||\mathbf{C}||_F^2\right] \ = \ N_t T \ = \ 2^k \cdot 2^k = 2^{2k}, \tag{2.29}$$

since the space-time signal $\mathbf{C}$ of Equation (2.28) is of size $(2^k \times 2^k)$. The energy of the signal $\mathbf{C}$ in Equation (2.28) is computed as follows

[2] A code of length n, containing M codewords and with minimum distance d is referred to as an (n, M, d)-code that can detect and correct upto $(d-1)/2$ errors [6].

$$\begin{aligned} E||\mathbf{C}||_F^2 &= \left(\frac{2^k}{k+1}\right) \cdot E\left[2^k|x_1|^2 + 2^k|x_2|^2 + \ldots + 2^k|x_{k+1}|^2\right] \\ &= \left(\frac{2^k}{k+1}\right) \cdot 2^k \cdot E\left[|x_1|^2 + |x_2|^2 + \ldots + |x_{k+1}|^2\right] \\ &= \left(\frac{2^k}{k+1}\right) \cdot 2^k \cdot (k+1) \\ &= 2^{2k}, \end{aligned}$$

which satisfies the energy constraint of Equation (2.29).

Let $\mathbf{C}$ and $\tilde{\mathbf{C}}$ be two distinct space-time signals directly constructed from the orthogonal ST-code design $\mathbf{G}_{2^k}$ of Equation (2.27)

$$\mathbf{C} = \sqrt{\frac{2^k}{k+1}}\, \mathbf{G}_{2^k}(x_1, x_2, \ldots, x_{k+1}) \qquad \text{and} \qquad \tilde{\mathbf{C}} = \sqrt{\frac{2^k}{k+1}}\, \mathbf{G}_{2^k}(\tilde{x}_1, \tilde{x}_2, \ldots, \tilde{x}_{k+1}),$$

then we have

$$\mathbf{C} - \tilde{\mathbf{C}} = \sqrt{\frac{2^k}{k+1}}\, \mathbf{G}_{2^k}(x_1 - \tilde{x}_1, x_2 - \tilde{x}_2, \ldots, x_{k+1} - \tilde{x}_{k+1}),$$

and

$$\mathbf{\Delta} = \left(\mathbf{C} - \tilde{\mathbf{C}}\right)\left(\mathbf{C} - \tilde{\mathbf{C}}\right)^{\mathcal{H}} = \left(\mathbf{C} - \tilde{\mathbf{C}}\right)^{\mathcal{H}}\left(\mathbf{C} - \tilde{\mathbf{C}}\right) = \frac{2^k}{k+1}\sum_{i=1}^{k+1}|x_i - \tilde{x}_i|^2\mathbf{I}_{2^k}, \tag{2.30}$$

implying that $\mathbf{\Delta}$ is a diagonal matrix of size $(2^k \times 2^k)$. Observe that all of the diagonal entries in $\breve{\mathbf{R}}$ of Equation (2.19) are unity, yielding

$$\mathbf{\Delta} \circ \breve{\mathbf{R}} = \begin{bmatrix} \frac{2^k}{k+1}\sum_{i=1}^{k+1}|x_i - \tilde{x}_i|^2 & 0 & \cdots & 0 \\ 0 & \frac{2^k}{k+1}\sum_{i=1}^{k+1}|x_i - \tilde{x}_i|^2 & \cdots & 0 \\ \vdots & \vdots & \ddots & \vdots \\ 0 & 0 & \cdots & \frac{2^k}{k+1}\sum_{i=1}^{k+1}|x_i - \tilde{x}_i|^2 \end{bmatrix}_{2^k \times 2^k}, \tag{2.31}$$

and therefore

$$\det(\mathbf{\Delta} \circ \breve{\mathbf{R}}) = \left(\frac{2^k}{k+1}\sum_{i=1}^{k+1}|x_i - \tilde{x}_i|^2\right)^{2^k}. \tag{2.32}$$

Now, with the aid of Equations (2.23) and (2.32), as well as by observing that $T = N_t = 2^k$, the diversity product evaluated for space-time signals constructed from the orthogonal ST-code design $\mathbf{G}_{2^k}$ of Equation (2.27) can written as [190]

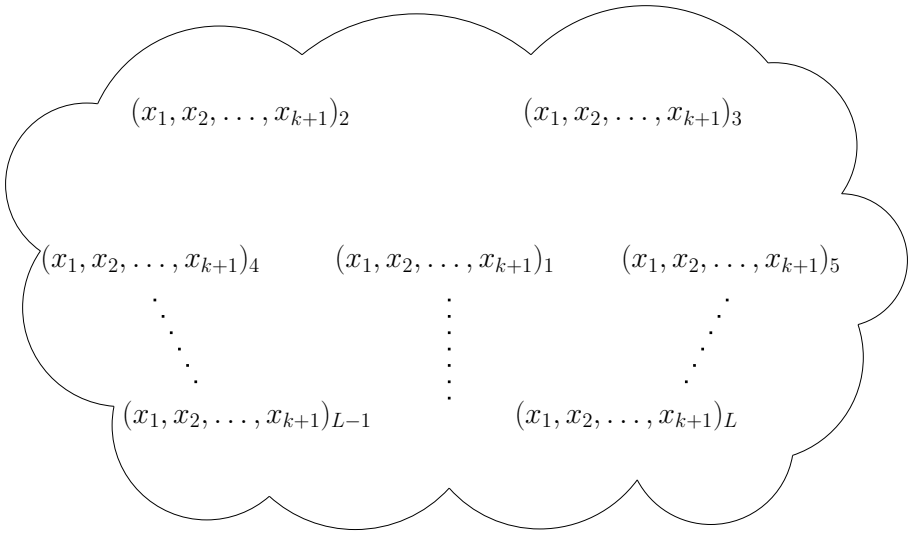

Figure 2.2: The L legitimate $(k+1)$-dimensional complex vectors.

$$\begin{aligned}
\zeta_R &= \frac{1}{2\sqrt{2^k}} \min_{\mathbf{C}\neq\tilde{\mathbf{C}}} |\det\left(\mathbf{\Delta} \circ \breve{\mathbf{R}}\right)|^{\frac{1}{2\cdot 2^k}} \\
&= \frac{1}{2\sqrt{2^k}} \min_{\mathbf{C}\neq\tilde{\mathbf{C}}} \left(\frac{2^k}{k+1} \sum_{i=1}^{k+1} |x_i - \tilde{x}_i|^2\right)^{\frac{2^k}{2\cdot 2^k}} \\
&= \frac{1}{2\sqrt{k+1}} \min_{\mathbf{C}\neq\tilde{\mathbf{C}}} \left(\sum_{i=1}^{k+1} |x_i - \tilde{x}_i|^2\right)^{\frac{1}{2}} \\
&= \frac{1}{2\sqrt{k+1}} \min_{(x_1,x_2,\ldots,x_{k+1})\neq(\tilde{x}_1,\ldots,\tilde{x}_{k+1})} \left(\sum_{i=1}^{k+1} |x_i - \tilde{x}_i|^2\right)^{\frac{1}{2}}, \qquad (2.33)
\end{aligned}$$

which shows that the diversity product of space-time signals constructed from the orthogonal design $\mathbf{G}_{2^k}$ of Equation (2.27) is independent of the correlation matrix $\breve{\mathbf{R}}$, provided that the space-time signals achieve full diversity (i.e. that $\mathbf{\Delta} \circ \breve{\mathbf{R}}$ is of full rank).

Assuming that there are L legitimate space-time signals, which the encoder can choose from, Equation (2.33) dictates that the diversity product is determined by the minimum Euclidean distance (MED) of the L number of $(k+1)$-dimensional complex vectors $(x_1, x_2, \ldots, x_{k+1})_l \in \mathbb{C}^{k+1}$, $l = 0, \ldots, L-1$. Therefore, in order to maximise the diversity product, the L number of $(k+1)$-dimensional complex vectors must be designed by ensuring that they have the best MED in the $(k+1)$-dimensional complex-valued space $\mathbb{C}^{k+1}$, as illustrated in Figure 2.2. If each of the L number of $(k+1)$-dimensional complex vectors is expressed using its real and imaginary components, so that we have

$$(x_1, \ldots, x_{k+1})_l \Longleftrightarrow (a_1 + ja_2, \ldots, a_{2(k+1)-1} + ja_{2(k+1)})_l, \qquad (2.34)$$

for $l = 0, \ldots, L-1$, then each of these complex vectors can be represented in the stylised space shown in Figure 2.3. It may be directly observed from Figure 2.3 that the design problem can be readily transformed from the $(k+1)$-dimensional complex-valued space $\mathbb{C}^{k+1}$ to the $2(k+1)$-dimensional real-valued Euclidean space $\mathbb{R}^{2(k+1)}$, as portrayed in Figure 2.4. It was proposed

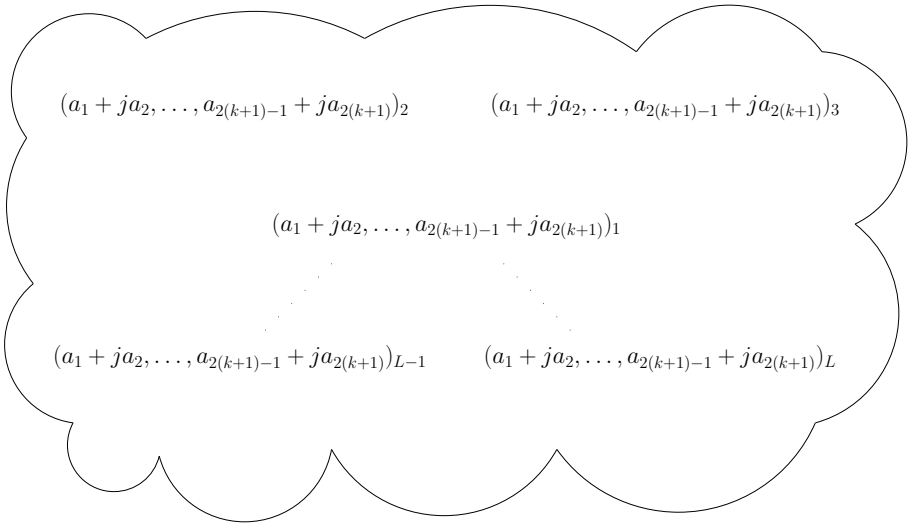

Figure 2.3: The L legitimate $(k+1)$-dimensional complex vectors represented by their real and imaginary components.

in [190] to use sphere packing (SP) for combining the individual antennas signals into a joint ST design, since they have the best known MED in the $2(k+1)$-dimensional real-valued Euclidean space $\mathbb{R}^{2(k+1)}$ [236], which directly maximises the diversity product expression of Equation (2.33).

To summarise the general concept, space-time signals having the maximum Euclidean distance may be constructed from Alamouti-style orthogonal design using sphere packing modulation for $N_t = 2^k, k = 1, 2, 3, \ldots$, transmit antennas. When conventional modulation methods (i.e. QAM, PSK) are used in the design of space-time signals, the symbols $x_1, x_2, \ldots, x_{k+1}$ are chosen independently from the modulation constellation. By contrast, in the case of sphere packing, these symbols are designed jointly in order to further increase the coding advantage, as suggested above. Assuming that there are L space-time signals that the encoder can choose from and each ST signal is transmitted over $T = N_t$ number of consecutive time slots, the effective throughput of the space-time modulated scheme is $(\log_2 L)/N_t$ bits per ST channel access, where an ST channel access is again defined as the transmission of one of the L legitimate ST signals over the N_t transmit antennas within the corresponding N_t time slots. When assuming rectangular Nyquist filtering, the resultant spectral efficiency becomes $(\log_2 L)/N_t$ $b/s/Hz$. Without loss of generality, $\mathbf{G}_2(x_1, x_2)$ will be considered in Section 2.4.3, in order to illustrate the concept of orthogonal ST code design using sphere packing for $N_t = 2$ transmit antennas.

2.4.3 Signal Design for Two Transmit Antennas

The orthogonal ST signal design for $N_t = 2$ transmit antennas is characterised as

$$\mathbf{G}_2(x_1, x_2) = \begin{bmatrix} x_1 & x_2 \\ -x_2^* & x_1^* \end{bmatrix}, \tag{2.35}$$

which was introduced by Alamouti [215], where the rows and columns of Equation (2.35) represent the temporal and spatial dimensions, corresponding to two consecutive time slots and two transmit antennas, respectively. In this section, space-time encoding designed for systems employing $N_t = 2$ transmit antennas will be presented first in Section 2.4.3.1, while in Section 2.4.3.2 the receiver

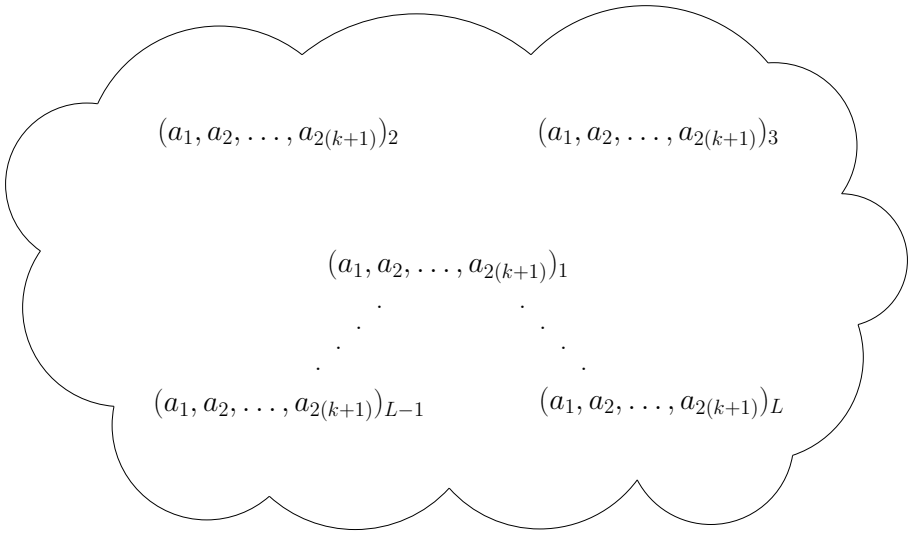

Figure 2.4: The L legitimate $2(k+1)$-dimensional real-valued vectors.

and maximum likelihood detection algorithm will be detailed. Then, in Section 2.4.3.3 a range of systems using $N_t = 2$ transmit antennas and multiple receive antennas will be discussed. Finally, in Section 2.4.3.4 it will be shown how sphere packing is combined with orthogonal ST signal design employing N_t transmit antennas.

2.4.3.1 G_2 Space-Time Encoding

As shown in Figure 2.5, the space-time encoder is preceded by a modulator. Each group of B information bits is first modulated using an L-ary modulation scheme, where we have $B = \log_2 L$. Then, the encoder operates on a block of two consecutive modulated symbols x_1 and x_2, mapping them to the transmit antennas according to the generator matrix seen in Equation (2.35).

Each activation of the encoder considers two consecutive time slots. During the first time slot, x_1 is transmitted from the first antenna and simultaneously x_2 is transmitted from the second an-

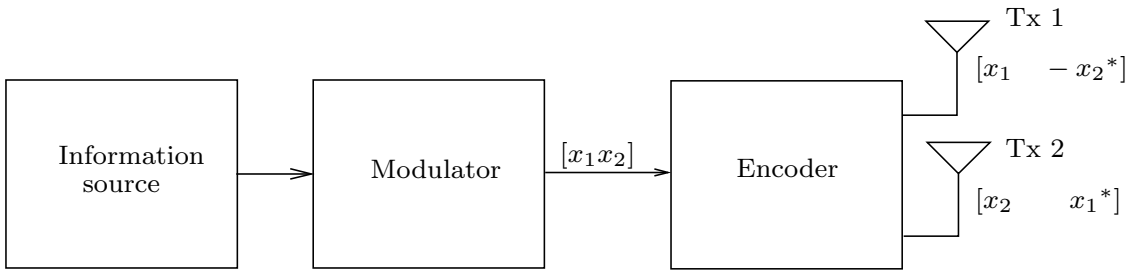

Figure 2.5: Block diagram of the two-transmitter STBC scheme.

tenna. During the second time slot, $-x_2^*$ is transmitted from the first antenna and simultaneously x_1^* is transmitted from the second antenna. The columns of the generator matrix represent antennas and the rows represent time slots. Therefore, encoding is carried out in both the space and time domains. Table 2.2 shows the encoding and transmission sequence for the two-transmitter STBC scheme.

	antenna 1	antenna 2
time slot t	x_1	x_2
time slot $t+1$	$-x_2^*$	x_1^*

Table 2.2: Encoding and transmission sequence for the two-transmitter STBC.

2.4.3.2 Receiver and Maximum Likelihood Decoding

Figure 2.6 shows the block diagram for the receiver, when a single receive antenna is employed. Let $h_1(t)$ and $h_2(t)$ denote the complex-valued fading channel coefficients of the first and second antennas with respect to the receive antenna at time instant t, respectively. It is assumed that the channel coefficients are constant over two consecutive time slots. Hence, they can be written as follows

$$h_1(t) = h_1(t+1) = h_1 = |h_1|e^{j\theta_1} \tag{2.36}$$
$$h_2(t) = h_2(t+1) = h_2 = |h_2|e^{j\theta_2}, \tag{2.37}$$

where $|h_i|$ and θ_i, $i = 1, 2$, are the amplitude and phase shift of the complex-valued channel coefficient for the path spanning from transmit antenna i to the receive antenna.

As shown in Figure 2.6, r_1 and r_2 represent the signals received over the two consecutive time slots t and $t+1$, respectively, which can be written as

$$r_1 = h_1x_1 + h_2x_2 + n_1 \tag{2.38}$$
$$r_2 = -h_1x_2^* + h_2x_1^* + n_2, \tag{2.39}$$

where n_1 and n_2 are independent complex-valued additive white Gaussian noise (AWGN) samples at time t and $t+1$, respectively, with zero mean and a power spectral density of $N_0/2$ per dimension.

Assuming perfect channel estimation, the channel's fading coefficients, h_1 and h_2, are known at the receiver. The availability of the channel state information (CSI) at the receiver will improve the performance of the decoder. The fading coefficient estimates h_1 and h_2 are used by the decoder to find the most likely transmitted signals, as we will show in Equations (2.43) and (2.43). The maximum likelihood decoder decides on the specific pair of signals $(\hat{x}_1, \hat{x}_2)$ that minimises the following distance metric:

$$d^2(r_1, h_1\hat{x}_1 + h_2\hat{x}_2) + d^2(r_2, -h_1\hat{x}_2^* + h_2\hat{x}_1^*), \tag{2.40}$$

over all possible values of $\hat{x}_1$ and $\hat{x}_2$, while assuming that all the signals in the modulation constellation are equiprobable. The squared Euclidean distance between two complex-valued signals, say x and y, can be expressed as

$$d^2(x, y) = (x - y)(x^* - y^*). \tag{2.41}$$

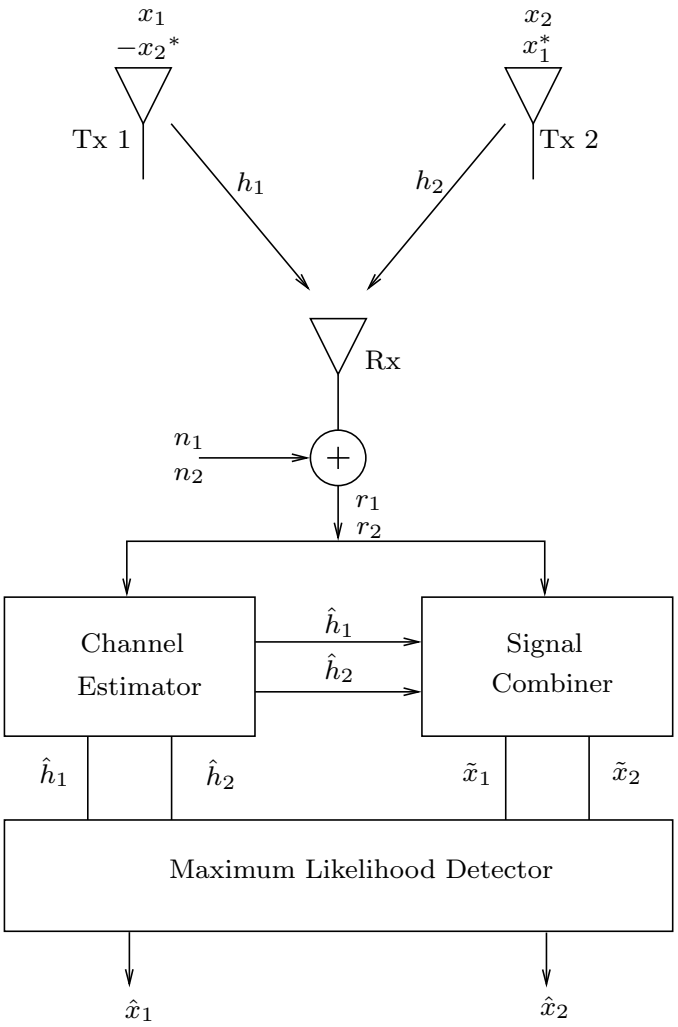

Figure 2.6: Receiver for the two-transmitter STBC.

Upon, using Equation (2.41), the detection criterion of Equation (2.40) can be further manipulated as follows

$$\begin{aligned} & d^2(r_1, h_1\hat{x}_1 + h_2\hat{x}_2) + d^2(r_2, -h_1\hat{x}_2^* + h_2\hat{x}_1^*) \\ & \qquad = (r_1 - h_1\hat{x}_1 - h_2\hat{x}_2)(r_1^* - h_1^*\hat{x}_1^* - h_2^*\hat{x}_2^*) \\ & \qquad + (r_2 + h_1\hat{x}_2^* - h_2\hat{x}_1^*)(r_2^* + h_1^*\hat{x}_2 - h_2^*\hat{x}_1) \\ & \qquad = (|h_1|^2 + |h_2|^2)(|\hat{x}_1|^2 + |\hat{x}_2|^2) \\ & \qquad - h_1^* r_1 \hat{x}_1^* - h_2 r_2^* \hat{x}_1^* - h_1 r_1^* \hat{x}_1 - h_2^* r_2 \hat{x}_1 \\ & \qquad - h_2^* r_1 \hat{x}_2^* + h_1 r_2^* \hat{x}_2^* - h_2 r_1^* \hat{x}_2 + h_1^* r_2 \hat{x}_2 \\ & \qquad + |r_1|^2 + |r_2|^2. \end{aligned} \tag{2.42}$$

Let us define $\tilde{x}_1$ and $\tilde{x}_2$ as two decision statistics constructed by combining the received signals r_1

and r_2 with the perfectly estimated CSI as follows

$$\tilde{x}_1 = h_1^* r_1 + h_2 r_2^* \quad (2.43)$$
$$\tilde{x}_2 = h_2^* r_1 - h_1 r_2^*. \quad (2.44)$$

Moreover, $d^2(\tilde{x}_1, \hat{x}_1)$ and $d^2(\tilde{x}_2, \hat{x}_2)$ can be expressed using Equations (2.43) and (2.44) along with Equation (2.41) as follows

$$\begin{aligned} d^2(\tilde{x}_1, \hat{x}_1) &= (\tilde{x}_1 - \hat{x}_1)(\tilde{x}_1^* - \hat{x}_1^*) \\ &= |\hat{x}_1|^2 + |\tilde{x}_1|^2 - h_1^* r_1 \hat{x}_1^* - h_2 r_2^* \hat{x}_1^* - h_1 r_1^* \hat{x}_1 - h_2^* r_2 \hat{x}_1, \end{aligned} \quad (2.45)$$

and,

$$\begin{aligned} d^2(\tilde{x}_2, \hat{x}_2) &= (\tilde{x}_2 - \hat{x}_2)(\tilde{x}_2^* - \hat{x}_2^*) \\ &= |\hat{x}_2|^2 + |\tilde{x}_2|^2 - h_2^* r_1 \hat{x}_2^* + h_1 r_2^* \hat{x}_2^* - h_2 r_1^* \hat{x}_2 + h_1^* r_2 \hat{x}_2. \end{aligned} \quad (2.46)$$

Upon substituting Equations (2.45) and (2.46) into Equation (2.42) and omitting all terms that are not functions of $\hat{x}_1$ or $\hat{x}_2$, the resultant decoding criterion can be expressed as

$$(\hat{x}_1, \hat{x}_2) = \arg \min_{(\hat{x}_1, \hat{x}_2) \in C} (|h_1|^2 + |h_1|^2 - 1)(|\hat{x}_1|^2 + |\hat{x}_2|^2) + d^2(\tilde{x}_1, \hat{x}_1) + d^2(\tilde{x}_2, \hat{x}_2), \quad (2.47)$$

where C is the set of all possible modulated symbol pairs $(\hat{x}_1, \hat{x}_2)$. Furthermore, expressing r_1 and r_2 in Equations (2.43) and (2.44), respectively, using Equations (2.38) and (2.39) yields,

$$\tilde{x}_1 = (|h_1|^2 + |h_2|^2) x_1 + h_1^* n_1 + h_2 n_2^* \quad (2.48)$$
$$\tilde{x}_2 = (|h_1|^2 + |h_2|^2) x_2 - h_1 n_2^* + h_2^* n_1. \quad (2.49)$$

The fact that the decision statistics $\tilde{x}_i$ only depend on x_i, $i = 1,\ 2$, enables us to separate the maximum likelihood decoding rule of Equation (2.47) into two independent decoding criteria for x_1 and x_2 as follows

$$\hat{x}_1 = \arg \min_{\hat{x}_1 \in S} (|h_1|^2 + |h_2|^2 - 1)|\hat{x}_1|^2 + d^2(\tilde{x}_1, \hat{x}_1) \quad (2.50)$$
$$\hat{x}_2 = \arg \min_{\hat{x}_2 \in S} (|h_1|^2 + |h_2|^2 - 1)|\hat{x}_2|^2 + d^2(\tilde{x}_2, \hat{x}_2), \quad (2.51)$$

where S represents the legitimate constellation set. Observe further more in Equations (2.48) and (2.49) that even if one of the fading coefficients is small owing to a deep magnitude fade, the chances are that the other coefficient is simultaneously high owing to their independent fading. For the special case of M-PSK signal constellations, the amplitude of all possible modulated symbols, $\hat{x}_i$, $i = 1,\ 2$, are constant leading to the following further simplified decoding criteria:

$$\hat{x}_1 = \arg \min_{\hat{x}_1 \in S} d^2(\tilde{x}_1, \hat{x}_1) \quad (2.52)$$
$$\hat{x}_2 = \arg \min_{\hat{x}_2 \in S} d^2(\tilde{x}_2, \hat{x}_2). \quad (2.53)$$

2.4.3.3 G_2 Space-Time Coding Using Multiple Receive Antennas

As a motivation of this section, it is worth noting at this early stage that the employment of multiple transmit antennas requires the proportionate reduction of the individual antennas' transmit power for the sake of their fair comparison. This requires for example for $N_t = 2$ that transmit diversity provides more than 3dB gain in order to compensate for halving the transmit power of both antennas, which is typically only realistic with the aid of multiple receiver antennas. Motivated by this, the two-transmitter space-time coding scheme of Section 2.4.3.2 can be extended to systems employing an arbitrary number of receive antennas, N_r. The decoding criteria must be modified to include the effect of the multiple receive antennas. However, the encoding and transmission is identical to the case of a single receive antenna. Let r_1^j and r_2^j denote the received signals by the jth receive antenna at time t and $t+1$, respectively

$$\begin{aligned} r_1^j &= h_{1,j}x_1 + h_{2,j}x_2 + n_1^j \\ r_2^j &= -h_{1,j}x_2^* + h_{2,j}x_1^* + n_2^j, \end{aligned} \tag{2.54}$$

where $h_{i,j}$, $i = 1,\ 2$, $j = 1, \ldots, N_r$, represents the complex-valued fading coefficient for the path spanning from transmit antenna i to receive antenna j, and n_1^j as well as n_2^j are the AWGN samples at time instants t and $t+1$, respectively, at receive antenna j.

The decision statistics $\tilde{x}_1$ and $\tilde{x}_2$ which are constructed by the receiver based on the linear combination of the received signals are expressed as [215, 261, 262]

$$\begin{aligned} \tilde{x}_1 &= \sum_{j=1}^{N_r} h_{1,j}^* r_1^j + h_{2,j}(r_2^j)^* \\ &= \sum_{j=1}^{N_r} \Big[\Big(|h_{1,j}|^2 + |h_{2,j}|^2 \Big) x_1 + h_{1,j}^* n_1^j + h_{2,j}(n_2^j)^* \Big] \end{aligned} \tag{2.55}$$

$$\begin{aligned} \tilde{x}_2 &= \sum_{j=1}^{N_r} h_{2,j}^* r_1^j - h_{2,j}(r_2^j)^* \\ &= \sum_{j=1}^{N_r} \Big[\Big(|h_{1,j}|^2 + |h_{2,j}|^2 \Big) x_2 + h_{2,j}^* n_1^j - h_{1,j}(n_2^j)^* \Big]. \end{aligned} \tag{2.56}$$

Based on Equations (2.43), (2.44), (2.55) and (2.56), the following rule can be deduced for the linear combination of the received signals [261]:

> For $\tilde{x}_i$, $i = 1,\ 2$, multiply r_j, $j = 1,\ 2$, with the conjugate of the corresponding complex-valued fading coefficient h if x_i is present in r_j as suggested by Equations (2.43), (2.44), (2.55) and (2.56). Otherwise, if x_i^* is present in r_j, multiply r_j^* with the corresponding complex-valued fading coefficient h. Then, the resultant products are added or subtracted from the rest, depending on the sign of the term in the expression of the received signal r_j.

It is plausible from Equations (2.55) and (2.56) that the number of independent propagation paths is proportional to the number of receivers N_r, namely $2 \cdot N_r$. Therefore, as argued at the beginning of this section, if one path is in a deep fade, other paths are still likely to provide a high-reliability link for the transmitted signal, provided that the paths are spatially uncorrelated.

This advantage is valid even if a single receive antenna is used, because in that case there are two independent paths corresponding to the first and second transmit antennas.

The maximum likelihood decoding criteria used by the receiver for the two independent signals x_1 and x_2 are given by [215, 262]

$$\hat{x}_1 = \arg\min_{\hat{x}_1 \in S} \left[\left(\sum_{j=1}^{N_r} (|h_{1,j}|^2 + |h_{2,j}|^2) - 1 \right) |\hat{x}_1|^2 + d^2(\tilde{x}_1, \hat{x}_1) \right], \tag{2.57}$$

$$\hat{x}_2 = \arg\min_{\hat{x}_2 \in S} \left[\left(\sum_{j=1}^{N_r} (|h_{1,j}|^2 + |h_{2,j}|^2) - 1 \right) |\hat{x}_2|^2 + d^2(\tilde{x}_2, \hat{x}_2) \right]. \tag{2.58}$$

2.4.3.4 $\mathbf{G}_2$ Orthogonal Design Using Sphere Packing

The $\mathbf{G}_2$ generator matrix of Equation (2.35) is reproduced here for convenience

$$\mathbf{G}_2(x_1, x_2) = \begin{bmatrix} x_1 & x_2 \\ -x_2^* & x_1^* \end{bmatrix}.$$

According to Alamouti's design [215] for example, x_1 and x_2 represent conventional binary phase shift keying (BPSK) modulated symbols transmitted in the 1^{st} and 2^{nd} time slots and no effort is made to jointly design a signal constellation for the various combinations of x_1 and x_2. For the sake of generalising our treatment, let us assume that there are L legitimate space-time signals $\mathbf{G}_2(x_{l,1}, x_{l,2})$, $l = 0, 1, \ldots, L-1$, where L represents the number of sphere-packed modulated symbols. The transmitter has to choose the modulated signal from these L legitimate symbols, which have to be transmitted over the two antennas in two consecutive time slots, where the throughput of the system is given by $(\log_2 L)/2$ bits per channel access. In contrast to Alamouti's independent design of the two time slots' signals [215], our aim is to design $x_{l,1}$ and $x_{l,2}$ jointly, so that they have the best MED from all other $(L-1)$ legitimate transmitted space-time signals [190], since this minimises the system's ST symbol error probability. Let $(a_{l,1}, a_{l,2}, a_{l,3}, a_{l,4})$, $l = 0, \ldots, L-1$, be phasor points belonging the four-dimensional real-valued Euclidean space $\mathbb{R}^4$, where each of the four elements $a_{l,d}$, $d = 1, \ldots, 4$, gives one coordinate of the two time-slots' complex-valued phasor points. Hence, $x_{l,1}$ and $x_{l,2}$ may be written as

$$\begin{aligned} \{x_{l,1}, x_{l,2}\} &= T_{sp}(a_{l,1}, a_{l,2}, a_{l,3}, a_{l,4}) \\ &= \{a_{l,1} + j a_{l,2}, a_{l,3} + j a_{l,4}\}, \end{aligned} \tag{2.59}$$

where the SP-function T_{sp} represents the mapping of the SP symbols $(a_{l,1}, a_{l,2}, a_{l,3}, a_{l,4})$ to the complex-valued symbols $x_{l,1}$ and $x_{l,2}$, $l = 0, \ldots, L-1$.

In the four-dimensional real-valued Euclidean space $\mathbb{R}^4$, the lattice D_4 is defined as a sphere packing having the best minimum Euclidean distance from all other $(L-1)$ legitimate constellation points in $\mathbb{R}^4$ [236]. More specifically, D_4 may be defined as a lattice that consists of all legitimate sphere packed constellation points having integer coordinates $(a_{l,1}, a_{l,2}, a_{l,3}, a_{l,4})$, $l = 0, \ldots, L-1$, uniquely and unambiguously describing the L legitimate combinations of the two time-slots' modulated symbols in Alamouti's scheme, but subjected to the sphere packing constraint of [236]

$$a_{l,1} + a_{l,2} + a_{l,3} + a_{l,4} = k_l, \qquad l = 0, \ldots, L-1, \tag{2.60}$$

where k_l may assume any even integer value. Alternatively, D_4 may be defined as the integer span of the vectors $\mathbf{v}_1,\ \mathbf{v}_2,\ \mathbf{v}_3$ and $\mathbf{v}_4$ that form the rows of the following generator matrix [236]

$$\begin{bmatrix} \mathbf{v}_1 \\ \mathbf{v}_2 \\ \mathbf{v}_3 \\ \mathbf{v}_4 \end{bmatrix} \triangleq \begin{bmatrix} 2 & 0 & 0 & 0 \\ 1 & 1 & 0 & 0 \\ 1 & 0 & 1 & 0 \\ 1 & 0 & 0 & 1 \end{bmatrix}. \tag{2.61}$$

We may infer from the above definition in Equation (2.61) that D_4 contains the centres $(2,0,0,0)$, $(1,1,0,0)$, $(1,0,1,0)$, and $(1,0,0,1)$. It also contains all linear combinations of these points. For example, $\mathbf{v}_1 - 3\cdot\mathbf{v}_3 = (2,0,0,0) - 3\cdot(1,0,1,0) = (-1,0,-3,0)$, is a legitimate phasor point in D_4.

Assuming that $S = \{\mathbf{s}^l = [a_{l,1}\ a_{l,2}\ a_{l,3}\ a_{l,4}] \in \mathbb{R}^4 :\ 0 \le l \le L-1\}$ constitutes a set of L legitimate constellation points from the lattice D_4 having a total energy of

$$E_{\text{total}} \triangleq \sum_{l=0}^{L-1} (|a_{l,1}|^2 + |a_{l,2}|^2 + |a_{l,3}|^2 + |a_{l,4}|^2), \tag{2.62}$$

and upon introducing the notation

$$\begin{aligned} \mathbf{C}_l &= \sqrt{\frac{2L}{E_{\text{total}}}}\mathbf{G}_2(x_{l,1}, x_{l,2}), \\ &= \sqrt{\frac{2L}{E_{\text{total}}}}\mathbf{G}_2(a_{l,1} + ja_{l,2}, a_{l,3} + ja_{l,4}), \qquad l = 0,\ldots,L-1, \end{aligned} \tag{2.63}$$

we have a set of space-time signals, $\{\mathbf{C}_l{:}0 \le l \le L-1\}$, whose diversity product is determined by the MED of the set of L legitimate constellation points in S. The transformation of the L legitimate 2-dimensional complex vectors $(x_{l,1}, x_{l,2})$, $l = 0,\ldots,L-1$, to the L legitimate 4-dimensional real-valued vectors $(a_{l,1}, a_{l,2}, a_{l,3}, a_{l,4})$, $l = 0,\ldots,L-1$, is depicted in Figures 2.7 and 2.8.

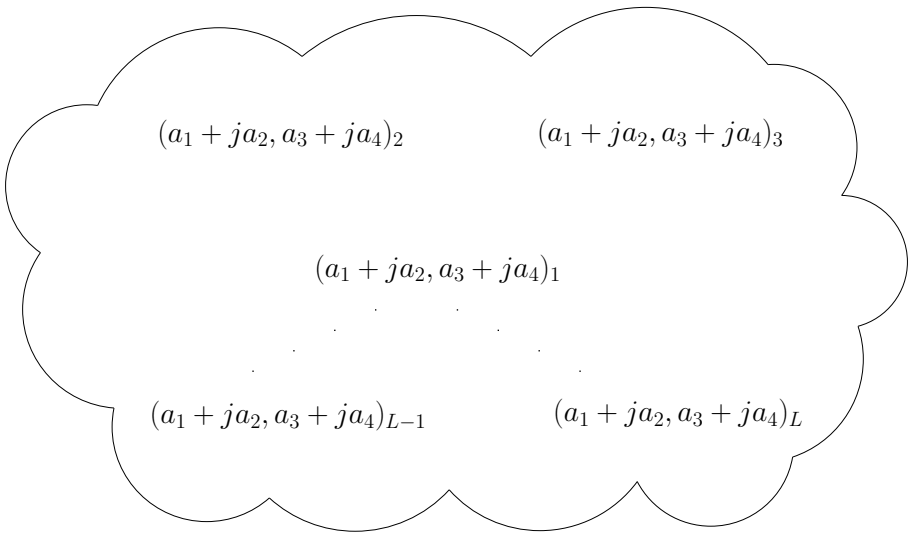

Figure 2.7: The L legitimate 2-dimensional complex vectors for $\mathbf{G}_2$ space-time signals.

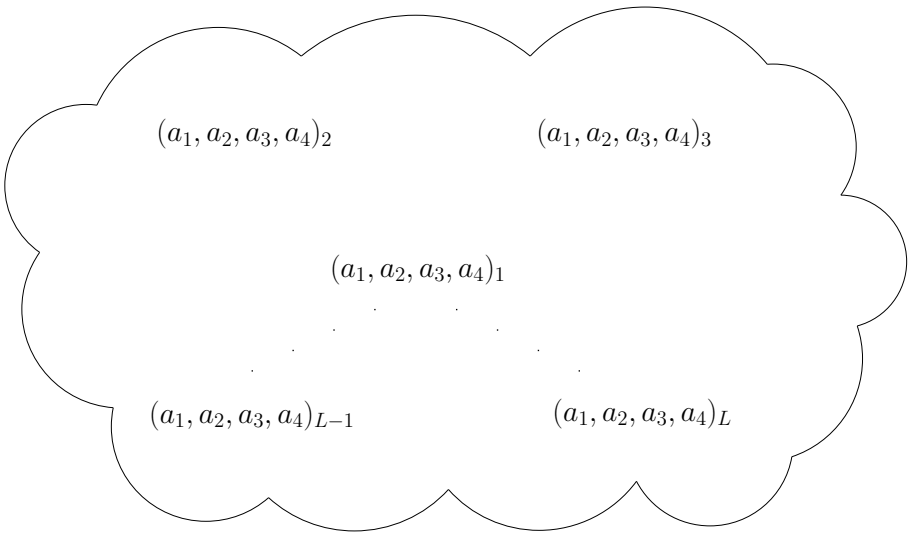

Figure 2.8: The L legitimate 4-dimensional real-valued vectors for $\mathbf{G}_2$ space-time signals.

The normalisation factor $\sqrt{2L/E_{\text{total}}}$ in Equation (2.63) is used for ensuring that the space-time signal of Equation (2.63) satisfies the energy constraint of Equation (2.2), which can be derived as follows.

Let us define n_f as a normalisation factor to be used in Equation (2.63) for ensuring that the space-time signal satisfies the energy constraint of Equation (2.2). Then the space-time signal of Equation (2.63) can be written as

$$\mathbf{C}_l = n_f \begin{bmatrix} x_{l,1} & x_{l,2} \\ -x_{l,2}^* & x_{l,1}^* \end{bmatrix}. \tag{2.64}$$

The energy of the space-time signal formulated in Equation (2.64) is given by

$$\begin{aligned} E\big[||\mathbf{C}_l||_F^2\big] &= E\big[\, n_f^2 \cdot \big(|x_{l,1}|^2 + |x_{l,2}|^2 + |x_{l,2}^*|^2 + |x_{l,1}^*|^2\big) \,\big] \\ &= 2 \cdot n_f^2 \cdot E\big[|x_{l,1}|^2 + |x_{l,2}|^2\big]. \end{aligned} \tag{2.65}$$

Expressing Equation (2.65) with the aid of Equation (2.59) yields

$$E\big[||\mathbf{C}_l||_F^2\big] = 2 \cdot n_f^2 \cdot E\big[|a_{l,1}|^2 + |a_{l,2}|^2 + |a_{l,3}|^2 + |a_{l,4}|^2\big]. \tag{2.66}$$

Observe from Equation (2.62) that the average energy of a single sphere packing symbol is given by

$$E\big[|a_{l,1}|^2 + |a_{l,2}|^2 + |a_{l,3}|^2 + |a_{l,4}|^2\big] = \frac{E_{\text{total}}}{L}. \tag{2.67}$$

Then, Equation (2.66) becomes

$$\begin{aligned} E\big[||\mathbf{C}_l||_F^2\big] &= 2 \cdot n_f^2 \cdot \frac{E_{\text{total}}}{L} \\ &= T \cdot N_t \qquad \text{(from Equation(2.2))} \\ &= 2 \cdot 2 = 4. \end{aligned} \tag{2.68}$$

Hence, with the aid of Equation (2.68) we arrive at

$$n_f = \sqrt{\frac{2L}{E_{\text{total}}}}. \tag{2.69}$$

The following example illustrates, how sphere packing modulation may be implemented in combination with $\mathbf{G}_2$ space-time coded systems.

Example 2.4.1. *Assume that there are $L = 16$ different legitimate space-time signals, $\mathbf{G}_2(x_{l,1}, x_{l,2})$, $l = 0, \ldots, 15$, that the encoder can choose from. We will consider two optional modulation schemes, namely conventional QPSK modulation and sphere packing modulation.*

- **Conventional QPSK Modulation:**
  There are four legitimate two-bit QPSK symbols, $S0$, $S1$, $S2$, and $S3$, that can be used for representing any of the symbols $x_{l,1}$ and $x_{l,2}$, $l = 0, \ldots, 15$. The transmission regime of the two consecutive time slots is demonstrated in Figure 2.9.

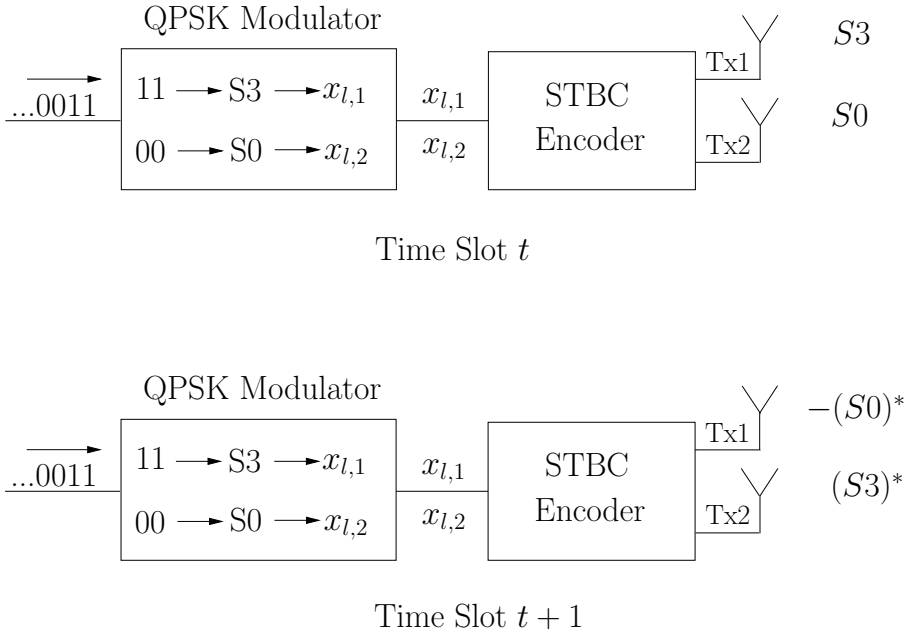

Figure 2.9: Transmission of two QPSK symbols during two consecutive time slots.

- **Sphere Packing Modulation:**
  We need $L = 16$ phasor points selected from the lattice D_4, $(a_{l,1}, a_{l,2}, a_{l,3}, a_{l,4})$, $l = 0, \ldots, 15$, in order to jointly represent each space-time signal $(x_{l,1}, x_{l,2})$, $l = 0, \ldots, 15$, according to Equation (2.59), as depicted in Figure 2.10. Table 2.3 shows the effective throughput and the associated transmission block sizes for different values of L.

2.4.4 Sphere Packing Constellation Construction

Since the orthogonal $\mathbf{G}_2$ space-time signal, which is constructed from the sphere packing scheme of Equation (2.63) is multiplied by a factor that is inversely proportional to $\sqrt{E_{\text{total}}}$, namely by

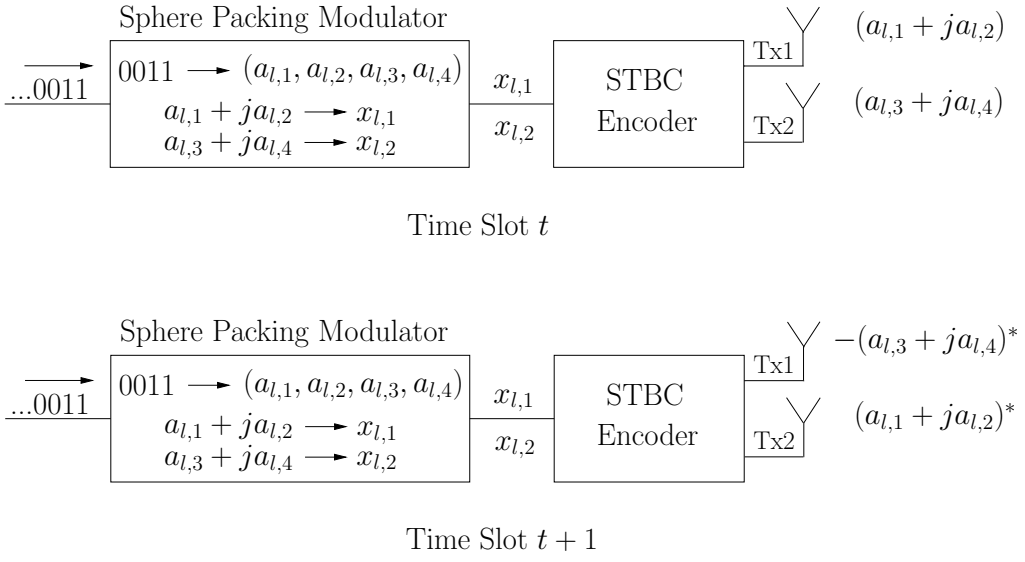

Figure 2.10: Transmission of a single sphere-packed symbol during two consecutive time slots.

L	Block Size (bits)	Throughput (b/s/Hz)
4	2	1
8	3	1.5
16	4	2
32	5	2.5
64	6	3
128	7	3.5
256	8	4
512	9	4.5
1024	10	5
2048	11	5.5
4096	12	6

Table 2.3: Throughput of sphere packing aided $\mathbf{G}_2$ systems for different SP signal set sizes L.

$\sqrt{\frac{2L}{E_{\text{total}}}}$, it is desirable to choose a specific subset of L points from the entire set of legitimate constellation points hosted by D_4, which results in the minimum total energy E_{total} while maintaining a certain minimum distance amongst the SP symbols. Viewing this design trade-off from a different perspective, if more than L points satisfy the minimum total energy constraint, an exhaustive computer search is carried out for determining the optimum choice of the L points out of all possible points, which possess the highest MED, hence minimising the SP-symbol error probability. For this purpose, the legitimate constellation points hosted by D_4 are categorised into layers or shells based on their norms or energy (i.e. distance from the origin) as seen in Table 2.4 . For example, it was shown in [236] that the first layer consists of 24 legitimate constellation points hosted by D_4 having an identical minimum energy of $E = 2$. In simple terms, the SP symbol centred at $(0, 0, 0, 0)$ has 24 minimum-distance or closest-neighbour SP symbols around it, centred at the points $(+/-1, +/-1, 0, 0)$, where any choice of signs and any ordering of the coordinates is legitimate.

Example 2.4.2. *Assume that there are $L = 16$ different legitimate space-time signals, $\mathbf{G}_2(x_{l,1}, x_{l,2})$, $l = 0, \ldots, 15$, which the encoder can choose from. Then, we need the most 'meritorious' $L = 16$ phasor points from the lattice D_4 for representing the ST-signals. According to the above-mentioned minimum energy constraint, only the 24 legitimate constellation points hosted by the first SP layer of Table 2.4 are considered, as shown in Figure 2.11. Then, an exhaustive computer search is employed for determining the optimum choice of the $L = 16$ points out of the 24 possible first-layer points, which possess the highest MED.*

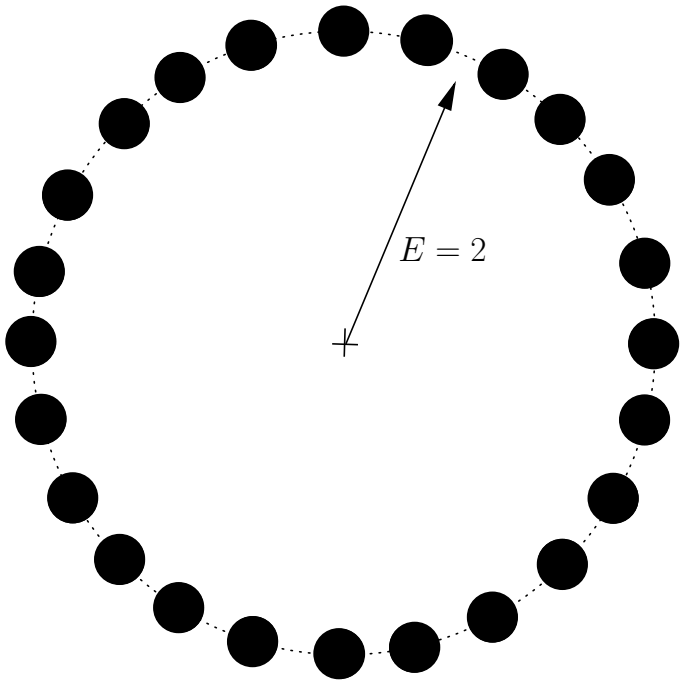

Figure 2.11: The 24 first-layer SP constellation points hosted by D_4 having the minimum energy of $E = 2$.

Table 2.4 provides a summary of the constellation points hosted by the first 10 layers in the 4-dimensional lattice D_4. In order to generate the full list of SP regimes for a specific layer, we have to apply all legitimate permutations and signs for the corresponding constellation points given in Table 2.4.

Layer	Constellation Points				Norm	Number of Combinations
0	0	0	0	0	0	1
1	+/-1	+/-1	0	0	2	24
2	+/-2	0	0	0	4	8
	+/-1	+/-1	+/-1	+/-1	4	16
3	+/-2	+/-1	+/-1	0	6	96
4	+/-2	+/-2	0	0	8	24
5	+/-2	+/-2	+/-1	+/-1	10	96
	+/-3	+/-1	0	0	10	48
6	+/-3	+/-1	+/-1	+/-1	12	64
	+/-2	+/-2	+/-2	0	12	32
7	+/-3	+/-2	+/-1	0	14	192
8	+/-2	+/-2	+/-2	+/2	16	16
	+/-4	0	0	0	16	8
9	+/-4	+/-1	+/-1	0	18	96
	+/-3	+/-2	+/-2	+/-1	18	192
	+/-3	+/-3	0	0	18	24
10	+/-4	+/-2	0	0	20	48
	+/-3	+/-3	+/-1	+/-1	20	96

Table 2.4: The first 10 layers of D_4.

2.4.5 Capacity of STBC-SP Schemes

In this section, the capacity of STBC-SP schemes having $N_t = 2$ transmit and N_r receive antennas is derived based on the results found in [263]. Assuming perfect channel estimation, the complex-valued channel output symbols received during two consecutive STBC time slots at receiver j are first diversity-combined in order to extract the estimates $\tilde{x}_{1,j}$ and $\tilde{x}_{2,j}$ of the most likely transmitted symbols $x_{l,1}$ and $x_{l,2}$, as seen in Equations (2.48) and (2.49), resulting in [264]

$$\tilde{x}_{1,j} = \sum_{i=1}^{N_t} |h_{i,j}|^2 \cdot x_{l,1} + \acute{n}_{1,j} = \chi^2_{2N_t,j} \cdot x_{l,1} + \acute{n}_{1,j} \quad (2.70)$$

$$\tilde{x}_{2,j} = \sum_{i=1}^{N_t} |h_{i,j}|^2 \cdot x_{l,2} + \acute{n}_{2,j} = \chi^2_{2N_t,j} \cdot x_{l,2} + \acute{n}_{2,j}, \quad (2.71)$$

for $j = 1, \ldots, N_r$, where again, $h_{i,j}$ represents the complex-valued Rayleigh channel coefficient between the i-th transmit antenna and the j-th receive antenna; $\chi^2_{2N_t,j} = \sum_{i=1}^{N_t} |h_{i,j}|^2$ represents the chi-squared distributed random variable having $2N_t$ degrees of freedom at receiver j; $\acute{n}_{1,j}$ as well as $\acute{n}_{2,j}$ are the zero-mean complex Gaussian random variables at receiver j during the first and second time slots, respectively, an having a variance of $\sigma^2_{\acute{n}_j} = \chi^2_{2N_t,j} \cdot \sigma^2_n$, where σ^2_n is the original noise variance per dimension. The received sphere-packed symbol $\mathbf{r}_j$ of receiver j is then constructed from the estimates $\tilde{x}_{1,j}$ and $\tilde{x}_{2,j}$ using the inverse function of T_{sp} introduced in

Equation (2.59) as

$$\mathbf{r}_j = T_{sp}^{-1}(\tilde{x}_{1,j}, \tilde{x}_{2,j}), \tag{2.72}$$

where we have $\mathbf{r}_j = [\tilde{a}_{j,1}\ \tilde{a}_{j,2}\ \tilde{a}_{j,3}\ \tilde{a}_{j,4}] \in \mathbb{R}^4$. The received sphere-packed symbol $\mathbf{r}_j$ can be written as

$$\mathbf{r}_j = \chi_{2N_t,j}^2 \cdot \sqrt{\frac{2L}{E_{\text{total}}}} \cdot \mathbf{s}^l + \mathbf{w}_j, \tag{2.73}$$

where we have $\mathbf{s}^l = [a_{l,1}\ a_{l,2}\ a_{l,3}\ a_{l,4}] \in S$, $0 \leq l \leq L-1$. Furthermore, $\mathbf{w}_j = [w_{j,1}\ w_{j,2}\ w_{j,3}\ w_{j,4}] \in \mathbb{R}^4$ is a four-dimensional real-valued Gaussian random variable having a covariance matrix of $\sigma_{w_j}^2 \cdot \mathbf{I}_{N_D} = \sigma_{\acute{n}_j}^2 \cdot \mathbf{I}_{N_D} = \chi_{2N_t,j}^2 \cdot \sigma_n^2 \cdot \mathbf{I}_{N_D}$, where we have $N_D = 4$, since the sphere packing symbol constellation S is four-dimensional. According to Equation (2.73), the conditional probability $p(\mathbf{r}_j|\mathbf{s}^l)$ of receiving a 4-dimensional signal $\mathbf{r}_j$, given that a 4-dimensional L-ary sphere packing symbol $\mathbf{s}^l \in S$, $0 \leq l \leq L-1$, was transmitted over the Rayleigh channel of Equation (2.73), is given by the following probability density function (PDF):

$$\begin{aligned} p(\mathbf{r}_j|\mathbf{s}^l) &= \frac{1}{(2\pi\sigma_{w_j}^2)^{\frac{N_D}{2}}} \exp\Big(-\frac{1}{2\sigma_{w_j}^2}(\mathbf{r}_j - \beta_j \cdot \mathbf{s}^l)(\mathbf{r}_j - \beta_j \cdot \mathbf{s}^l)^T\Big) \\ &= \frac{1}{(2\pi\sigma_{w_j}^2)^{\frac{N_D}{2}}} \exp\left(-\frac{1}{2\sigma_{w_j}^2}\left(\sum_{d=1}^{N_D}(\tilde{a}_{j,d} - \beta_j \cdot a_{l,d})^2\right)\right), \end{aligned} \tag{2.74}$$

where $\beta_j = \chi_{2N_t,j}^2 \cdot \sqrt{\frac{2L}{E_{\text{total}}}}$. Let us define $\vec{\mathbf{r}} = (\mathbf{r}_1, \ldots, \mathbf{r}_{N_r})^T$ as the N_r-element real-valued 4-dimensional received signal vector. Using Equation (2.74), the conditional probability $p(\vec{\mathbf{r}}|\mathbf{s}^l)$ is given by [6]:

$$\begin{aligned} p(\vec{\mathbf{r}}|\mathbf{s}^l) &= \prod_{j=1}^{N_r} p(\mathbf{r}_j|\mathbf{s}^l), \\ &= \frac{1}{\prod_{j=1}^{N_r}(2\pi\sigma_{w_j}^2)^{\frac{N_D}{2}}} \exp\left(-\sum_{d=1}^{N_D}\sum_{j=1}^{N_r}\frac{(\tilde{a}_{j,d} - \beta_j \cdot a_{l,d})^2}{2\sigma_{w_j}^2}\right). \end{aligned} \tag{2.75}$$

The channel capacity valid for STBC schemes using N_D-dimensional L-ary signalling [265] over the discrete-input continuous-output memoryless channel (DCMC) [6] was derived in [263] from that of the discrete memoryless channel (DMC) [266]. Accordingly, the channel capacity derived for STBC-SP schemes using N_D-dimensional L-ary signalling may be written as [263, 267]

$$\begin{aligned} C_{\text{DCMC}}^{\text{STBC-SP}} = \max_{p(\mathbf{s}^0),\ldots,p(\mathbf{s}^{L-1})} \sum_{l=0}^{L-1} \underbrace{\int_{-\infty}^{\infty}\cdots\int_{-\infty}^{\infty}}_{N_D\text{-fold}} p(\vec{\mathbf{r}}|\mathbf{s}^l)p(\mathbf{s}^l) \\ \cdot \log_2\left(\frac{p(\vec{\mathbf{r}}|\mathbf{s}^l)}{\sum_{k=0}^{L-1} p(\vec{\mathbf{r}}|\mathbf{s}^k)p(\mathbf{s}^k)}\right)\mathrm{d}\vec{\mathbf{r}}, \quad \text{[bit/symbol]} \end{aligned} \tag{2.76}$$

where $p(\mathbf{s}^l)$ is the probability of occurrence for the transmitted sphere packing symbol $\mathbf{s}^l$ and $p(\vec{\mathbf{r}}|\mathbf{s}^l)$ is expressed in Equation (2.75). The right-hand side of Equation (2.76) is maximised, when the transmitted sphere packing symbols are equiprobably distributed, i.e. when we have $p(\mathbf{s}^l) = 1/L$, $l = 0, \ldots, L-1$, which leads to achieving the full capacity [266]. The right-hand side

of Equation (2.76) may be further simplified as follows [263]:

$$\begin{aligned}\log_2\left(\frac{p(\vec{\mathbf{r}}|\mathbf{s}^l)}{\sum_{k=0}^{L-1} p(\vec{\mathbf{r}}|\mathbf{s}^k)p(\mathbf{s}^k)}\right) &= -\log_2\left(\frac{1}{L}\sum_{k=0}^{L-1}\frac{p(\vec{\mathbf{r}}|\mathbf{s}^k)}{p(\vec{\mathbf{r}}|\mathbf{s}^l)}\right)\\ &= \log_2(L) - \log_2\sum_{k=0}^{L-1}\exp(\Psi_{l,k}),\end{aligned} \tag{2.77}$$

where $\Psi_{l,k}$ is expressed as [263]:

$$\begin{aligned}\Psi_{l,k} &= \sum_{d=1}^{N_D}\sum_{j=1}^{N_r}\left(\frac{-(\tilde{a}_{j,d}-\beta_j\cdot a_{k,d})^2+(\tilde{a}_{j,d}-\beta_j\cdot a_{l,d})^2}{2\sigma_{w_j}^2}\right)\\ &= \sum_{d=1}^{N_D}\sum_{j=1}^{N_r}\left(\frac{(\beta_j\cdot(a_{l,d}-a_{k,d})+w_{j,d})^2+(w_{j,d})^2}{2\sigma_{w_j}^2}\right).\end{aligned} \tag{2.78}$$

Now, substituting Equation (2.77) into Equation (2.76) and observing that we have $p(\mathbf{s}^l) = 1/L$, yields [263]

$$\begin{aligned}C_{\text{DCMC}}^{\text{STBC-SP}} &= \frac{\log_2(L)}{L}\sum_{l=0}^{L-1}\underbrace{\int_{-\infty}^{\infty}\cdots\int_{-\infty}^{\infty}}_{N_D\text{-fold}} p(\vec{\mathbf{r}}|\mathbf{s}^l)\,\mathrm{d}\vec{\mathbf{r}}\\ &- \frac{1}{L}\sum_{l=0}^{L-1}\underbrace{\int_{-\infty}^{\infty}\cdots\int_{-\infty}^{\infty}}_{N_D\text{-fold}} p(\vec{\mathbf{r}}|\mathbf{s}^l)\log_2\sum_{k=0}^{L-1}\exp(\Psi_{l,k})\,\mathrm{d}\vec{\mathbf{r}}\\ &= \log_2(L) - \frac{1}{L}\sum_{l=0}^{L-1} E\left[\log_2\sum_{k=0}^{L-1}\exp(\Psi_{l,k})\middle|\mathbf{s}^l\right]\ \text{[bit/sym]},\end{aligned} \tag{2.79}$$

where $E[\xi|\mathbf{s}^l]$ is the expectation of ξ conditioned on $\mathbf{s}^l$. The expectation in Equation (2.79) can be estimated using a sufficiently high number of $\chi^2_{2N_t,j}$ and $\mathbf{w}_j$ realisations with the aid of Monte Carlo simulations for $j = 1, \ldots, N_r$.

The resultant bandwidth efficiency as defined in [267] is computed by normalising the channel capacity with respect to the bandwidth W and the signalling period T_s, resulting in [263, 267]

$$\eta_{\text{DCMC}}^{\text{STBC-SP}}(E_b/N_0) = \frac{C_{\text{DCMC}}^{\text{STBC-SP}}}{N_D/2} = \text{[bit/s/Hs]}. \tag{2.80}$$

Figure 2.12 shows the DCMC capacity evaluated from Equation (2.79) for the 4-dimensional SP modulation assisted STBC scheme for $L = 4$, 16, 64 and 256, when employing $N_t = 2$ transmit antennas as well as $N_r = 1$, 2 and 6 receive antennas, respectively. The Continuous-Input Continuous-Output Memoryless Channel (CCMC) [6] capacity of the MIMO scheme was also plotted for comparison in Figure 2.12 based on [268]. Figure 2.13 demonstrates and compares the achievable bandwidth efficiency of various SP modulated STBC schemes and identical-throughput conventionally modulated STBC schemes. The specific modulation type employed for the various schemes is outlined in Table 2.5. Figure 2.13 explicitly illustrates that a higher bandwidth efficiency may attained, when employing sphere packing modulation in conjunction with STBC schemes having $N_t = 2$ transmit antennas.

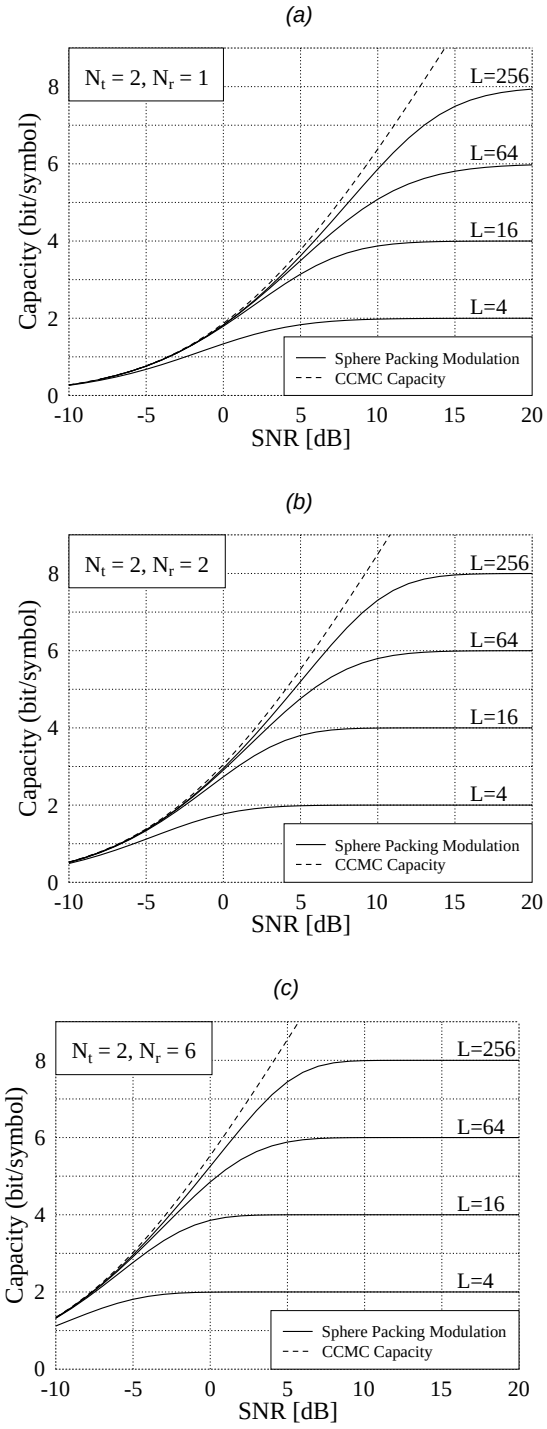

Figure 2.12: Capacity of STBC-SP based schemes evaluated form Equation (2.79) and using $L = 4$, 16, 64 and 256, when employing $N_t = 2$ transmit and N_r receive antennas for communicating over a correlated SPSI Rayleigh fading channel having a normalised Doppler frequency of $f_D = 0.1$. (a) $\mathbf{N_r = 1}$, (b) $\mathbf{N_r = 2}$, (c) $\mathbf{N_r = 6}$.

2.5 STBC-SP Performance

In this section, the two transmit antenna based scheme of Section 2.4.3 is considered. Simulation results are provided for systems having different *bits-per-symbol* (BPS) throughputs in conjunction

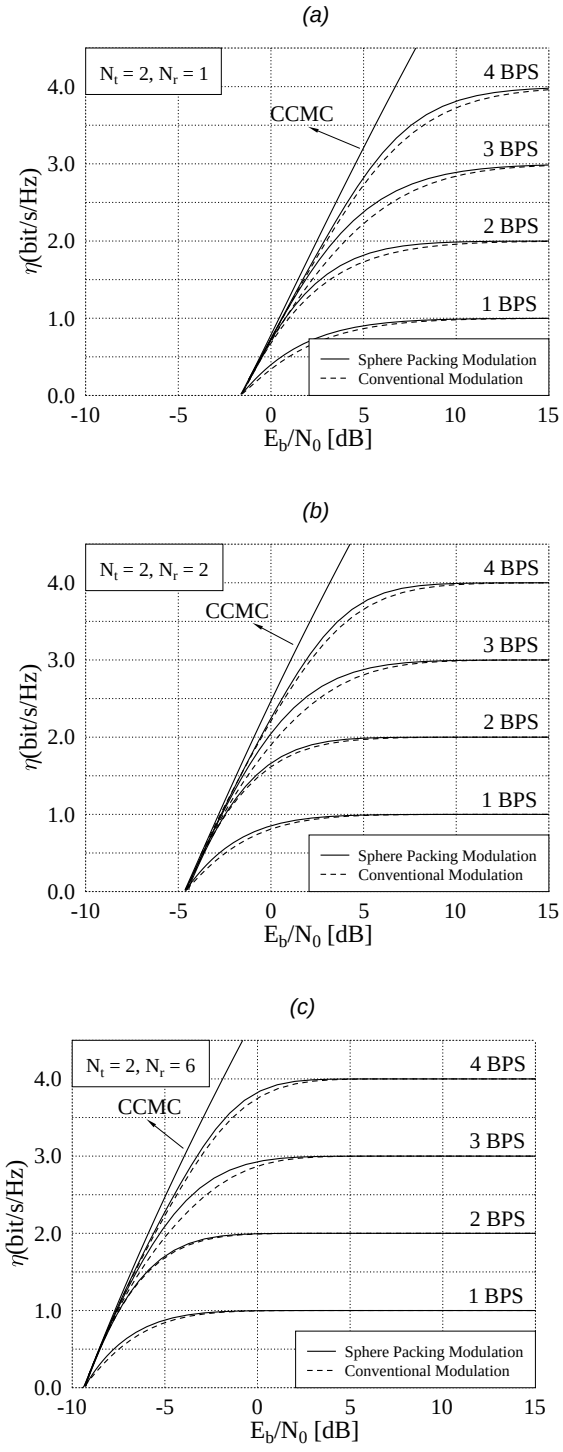

Figure 2.13: Bandwidth efficiency of STBC-SP based schemes evaluated from Equation (2.80) for $L = 4$, 16, 64 and 256, when employing $N_t = 2$ transmit and N_r receive antennas for communicating over a correlated SPSI Rayleigh fading channel having a normalised Doppler frequency of $f_D = 0.1$. (a) $\mathbf{N_r = 1}$, (b) $\mathbf{N_r = 2}$, (c) $\mathbf{N_r = 6}$.

with the appropriate conventional and sphere packing modulation schemes, as outlined in Table 2.5. Observe that $T = 2$ time slots are required for transmitting *a single* sphere packed symbol, when

using the $N_t = 2$ transmit antenna based scheme of Section 2.4.3. By contrast, *two* conventionally modulated symbols are transmitted during the same time period. Therefore, the throughput of the sphere packing modulation scheme has to be twice that of the conventional modulation scheme in order to create systems having an identical overall BPS throughput. This explains the specific choices of L in Table 2.5. Results are also shown for systems employing $N_r = 1$, 2, 3, 4, 5, and 6 receive antennas, when communicating over a correlated Rayleigh fading channel having a normalised Doppler frequency of $f_D = 0.1$. The channel's complex fading envelope is assumed to be constant over the transmission period of $T = 2$ time slots of a single space-time signal or, equivalently, the transmission period of a sphere packed symbol. This type of channel will be referred to here as a *sphere packing symbol invariant* (SPSI) channel. In this section, both the achievable *bit error rate* (BER) and *sphere packing symbol error rate* (SP-SER) are considered. The SP-SER represents the block error rate, where the block size is $B = \log_2 L$ bits, which is also synonymous to the *space-time symbol error rate* (ST-SER).

Throughput (BPS)	Conventional Modulation	Sphere Packing Modulation
1	BPSK	$L = 4$
2	QPSK	$L = 16$
3	8-PSK	$L = 64$
4	16-QAM	$L = 256$

Table 2.5: Conventional and sphere packing modulation employed for different BPS throughputs.

Sphere packing aided orthogonal design schemes promise to provide improved SP-SER (or ST-SER), when compared to the same metric of conventionally modulated orthogonal STBC based schemes. This promise is based on the fact that sphere packing modulation improves the diversity product (or coding advantage) of Equation (2.33), which is derived from the upper bound outlined in Equation (2.22) for the pairwise error probability between any two distinct *space-time signals*. On the other hand, the BER performance of sphere packing aided orthogonal ST-code design schemes is not always guaranteed to be better than that of conventionally modulated space-time signals, since sphere packing modulation specifically optimises the MED between two distinct space-time signals constructed using Equation (2.28), but not between the individual constituent symbols, $x_1, x_2, \ldots, x_{k+1}$, which conventional modulation based STBC optimises. However, it will be demonstrated later in this section that upon increasing the number of receive antennas, the achievable SP-SER performance improvement increases, which in turn leads to further BER performance improvements for the sphere packing aided orthogonal STBC schemes, as compared to conventionally modulated orthogonal STBC schemes.

Figure 2.14 shows the SP-SER performance curves of different orthogonal STBC schemes in combination with both conventional and sphere packing modulation for the different BPS throughputs, as outlined in Table 2.5. The systems employ $N_t = 2$ transmit antennas and $N_r = 1$ receive antenna for communicating over a correlated SPSI Rayleigh fading channel having a normalised Doppler frequency of $f_D = 0.1$. It is seen from Figure 2.14 that for a particular BPS throughput, the two curves corresponding to both the conventional scheme and to the sphere packing modulation scheme have the same asymptotic slope (i.e. diversity level). This agrees with the observation stated in [215], namely that $\mathbf{G}_2$-based space-time schemes dispensing with SP modulation also achieve full diversity. Therefore, SP is not expected to improve the asymptotic slope of the performance curves. Nonetheless, Figure 2.14 shows that orthogonal STBC using sphere packing offers a coding advantage over the conventionally modulated orthogonal STBC design. For example, sphere packing modulation having a throughput of 3 BPS and $L = 64$ achieves a coding gain of about 1.2dB over classic 8-PSK modulated STBC at an SP-SER of 10^{-4}. The corresponding BER

performance curves are shown in Figure 2.15. The BER performances of sphere packing modulation and conventional modulation are identical for systems having rates of 1 and 2 BPS since it can be shown that QPSK for example constitutes an SP scheme. However, Figure 2.15 also shows that conventional modulation based STBC outperforms sphere packing modulation, when higher BPS throughputs are considered, when employing $N_r = 1$ receive antenna.

Figures 2.16 to 2.25 illustrates the effect of increasing the number of receive antennas from $N_r =$ 2 to 6, respectively. The figures demonstrate that upon increasing the number of receive antennas, the SP-SER performance advantage of sphere packing modulation over conventional modulation increases. However, this increase becomes negligible, when employing more than $N_r = 3$ antennas. It is also illustrated in Figures 2.17, 2.19, 2.21, 2.23 and 2.25 that the BER performance of sphere packing modulation improves compared to that of conventional modulation, when increasing the number of receive antennas.

For example as seen in Figure 2.15, the BER performance of 8-PSK is better than that of sphere packing modulation having $L = 64$ when employing $N_r = 1$ receive antenna. However, the BER performance of sphere packing improves, when increasing the number of receive antennas leading to a coding advantage of about 1dB over 8-PSK, when employing $N_r = 6$ receive antennas. The coding gains achieved by sphere packing modulation over conventional modulation schemes at an SP-SER and a BER of 10^{-4} for the schemes characterised in Figures 2.14 to 2.25 are summarised in Tables 2.6 and 2.7. The negative coding gain values indicate, where conventional modulation outperforms sphere packing modulation. Figures 2.26-2.28 illustrate the SNR values required to achieve an SP-SER of 10^{-4} by the different orthogonal STBC schemes in combination with both conventional and sphere packing modulation for the different BPS throughputs of Table 2.5, when employing $N_t = 2$ transmit and $N_r = 1$, 3 and 6 receive antennas, respectively, for communicating over a correlated SPSI Rayleigh fading channel having a normalised Doppler frequency of $f_D = 0.1$.

Observe in Figures 2.14 to 2.25 that as alluded to before, the performance curves of QPSK modulation and sphere packing modulation having $L = 16$ (i.e. 2 BPS schemes) are identical. This phenomenon is due to the fact that QPSK modulation constitutes a special case of sphere packing modulation, when it is combined with $\mathbf{G}_2$ space-time signals. More specifically, consider the $\mathbf{G}_2$ space-time signal defined as $\mathbf{G}_2(x_{l,1}, x_{l,2})$, $l = 0, \ldots, 15$. If $x_{l,1}$ and $x_{l,2}$ are chosen independently from the QPSK modulation constellation, then the 16 legitimate space-time signals produced will be identical to the 16 legitimate space-time signals constructed using Equation (2.63), where $(a_{l,1}, a_{l,2}, a_{l,3}, a_{l,4})$, $l = 0, \ldots, 15$, correspond to the 16 SP constellation points hosted by D_4 that are centred at all possible permutations of (+/-1,+/-1,+/-1,+/-1) and have a normalisation factor of $1/\sqrt{2}$. These SP constellation points belong to the second layer of D_4 seen in Table 2.4.

	1 BPS	2 BPS	3 BPS	4 BPS
$N_r = 1$	0.4dB	0.0dB	1.2dB	0.6dB
$N_r = 2$	0.5dB	0.0dB	1.6dB	0.6dB
$N_r = 3$	0.6dB	0.0dB	2.0dB	0.9dB
$N_r = 4$	0.4dB	0.0dB	1.9dB	0.7dB
$N_r = 5$	0.5dB	0.0dB	1.9dB	0.9dB
$N_r = 6$	0.4dB	0.0dB	2.1dB	0.9dB

Table 2.6: Coding gains of sphere packing modulation aided STBC over conventional STBC at an SP-SER of 10^{-4} for the schemes characterised in Figures 2.14 to 2.25.

	1 BPS	2 BPS	3 BPS	4 BPS
$N_r = 1$	0.0dB	0.0dB	−0.5dB	−1.0dB
$N_r = 2$	0.3dB	0.0dB	0.5dB	−0.5dB
$N_r = 3$	0.5dB	0.0dB	0.9dB	−0.3dB
$N_r = 4$	0.4dB	0.0dB	1.0dB	−0.3dB
$N_r = 5$	0.4dB	0.0dB	1.0dB	0.0dB
$N_r = 6$	0.4dB	0.0dB	1.0dB	0.1dB

Table 2.7: Coding gains of sphere packing modulation aided STBC over conventional STBC at a BER of 10^{-4} for the schemes characterised in Figures 2.14 to 2.25.

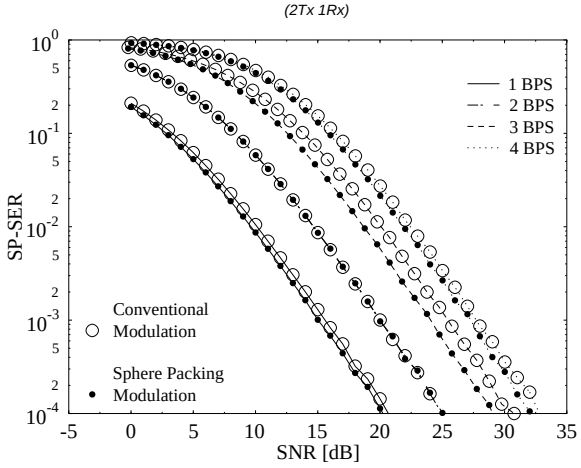

Figure 2.14: Sphere packing symbol error rate of different orthogonal STBC schemes in combination with both conventional and sphere packing modulation for the different BPS throughputs of Table 2.5, when employing $N_t = 2$ transmit and $\mathbf{N_r} = \mathbf{1}$ receive antennas for communicating over a correlated SPSI Rayleigh fading channel having a normalised Doppler frequency of $f_D = 0.1$.

2.6 Chapter Conclusion

It was shown in this chapter that the diversity product of orthogonal space-time signals is determined by the MED of the $(k+1)$-dimensional complex vectors $(x_1, x_2, \ldots, x_{k+1})$. In order to maximise the diversity product, it was proposed in [190] to use sphere packing having the best known MED in the $2(k+1)$-dimensional real-valued Euclidean space $\mathbb{R}^{2(k+1)}$ [236]. The capacity analysis provided in Section 2.4.5 demonstrated that sphere packing aided orthogonal STBC design has potential performance improvements over conventionally modulated orthogonal STBC schemes. Furthermore, our simulation results presented in Section 2.5 showed that sphere packing aided orthogonal STBC provides some coding gain over conventionally modulated orthogonal STBC schemes. Table 2.6 and 2.7 summarises the coding gains achieved by sphere packing modulation over conventional modulation at an SP-SER and a BER of 10^{-4} for the schemes characterised in Figures 2.14 to 2.25.

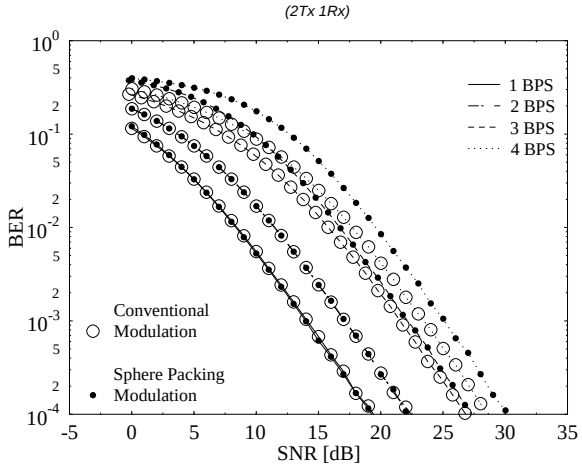

Figure 2.15: Bit error rate of different orthogonal STBC schemes in combination with both conventional and sphere packing modulation for the different BPS throughputs of Table 2.5, when employing $N_t = 2$ transmit and $\mathbf{N_r = 1}$ receive antennas for communicating over a correlated SPSI Rayleigh fading channel having a normalised Doppler frequency of $f_D = 0.1$.

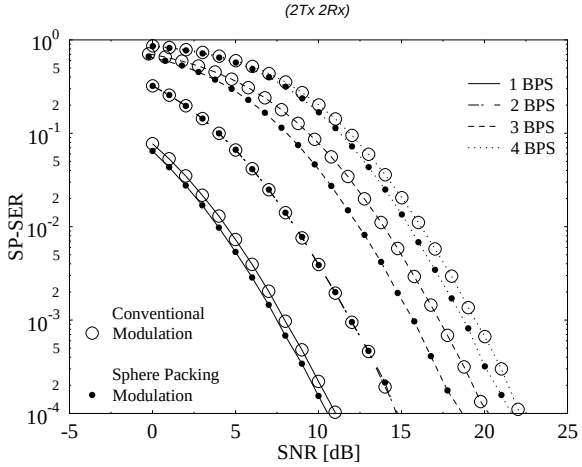

Figure 2.16: Sphere packing symbol error rate of different orthogonal STBC schemes in combination with both conventional and sphere packing modulation for the different BPS throughputs of Table 2.5, when employing $N_t = 2$ transmit and $\mathbf{N_r = 2}$ receive antennas for communicating over a correlated SPSI Rayleigh fading channel having a normalised Doppler frequency of $f_D = 0.1$.

2.7 Chapter Summary

This chapter first summarised the design criteria of space-time coded communication systems in Section 2.2. Specifically, our quasi-static and rapidly fading channels are described in Sections 2.2.1 and 2.2.2, respectively. In Section 2.3, we outlined the design criteria used for time-correlated fading

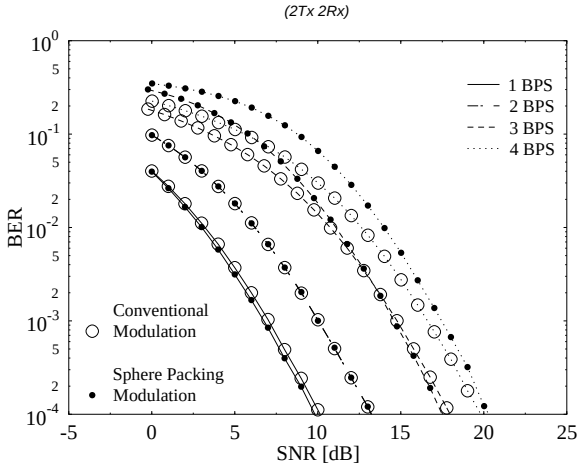

Figure 2.17: Bit error rate of different orthogonal STBC schemes in combination with both conventional and sphere packing modulation for the different BPS throughputs of Table 2.5, when employing $N_t = 2$ transmit and $\mathbf{N_r = 2}$ receive antennas for communicating over a correlated SPSI Rayleigh fading channel having a normalised Doppler frequency of $f_D = 0.1$.

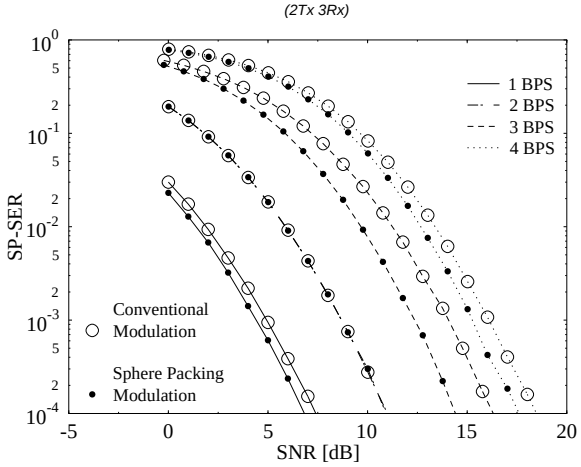

Figure 2.18: Sphere packing symbol error rate of different orthogonal STBC schemes in combination with both conventional and sphere packing modulation for the different BPS throughputs of Table 2.5, when employing $N_t = 2$ transmit and $\mathbf{N_r = 3}$ receive antennas for communicating over a correlated SPSI Rayleigh fading channel having a normalised Doppler frequency of $f_D = 0.1$.

channels, where both the pairwise SP-symbol error probability as well as the corresponding design criteria were presented in Section 2.3.2. The concept of diversity product, which was introduced in [222, 223] and generalised in [190] in order to account for the effects of temporal correlation was discussed in Section 2.3.3.1. Furthermore, both lower and upper bounds on the generalised diversity product discussed in Section 2.3.3.1 were provided in Section 2.3.3.2.

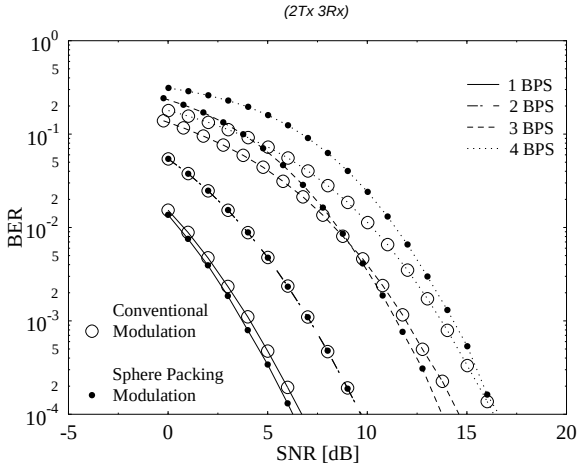

Figure 2.19: Bit error rate of different orthogonal STBC schemes in combination with both conventional and sphere packing modulation for the different BPS throughputs of Table 2.5, when employing $N_t = 2$ transmit and $\mathbf{N_r = 3}$ receive antennas for communicating over a correlated SPSI Rayleigh fading channel having a normalised Doppler frequency of $f_D = 0.1$.

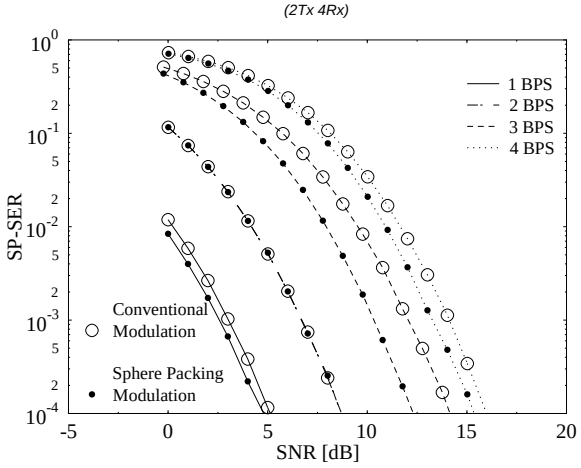

Figure 2.20: Sphere packing symbol error rate of different orthogonal STBC schemes in combination with both conventional and sphere packing modulation for the different BPS throughputs of Table 2.5, when employing $N_t = 2$ transmit and $\mathbf{N_r = 4}$ receive antennas for communicating over a correlated SPSI Rayleigh fading channel having a normalised Doppler frequency of $f_D = 0.1$.

In Section 2.4, the philosophy of orthogonal STBC design using sphere packing modulation was considered for space-time signals, where the motivation behind the adoption of sphere packing modulation was discussed in Section 2.4.2. The SP signal design derived for $N_t = 2$ transmit antennas was provided in Section 2.4.3, further illustrating the concept of combining an orthogonal STBC design with sphere packing. Section 2.4.4 discussed the problem of constructing a sphere packing constellation having a particular size L. The constellation points were first chosen based

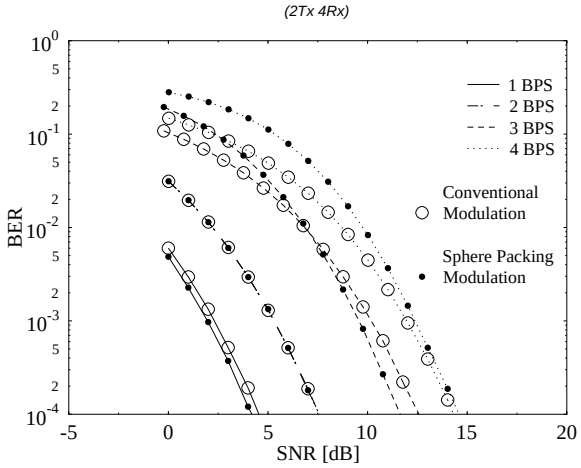

Figure 2.21: Bit error rate of different orthogonal STBC schemes in combination with both conventional and sphere packing modulation for the different BPS throughputs of Table 2.5, when employing $N_t = 2$ transmit and $\mathbf{N_r = 4}$ receive antennas for communicating over a correlated SPSI Rayleigh fading channel having a normalised Doppler frequency of $f_D = 0.1$.

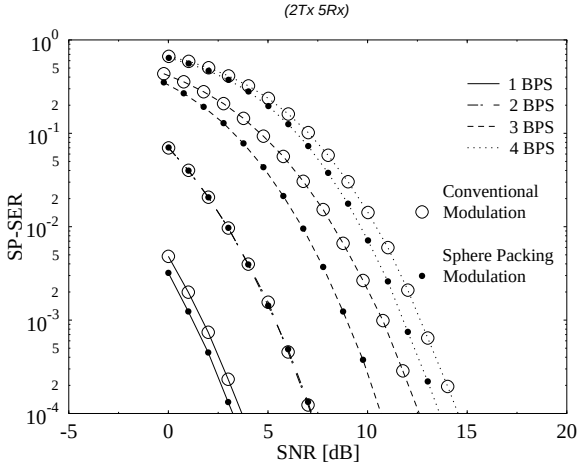

Figure 2.22: Sphere packing symbol error rate of different orthogonal STBC schemes in combination with both conventional and sphere packing modulation for the different BPS throughputs of Table 2.5, when employing $N_t = 2$ transmit and $\mathbf{N_r = 5}$ receive antennas for communicating over a correlated SPSI Rayleigh fading channel having a normalised Doppler frequency of $f_D = 0.1$.

on the minimum energy criterion. Then, an exhaustive computer search was conducted for all the SP symbols having the lowest possible energy, in order to find the specific set of L points having the best MED from all the other constellation points satisfying the minimum energy criterion. The capacity of STBC-SP schemes employing $N_t = 2$ transmit antennas was derived in Section 2.4.5. Finally, the performance of STBC-SP schemes was characterised in Section 2.5, demonstrating that STBC-SP schemes are capable of outperforming STBC schemes that employ conventional

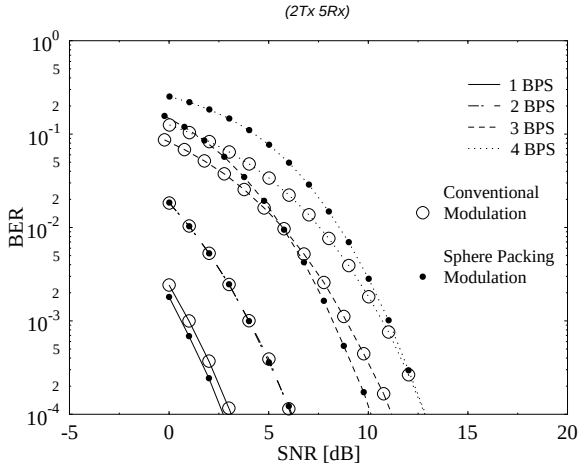

Figure 2.23: Bit error rate of different orthogonal STBC schemes in combination with both conventional and sphere packing modulation for the different BPS throughputs of Table 2.5, when employing $N_t = 2$ transmit and $\mathbf{N_r = 5}$ receive antennas for communicating over a correlated SPSI Rayleigh fading channel having a normalised Doppler frequency of $f_D = 0.1$.

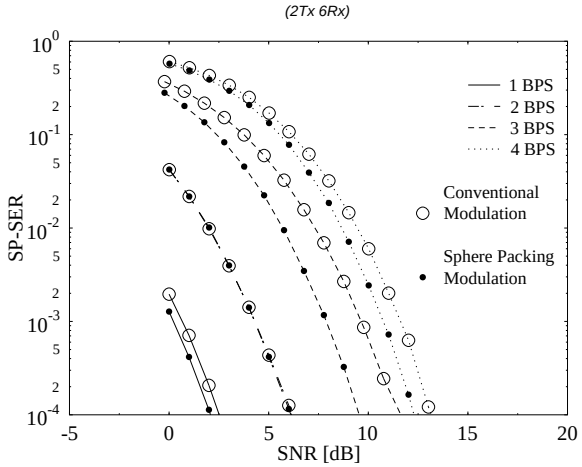

Figure 2.24: Sphere packing symbol error rate of different orthogonal STBC schemes in combination with both conventional and sphere packing modulation for the different BPS throughputs of Table 2.5, when employing $N_t = 2$ transmit and $\mathbf{N_r = 6}$ receive antennas for communicating over a correlated SPSI Rayleigh fading channel having a normalised Doppler frequency of $f_D = 0.1$.

modulation (i.e. PSK, QAM). The coding gains achieved by the sphere packing assisted STBC over conventional STBC at an SP-SER and a BER of 10^{-4} are summarised in Tables 2.6 and 2.7 for the schemes characterised in Figures 2.14 to 2.25.

In the next chapter, we will demonstrate that the performance of STBC-SP systems can be further improved by concatenating sphere packing aided modulation with channel coding and

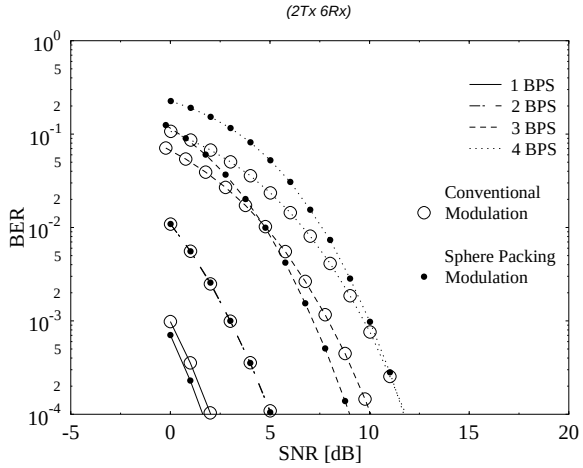

Figure 2.25: Bit error rate of different orthogonal STBC schemes in combination with both conventional and sphere packing modulation for the different BPS throughputs of Table 2.5, when employing $N_t = 2$ transmit and $\mathbf{N_r = 6}$ receive antennas for communicating over a correlated SPSI Rayleigh fading channel having a normalised Doppler frequency of $f_D = 0.1$.

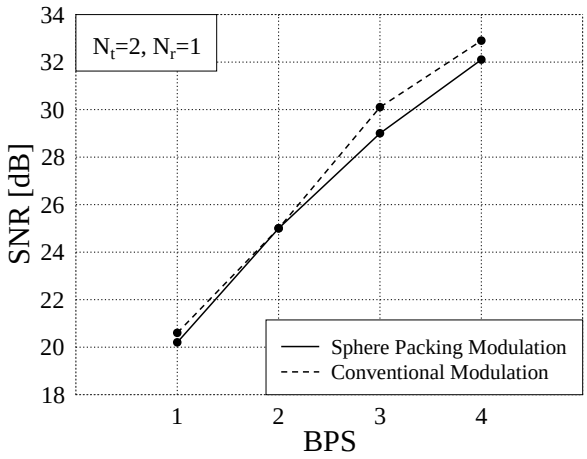

Figure 2.26: SNR required to achieve an SP-SER of 10^{-4} by different orthogonal STBC schemes in combination with both conventional and sphere packing modulation for the different BPS throughputs of Table 2.5, when employing $N_t = 2$ transmit and $\mathbf{N_r = 1}$ receive antennas for communicating over a correlated SPSI Rayleigh fading channel having a normalised Doppler frequency of $f_D = 0.1$.

performing demapping as well as channel decoding iteratively. The sphere packing demapper of [190] will be further developed for the sake of accepting the *a priori* information passed to it from the channel decoder as extrinsic information. The convergence behaviour of this concatenated scheme is investigated with the aid of extrinsic information transfer (EXIT) charts.

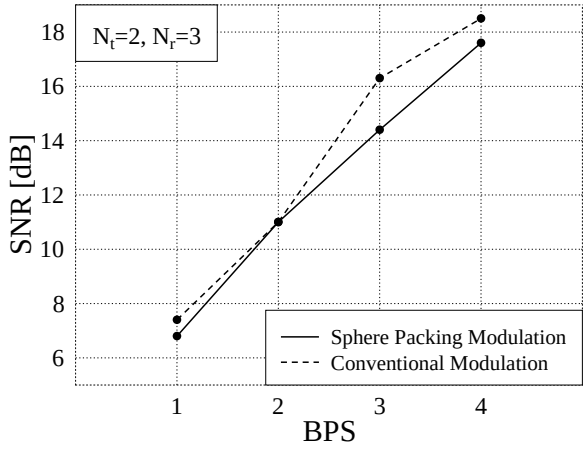

Figure 2.27: SNR required to achieve an SP-SER of 10^{-4} by different orthogonal STBC schemes in combination with both conventional and sphere packing modulation for the different BPS throughputs of Table 2.5, when employing $N_t = 2$ transmit and $\mathbf{N_r = 3}$ receive antennas for communicating over a correlated SPSI Rayleigh fading channel having a normalised Doppler frequency of $f_D = 0.1$.

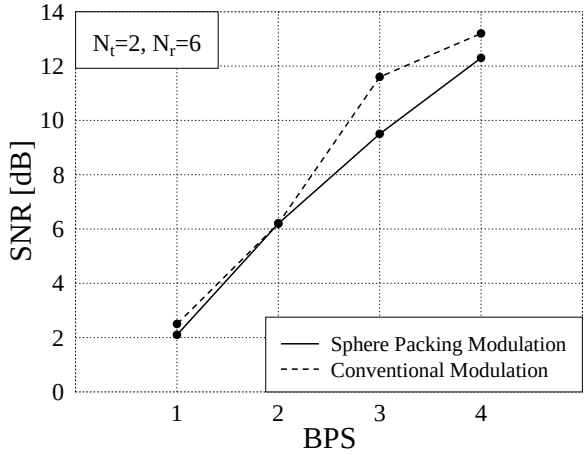

Figure 2.28: SNR required to achieve an SP-SER of 10^{-4} by different orthogonal STBC schemes in combination with both conventional and sphere packing modulation for the different BPS throughputs of Table 2.5, when employing $N_t = 2$ transmit and $\mathbf{N_r = 6}$ receive antennas for communicating over a correlated SPSI Rayleigh fading channel having a normalised Doppler frequency of $f_D = 0.1$.

Chapter 3

Turbo Detection of Channel-Coded STBC-SP Schemes*

3.1 Introduction

In Chapter 2, a recently proposed space-time signal construction method that combines orthogonal design with sphere packing ((STBC-SP)) has been introduced. STBC-SP schemes have shown useful performance improvements over Alamouti's conventional orthogonal design. In this chapter, the performance of STBC-SP systems is improved by developing novel bit-based turbo-detected schemes.

Iterative decoding of spectrally efficient modulation schemes was considered by several authors [261, 269–271]. In [272], the employment of the turbo principle was considered for iterative soft demapping in the context of bit-interleaved coded modulation ((BICM)), where a soft demapper was used between the multilevel demodulator and the channel decoder. In [273], a turbo coding scheme was proposed for the multiple-input multiple-output ((MIMO)) Rayleigh fading channel, where a block code was employed as an outer channel code, while an orthogonal STBC scheme was considered as the inner code.

Recently, studying the convergence behaviour of iterative decoding has attracted considerable attention [274–282]. In order to determine the E_b/N_0 convergence threshold of randomly constructed irregular low-density parity-check ((LDPC)) codes transmitted over the AWGN channel, the authors of [274] proposed the employment of a density evolution algorithm, which was also invoked in [275, 276] for the sake of constructing LDPC codes capable of operating at low E_b/N_0 values. signal to noise ratio ((SNR)) based measures were used in [277, 278] for studying the convergence of iterative decoders, while the authors of [279] investigated the convergence behaviour of unity-rate inner codes based on a combination of SNR measures and mutual information. In [280, 281], ten Brink proposed the employment of the so-called extrinsic information transfer ((EXIT)) characteristics between a concatenated decoder's output and input for describing the flow of extrinsic information through the soft in/soft out constituent decoders. A tutorial introduction to EXIT charts can be found in [283]. Additionally, several algorithms predicting the convergence of iterative decoding schemes were compared in [282].

*Parts of this chapter are based on the collaborative research outlined in [197].

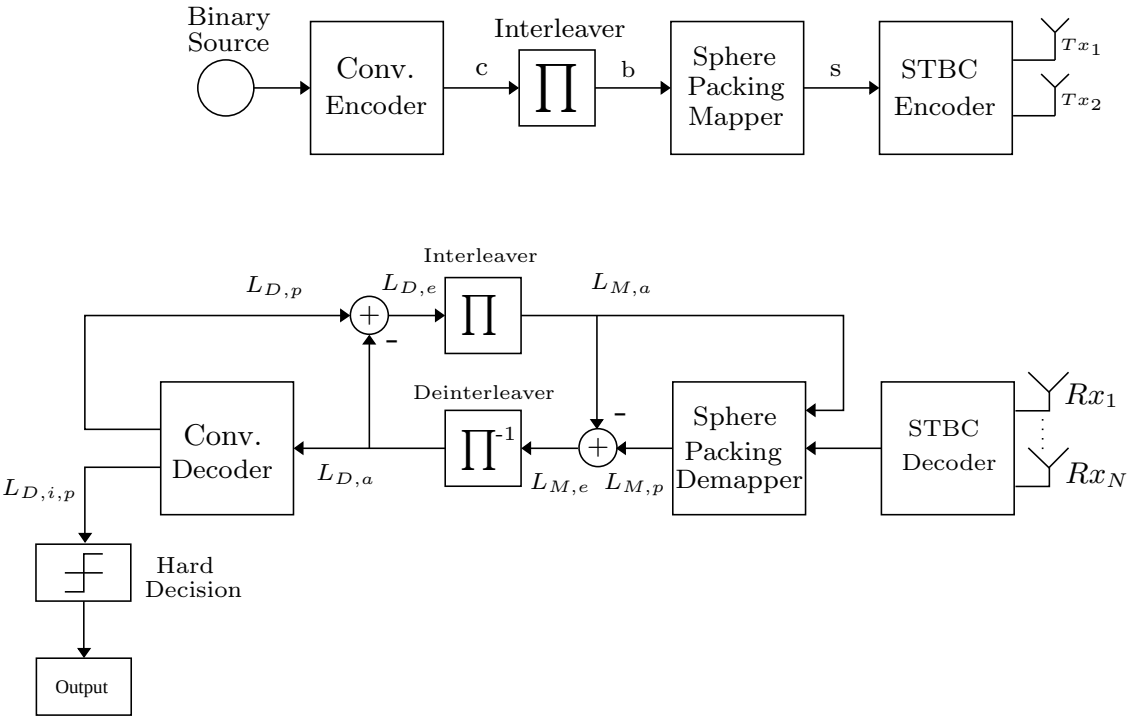

Figure 3.1: Bit-based turbo detection RSC-coded STBC-SP system.

Motivated by the performance improvements reported in [190] and [272], we propose a novel bit-based system that exploits the advantages of both the iterative demapping and decoding techniques of [272] as well as those of the STBC-SP scheme of [190]. The STBC-SP demapper of [190] was further developed for the sake of accepting the *a priori* information passed to it from the channel decoder as extrinsic information. As a benefit of the proposed solution, it will be demonstrated in Section 3.5 that the proposed turbo detection aided STBC-SP scheme is capable of providing an E_b/N_0 gain of 20.2dB at a BER of 10^{-5} over the STBC-SP scheme of [190].

In this chapter, two realisations of a novel bit-based iterative-detection aided STBC-SP scheme are presented, namely a recursive systematic convolutional (RSC) coded turbo-detected STBC-SP scheme and a binary LDPC coded turbo-detected STBC-SP arrangement. Our system overview is provided in Section 3.2. Section 3.3 shows how the STBC-SP demapper is modified for exploiting the *a priori* knowledge provided by the channel decoder. Section 3.4 provides the EXIT chart analysis of the turbo-detected bit-based scheme, while our simulation results and discussions are provided in Section 3.5. Finally, the chapter is concluded in Section 3.6.

3.2 System Overview

3.2.1 RSC-Coded Turbo-Detected STBC-SP scheme

The schematic of the entire RSC-coded turbo-detected STBC-SP scheme is shown in Figure 3.1, where the transmitted source bits are first convolutionally encoded and then interleaved by a random bit interleaver. A rate $R = \frac{1}{2}$ RSC code is considered in this chapter. After channel interleaving, the sphere packing mapper first maps B channel-coded binary bits $\mathbf{b} = (b_0, \ldots, b_{B-1})$ to a sphere packing modulated symbol $\mathbf{s} \in S$ such that we have $\mathbf{s} = map_{sp}(\mathbf{b})$, where $B = \log_2 L$.

The STBC-SP encoder then maps the sphere packing modulated symbol $\mathbf{s}$ to a space-time signal $\mathbf{C}_l = \sqrt{\frac{2L}{E_{\text{total}}}}\mathbf{G}_2(x_{l,1}, x_{l,2})$, $0 \leq l \leq L-1$, using Equation (8.63). Subsequently, each space-time signal is transmitted over $T = 2$ time slots using two transmit antennas, as shown in Equation (2.35) and Table 2.2.

In this chapter, we consider an SPSI correlated narrowband Rayleigh fading channel, based on the Jakes fading model [235] and associated with a normalised Doppler frequency of $f_D = f_d T_{sym} = 0.1$, where f_d is the Doppler frequency and T_{sym} is the symbol period. The complex fading envelope is thus assumed to be constant across the transmission period of a space-time coded symbol spanning $T = 2$ time slots. The complex AWGN of $n = n_I + jn_Q$ is also added to the received signal, where n_I and n_Q are two independent zero mean Gaussian random variables having a variance of $\sigma_n^2 = \sigma_{n_I}^2 = \sigma_{n_Q}^2 = N_0/2$ per dimension, where $N_0/2$ represents the double-sided noise power spectral density expressed in W/Hz.

As shown in Figure 3.1, the received complex-valued symbols are demapped to their log-likelihood ratio ((LLR)) representation for each of the B coded bits per STBC-SP symbol. The *a priori* LLR values of the demodulator are subtracted from the *a posteriori* LLR values for the sake of generating the extrinsic LLR values $L_{M,e}$, and then the LLRs $L_{M,e}$ are deinterleaved by a soft-bit deinterleaver, as seen in Figure 3.1. Next, the soft bits $L_{D,a}$ are passed to the convolutional decoder in order to compute the *a posteriori* LLR values $L_{D,p}$ provided by the Log-MAP algorithm [284] for all the channel-coded bits. During the last iteration, only the LLR values $L_{D,i,p}$ of the original uncoded systematic information bits are required, which are passed to a hard decision decoder in order to determine the estimated transmitted source bits. The extrinsic information $L_{D,e}$, is generated by subtracting the *a priori* information from the *a posteriori* information according to $L_{D,p} - L_{D,a}$, which is then fed back to the STBC-SP demapper as the *a priori* information $L_{M,a}$ after appropriately reordering them using the interleaver of Figure 3.1. The STBC-SP demapper exploits the *a priori* information for the sake of providing improved *a posteriori* LLR values, which are then passed to the channel decoder and in turn back to the STBC-SP demodulator for further iterations.

3.2.2 Binary LDPC-Coded Turbo-Detected STBC-SP scheme

The schematic of the entire binary LDPC-coded turbo-detected STBC-SP scheme is shown in Figure 3.2, where a rate $R = \frac{1}{2}$ binary LDPC code is employed. Observe that channel interleaving is not required between the binary LDPC encoder and the sphere packing mapper, since the LDPC parity check matrix is randomly constructed, where each of the parity check equations is checking several random bit positions in a codeword, which has a similar effect to that of the channel interleaver. A sophisticated encoding as well as turbo detection procedure similar to that described in Section 3.2.1 is outlined in Figure 3.2. However, based on the *a posteriori* LLR values $L_{D,p}$ recorded at the output of the LDPC decoder, a tentative hard decision will be made during each turbo detection iteration and the resultant codeword will be checked by the LDPC code's parity check matrix. If the resultant vector is an all-zero sequence, then a legitimate codeword has been found, and the hard-decision based sequence will be output. Otherwise, if the maximum affordable number of iterations has not been reached, the *a priori* information, $L_{D,a}$, is subtracted from the *a posteriori* LLR values, $L_{D,p}$, for the sake of generating the extrinsic information, $L_{D,e}$ which is appropriately interleaved and fed back to the demodulator for the next iteration, as seen in Figure 3.2. The process continues, until the affordable maximum number of iterations has been encountered or a legitimate codeword has been found.

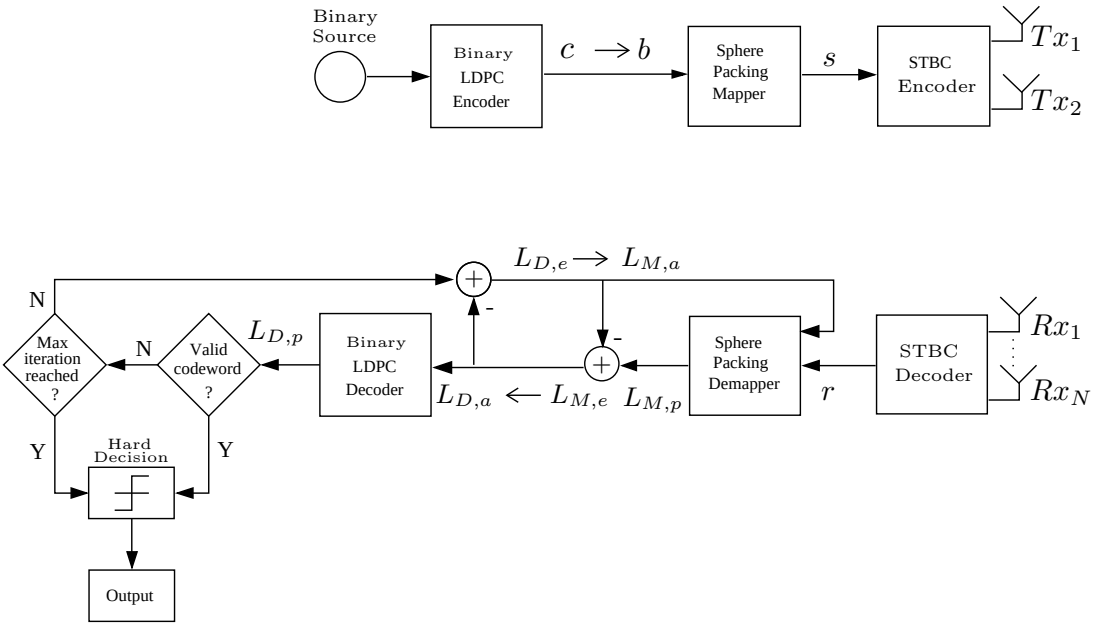

Figure 3.2: Bit-based turbo detection LDPC-coded STBC-SP system.

3.3 Iterative Demapping

For the sake of simplicity, a system having a single receive antenna is considered, although its extension to systems having more than one receive antenna is straightforward. Assuming perfect channel estimation, the complex-valued channel output symbols received during two consecutive time slots are first diversity-combined in order to extract the estimates $\tilde{x}_1$ and $\tilde{x}_2$ of the most likely transmitted symbols $x_{l,1}$ and $x_{l,2}$ as was described in Section 2.4.3.2, resulting in

$$\tilde{x}_1 = (|h_1|^2 + |h_2|^2) \cdot x_{l,1} + \acute{n}_1 \quad (3.1)$$

$$\tilde{x}_2 = (|h_1|^2 + |h_2|^2) \cdot x_{l,2} + \acute{n}_2, \quad (3.2)$$

where h_1 and h_2 represent the complex-valued channel coefficients corresponding to the first and second transmit antenna, respectively, and $\acute{n}_1$ as well as $\acute{n}_2$ are zero-mean complex Gaussian random variables with variance $\sigma_{\acute{n}}^2 = (|h_1|^2 + |h_2|^2) \cdot \sigma_n^2$. A received sphere-packed symbol $\mathbf{r}$ is then constructed from the estimates $\tilde{x}_1$ and $\tilde{x}_2$ using Equation (8.63) as

$$\mathbf{r} = T_{sp}^{-1}(\tilde{x}_1, \tilde{x}_2), \quad (3.3)$$

where $\mathbf{r} = \{[\tilde{a}_1\ \tilde{a_2}\ \tilde{a_3}\ \tilde{a_4}] \in \mathbb{R}^4\}$. The received sphere-packed symbol $\mathbf{r}$ can be written as

$$\mathbf{r} = h \cdot \sqrt{\frac{2L}{E_{\text{total}}}} \cdot \mathbf{s}^l + \mathbf{w}, \quad (3.4)$$

where $h = (|h_1|^2 + |h_2|^2)$, $\mathbf{s}^l \in S$, $0 \leq l \leq L-1$, and $\mathbf{w}$ is a four-dimensional real-valued Gaussian random variable having a covariance matrix of $\sigma_w^2 \cdot \mathbf{I}_{N_D} = \sigma_{\acute{n}}^2 \cdot \mathbf{I}_{N_D} = h \cdot \sigma_n^2 \cdot \mathbf{I}_{N_D}$, where $N_D = 4$, since the symbol constellation S is four-dimensional. According to Equation (3.4), the conditional

PDF $p(\mathbf{r}|\mathbf{s}^l)$ is given by

$$\begin{aligned} p(\mathbf{r}|\mathbf{s}^l) &= \frac{1}{(2\pi\sigma_w^2)^{\frac{N_D}{2}}} \exp\Big(-\frac{1}{2\sigma_w^2}(\mathbf{r}-\alpha\cdot\mathbf{s}^l)(\mathbf{r}-\alpha\cdot\mathbf{s}^l)^T\Big), \\ &= \frac{1}{(2\pi\sigma_w^2)^{\frac{N_D}{2}}} \exp\left(-\frac{1}{2\sigma_w^2}\left(\sum_{i=1}^{N_D}(\tilde{a}_i-\alpha\cdot a_{l,i})^2\right)\right), \end{aligned} \tag{3.5}$$

where we have $\alpha = h\cdot\sqrt{\frac{2L}{E\text{total}}}$.

The sphere packing symbol $\mathbf{r}$ carries B channel-coded binary bits $\mathbf{b} = (b_0,\ldots,b_{B-1})$. The LLR-value of bit b_k for $k = 0,\ldots,B-1$, can be written as [272]

$$L(b_k|\mathbf{r}) = L_a(b_k) + \ln\frac{\sum_{\mathbf{s}^l\in S_1^k} p(\mathbf{r}|\mathbf{s}^l)\cdot\exp\Big(\sum_{j=0,j\neq k}^{B-1} b_j L_a(b_j)\Big)}{\sum_{\mathbf{s}^l\in S_0^k} p(\mathbf{r}|\mathbf{s}^l)\cdot\exp\Big(\sum_{j=0,j\neq k}^{B-1} b_j L_a(b_j)\Big)}, \tag{3.6}$$

where S_1^k and S_0^k are subsets of the symbol constellation S such that $S_1^k \triangleq \{\mathbf{s}^l\in S : b_k = 1\}$ and likewise, $S_0^k \triangleq \{\mathbf{s}^l\in S : b_k = 0\}$. In other words, S_i^k represents all symbols of the set S, where we have $b_k = i\in\{0,1\}$, $k = 0,\ldots,B-1$. Using Equation (3.5), we can write Equation (3.6) as

$$\begin{aligned} L(b_k|\mathbf{r}) &= L_a(b_k) + \ln\frac{\sum_{\mathbf{s}^l\in S_1^k}\exp\left(-\frac{1}{2\sigma_w^2}(\mathbf{r}-\alpha\cdot\mathbf{s}^l)(\mathbf{r}-\alpha\cdot\mathbf{s}^l)^T + \sum_{j=0,j\neq k}^{B-1} b_j L_a(b_j)\right)}{\sum_{\mathbf{s}^l\in S_0^k}\exp\left(-\frac{1}{2\sigma_w^2}(\mathbf{r}-\alpha\cdot\mathbf{s}^l)(\mathbf{r}-\alpha\cdot\mathbf{s}^l)^T + \sum_{j=0,j\neq k}^{B-1} b_j L_a(b_j)\right)} \\ &= L_{M,a} + L_{M,e}. \end{aligned} \tag{3.7}$$

Finally, the max-log approximation of Equation (3.7) is as follows

$$\begin{aligned} L(b_k|\mathbf{r}) = L_a(b_k) &+ \max_{\mathbf{s}^l\in S_1^k}\left[-\frac{1}{2\sigma_w^2}(\mathbf{r}-\alpha\cdot\mathbf{s}^l)(\mathbf{r}-\alpha\cdot\mathbf{s}^l)^T + \sum_{j=0,j\neq k}^{B-1} b_j L_a(b_j)\right] \\ &- \max_{\mathbf{s}^l\in S_0^k}\left[-\frac{1}{2\sigma_w^2}(\mathbf{r}-\alpha\cdot\mathbf{s}^l)(\mathbf{r}-\alpha\cdot\mathbf{s}^l)^T + \sum_{j=0,j\neq k}^{B-1} b_j L_a(b_j)\right]. \end{aligned} \tag{3.8}$$

Example 3.3.1 (Iterative demapping for $L = 4$)**.** *:*
In order to explain the theory behind Equation (3.6), let us consider a sphere packing modulation scheme associated with $L = 4$. The binary bits b_k, $k = 0,\ 1$, corresponding to each sphere packing symbol $\mathbf{s}^l$, $l = 0,\ldots,3$, are outlined in Table 3.1. The LLR-value of b_0, for example, may be written as [272]

$$\begin{aligned} L(b_0|\mathbf{r}) &= \ln\frac{p(b_0=1|\mathbf{r})}{p(b_0=0|\mathbf{r})} \\ &= \ln\frac{p(b_0=1,b_1=0|\mathbf{r}) + p(b_0=1,b_1=1|\mathbf{r})}{p(b_0=0,b_1=0|\mathbf{r}) + p(b_0=0,b_1=1|\mathbf{r})}. \end{aligned} \tag{3.9}$$

SP Symbol	Binary Bits	
	b_0	b_1
$\mathbf{s^0}$	0	0
$\mathbf{s^1}$	1	0
$\mathbf{s^2}$	0	1
$\mathbf{s^3}$	1	1

Table 3.1: Binary bits corresponding to sphere packing symbols, when $L = 4$.

Using Bayes' rule[1]*, Equation (3.9) may be expressed as*

$$L(b_0|\mathbf{r}) = \ln \frac{p(\mathbf{r}|b_0=1,b_1=0)\cdot p(b_0=1,b_1=0) + p(\mathbf{r}|b_0=1,b_1=1)\cdot p(b_0=1,b_1=1)}{p(\mathbf{r}|b_0=0,b_1=0)\cdot p(b_0=0,b_1=0) + p(\mathbf{r}|b_0=0,b_1=1)\cdot p(b_0=0,b_1=1)}. \tag{3.10}$$

Since bit-interleaving is employed, it is reasonable to assume that b_0 *and* b_1 *are independent of each other. Hence, Equation (3.10) may be manipulated as follows*

$$\begin{aligned}
L(b_0|\mathbf{r}) &= \ln \frac{p(\mathbf{r}|b_0=1,b_1=0)\cdot p(b_0=1)\cdot p(b_1=0) + p(\mathbf{r}|b_0=1,b_1=1)\cdot p(b_0=1)\cdot p(b_1=1)}{p(\mathbf{r}|b_0=0,b_1=0)\cdot p(b_0=0)\cdot p(b_1=0) + p(\mathbf{r}|b_0=0,b_1=1)\cdot p(b_0=0)\cdot p(b_1=1)} \\
&= \ln \frac{p(b_0=1)}{p(b_0=0)} + \ln \frac{p(\mathbf{r}|b_0=1,b_1=0)\cdot p(b_1=0) + p(\mathbf{r}|b_0=1,b_1=1)\cdot p(b_1=1)}{p(\mathbf{r}|b_0=0,b_1=0)\cdot p(b_1=0) + p(\mathbf{r}|b_0=0,b_1=1)\cdot p(b_1=1)} \\
&= L_a(b_0) + \ln \frac{p(\mathbf{r}|b_0=1,b_1=0) + p(\mathbf{r}|b_0=1,b_1=1)\cdot \big(p(b_1=1)/p(b_1=0)\big)}{p(\mathbf{r}|b_0=0,b_1=0) + p(\mathbf{r}|b_0=0,b_1=1)\cdot \big(p(b_1=1)/p(b_1=0)\big)} \\
&= L_a(b_0) + \ln \frac{p(\mathbf{r}|b_0=1,b_1=0) + p(\mathbf{r}|b_0=1,b_1=1)\cdot \exp\big(\ln\big(p(b_1=1)/p(b_1=0)\big)\big)}{p(\mathbf{r}|b_0=0,b_1=0) + p(\mathbf{r}|b_0=0,b_1=1)\cdot \exp\big(\ln\big(p(b_1=1)/p(b_1=0)\big)\big)} \\
&= L_a(b_0) + \ln \frac{p(\mathbf{r}|b_0=1,b_1=0) + p(\mathbf{r}|b_0=1,b_1=1)\cdot \exp\big(L_a(b_1)\big)}{p(\mathbf{r}|b_0=0,b_1=0) + p(\mathbf{r}|b_0=0,b_1=1)\cdot \exp\big(L_a(b_1)\big)} \\
&= L_a(b_0) + \ln \frac{p(\mathbf{r}|\mathbf{s}^1) + p(\mathbf{r}|\mathbf{s}^3)\cdot \exp\big(L_a(b_1)\big)}{p(\mathbf{r}|\mathbf{s}^0) + p(\mathbf{r}|\mathbf{s}^2)\cdot \exp\big(L_a(b_1)\big)},
\end{aligned} \tag{3.11}$$

which is generalised in Equation (3.6).

3.4 Binary EXIT Chart Analysis

The main objective of employing EXIT charts proposed by Stephan ten Brink [280, 281], is to predict the convergence behaviour of the iterative decoder by examining the evolution of the in-

[1] Let X and Y denote two random variables. According to Bayes' rule, the conditional probability $p(X|Y)$ may be written as [285]

$$p(X|Y) = \frac{p(Y|X)\cdot p(X)}{p(Y)}.$$

put/output mutual information exchange between the inner and outer decoders in consecutive iterations. The application of EXIT charts is based on two assumptions, namely that upon assuming large interleaver lengths,

- the *a priori* LLR values are fairly uncorrelated;
- The probability density function of the *a priori* LLR values is Gaussian.

3.4.1 Transfer Characteristics of the Demapper

As seen in Figures 3.1 and 3.2, the inputs of the sphere-packing demapper are the noise-contaminated channel observations and the *a priori* information $L_{M,a}$ generated by the outer channel decoder. The demapper outputs the *a posteriori* information $L_{M,p}$, subtracts the *a priori* and hence produces the extrinsic information $L_{M,e}$ as shown in Section 3.3. Based on the above-mentioned two assumptions, the *a priori* input $L_{M,a}$ can be modelled by applying an independent zero-mean Gaussian random variable n_A having a variance of σ_A^2. In conjunction with the outer channel coded and interleaved bits $b \in \{0,1\}$ of Figures 3.1 and 3.2 or equivalently $x \in \{-1,+1\}$, the *a priori* input $L_{M,a}$ can be written as [280]

$$L_{M,a} \;=\; \mu_A \cdot x + n_A, \tag{3.12}$$

where $\mu_A = \sigma_A^2/2$ since $L_{M,a}$ is an LLR-value obeying the Gaussian distribution [286]. Accordingly, the conditional probability density function of the *a priori* input $L_{M,a}$ is

$$p_A(\zeta|X=x) \;=\; \frac{1}{\sqrt{2\pi}\sigma_A}\;\exp\left(-\frac{(\zeta-\frac{\sigma_A^2}{2}\cdot x)^2}{2\sigma_A^2}\right). \tag{3.13}$$

The mutual information of $I_{A_M} = I(X; L_{M,a})$, $0 \le I_{A_M} \le 1$, between the outer coded and interleaved bits x and the LLR values $L_{M,a}$ is used to quantify the information content of the *a priori* knowledge [287]:

$$I_{A_M} \;=\; \frac{1}{2}\cdot\sum_{x=-1,+1}\int_{-\infty}^{+\infty} p_A(\zeta|X=x)\cdot\log_2\frac{2\cdot p_A(\zeta|X=x)}{p_A(\zeta|X=-1)+p_A(\zeta|X=+1)}\;\mathrm{d}\zeta. \tag{3.14}$$

Using Equation (3.13), Equation (3.14) can be expressed as

$$I_{A_M}(\sigma_A) \;=\; 1-\frac{1}{\sqrt{2\pi}\sigma_A}\;\int_{-\infty}^{+\infty}\exp\left(-\frac{(\zeta-\frac{\sigma_A^2}{2})^2}{2\sigma_A^2}\right)\cdot\log_2\left[1+e^{-\zeta}\right]\mathrm{d}\zeta. \tag{3.15}$$

For notational simplicity and in order to highlight the dependence of I_{A_M} on σ_A, the following abbreviation is introduced [280, 281]

$$J(\sigma) \;:=\; I_{A_M}(\sigma_A=\sigma) \tag{3.16}$$

$$\lim_{\sigma\leftarrow 0} J(\sigma) \;=\; 0, \quad \lim_{\sigma\leftarrow\infty} J(\sigma) \;=\; 1, \qquad \sigma>0. \tag{3.17}$$

The function $J(\sigma)$ is monotonically increasing and therefore its inverse exists. Figure 3.3 shows a plot of $J(\sigma)$ as a function of σ. It was shown in [191] that the mutual information between the

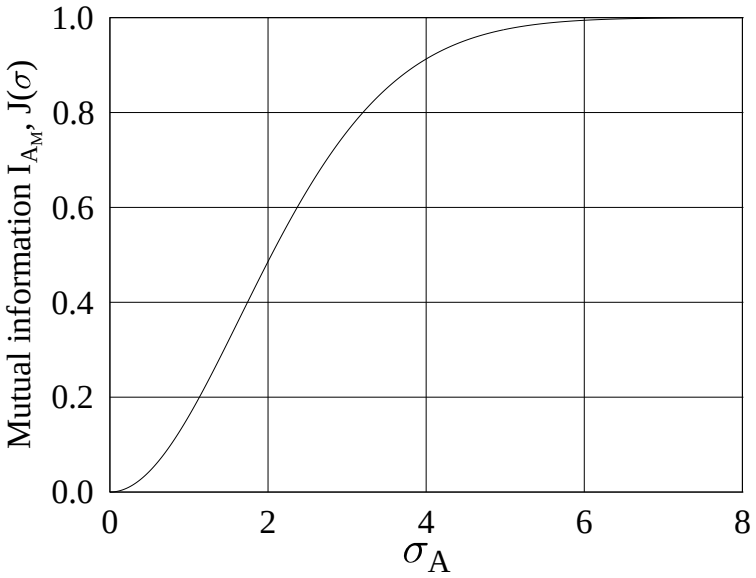

Figure 3.3: Mutual information I_{A_M} as a function of σ_A and evaluated from Equation (3.15).

equiprobable bits X and their respective LLRs L for *symmetric* and *consistent*[2] L-values always simplifies to

$$\begin{aligned} I(X;L) &= 1 - \int_{-\infty}^{+\infty} p(L|X=+1) \cdot \log_2\left[1+e^{-L}\right] \, \mathrm{d}L \\ I(X;L) &= 1 - E_{X=+1}\{\log_2\left[1+e^{-L}\right]\}. \end{aligned} \tag{3.18}$$

In order to quantify the information content of the extrinsic LLR values $L_{M,e}$ at the output of the demapper, the mutual information $I_{E_M} = I(X; L_{M,e})$ can be used, which is computed as in Equation (3.14) using the PDF p_E of the extrinsic output expressed as

$$I_{E_M} = \frac{1}{2} \cdot \sum_{x=-1,+1} \int_{-\infty}^{+\infty} p_E(\zeta|X=x) \cdot \log_2 \frac{2 \cdot p_E(\zeta|X=x)}{p_E(\zeta|X=-1) + p_E(\zeta|X=+1)} \, \mathrm{d}\zeta. \tag{3.19}$$

Considering I_{E_M} as a function of both I_{A_M} and the E_b/N_0 value encountered, the demapper's extrinsic information transfer characteristic is defined as [280, 281]

$$I_{E_M} = T_M(I_{A_M}, E_b/N_0). \tag{3.20}$$

[2]The LLR values are symmetric if their PDF is symmetric $p(-\zeta|X=+1) = p(\zeta|X=-1)$. Additionally, all LLR values with symmetric distributions satisfy the consistency condition [191]:

$$p(-\zeta|X=x) = e^{-x\zeta} p(\zeta|X=x).$$

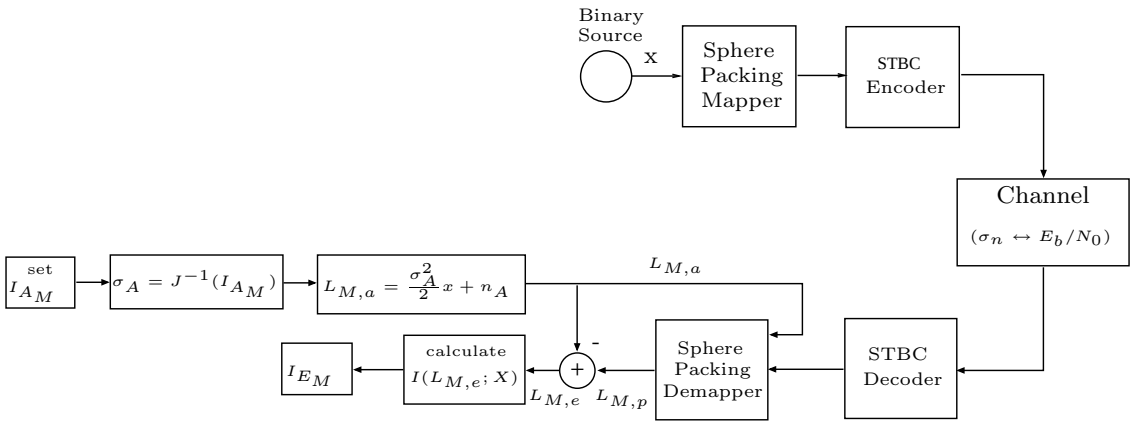

Figure 3.4: Evaluation of the demapper transfer characteristic.

Figure 3.4 illustrates how the EXIT characteristic $T_M(I_{A_M}, E_b/N_0)$ is calculated for a specific $(I_{A_M}, E_b/N_0)$-input combination. First the noise variance σ_n of the wireless channel is set according to the E_b/N_0 value considered. Then, σ_A is calculated based on the specific value of I_{A_M} where the EXIT curve has to be evaluated using $\sigma_A = J^{-1}(I_{A_M})$ expressed from Equation (3.16) and plotted in Figure 3.3. Next, σ_A is used for creating $L_{M,a}$ according to Equation (3.12), which is applied as the *a priori* input of the demapper. Finally, the mutual information of $I_{E_M} = I(X; L_{M,e})$, $0 \leq I_{E_M} \leq 1$, between the outer coded and interleaved bits x and the LLR values $L_{M,e}$ is calculated using Equation (3.19) with the aid of the PDF p_E of the extrinsic output $L_{M,e}$. This requires the determination of the distribution p_E by means of Monte Carlo simulations. However, according to [191], by invoking the ergodicity theorem in Equation (3.18), namely by replacing the expected value by the time average, the mutual information can be estimated using sufficiently large number of samples even for non-Gaussian or unknown distributions, which may be expressed as [191]

$$I(X; L_{M,e}) \;=\; 1 - E_{X=+1}\big\{ \log_2 \big[1 + e^{-L_{M,e}}\big] \big\} \;\approx\; 1 - \frac{1}{N} \sum_{n=1}^{N} \log_2 \big[1 + e^{-x(n) \cdot L_{M,e}(n)}\big]. \quad (3.21)$$

Figure 3.5 shows the extrinsic information transfer characteristics of the sphere-packing demapper in conjunction with $L = 16$ and different mapping schemes between the interleaver's output and the STBC encoder. As expected, Gray mapping does not provide any iteration gain upon increasing the mutual information at the input of the demapper. However, using a variety of different anti-Gray mapping ((AGM)) schemes [272] results in different extrinsic information transfer characteristics, as illustrated by the different slopes seen in Figure 3.5. The 10 different AGM mapping schemes shown in Figure 3.5 are specifically selected from all the possible mapping schemes for $L = 16$ in order to demonstrate the different extrinsic information transfer characteristics associated with different bit-to-symbol mapping schemes. There are a total of 16! different mapping schemes. Both the Gray mapping as well as the various AGM mapping schemes considered in this chapter are detailed in Appendix A.

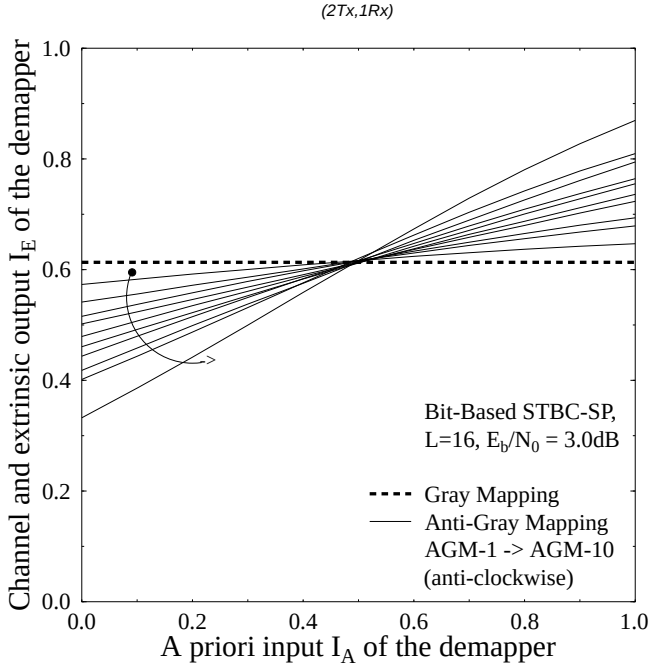

Figure 3.5: Sphere packing demapper extrinsic information transfer characteristics for different bits to sphere-packing symbol mapping schemes at $E_b/N_0 = 3.0$dB for $L = 16$.

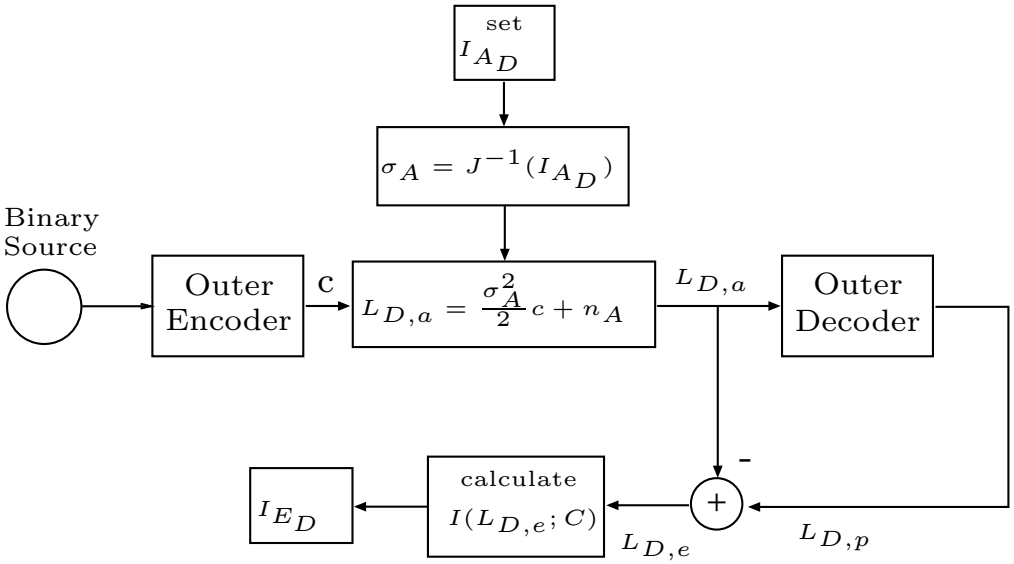

Figure 3.6: Evaluation of the outer channel decoder transfer characteristic.

Constraint Length $\mathcal{K}$	Generator Polynomials in Octals	
	G_r	G
3	05	07
4	15	17
5	35	23
6	53	75
7	133	171
8	247	371
9	561	753

Table 3.2: 1/2-rate RSC codes parameters.

3.4.2 Transfer Characteristics of the Outer Decoder

The extrinsic transfer characteristic of the outer channel decoder describes the relationship between the outer channel coded input $L_{D,a}$ and the outer channel decoded extrinsic output $L_{D,e}$. The input of the outer channel decoder consists only of the *a priori* input $L_{D,a}$ provided by the sphere-packing demapper. Therefore, the extrinsic information transfer characteristic of the outer channel decoder is independent of the E_b/N_0-value and hence may be written as

$$I_{E_D} \;=\; T_D(I_{A_D}), \tag{3.22}$$

where $I_{A_D} = I(C; L_{D,a})$, $0 \leq I_{A_D} \leq 1$, is the mutual information between the outer channel coded bits c and the LLR values $L_{D,a}$ and similarly $I_{E_D} = I(C; L_{D,e})$, $0 \leq I_{E_D} \leq 1$, is the mutual information between the outer channel coded bits c and the LLR values $L_{D,e}$. The computational model of evaluating the EXIT characteristics of the outer channel decoder is shown in Figure 3.6. As can be seen from the figure, the procedure is similar to that of the sphere-packing demapper shown in Figure 3.4, except that its value is independent of the signal-to-noise ratio. Again, $I_{E_D} = I(C; L_{D,e})$ can be computed either by evaluating the histogram approximation of p_E [280, 281] and then applying Equation (3.19) or, more conveniently, by the time averaging method [191] of Equation (3.21) as

$$I(C; L_{D,e}) \;=\; 1 - E\big\{\log_2\big[1 + e^{-L_{D,e}}\big]\big\} \;\approx\; 1 - \frac{1}{N}\sum_{n=1}^{N}\log_2\big[1 + e^{-c(n)\cdot L_{D,e}(n)}\big]. \tag{3.23}$$

The extrinsic transfer characteristics of several 1/2-rate RSC codes having different constraint lengths are shown in Figure 3.7. The generator polynomials employed are given in Table 3.2 in their octal representation, where G_r is the feedback polynomial and G is the feedforward polynomial. Figure 3.7 demonstrates that for $I_{A_D} > 0.5$, the set of RSC codes having higher constraint lengths converge faster upon increasing I_{A_D} than the RSC codes having smaller constraint lengths. This behaviour is due to the fact that the higher constraint-length RSC codes exhibit a better minimum free distance than shorter constraint-length RSC codes [6]. Similarly, Figure 3.8 illustrates the extrinsic transfer characteristics of a 1/2-rate binary LDPC code having an average column weight of 2.5 and using different numbers of internal LDPC iterations. As intuitively expected, the figure confirms that the extrinsic transfer characteristics of the LDPC decoder improve, as the number of internal LDPC iterations is increased.

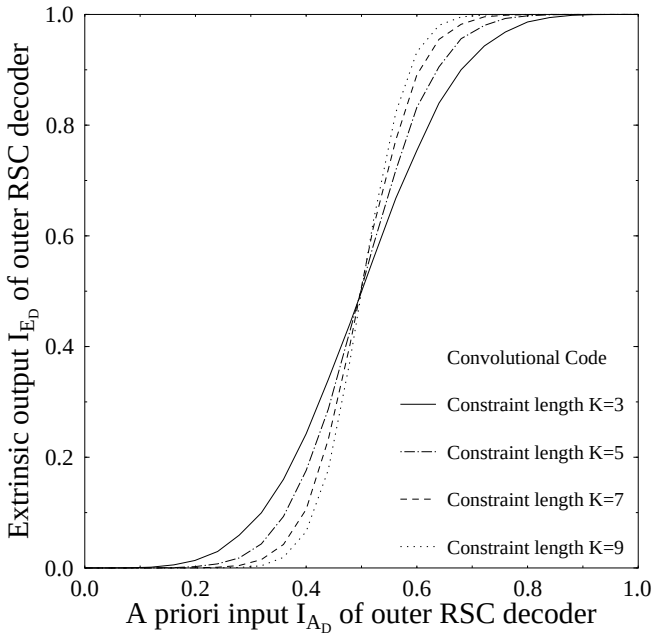

Figure 3.7: Extrinsic transfer characteristics of several 1/2-rate RSC codes having different constraint lengths.

3.4.3 Extrinsic Information Transfer Chart

The exchange of extrinsic information in the decoder schematics of Figures 3.1 and 3.2 is visualised by plotting the extrinsic information transfer characteristics of the sphere-packing demapper and outer channel decoder in a joint diagram. This diagram is known as the extrinsic information transfer ((EXIT)) chart [280, 281]. The outer channel decoder's extrinsic output I_{E_D} becomes the sphere-packing demapper's *a priori* input I_{A_M}, which is represented on the x-axis. Similarly, on the y-axis, the sphere-packing demapper's extrinsic output I_{E_M} becomes the outer channel decoder's *a priori* input I_{A_D}. Accordingly, the axes of Figures 3.7 and 3.8 are swapped intentionally for the sake of creating the EXIT chart as seen in Figures 3.9 and 3.10.

Figure 3.9 shows the EXIT chart of a turbo-detection channel-coded STBC-SP scheme employing anti-Gray mapping (AGM-9) of Figure 3.5 in combination with outer RSC code having constraint length $\mathcal{K} = 5$ when communicating over a correlated Rayleigh fading channel having $f_D = 0.1$. Ideally, in order for the exchange of extrinsic information between the sphere-packing demapper and the outer RSC decoder to converge at a specific E_b/N_0 value, the extrinsic transfer characteristic curve of the sphere-packing demapper at the E_b/N_0 value of interest and the extrinsic transfer characteristic curve of the outer RSC decoder should only intersect at the $(1.0, 1.0)$ point. If this condition is satisfied, then a so-called *convergence tunnel* [280, 281] appears on the EXIT chart. The narrower the tunnel, the more iterations are required to reach the $(1.0, 1.0)$ point. If the two extrinsic transfer characteristic curves, however, intersect at a point infinitesimally close to the $I_{E_D} = 1.0$ line rather than at the $(1.0, 1.0)$ point, then a moderately low BER could be still achieved, but the BER will not become as low as in the schemes, when the intersection is at the $(1.0, 1.0)$ point. These type of tunnels are referred to here as *semi-convergent tunnels*. Observe in Figure 3.9 that a semi-convergent tunnel exists at $E_b/N_0 = 2.5$dB. This implies that according

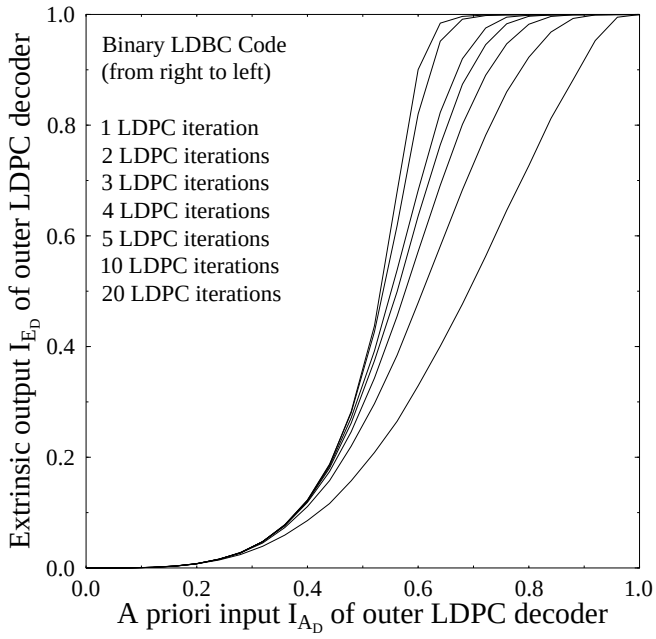

Figure 3.8: Extrinsic transfer characteristics of a 1/2-rate binary LDPC code having an average column weight of 2.5 and using different numbers of LDPC internal iterations.

to the predictions of the EXIT chart seen in Figure 3.9, the iterative decoding process is expected to converge to a moderately low BER at $E_b/N_0 = 2.5$dB. The validity of this prediction is, however, dependent on how accurately the two EXIT chart assumptions outlined at the beginning of Section 3.4 are satisfied. These EXIT chart based convergence predictions are usually verified by the actual iterative decoding trajectory, as it will be discussed in Section 3.5. Similarly, the EXIT chart of the turbo-detected channel-coded STBC-SP scheme of Figure 3.2 employing the anti-Gray mapping (AGM-6) scheme of Figure 3.5 in combination with a binary outer LDPC code having an average column weight of 2.5 and using 10 internal LDPC iterations is portrayed in Figure 3.10 when communicating over an SPSI correlated Rayleigh fading channel having $f_D = 0.1$. According to the figure, iterative decoding convergence tending to moderately low BER values becomes possible for $E_b/N_0 > 2.0$dB for this particular system arrangement, as a semi-convergent tunnel is beginning to take shape upon increasing the signal-to-noise ratio beyond $E_b/N_0 = 2.0$dB.

Appendix B provides the complete list of EXIT charts for the bit-based turbo-detected STBC-SP schemes of Figures 3.1 and 3.2, when employing the mapping schemes of Figure 3.5 in combination with outer RSC and binary LDPC codes.

3.5 Performance of Turbo-Detected Bit-Based STBC-SP Schemes

Without loss of generality, we considered a sphere packing modulation scheme associated with $L = 16$ using two transmit and a single receiver antenna in order to demonstrate the performance improvements achieved by the proposed system. All simulation parameters are listed in Table 3.3.

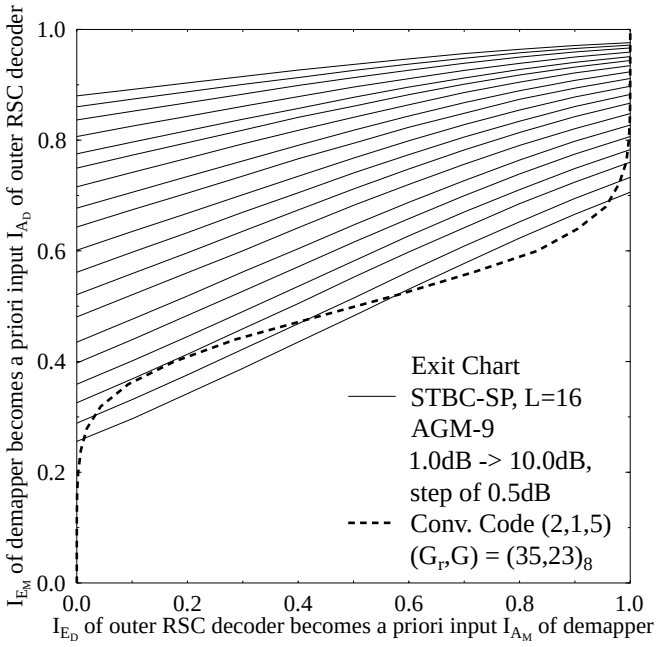

Figure 3.9: EXIT chart of a turbo-detected RSC channel-coded STBC-SP scheme employing anti-Gray mapping (AGM-9) of Figure 3.5 in combination with outer RSC code having constraint length $\mathcal{K} = 5$ when communicating over a correlated Rayleigh fading channel having $f_D = 0.1$.

3.5.1 Performance of RSC-coded STBC-SP Scheme

3.5.1.1 Mutual Information and Achievable BER

Observe in the EXIT charts provided in Appendix B.1 that once a semi-convergent tunnel is formed, the intersection point of the extrinsic transfer characteristic curves of the sphere-packing demapper and the outer RSC decoder slides gradually towards the $(1.0, 1.0)$ point upon increasing the signal-to-noise ratio. In order to investigate how the position of the intersection point affects the BER performance, Figure 3.11 shows the achievable BER as a function of the mutual information I_{E_D} at the output of the RSC decoder for different constraint lengths. According to Figure 3.11, the intersection point should be at least at $I_{E_D} = 0.985$ in order to achieve a BER of 10^{-3}, which is independent of the RSC code's constraint length. This is true because Figure 3.11 relates the mutual information at the *output* of the RSC decoder to the achievable BER. Figure 3.12, however, relates the mutual information at the *input* of the RSC decoder to the achievable BER. The effect of the code's constraint length becomes evident in Figure 3.12, since RSC codes having higher constraint lengths require lower I_{A_D} values in order to achieve a similar BER. Table 3.4 summarises the I_{A_D} values required for achieving BER of 10^{-4} at the input of the RSC decoders of Table 3.2.

It was reported in [272] that there is a strong correlation between the average bit-wise capacity computed using no a priori information, which corresponds to the unconditional average bit-wise mutual information I_0 of the symbol constellation and the achievable BER performance when iterative demapping and turbo detection are employed. The achievable performance depends on the specific assignment of the bits to each symbol in the constellation. In other words, the achievable

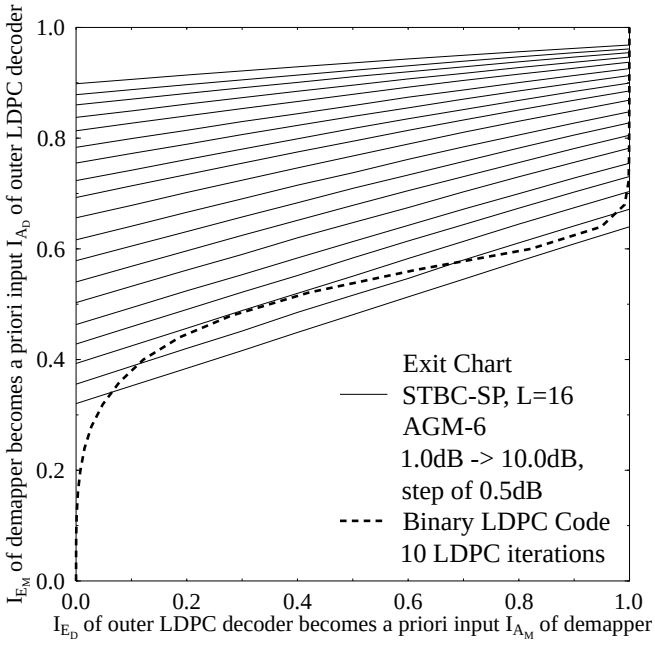

Figure 3.10: EXIT chart of a turbo-detected binary LDPC channel-coded STBC-SP scheme employing anti-Gray mapping (AGM-6) of Figure 3.5 in combination with outer binary LDPC code having an average column weight of 2.5 and using 10 internal LDPC iterations when communicating over a correlated Rayleigh fading channel having $f_D = 0.1$.

performance depends on the mapping scheme. Different STBC-SP mapping schemes spanning a wide range of different I_0 values were investigated in Figure 3.13 for the sake of demonstrating this phenomenon. Figure 3.13 characterises the achievable BER performance against the unconditional bit-wise mutual information I_0 for different STBC-SP mappings at $E_b/N_0 = 4.0$dB in conjunction with $L = 16$ and an outer RSC code having a constraint length of $\mathcal{K} = 5$, when employing the system parameters outlined in Table 3.3 and using an interleaver depth of $\mathcal{D} = 4000$ bits. The unconditional average bit-wise mutual information I_0 of a specific mapping scheme at a particular channel condition can be computed using the model in Figure 3.4 when $I_{A_M} = 0$. Figure 3.13 also confirms the interesting fact stated in [272] that the choice of the optimum bits-to-symbol mapping scheme is dependent on the number of iterations used. For example, at $E_b/N_0 = 4.0$dB Gray mapping is the optimum scheme when no iteration is used at $I_0 = 0.68$. Additionally, as shown in Figure 3.13, the bits-to-symbol mapping scheme associated with $I_0 = 0.54$ at $E_b/N_0 = 4.0$dB is the optimum mapping, when three or more iterations are employed. These observations are only valid for the specific RSC code under consideration. Other RSC codes are usually associated with different optimum mapping schemes, as illustrated by the EXIT charts seen in Appendix B.1.

3.5.1.2 Decoding Trajectory and Effect of Interleaver Depth

Figure 3.14 illustrates the actual decoding trajectory of the turbo-detected RSC channel-coded STBC-SP scheme of Figure 3.9 at $E_b/N_0 = 2.5$dB and using an interleaver depth of $\mathcal{D} = 10^6$ bits. The zigzag-path in Figure 3.14 represents the actual extrinsic information transfer between the sphere-packing demapper and the outer RSC channel decoder. Since a long interleaver is

Modulation	Sphere Packing with $L = 16$
Number of transmitters	2
Number of receivers	1
Channel type	SPSI Correlated Rayleigh Fading
Normalised Doppler frequency	0.1
RSC code rate	0.5
Average LDPC column weight	2.5
LDPC code rate	0.5
LDPC decoding field	$GF(2)$
System throughput	1 bit/symbol

Table 3.3: Bit-based system parameters.

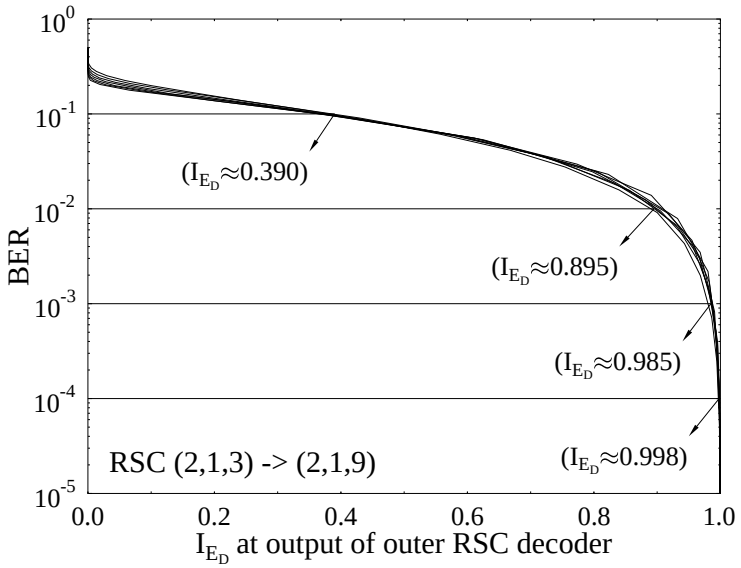

Figure 3.11: Bit error rate of different 1/2-rate RSC decoders versus their extrinsic output I_{E_D}, when increasing the code's constraint length from $\mathcal{K} = 3$ to $\mathcal{K} = 9$.

Constraint length	Required I_{A_D}
3	0.863
4	0.832
5	0.813
6	0.783
7	0.764
8	0.731
9	0.710

Table 3.4: Required I_{A_D} at the input of the RSC decoders of Table 3.2 for achieving BER of 10^{-4}.

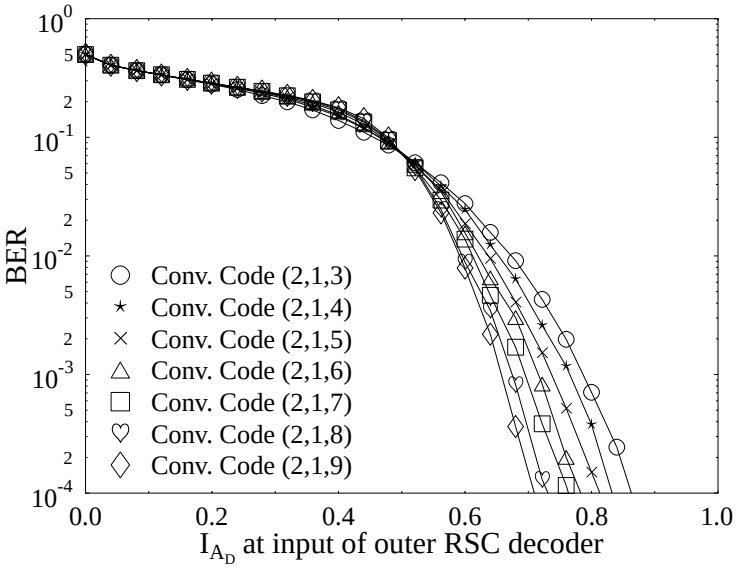

Figure 3.12: Bit error rate of different 1/2-rate RSC decoders versus their *a priori* input I_{A_D}.

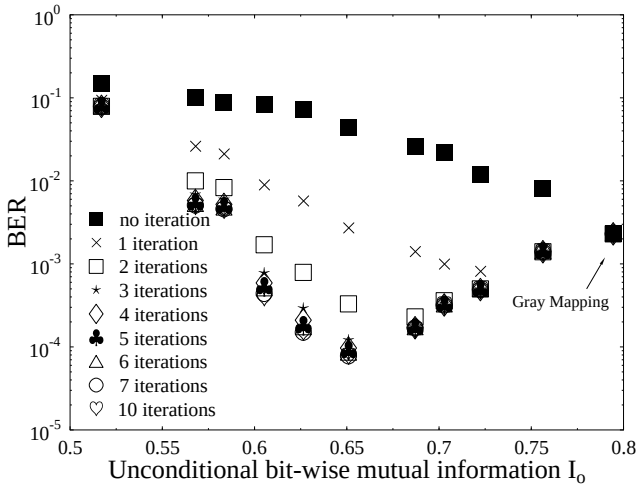

Figure 3.13: BER versus unconditional bit-wise mutual information I_0 between 0.4205 and 0.6785 for different STBC-SP mappings at $E_b/N_0 = 4.0$dB in conjunction with $L = 16$, when employing the system parameters outlined in Table 3.3 and using an interleaver depth of $\mathcal{D} = 4000$ bits.

employed, the assumptions outlined at the beginning of Section 3.4 are justified and hence the EXIT chart prediction has been attained. However, the decoding trajectories shown in Figures 3.15 and 3.16 are different from the EXIT chart prediction because shorter interleaver lengths are used. The achievable I_{E_D} when employing different interleaver lengths is demonstrated in Figure 3.17. The BER of the schemes of Figure 3.17 is shown in Figure 3.18 when using 10 external joint iterations where the difference in the achievable BER at $E_b/N_0 = 2.5$dB is evident when increasing the interleaver length to $\mathcal{D} = 10^6$ bits. Additionally, observe the turbo cliff at $E_b/N_0 = 2.5$dB upon increasing the interleaver length.

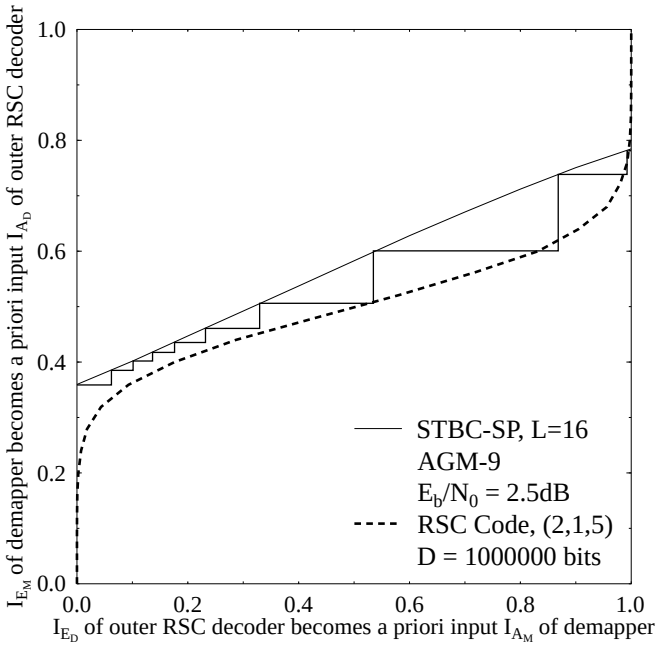

Figure 3.14: Decoding trajectory of turbo-detected RSC channel-coded STBC-SP scheme employing anti-Gray mapping (AGM-9) in combination with the outer RSC code (2,1,5) and the system parameters outlined in Table 3.3 and operating at $E_b/N_0 = 2.5$dB with an interleaver depth of $\mathcal{D} = 10^6$ bits.

3.5.1.3 BER Performance

Figure 3.19 compares the performance of the proposed convolutional-coded STBC-SP scheme employing anti-Gray mapping (AGM-9) and Gray mapping ((GM)) against that of an identical-throughput 1 Bit Per Symbol (1BPS) uncoded STBC-SP scheme and a conventional orthogonal STBC design as well as against an RSC-coded QPSK modulated STBC scheme, when employing the system parameters outlined in Table 3.3 and using an interleaver depth of $\mathcal{D} = 10^6$ bits. The QPSK modulated STBC system employs a set-partitioning mapping scheme reminiscent of trellis coded modulation ((TCM)) [288]. Observe in Figure 3.19 by comparing the two Gray mapping (GM) STBC-SP curves that no BER improvement was obtained, when 10 turbo-detection iterations were employed in conjunction with Gray mapping, which was reported also in [272] and evident from the flat curve of the Gray mapping in Figure 3.5. By contrast, anti-Gray mapping (AGM-9) achieved a useful performance improvement in conjunction with iterative demapping and decod-

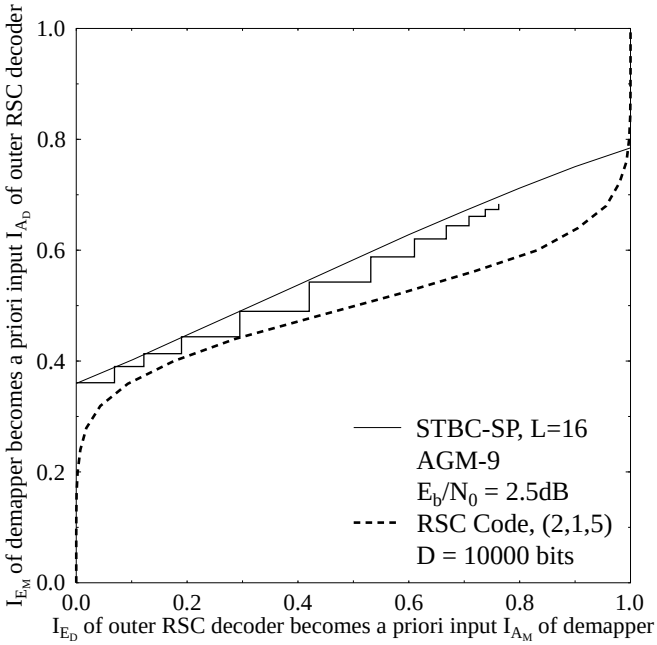

Figure 3.15: Decoding trajectory of turbo-detected RSC channel-coded STBC-SP scheme employing anti-Gray mapping (AGM-9) in combination with the outer RSC code (2,1,5) and the system parameters outlined in Table 3.3 and operating at $E_b/N_0 = 2.5$dB with an interleaver depth of $\mathcal{D} = 10^4$ bits.

ing. Explicitly, Figure 3.19 demonstrates that a coding advantage of about 20.2dB was achieved at a BER of 10^{-5} after 10 iterations by the convolutional-coded AGM-9 STBC-SP system over both the uncoded STBC-SP [190] and the conventional orthogonal STBC design based [215, 216] schemes for transmission over the correlated Rayleigh fading channel considered. Additionally, coding advantages of approximately 3.2 dB and 2.0 dB were attained over the 1BPS-throughput RSC-coded GM STBC-SP and the RSC-coded QPSK modulated STBC schemes, respectively.

Figure 3.20 demonstrates the attainable performance of various AGM based RSC-coded STBC-SP schemes in conjunction with $L = 16$, when employing the system parameters outlined in Table 3.3 and using an interleaver depth of $\mathcal{D} = 10^6$ bits after 10 iterations. Observe in Figure 3.20 that the three schemes perform differently. For example, the AGM-7 based scheme exhibits a turbo cliff at a lower E_b/N_0 value than the others, when combined with the specific RSC code having the octal generator polynomials of $(G_r, G) = (35, 23)_8$. However, the AGM-7 based scheme has the highest BER floor. Therefore, different AGM schemes may be combined with specific RSC codes for the sake of designing systems satisfying specific criteria, such as for example attaining an early convergence or a lower BER floor. The EXIT charts of the three different schemes seen in Figure 3.20 are illustrated in Figure 3.21.

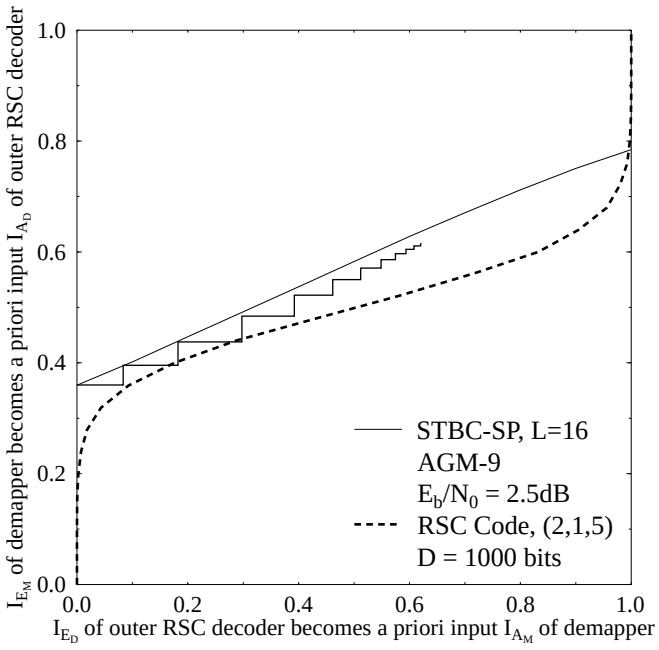

Figure 3.16: Decoding trajectory of turbo-detected RSC channel-coded STBC-SP scheme employing anti-Gray mapping (AGM-9) in combination with the outer RSC code (2,1,5) and the system parameters outlined in Table 3.3 and operating at $E_b/N_0 = 2.5$dB with an interleaver depth of $\mathcal{D} = 10^3$ bits.

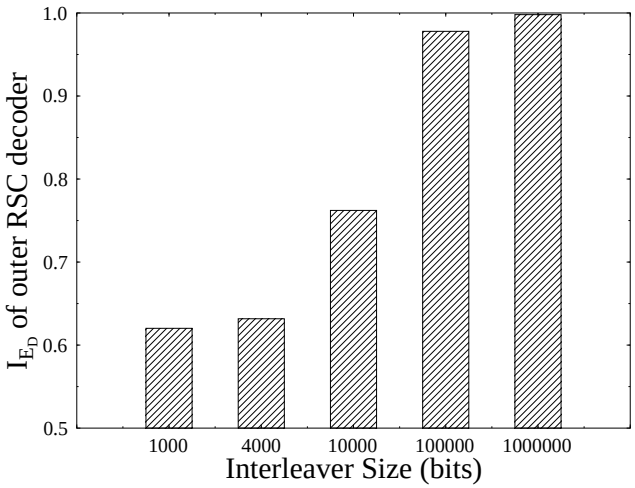

Figure 3.17: Achievable extrinsic information of turbo-detected RSC channel-coded STBC-SP scheme employing anti-Gray mapping (AGM-9) in combination with the outer RSC code (2,1,5) and the system parameters outlined in Table 3.3 and operating at $E_b/N_0 = 2.5$dB with different interleaver depths.

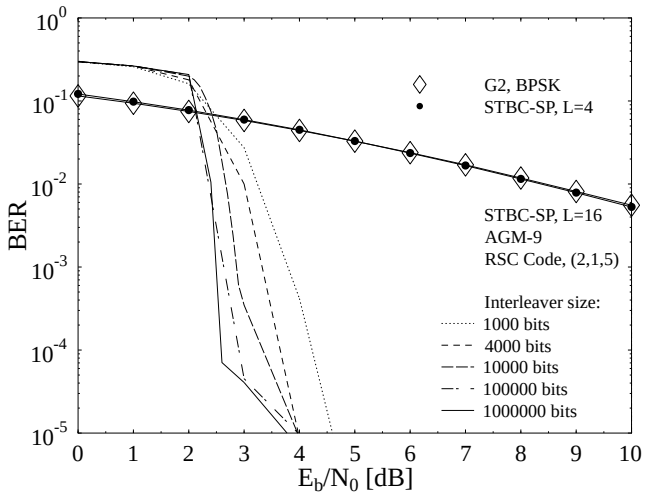

Figure 3.18: Performance comparison of anti-Gray mapping (AGM-9) based RSC-coded STBC-SP schemes in conjunction with $L = 16$ against an identical-throughput 1 bit/symbol (BPS) uncoded STBC-SP scheme using $L = 4$ and against Alamouti's conventional G_2-BPSK scheme, when employing the system parameters outlined in Table 3.3 and using different interleaver depths after 10 external joint iterations.

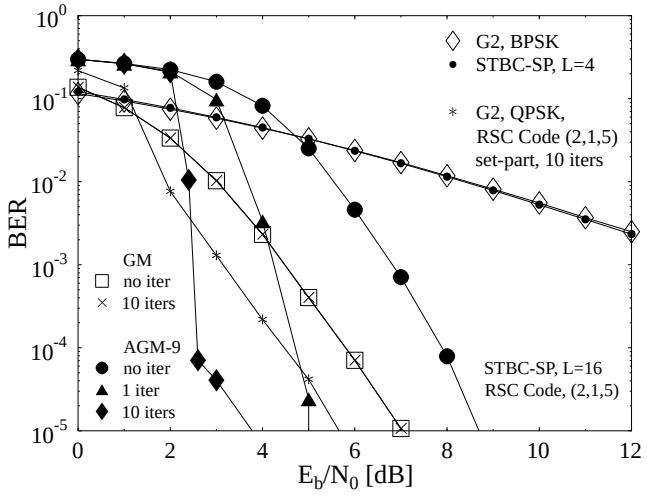

Figure 3.19: Performance comparison of anti-Gray mapping (AGM-9) and Gray mapping (GM) based RSC-coded STBC-SP schemes in conjunction with $L = 16$ against an identical-throughput 1 bit/symbol (BPS) uncoded STBC-SP scheme using $L = 4$ and against Alamouti's conventional G_2-BPSK scheme as well as against an RSC-coded QPSK modulated STBC scheme, when employing the system parameters outlined in Table 3.3 and using an interleaver depth of $\mathcal{D} = 10^6$ bits.

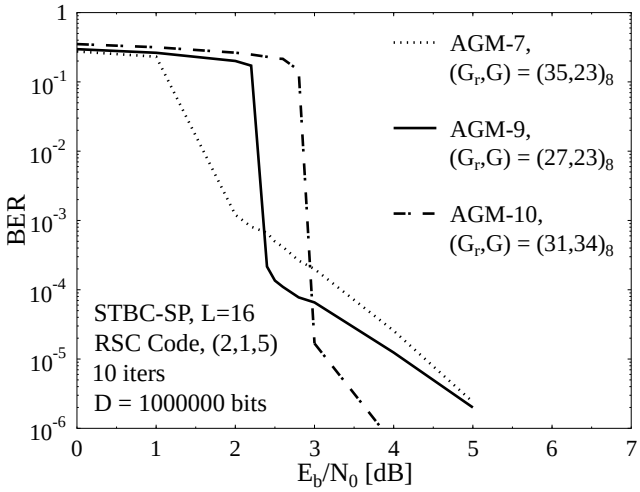

Figure 3.20: Performance comparison of various AGM based RSC-coded STBC-SP schemes in conjunction with $L = 16$, when employing the system parameters outlined in Table 3.3 and using an interleaver depth of $\mathcal{D} = 10^6$ bits.

Number of internal LDPC iterations	Required I_{A_D}
1	0.970
2	0.913
3	0.863
4	0.826
5	0.800
10	0.723
20	0.708

Table 3.5: Required I_{A_D} for achieving BER of 10^{-4} when performing different number of internal LDPC iterations.

3.5.2 Performance of Binary LDPC-coded STBC-SP scheme

3.5.2.1 Mutual Information and Achievable BER

Figure 3.22 shows the achievable BER as a function of the mutual information I_{A_D} at the input of the binary LDPC decoder, when performing different number of internal LDPC iterations. According to Figure 3.22, a mutual information of about $I_{A_D} = 0.97$ has to be forwarded to the binary LDPC decoder in order to achieve a BER of 10^{-4}, when performing *one* internal LDPC iteration. However, this requirement drops to about $I_{A_D} = 0.8$ and $I_{A_D} = 0.7$, when performing $five$ and 20 internal LDPC iterations, respectively. Table 3.5 summarises the I_{A_D} values at the input of the binary LDPC decoder required for achieving BER of 10^{-4}, when performing different number of internal LDPC iterations.

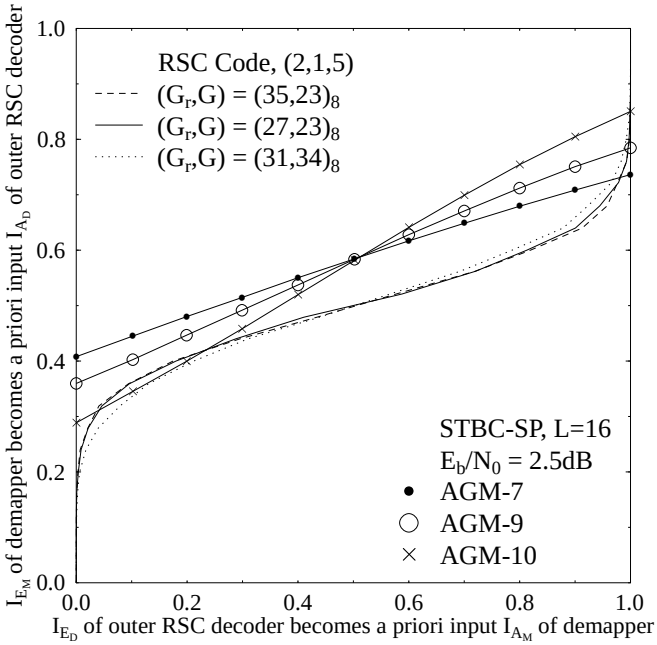

Figure 3.21: EXIT chart of turbo-detected RSC-coded STBC-SP systems employing various AGM schemes from Figure 3.5 in combination with outer RSC codes having constraint length $\mathcal{K} = 5$ and different generator polynomials, when employing the system parameters outlined in Table 3.3.

3.5.2.2 Decoding Trajectory and Effect of Interleaver Depth

Figure 3.23 illustrates the decoding trajectory of the turbo-detected binary LDPC channel-coded STBC-SP scheme employing anti-Gray mapping (AGM-6) in combination with a 1/2-rate outer binary LDPC code having an average column weight of 2.5 and using 10 internal LDPC iterations, when communicating over the channel outlined in Table 3.3 and operating at $E_b/N_0 = 2.5$dB after 10 joint external iterations. The actual iterative performance is different from the prediction of the EXIT chart, since a short interleaver depth of $\mathcal{D} = 1500$ bits is employed, which does not guarantee that the LLR values have a Gaussian distribution. Figure 3.24 shows our performance comparison of the anti-Gray mapping (AGM-6) and Gray mapping (GM) based LDPC-coded STBC-SP scheme in conjunction with $L = 16$ against an identical-throughput 1 bit/symbol (BPS) uncoded STBC-SP scheme using $L = 4$ and against Alamouti's conventional G_2-BPSK scheme, when communicating over the channel outlined in Table 3.3 and using an outer 1/2-rate binary LDPC code having an average column weight of 2.5 as well as 10 internal LDPC iterations. Figure 3.24 demonstrates that a coding gain of about 19.3dB is attained by the LDPC-coded STBC-SP scheme after 10 joint external iterations against both the identical-throughput uncoded STBC-SP scheme and Alamouti's conventional G_2-BPSK scheme, when using an output block length of $\mathcal{D} = 1500$ bits. However, a better performance is predicted by the EXIT chart seen in Figure 3.10, where a semi-convergent tunnel exits at $E_b/N_0 = 2.5$dB and hence a lower BER could be attained upon increasing the output block length or, equivalently, the interleaver length. Figure 3.25 shows the decoding trajectory of the turbo-detected binary LDPC channel-coded STBC-SP scheme of Figures 3.23 and 3.24, when using an increased output block length of $K_{ldpc} = 10000$ bits. It is evident from Figure

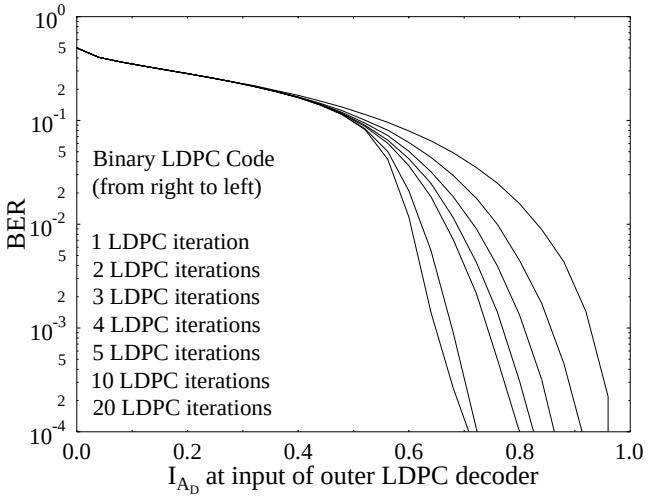

Figure 3.22: Bit error rate of a 1/2-rate binary LDPC decoder versus *a priori* input I_{A_D} when employing different number of internal LDPC iterations.

3.25 that an improved performance is achieved, when employing a larger interleaver length, which is also demonstrated by the BER curves in Figure 3.26. According to Figure 3.26, a coding gain of about 21.2dB is attained by the LDPC-coded STBC-SP scheme after 10 joint external iterations against both the identical-throughput uncoded STBC-SP scheme and Alamouti's conventional G_2-BPSK scheme, when using an output block length of $K_{ldpc} = 10000$ bits. Additionally, a coding advantage of approximately 1.8dB was attained over the 1BPS-throughput LDPC-coded GM STBC-SP scheme.

3.5.2.3 Effect of Internal LDPC Iterations and Joint External Iterations

In order to investigate the effects of performing different number of internal LDPC iterations and joint external iterations on the performance of the binary LDPC-coded STBC-SP scheme of Figure 3.2, Figure 3.27 demonstrates the achievable coding gain for different combinations of internal and external iterations. More specifically, Figure 3.27 shows the achievable coding gain of a bit-based binary LDPC-coded STBC-SP scheme employing AGM-6 in conjunction with different combinations of joint and LDPC iterations as compared to the identical-throughput 1BPS uncoded STBC-SP scheme of [190] and Alamouti's conventional G_2-BPSK scheme [215] at a BER of 10^{-5}, when communicating over the channel outlined in Table 3.3 and using a 1/2-rate outer binary LDPC code having an output block length of 1500 bits. The terms "0 joint iteration" and "no joint iterations", used in Figure 3.27 and subsequent figures, refer to the open-loop scenario, where no extrinsic information is fed back from the outer decoder to the sphere packing demapper). Observe in Figure 3.27 that for a specific fixed number of internal LDPC iterations, the attainable coding gain improvement becomes negligible after carrying out *two* joint external iterations. In other words, most of the BER improvements are achieved during the first two iterations. This observation is illustrated in both Figure 3.28 and Figure 3.29, which show the performance improvement attained upon increasing the number of joint external iterations, while fixing the number of internal LDPC iterations to *one* and $five$ iterations, respectively. The effect of increasing the number of internal LDPC iterations, while fixing the number of joint external iterations can also be observed from Figure 3.27, which demonstrates that the coding gain improvements become negligible after encountering $five$ internal LDPC iterations. Figure 3.30 and Figure 3.31 illustrate the effect of

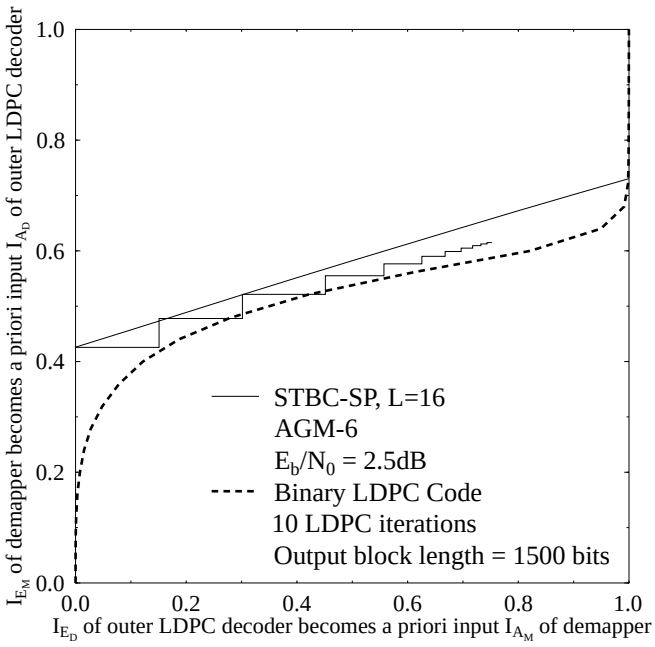

Figure 3.23: Decoding trajectory of turbo-detected binary LDPC channel-coded STBC-SP scheme employing anti-Gray mapping (AGM-6) in combination with outer 1/2-rate binary LDPC code and system parameters of Table 3.3 when using 10 internal LDPC iterations and operating at $E_b/N_0 = 2.5$dB after 10 joint external iterations.

increasing the number of internal LDPC iterations on the performance of the bit-based binary LDPC-coded STBC-SP scheme, while fixing the number of joint external iterations to *one* and $five$ iterations, respectively.

3.6 Chapter Conclusion

In this chapter, we proposed a novel system that exploits the advantages of both iterative demapping and turbo detection [272] as well as those of the STBC-SP scheme of [190]. Our investigations demonstrated that significant performance improvements may be achieved, when the AGM STBC-SP is combined with outer channel decoding and iterative demapping as compared to the Gray-mapping based systems. Subsequently, the EXIT chart was used to search for bits-to-symbol mapping schemes that converge at lower E_b/N_0 values. Several STBC-SP mapping schemes covering a wide range of extrinsic transfer characteristics were investigated. When using an appropriate bits-to-symbol mapping scheme and 10 turbo detection iterations, gains of about 20.4dB and 21.2dB at a BER of 10^{-5} were obtained by the convolutional-coded and LDPC-coded STBC-SP schemes, respectively, over the identical-throughput 1 bit/symbol uncoded STBC-SP benchmarker scheme [190]. Additionally, coding advantages of approximately 3.2dB and 2.0dB a BER of 10^{-5} were attained over the 1BPS-throughput RSC-coded GM STBC-SP and the RSC-coded QPSK modulated STBC schemes, respectively.

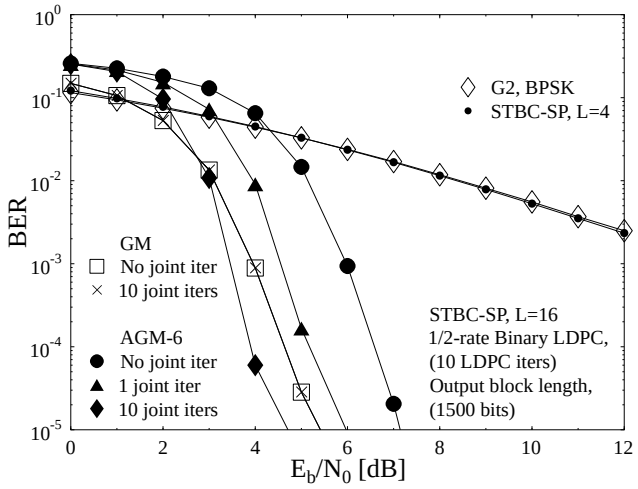

Figure 3.24: Performance comparison of anti-Gray mapping (AGM-6) and Gray mapping (GM) based LDPC-coded STBC-SP schemes in conjunction with $L = 16$ against an identical-throughput 1 bit/symbol (BPS) uncoded STBC-SP scheme using $L = 4$ and against Alamouti's conventional G_2-BPSK scheme, when employing system parameters of Table 3.3 and using an outer 1/2-rate binary LDPC code having an average column weight of 2.5 and 10 internal LDPC iterations.

3.7 Chapter Summary

In this chapter, two realisations of a novel bit-based iterative-detection aided STBC-SP scheme were presented, namely an RSC-coded turbo-detected STBC-SP scheme and a binary LDPC-coded turbo-detected STBC-SP arrangement. Our system overview was provided in Section 3.2. The LDPC-coded scheme of Figure 3.2 did not require channel interleaving, since the LDPC parity check matrix is randomly constructed, where each of the parity check equations is checking several random bit positions in a codeword, which has a similar effect to that of the channel interleaver. In Section 3.3, we showed how the STBC-SP demapper was modified for exploiting the *a priori* knowledge provided by the channel decoder, which is essential for the employment of iterative demapping and decoding.

EXIT chart analysis was invoked in Section 3.4 in order to study and design the turbo-detected schemes proposed in Section 3.2. Measuring the demapper's EXIT characteristics was explained in Section 3.4.1 and in Figure 3.4. We proposed 10 different anti-Gray mapping (AGM) schemes in Figure 3.5 that are specifically selected from all the possible mapping schemes for $L = 16$ in order to demonstrate the different extrinsic information transfer characteristics associated with different bit-to-symbol mapping schemes. Both the Gray mapping as well as the various AGM mapping schemes considered in this chapter are detailed in Appendix A. In Section 3.4.2, we discussed how the EXIT characteristics of an outer decoder in a serially concatenated scheme may be calculated. Figure 3.6 summarises the calculation process.

The performance of the turbo-detected bit-based STBC-SP schemes was presented in Section 3.5. Firstly, we considered the performance of the RSC-coded turbo-detected STBC-SP scheme in Section 3.5.1. The relation between the achievable BER and the mutual information at the input as well as at the output of the outer RSC decoder was discussed in Section 3.5.1.1. The predictions of our EXIT chart analysis outlined in Section 3.4.3 were verified by generating the actual decoding trajectories in Section 3.5.1.2. The effect of interleaver depth was also addressed in Section 3.5.1.2,

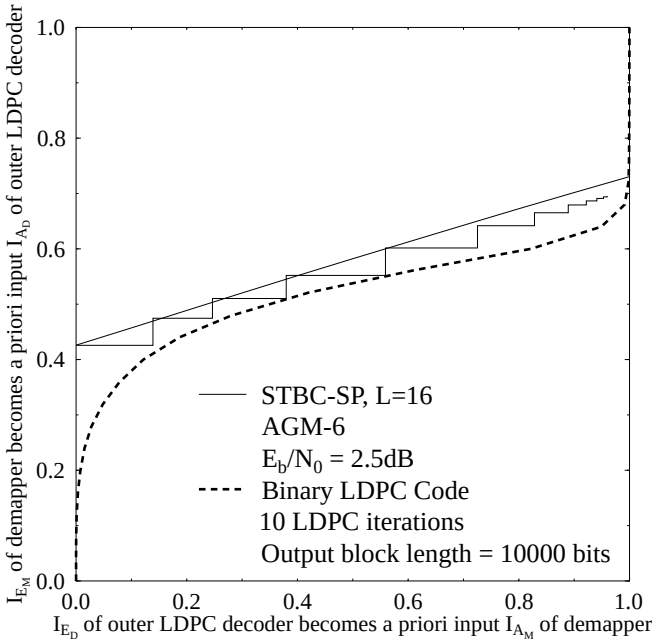

Figure 3.25: Decoding trajectory of turbo-detected binary LDPC channel-coded STBC-SP scheme employing anti-Gray mapping (AGM-6) in combination with outer 1/2-rate binary LDPC code and system parameters of Table 3.3 when using 10 internal LDPC iterations and operating at $E_b/N_0 = 2.5$dB after 10 joint external iterations.

since matching the predictions of the EXIT chart analysis is only guaranteed, when employing large interleaver depths. The BER performance of the proposed RSC-coded STBC-SP scheme was compared in Section 3.5.1.3 to that of an uncoded STBC-SP scheme [190] and to that of an RSC-coded conventionally modulated STBC scheme. Secondly, we considered the performance of the LDPC-coded turbo-detected STBC-SP scheme in Section 3.5.2. The relation between the achievable BER and the mutual information at the input of the outer LDPC decoder was discussed in Section 3.5.2.1 and Figure 3.22. The effect of the LDPC output block length K_{ldpc} on the achievable performance was investigated in Section 3.5.2.2, while the effect of internal LDPC iterations and joint external iterations was studied in Section 3.5.2.3.

In this chapter, we assumed that the channel state information is perfectly known at the receiver. This, however, requires sophisticated channel estimation techniques, which imposes excess cost and complexity. In the next chapter, we consider the design of various sphere packing modulated differential STBC schemes that require no channel estimation.

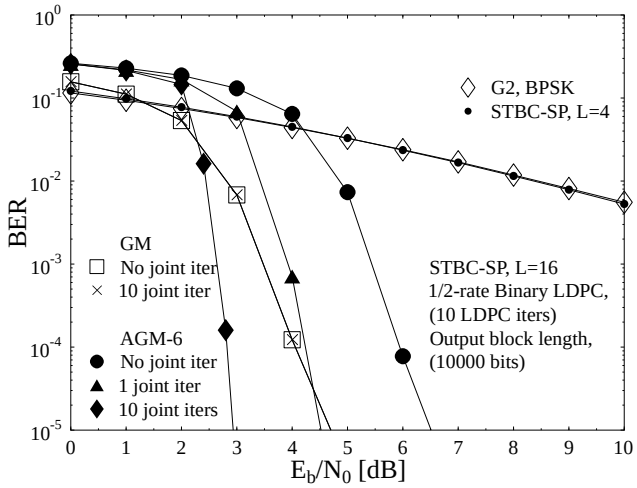

Figure 3.26: Performance comparison of anti-Gray mapping (AGM-6) and Gray mapping (GM) based LDPC-coded STBC-SP schemes in conjunction with $L = 16$ against an identical-throughput 1 bit/symbol (BPS) uncoded STBC-SP scheme using $L = 4$ and against Alamouti's conventional G_2-BPSK scheme, when employing system parameters of Table 3.3 and using an outer 1/2-rate binary LDPC code having an average column weight of 2.5 and 10 internal LDPC iterations.

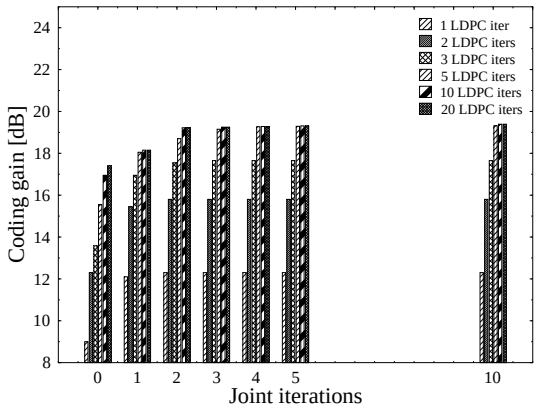

Figure 3.27: Coding gain of a bit-based binary LDPC-coded STBC-SP scheme employing AGM-6 in conjunction with different combinations of joint and LDPC iterations as compared to the identical-throughput 1BPS uncoded STBC-SP scheme of [190] and Alamouti's conventional G_2-BPSK scheme [215] at a BER of 10^{-5}, when communicating over the channel outlined in Table 3.3 and using an outer 1/2-rate binary LDPC code having an output block length of 1500 bits.

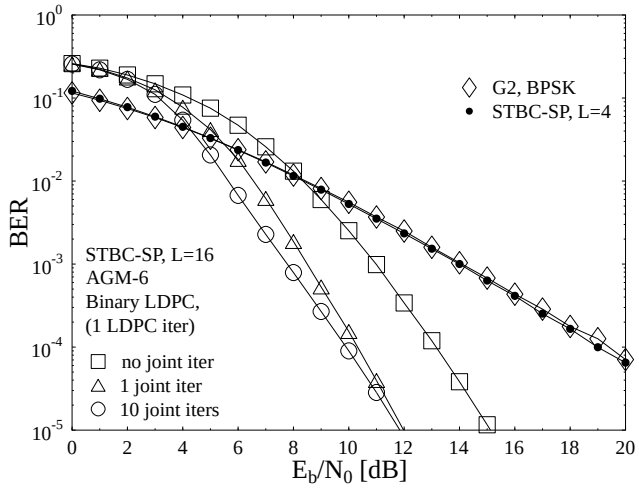

Figure 3.28: Performance of anti-Gray mapping (AGM-6) based LDPC-coded STBC-SP schemes in conjunction with $L = 16$, when employing system parameters of Table 3.3 and using an outer 1/2-rate binary LDPC code having an output block length of 1500 bits and *one* internal LDPC iteration.

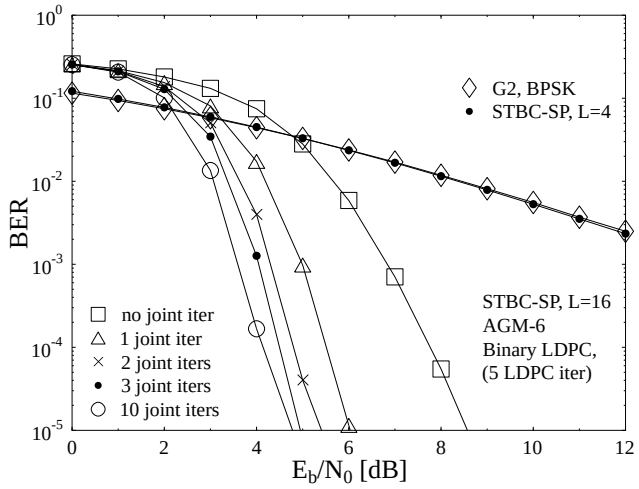

Figure 3.29: Performance of anti-Gray mapping (AGM-6) based LDPC-coded STBC-SP schemes in conjunction with $L = 16$, when employing system parameters of Table 3.3 and using an outer 1/2-rate binary LDPC code having an output block length of 1500 bits and $five$ internal LDPC iterations.

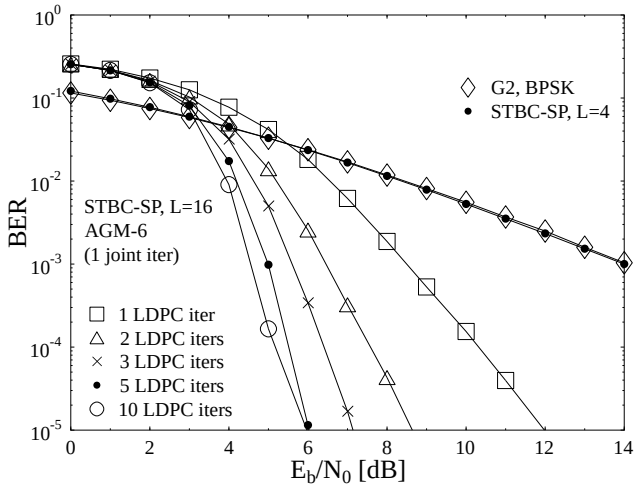

Figure 3.30: Performance of anti-Gray mapping (AGM-6) based LDPC-coded STBC-SP schemes in conjunction with $L = 16$, when employing system parameters of Table 3.3 and using an outer 1/2-rate binary LDPC code having an output block length of 1500 bits and *one* joint external iteration.

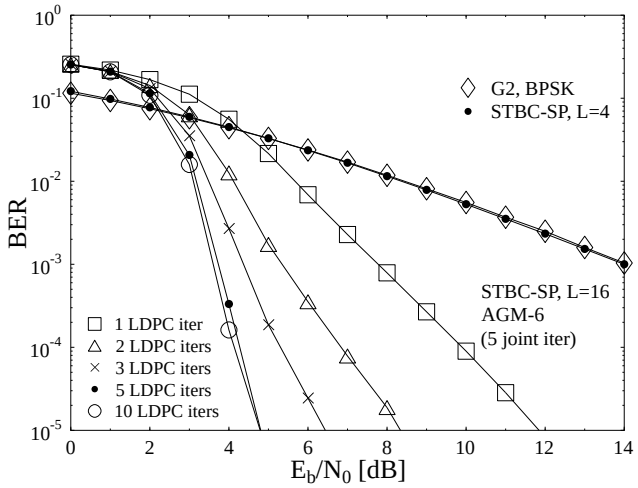

Figure 3.31: Performance of anti-Gray mapping (AGM-6) based LDPC-coded STBC-SP schemes in conjunction with $L = 16$, when employing system parameters of Table 3.3 and using an outer 1/2-rate binary LDPC code having an an output block length of 1500 bits and $five$ joint external LDPC iterations.

Part II

Coherent Versus Differential Turbo-Detection of Single-User and Cooperative MIMOs

Chapter 7

Linear Dispersion Codes: An EXIT Chart Perspective

7.1 Introduction and Outline

The design of coding schemes for MIMO systems illustrated in Figure 7.1 operating at high SNRs involves a tradeoff between the achievable rate at which the system's capacity increases and the rate at which the error probability decays [24]. This inherent tradeoff provides a distinction between transmit diversity schemes like the family of Orthogonal Space-Time Block Codes (OSTBCs) [26] that sacrifice the achievable rate in exchange for maximum reliability and the class of Spatial Division Multiplexing (SDM) arrangements, such as those belonging to Bell Labs' Layered-Space-Time (BLAST) architecture [16]. SDM schemes are capable of supporting transmission rates close to the MIMO channel's capacity, but do so without fully benefiting from the diversity potential of the channel. Since OSTBCs and BLAST schemes were designed for achieving the two extremes of the tradeoff scale, there is considerable interest in developing design methods for schemes that provide different trade-offs in terms of the achievable rate and the error probability, which are applicable for employment in a broad range of antenna configurations. In other words, the space-time transmission matrix $\mathbf{S}$ in Figure 7.1 provides a total of $(M \times T)$ transmission slots, when considering both the spatial and temporal domains. The design of Space-Time Block Codes (STBCs) aims for answering the question of how to use the available resources most efficiently.

Unitary Space-Time Modulation (USTM) was proposed independently by Hughes [57] and Hochwald [56] [66] in an early attempt to design flexible STBCs that are capable of achieving the highest attainable diversity gain. Instead of specifically designing either the modulation schemes used or the inner structure of the space time transmission matrix $\mathbf{S}$ of Figure 7.1, the philosophy of USTM [56] [57] is to directly maximize the mutual information between $\mathbf{S}$ and the received signal matrix $\mathbf{Y}$. However, the complexity of the optimization increases exponentially with both the number of antennas and the number of bits/symbol. Hence, the optimization of high-rate USTM becomes infeasible. Hence, the problem of designing simple STBCs that exhibiting both high-rate and full-diversity remains to be tackled.

The set of Linear Dispersion Codes (LDCs), first proposed by Hochwald and Hassibi [29], constitutes a wide-ranging class of space-time block codes exhibiting diverse characteristics. Hence, this family encompasses numerous existing schemes, providing a natural framework in which such design problems can be posed. While some recently developed codes, such as the Threaded Algebraic Space-Time Block Codes (TASTBCs) [319] as well as Time Variant Linear Transformation

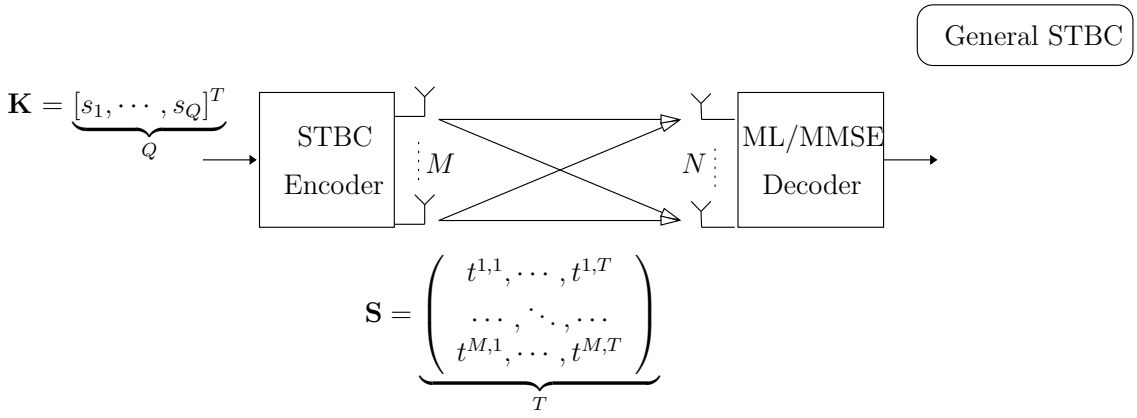

Figure 7.1: Schematic of MIMO system equipped with M transmit and N receive antenna, when transmitting Q symbols over T time slots using the space-time matrix $\mathbf{S}$.

(TVLT) codes [30] and those proposed in [320], possess many desirable features, they remain a subset of the LDC framework. Given the generality of the LDC framework and the high degrees of design freedom, the focus of this chapter is on the design and further development based on LDCs.

The revolutionary concept of LDCs [29] invokes a matrix-based linear modulation framework seen in Figures 7.2 and 7.3, where each space-time transmission matrix $\mathbf{S}$ is generated by a linear combination of so-called dispersion matrices and the weights of the components are determined by the transmitted symbol vector $\mathbf{K}$ of Figure 7.1. These figures will be revisited in more depth during our further discourse. The structure of the dispersion matrices is governed by the so-called Dispersion Character Matrix (DCM) χ to be outlined in detail in Equation (7.16) and the Appendix D. The dispersion matrices can be designed to maximize the ergodic MIMO capacity [321] as it will be further highlighted in Section 7.2. However, the LDCs proposed in [29] only optimized the ergodic capacity, which did not necessarily guarantee that a low error probability was achievable [28] [322]. It is often exploited that the probability of a codeword error can be upper bounded by the largest Pairwise Symbol Error Probability (PSEP) [323]. Therefore, LDCs minimizing the maximum PSEP based on frame theory [324] were proposed in [28]. On the other hand, LDCs can be optimized using the determinant criterion [54] using the same technique of the Golden code [325] [326]. However, in this treatise we propose a novel method to optimize the dispersion matrices, namely maximizing the Discrete-input Continuous-output Memoryless Channel (DCMC) capacity.

The achievable ergodic capacity of the LDCs [29] [28] [322] is also referred to as the Continuous-input Continuous-output Memoryless Channel (CCMC) capacity [323], where the channel's input is assumed to be a continuous-amplitude discrete-time Gaussian-distributed signal and the capacity is restricted only by either the signalling energy or the bandwidth. Therefore, we will refer to the CCMC capacity as the unrestricted bound. Naturally, in practice the channel's input is constituted by non-Gaussian symbols, although in certain circumstances, when for example high-order Quadrature Amplitude Modulation (QAM) aided symbols are transmitted over multiple Orthogonal Frequency-Division Multiplexing (OFDM) carriers this assumption becomes valid owing to the central limit theorem. In the more realistic context of discrete-amplitude Phase-Shift Keying (PSK) and QAM signals, we encounter a Discrete-input Continuous-output Memoryless Channel (DCMC) . Therefore, the DCMC capacity is more pertinent in the design of practical channel-coded modulation schemes. We will demonstrate in Section 7.2 that LDCs achieving the same CCMC capacity may attain a different DCMC capacity. Therefore, we propose an optimization method that is capable of maximizing both the CCMC and DCMC capacity of the LDCs at the same time.

Serial Concatenated Codes (SCCs) are capable of attaining an infinitesimally low BER, while

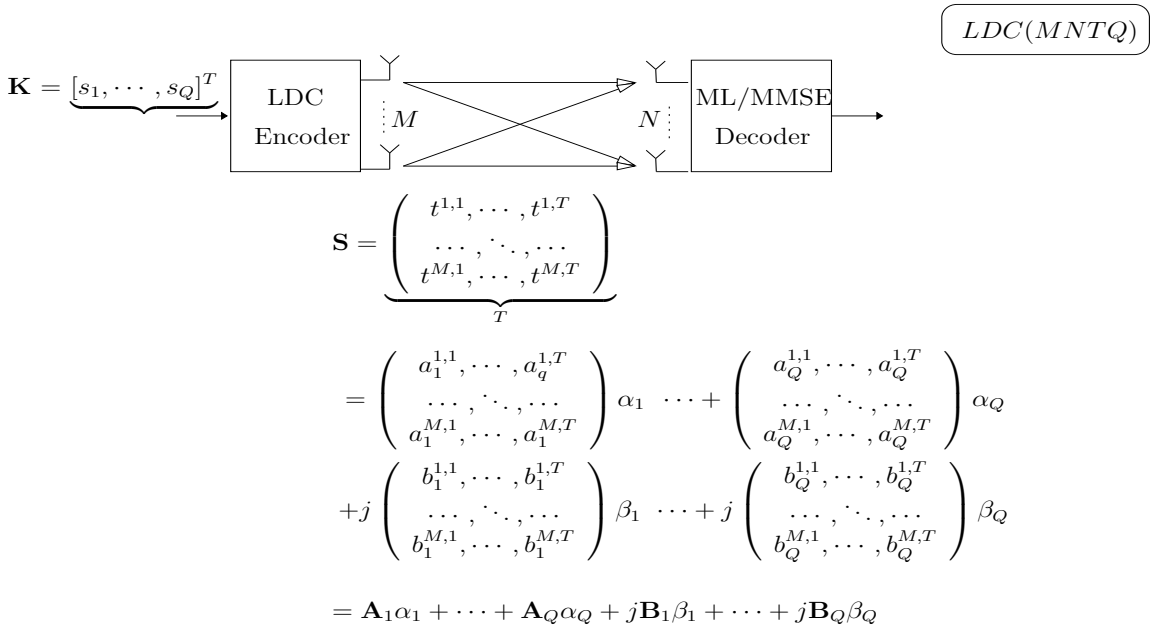

Figure 7.2: Schematic of a MIMO system equipped with M transmit and N receive antennas employing LDC($MNTQ$) structure of [29], while transmitting Q symbols over T time slots using the space-time matrix $\mathbf{S}$.

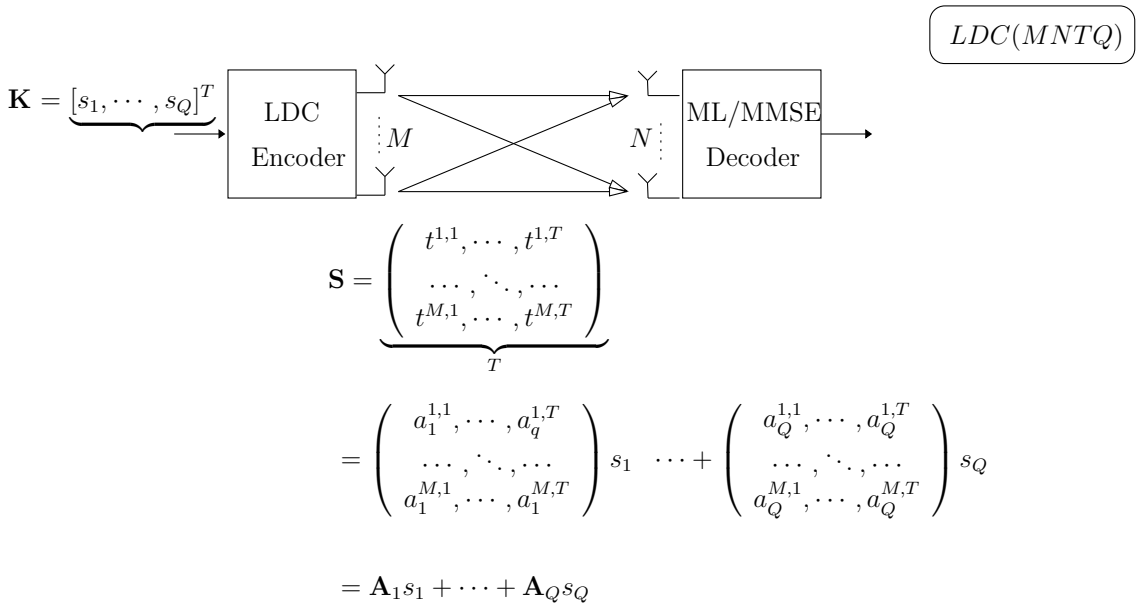

Figure 7.3: Schematic of a MIMO system equipped with M transmit and N receive antennas employing $LDC(MNTQ)$ structure of [28], while transmitting Q symbols over T time slots using the space-time matrix $\mathbf{S}$.

maintaining a manageable decoding complexity. The discovery of 'turbo codes' [151] [327] considerably improved the attainable performance gains of concatenated codes by exchanging extrinsic information between concatenated component codes. It has been shown in [154] that a high coding gain can be achieved using serially concatenated codes with the aid of iterative decoding. Since LDCs have the ability to approach the potential capacity of MIMO systems, it is natural to serially concatenate for example a simple convolutional channel code as the *outer* code and LDCs employed as the *inner* code in order to approach the MIMO capacity, while having a near error-free BER performance.

The concept of 'irregularity' was proposed in [204] [182] for SCCs, when IrRegular Convolutional Codes (IRCCs) were adopted as the *outer* channel code. Since IRCCs exhibited flexible EXIT characteristics [204], shaping the *outer* code's EXIT curve in order to match the *inner* code's EXIT curve becomes possible. However, near capacity IRCC schemes may require an excessive number of iterations at the receiver to achieve an infinitesimally low BER, which may exceed the affordable complexity budget of mobile handsets.

Motivated by the above-mentioned flexibility of the irregular *outer* code design philosophy, in this chapter we circumvent the IRCC-related *outer* code limitations by proposing IrRegular Precoded Linear Dispersion Codes (IR-PLDCs) as the *inner* rather than *outer* code and serially concatenate the resultant IR-PLDCs with regular/irregular *outer* channel codes in order to achieve an infinitesimally low BER, when employing iterative decoders. The novel contributions of this chapter are listed as follows [328] [33].

- LDCs are optimized by maximizing both the CCMC and DCMC capacity;
- The links between existing STBCs and LDCs are explored, and the necessary condition for STBCs to achieve both high-rate and full-diversity is investigated;
- We investigate the maximum achievable rate of precoded LDCs with the aid of EXIT charts, when using both Maximum Likelihood (ML) and Minimum Mean Squared Error (MMSE) detectors;
- We propose IR-PLDCs as the *inner* code of SCCs and employ regular/irregular convolutional codes as the *outer* code. Hence, the resultant SCCs become capable of operating near the attainable MIMO channel capacity for a wide range of SNRs.

The outline of this chapter is as follows. Section 7.2 presents the system models and the optimization of the LDCs, followed by the achievable performance in terms of their capacity and attainable BER. In Section 7.3, we characterize the link between existing STBCs found in the open literature and LDCs in terms of both mathematical representations and design philosophy. In Section 7.4, the EXIT chart analysis of LDCs is provided in order to characterize the convergence behaviour of the serial concatenated scheme with/without unity rate precoders. Section 7.5 presents the detailed design of the proposed IR-PLDCs with the aid of EXIT charts, when a simple *outer* code is employed. Numerical results are also presented for characterizing the IR-PLDCs operating at different SNRs, when the decoding complexity is also taken into account. Furthermore, in Section 7.5.2, we compare the IRCCs and the proposed IR-PLDCs, where the irregularity is imposed in the *outer* and *inner* codes, respectively. In order to further illustrate the irregular concept, in Section 7.5.3 we propose an IRCC-coded IR-PLDC scheme, where the irregularity is evenly distributed between the *inner* and *outer* codes. Finally, our concluding remarks are provided in Section 7.6.

7.2 Linear Dispersion Codes

7.2.1 Channel Model

A MIMO communication system equipped with M transmit antennas and N receive antennas is illustrated in Figure 7.1. The space-time encoder takes the input symbol vector $\mathbf{K} = [s_1, s_2, \ldots, s_Q]^T$ and generates a space-time transmission matrix $\mathbf{S}$. Then $\mathbf{S}$ is transmitted synchronously through the propagation environment using M transmit antennas. The signal received at each antenna is therefore given by a superposition of M transmitted signals corrupted both by Additive White Gaussian Noise (AWGN) and multiplicative fading. When the Space-Time (ST) transmission matrix $\mathbf{S}$ spans T symbol intervals, the received signal matrix $\mathbf{Y} \in \zeta^{N \times T}$ can be written as follow:

$$\mathbf{Y} = \mathbf{HS} + \mathbf{V}, \tag{7.1}$$

where $\mathbf{V}$ is a $(N \times T)$-element matrix whose columns represent realizations of an i.i.d. complex AWGN process with zero-mean and variance σ_0 determined by SNR ρ. The Channel Impulse Response (CIR) matrix $\mathbf{H} \in \zeta^{N \times M}$ is assumed to be constant during a space-time codeword of T symbol periods and change independently from one ST matrix to the next, which corresponds to experiencing quasi-static fading. Each entry of $\mathbf{H}$ represents the fading coefficient between a transmit-receive antenna pair. We will assume that the scattering imposed by the propagation environment is sufficiently rich for the channel coefficients to be modelled as i.i.d. zero-mean complex-valued Gaussian random variables having a common variance of 0.5 per real dimension. The entries of the channel matrix are assumed to be known to the receiver, but not to the transmitter. The space-time transmission matrix $\mathbf{S} \in \zeta^{M \times T}$ is given by

$$\mathbf{S} = \begin{pmatrix} t^{1,1} & \ldots & t^{1,T} \\ t^{2,1} & \ldots & t^{2,T} \\ \vdots & \ddots & \vdots \\ t^{M,1} & \ldots & t^{M,T} \end{pmatrix}, \tag{7.2}$$

where t^{i_1,i_2} denotes the signal transmitted from the i_1-th antenna in the i_2-th time slot. We are concerned with designing the signal matrix $\mathbf{S}$ obeying the power constraint $E\{tr(\mathbf{SS}^H)\} = T$, to ensure that the total transmission power is constant.

Given an arbitrary signal constellation, we follow [54] and define the symbol rate of a STBC having the structure of Figure 7.1 by

$$R_{STBC} = \frac{Q}{T}. \tag{7.3}$$

Under this definition, a rate-two code corresponds to a STBC transmits on average two symbols per channel use. For example, Alamouti's twin-antenna $\mathbf{G}_2$ code [10] has a rate of $R_{\mathbf{G}_2} = \frac{Q}{T} = 1$.

7.2.2 Linear Dispersion Code Model of [29]

Let each space-time transmission matrix $\mathbf{S}$ formulated in Equation (7.2) represents the linear combination of Q space-time symbols, such as for example L-PSK or L-QAM symbols, which are dispersed over both space and time with the motivation of exploiting both the spatial and temporal diversity, as seen in Figure 7.2. We simply refer to this structure as Linear Dispersion Code (LDC). Hence, $\mathbf{S}$ obeys

$$\mathbf{S} = \sum_{q=1}^{Q} (\mathbf{A}_q \alpha_q + j\mathbf{B}_q \beta_q), \tag{7.4}$$

where α_q and β_q are the real and imaginary parts of the q-th transmitted symbol having a variance of 0.5, while $\mathbf{A}_q$ and $\mathbf{B}_q$ are real-valued or complex-valued dispersion matrices. We normalize $\mathbf{S}$ to

$E\{tr(\mathbf{S}^H\mathbf{S})\} = T$, which limits the total transmit power of the ST codeword. It may be readily shown that this normalization imposes the following normalization on the matrices $\mathbf{A}_q$ and $\mathbf{B}_q$

$$\sum_{q=1}^{Q}(tr(\mathbf{A}_q^H\mathbf{A}_q) + tr(\mathbf{B}_q^H\mathbf{B}_q)) = 2T. \tag{7.5}$$

The idea behind the decoding of LDCs is to exploit the linearity of Equation (7.4) with respect to the variables, leading to efficient V-BLAST-like decoding schemes [16]. We denote the real part of the received signal matrix $\mathbf{Y}$ by $\mathbf{Y}_R$ and the imaginary part by $\mathbf{Y}_I$. Similarly, we introduce the notations $\mathbf{H}_R$, $\mathbf{H}_I$, $\mathbf{V}_R$ $\mathbf{V}_I$ and denote the i-th columns of these matrices by $y_{R,i}$, $y_{I,i}$, $h_{R,i}$, $h_{I,i}$, $v_{R,i}$ and $v_{I,i}$. Let us also define

$$\bar{\mathbf{A}}_q = \begin{bmatrix} \mathbf{A}_{R,q} & -\mathbf{A}_{I,q} \\ \mathbf{A}_{I,q} & \mathbf{A}_{R,q} \end{bmatrix}, \bar{\mathbf{B}}_q = \begin{bmatrix} -\mathbf{B}_{I,q} & -\mathbf{B}_{R,q} \\ \mathbf{B}_{R,q} & -\mathbf{B}_{I,q} \end{bmatrix}, \underline{\mathbf{h}}_i = \begin{bmatrix} h_{R,i} \\ h_{I,i} \end{bmatrix}, \tag{7.6}$$

where we have $\bar{\mathbf{A}}_q \in \zeta^{2T\times 2M}$, $\bar{\mathbf{B}}_q \in \zeta^{2T\times 2M}$ and $\underline{\mathbf{h}}_n \in \zeta^{2M\times 1}$. Furthermore, define

$$\bar{\mathbf{H}} = \begin{bmatrix} \bar{\mathbf{A}}_1\underline{\mathbf{h}}_1 & \bar{\mathbf{B}}_1\underline{\mathbf{h}}_1 & \cdots & \bar{\mathbf{A}}_Q\underline{\mathbf{h}}_1 & \bar{\mathbf{B}}_Q\underline{\mathbf{h}}_1 \\ \vdots & \vdots & \ddots & \vdots & \vdots \\ \bar{\mathbf{A}}_1\underline{\mathbf{h}}_N & \bar{\mathbf{B}}_1\underline{\mathbf{h}}_N & \cdots & \bar{\mathbf{A}}_Q\underline{\mathbf{h}}_N & \bar{\mathbf{B}}_Q\underline{\mathbf{h}}_N \end{bmatrix}, \tag{7.7}$$

where we have $\bar{\mathbf{H}} \in \zeta^{2NT\times 2Q}$ and each element of $\bar{\mathbf{H}}$ is hence an element of the $\zeta^{2T\times 1}$ matrix . For example, we have $\bar{\mathbf{A}}_1\underline{\mathbf{h}}_1 \in \zeta^{2T\times 1}$.

Then the whole system can be represented by [29]

$$\begin{bmatrix} y_{R,1} \\ y_{I,1} \\ \vdots \\ y_{R,N} \\ y_{I,N} \end{bmatrix} = \bar{\mathbf{H}} \begin{bmatrix} \alpha_1 \\ \beta_1 \\ \vdots \\ \alpha_Q \\ \beta_Q \end{bmatrix} + \begin{bmatrix} v_{R,1} \\ v_{I,1} \\ \vdots \\ v_{R,N} \\ v_{I,N} \end{bmatrix}, \tag{7.8}$$

where the matrix noting the received signal has a size of $(2NT \times 1)$, while the matrix hosting the transmitted symbols is of size $(2Q \times 1)$. The resultant equivalent channel $\bar{\mathbf{H}}$ is known to the receiver, because the original channel $\mathbf{H}$ and the dispersion matrices $\mathbf{A}_q$ and $\mathbf{B}_q$ are all known to the receiver. Equation (7.8) explicitly portrays the linear relation between the equivalent channel's the input and output vectors. Therefore, ML and MMSE detectors as well as sphere decoders [329] can be readily employed to recover the Q transmitted symbols.

The dispersion matrices $\mathbf{A}_q$ and $\mathbf{B}_q$ of Figure 7.2 are specifically designed to maximize the mutual information between the equivalent transmit and receive vectors in Equation (7.8). This guarantees that the resultant LDCs minimize the potential mutual information penalty. This design procedure can be formalized as follows [29].

Given the equivalent MIMO channel matrix $\bar{\mathbf{H}}$ of Equation (7.7), the achievable capacity C_{LDC} of this MIMO system employing LDCs at SNR ρ is given by [29]

$$C_{LDC}(\rho, M, N, T, Q) = \max(\frac{1}{2T}E\{\log_2[\det(\mathbf{I} + \frac{\rho}{M}\bar{\mathbf{H}}\bar{\mathbf{H}}^H)]\}), \tag{7.9}$$

where $\mathbf{I} \in \zeta^{2NT\times 2NT}$ denotes an identity matrix. Choosing $\mathbf{A}_q$ and $\mathbf{B}_q$ in order to maximize C_{LDC} for a given Q, subject to one of the following constraints:

- $\sum_{q=1}^{Q}(tr(\mathbf{A}_q^H\mathbf{A}_q) + tr(\mathbf{B}_q^H\mathbf{B}_q)) = 2T$, which represents our total transmission power constraint to be satisfied during T time slots;

- $tr(\mathbf{A}_q^H \mathbf{A}_q) = tr(\mathbf{B}_q^H \mathbf{B}_q) = \frac{T}{Q}$, $q = 1, ..., Q$, implying that each ST signal component is transmitted with the same overall power from the M antennas during the T consecutive time slots, which corresponds to T channel activations;

- $\mathbf{A}_q^H \mathbf{A}_q = \mathbf{B}_q^H \mathbf{B}_q = \frac{T}{MQ}\mathbf{I}$, $q = 1, ..., Q$, indicating that α_q and β_q are dispersed with equal energy in all spatial and temporal dimensions.

We now continue by offering a few remarks concerning this model.

1. Clearly, the mutual information achieved by the LDC obeying Equation (7.9) is less than or equal to the MIMO channel capacity C_{MIMO} of [321]

$$C_{MIMO}(\rho, M, N) = E\{\log_2[\det(\mathbf{I} + \frac{\rho}{M}\mathbf{H}\mathbf{H}^H)]\}, \tag{7.10}$$

   where we have $\mathbf{I} \in \zeta^{N \times N}$. The corresponding lower bond can be derived [321]:

$$C_{MIMO}(\rho, M, N) \geq \min(M, N) \log_2[\frac{\rho}{M}] + \sum_{i=\max(M,N)-\min(M,N)+1}^{\max(M,N)} E\{\log_2[\Theta_{2i}^2]\}, \tag{7.11}$$

   where Θ_{2i}^2 is a chi-square distributed random variable with dimension $2i$. Moreover, this lower bound is asymptotically tight at high SNRs. We observe that this is equivalent to the capacity of $\min(M, N)$ sub-channels. In other words, the multiple antenna aided channel has $\min(M, N)$ degrees of freedom to communicate.

2. The solution of Equation (7.9) subject to any of the above-mentioned three constraints is non-unique. The judicious choice of the dispersion matrices allows LDCs to satisfy other criteria, such as for example the rank criterion [54] detailed in Section 7.3.1 without sacrificing mutual information.

3. The optimization stipulated in Equation (7.9) is carried out for a specific SNR ρ, although the authors of [29] argue that the optimization process insensitive to the specific value of ρ in the range of $\rho \geq 20$ and the resultant LDCs generally perform well over a wide SNR range.

4. Observe that if Q is increased, the mutual information between the transmitted signal and the received signal is expected to increase. By contrast, when Q is decreased, a higher coding gain may be obtained. This implies a tradeoff between the achievable capacity C_{LDC} and the decoding complexity imposed, as we will detail later in Section 7.5.1.3.

5. This design criterion is not directly linked with the diversity design criterion given in [54], therefore, it does not guarantee good BER performance.

The general LDC model of Figure 7.2 is suitable for us to demonstrate that LDCs subsume the existing class of STBCs based on orthogonal designs. Since the conjugate operations seen in Equation (7.30) constitute the key feature of Alamouti scheme [10], as well as of other STBCs based on orthogonal constraints, it required the real and imaginary parts of the transmitted symbols to be modulated separately. However, for non-orthogonal STBCs, we do not have significant performance differences between separately modulated and in-phase/quadrature-phase combined modulated codes. Therefore, in order to simplify the related discussions as well as to reduce the size of the equivalent channel matrix $\bar{\mathbf{H}}$ of Equation (7.7), another LDC model is presented in the next section.

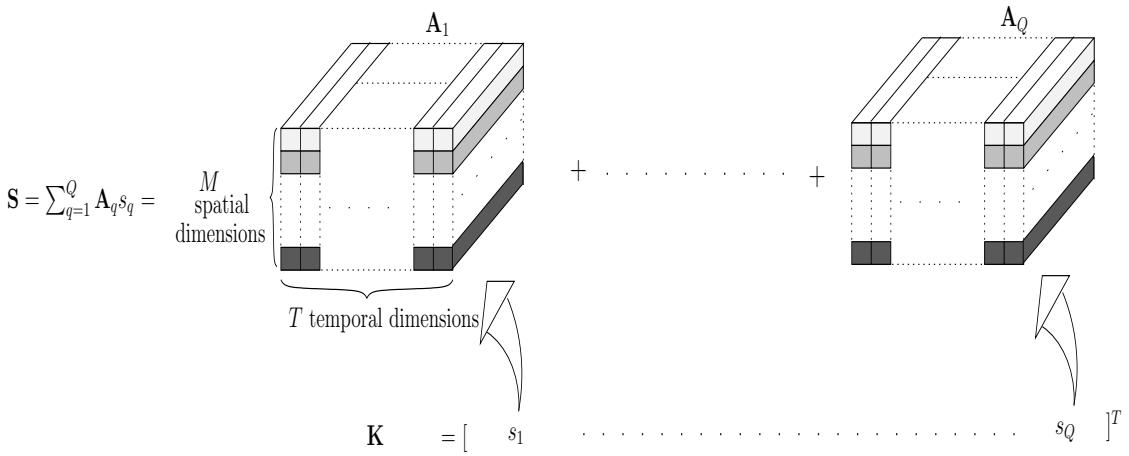

Figure 7.4: The space-time codeword **S** formulated base on Equation (7.12).

7.2.3 Linear Dispersion Code Model of [28]

The schematic of the LDCs using the model of [28] is illustrated in Figure 7.3. Given the vector $\mathbf{K} = [s_1, s_2, \ldots, s_Q]^T$ of L-PSK or L-QAM modulated transmission symbols seen in Figure 7.3, the transmitted space-time matrix $\mathbf{S}$ may be defined as [28]

$$\mathbf{S} = \sum_{q=1}^{Q} \mathbf{A}_q s_q, \tag{7.12}$$

which is visualized in Figure 7.4. More explicitly, each symbol s_q is dispersed to the M spatial- and T temporal dimensions using a specific dispersion matrix $\mathbf{A}_q$ and the transmission space-time codeword $\mathbf{S}$ is attained by the linear combination of all the weighted dispersion matrices, as seen in Figure 7.4.

Therefore, the codeword is uniquely and unambiguously determined by the set of dispersion matrices $\mathbf{A}_q$ that are known to both the transmitter as well as the receiver, which are arranged to be linked by $(M \times N)$ number of independent CIRs. Note that in contrast to Equation (7.4), this model modulates the real and imaginary parts of the symbols using the same dispersion matrix $\mathbf{A}_q$, rather than using another dispersion matrix $\mathbf{B}_q$. The transmitted codewords should satisfy the power constraint given by

$$tr(\sum_{q=1}^{Q} \mathbf{A}_q^H \mathbf{A}_q) = T. \tag{7.13}$$

More strictly, each spatial and temporal slot should be allocated the same transmission power of

$$tr(\mathbf{A}_q^H \mathbf{A}_q) = \frac{T}{Q}. \tag{7.14}$$

Similarly to Equation (7.8), it is desirable to rewrite the input-output matrix relationship of Equation (7.1) in an equivalent vectorial form. Define the $vec()$ operation as the vertical stacking of the columns of an arbitrary matrix. Subjecting both sides of Equation (7.1) to the $vec()$ operation gives the equivalent system matrix:

$$\bar{\mathbf{Y}} = \bar{\mathbf{H}}\chi\mathbf{K} + \bar{\mathbf{V}}, \tag{7.15}$$

where $\bar{\mathbf{Y}} \in \zeta^{NT\times 1}$, $\bar{\mathbf{H}} \in \zeta^{NT\times MT}$, $\chi \in \zeta^{MT\times Q}$, $\mathbf{K} \in \zeta^{Q\times 1}$ and $\bar{\mathbf{V}} \in \zeta^{NT\times 1}$. More explicitly, χ is referred to as the Dispersion Character Matrix (DCM) , which is defined as

$$\chi = [vec(\mathbf{A}_1), vec(\mathbf{A}_2), \ldots, vec(\mathbf{A}_Q)], \tag{7.16}$$

while $\bar{\mathbf{H}}$ in Equation (7.15) is given by

$$\bar{\mathbf{H}} = \mathbf{I} \otimes \mathbf{H}, \tag{7.17}$$

where $\otimes$ denotes the Kronecker product and $\mathbf{I}$ is the identity matrix having a size of $(T \times T)$. The ML estimation of the transmitted signal vector $\mathbf{K}$ is formulated as:

$$\bar{\mathbf{K}} = arg\{\min(||\bar{\mathbf{Y}} - \bar{\mathbf{H}}\chi\mathbf{K}_f||^2)\}, \tag{7.18}$$

where $\mathbf{K}_f$ denotes all the possible combinations of the Q transmitted symbols.

Using the equivalent input-output relationship of Equation (7.15) and applying the results of [268], the ergodic capacity of the LDCs subjected to quasi-static Rayleigh fading is given by

$$C_{LDC}(\rho, M, N, T, Q) = \max_{tr(\chi\chi^H)} \frac{1}{T} E\{\log[\det(\mathbf{I} + \rho\bar{\mathbf{H}}\chi\chi^H\bar{\mathbf{H}}^H)]\}, \tag{7.19}$$

where we have $\mathbf{I} \in \zeta^{NT \times NT}$.

The equivalent system model of Equation (7.15) is important, because it provides another view of the LDC structure. More explicitly, when transmitting space-time matrix $\mathbf{S} \in \zeta^{M \times T}$ over a MIMO channel $\mathbf{H} \in \zeta^{N \times M}$, it is equivalent to the transmission of the corresponding symbol vector $\mathbf{K}$ over an equivalent MIMO channel $\bar{\mathbf{H}}\chi \in \zeta^{NT \times Q}$. Applying the lower bound of Equation (7.11) to the equivalent MIMO channel $\bar{\mathbf{H}}\chi$, it can be shown that the capacity achieved by LDCs spanning T time slots is determined by $\min(NT, Q)$. Therefore, when we have $Q \geq MT$, there will be no further improvement of LDC's CCMC capacity of Equation (7.19).

Recall that the optimization procedure of Equation (7.9) may be used to find near-capacity LDCs by exhaustively searching the entire design space of LDCs. The resultant solution is not guaranteed to find the global maximum of the cost function. However, by maximizing the ergodic capacity of Equation (7.19) it is possible to obtain a near-capacity LDC by choosing Q according to M and T. More explicitly, upon substituting $Q \geq MT$ into Equation (7.19) and ensuring that

$$\chi\chi^H = \frac{1}{M}\mathbf{I}, \tag{7.20}$$

which satisfies the power constraint of $tr(\chi\chi^H) = T$, we arrive at an equivalent channel in the form of the $(M \times N)$-element MIMO channel of Equation (7.10). Since the Q transmitted symbols hosted by the vector $\mathbf{K}$ of Figure 7.3 are jointly decoded as in Equation (7.18), the decoding complexity increases exponentially with Q. Hence, it is sufficient to choose $Q = MT$ rather than $Q > MT$ to achieve full the CCMC capacity of Equation (7.10).

In many practical scenarios, it may be desirable to maintain $Q < MT$ in order to reduce the decoding complexity, memory and latency or to satisfy various rate constraints. To accommodate these constraints, χ can be designed by removing the appropriate number of columns from a scaled unitary matrix to arrive at a DCM χ that satisfies:

$$\chi^H\chi = \frac{T}{Q}\mathbf{I}. \tag{7.21}$$

Typically, when we have $Q < MT$, there is a loss of ergodic capacity, since it is no longer possible to exploit all the degrees of freedom $\min(NT, Q)$ of Equation (7.11) provided by the equivalent MIMO channel $\bar{\mathbf{H}}\chi$.

This structure of LDCs guarantees to approach the MIMO channel's capacity quantified in Equation (7.10), depending on the specific choice of Q and T. It does not, however, guarantee a good performance in terms of error probability. By minimizing the maximum PSEP [54] of Equation (7.26), the authors of [28] optimized LDCs that achieve both high rates and full diversity.

We now make a range of further remarks concerning this model.

- LDCs are suitable for arbitrary transmit and receive antenna configurations, combined with arbitrary modulation schemes;
- LDCs are capable of transforming an $(M \times N)$-antenna MIMO system into a $(Q \times NT)$-element equivalent MIMO system by exploiting their inherent linearity;
- Since the real and imaginary parts of the transmitted symbols are dispersed using different dispersion matrices obeying the LDC model of Figure 7.2, the size of the equivalent MIMO system is $(2Q \times 2NT)$, as explicitly shown in Equation (7.8). The non-orthogonal model of Equation (7.15) reduces the equivalent model to a size of $(Q \times NT)$;
- All the dispersion matrices $\mathbf{A}_q$ of Equation (7.12) can be described with the aid of the a single DCM χ characterized in Equation (7.16);
- The LDC's equivalent CIR of Equation (7.15) can be appropriately adjusted by employing different DCM χ;
- **Theorem 1.** When we have $Q \geq MT$, any dispersion character matrix χ satisfying Equation (7.20) is an optimal LDC which is capable of approaching the MIMO channel's capacity. For the proof of the theorem please refer to [28];
- **Theorem 2.** When we have $Q < MT$, the ergodic capacity is approached within a margin which is in proportional to $\frac{Q}{T}$. For the proof of the theorem please refer to [28];
- **Theorem 3.** The diversity order of the LDC scheme is less than or equal to $N \cdot \min(M, T)$. This implies that increasing T beyond M does not provide any further advantage in terms of an increased spatial transmit diversity, where the receive diversity is determined by N alone. For the proof of the theorem please refer to [28].

7.2.4 Maximizing the Discrete LDC Capacity

In order to generate a DCM χ defined in Equation (7.16), a random search algorithm was adopted [28]. To elaborate a little further, the random search algorithm of [28] randomly generates a matrix χ from some specific distribution, for example the Gaussian distribution, to satisfy the capacity constraint formulated in Theorems 1 and 2. Then, the corresponding diversity order and the coding gain is maximized by checking the *rank* and *determinant* criteria [54] detailed in Section 7.3.1, when performing an exhaustive search through the entire set of legitimate dispersion matrices.

The random search algorithm has the advantage of providing a wide variety of legitimate LDCs and typically provides a good performance [28]. In fact, codes obtained using a random dispersion character matrix often perform well without checking the *rank* and the *determinant* criteria. Since the search is random, they are unable to guarantee finding the maximum of the determinant function of Equation (7.27). Other efforts found in the literature of optimizing LDCs include schemes designed for minimizing the BLock Error Ratio (BLER [330].

In this section, we adopt the aforementioned random search algorithm to optimize LDCs. However, we propose to optimize the LDCs by maximizing the corresponding DCMC capacity. The rationale and advantage of optimizing the DCMC capacity are listed as follows:

- According to the equivalent system matrix of Equation (7.15), transmitting the signal matrix $\mathbf{S}$ through the MIMO channel $\mathbf{H}$ employing the LDC structure of Figure 7.3 can be viewed as transmitting a symbol vector $\mathbf{K}$ through an equivalent MIMO channel given by $\bar{\mathbf{H}}\chi$ of Equation (7.15). Therefore, we propose to directly maximize the equivalent MIMO channel's capacity;

- The LDCs that achieve a higher DCMC capacity at a certain SNR typically exhibit a good BER performance in the high SNR region, since achieving a higher DCMC capacity implies that they are capable of providing a higher integrity as a result of their higher diversity gain and coding gain;
- The proposed optimization procedure is capable of taking into account the modulated signal constellations, such the specific L-PSK or L-QAM constellations. Hence the total number of possible combinations for the legitimate ST symbol vector $\mathbf{K}$ is $F = L^Q$.

The conditional probability of receiving the ST signal vector $\bar{\mathbf{Y}}$ of Equation (7.15), given a signal vector K_f for $f \in (1, \ldots, F)$ transmitted over a slowly Rayleigh fading channel is determined by the Probability Density Function (PDF) of the noise, as seen below:

$$p(\bar{\mathbf{Y}}|K_f) \quad = \quad \frac{1}{\pi} \cdot \exp(-||\bar{\mathbf{Y}} - \bar{\mathbf{H}}\chi K_f||^2). \tag{7.22}$$

The DCMC capacity of the ML-detected MIMO system using L-QAM or L-PSK signalling, when we have the equivalent CIR $\bar{\mathbf{H}}\chi$ of Equation (7.15), is given by:

$$C_{LDC}^{DCMC} = \frac{1}{T} \max_{p(K_1),\ldots,p(K_F)} \sum_{f=1}^{F} \int_{-\infty}^{\infty} \cdots \int_{-\infty}^{\infty} p(\bar{\mathbf{Y}}|K_f)p(K_f)$$
$$\cdot log_2 \left[\frac{p(\bar{\mathbf{Y}}|K_f)}{\sum_{g=1}^{F} p(\bar{\mathbf{Y}}|K_g)p(K_g)} \right] d\bar{\mathbf{Y}} \qquad (bits/sym/Hz), \tag{7.23}$$

where the right hand side of Equation (7.23) is maximized, when we have equiprobable ST symbols obeying $p(K_f) = \frac{1}{F}$ for $f = 1, \ldots, F$. Hence, (7.23) can be simplified as [331]

$$C_{LDC}^{DCMC} = \frac{1}{T} \left(log_2[F] - \frac{1}{F} \sum_{f=1}^{F} E\{log_2[\sum_{g=1}^{F} \exp(\Psi_{f,g})|K_f]\} \right). \tag{7.24}$$

where $\Psi_{f,g}$ within the curly-bracketed expectation value of Equation (7.24) is given by:

$$\Psi_{f,g} \quad = \quad -||\bar{\mathbf{H}}\chi(K_f - K_g) + \bar{\mathbf{V}}||^2 + ||\bar{\mathbf{V}}||^2. \tag{7.25}$$

Since the equivalent system model represents the transmission regime of T time slots, the DCMC capacity of LDCs has to be divided by T, as seen in Equations (7.23) and (7.24).

Given the DCMC capacity of the LDC($MNTQ$) family, the following random search algorithm can be derived:

1. Randomly generate the complex-valued matrix $\bar{\chi} \in \zeta^{MT \times MT}$ using the Gaussian distribution.
2. If we arrange the system to satisfy $Q \geq MT$, the candidate DCM has to be a unitary matrix according to Theorem 1. It has been shown in [332] that a complex-valued matrix can be factored into the product of a unitary matrix and an upper triangular matrix using the QR decomposition [332]. Thus, a random dispersion character matrix can be obtained by $\chi = \frac{1}{\sqrt{M}} QR(\bar{\chi})$, which satisfies Equation (7.20).
3. By contrast, if we confine the LDC schemes to $Q < MT$, the DCM χ has to satisfy Equation (7.21) and it can be generated by retaining the first Q columns of the unitary matrix obtained using the QR decomposition of $\sqrt{\frac{T}{Q}} QR(\bar{\chi})$.
4. Having searched through the entire set of legitimate dispersion character matrices, we choose that particular one, which maximizes the DCMC capacity of Equation (7.24).

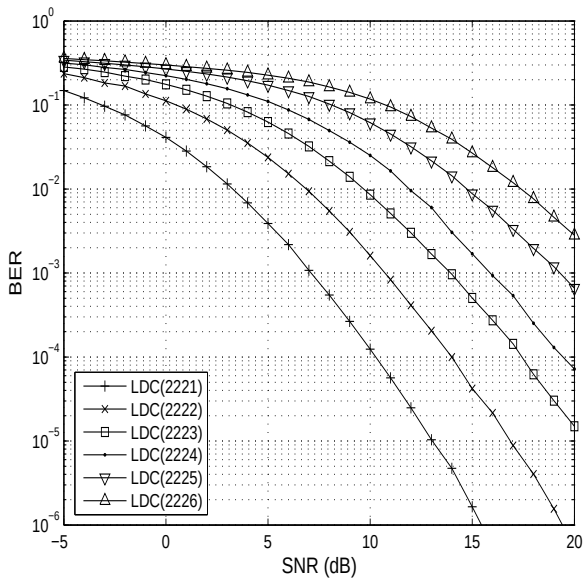

Figure 7.5: BER of a family of QPSK modulated LDCs obeying the structure of Figure 7.3 having $M = 2$, $N = 2$, $T = 2$ and $Q = 1, 2, 3, 4, 5, 6$ using an ML detector, when transmitting over i.i.d. Rayleigh-fading channels.

The LDCs generated by the above algorithm are sufficiently diverse to represent the entire legitimate space and additionally they are capable of maximizing the DCMC capacity. We found that $100,000$ random searches are typically sufficient for generating LDCs exhibiting a good BER performance. In Appendix D, we summarize all the dispersion character matrices χ derived for all the LDCs used in this chapter.

7.2.5 Performance Results

above that LDCs described by the parameters $(MNTQ)$ are suitable for arbitrary transmit and receive antenna configurations, when transmitting the Q symbols of the vector $\mathbf{K}$ during T time periods as seen in Figure 7.3. In this section, we present our simulation results for characterizing LDCs having different parameters and quantify their capacity with the aid of Theorems 1, 2 and 3. For the moment, we concentrate on the achievable LDC performance in terms of the attainable ergodic capacity and BER. Gray labelling was assumed for the bit-to-symbol mapping and an ML detector using Equation (7.18) was employed. Quadrature Phase Shift Keying (QPSK) modulation was employed in all the simulations. We adopted the non-orthogonal LDC structure of Figure 7.3 and the DCM χ was generated using the method presented in Section 7.2.4.

Figure 7.5 portrays the BER performance of LDCs having rates of R_{LDC}=0.5, 1, 1.5, 2, 2.5 and 3, which were adjusted by fixing (MNT) while gradually increasing Q. Observe from the shape of the curves in Figure 7.5 that all the codes do achieve the maximum diversity order of $D = 4$ that a (2×2)-element MIMO system is capable of providing. Owing to the power constraint of Equation (7.13), the average transmit energy of each symbol was decreased when increasing Q, which results in a BER degradation. The ML detector jointly and simultaneously decodes the Q symbols of the vector $\mathbf{K}$ seen in Figure 7.3. When we have $Q = 1$, the transmitted signal is a single element in a two-dimensional (2D) space obeying Equation (7.15). Since Gray labelling is used, the minimum Euclidean distance is maximized. However, when we have $Q > 1$, since each transmitted symbol is expected to fade independently, as seen in Equations (7.8) and (7.15), there is no guarantee that

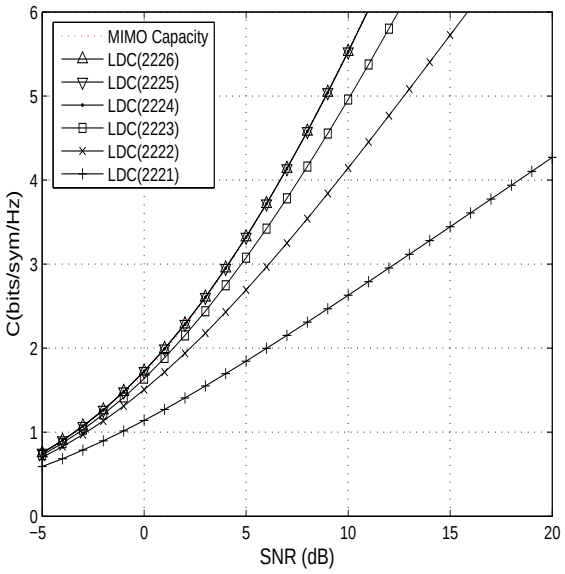

Figure 7.6: CCMC capacity comparison of a family of LDCs obeying the structure of Figure 7.3 having $M = 2$, $N = 2$, $T = 2$ and $Q = 1, 2, 3, 4, 5, 6$ using an ML detector, as plotted from Equation (7.9).

Gray mapping will ensure that the maximum minimum Euclidean distance is maximized within the $2Q$-dimensional space.

The corresponding achievable CCMC capacity of LDCs having $M = 2$, $N = 2$, $T = 2$ and $Q = 1, 2, 3, 4, 5, 6$ using an ML detector is shown in Figure 7.6. The MIMO channel capacity of Equation (7.10) is also shown as an upper bound. Observe that LDCs having $Q \geq MT = 4$ have already achieved the maximum attainable diversity order of $D = 4$ and the MIMO channel capacity of Equation (7.10). Therefore, there is no point in selecting $Q > MT$ in terms of the achievable CCMC capacity of Equation (7.19), especially since this will increase the decoding complexity. In case of $Q < MT$, observe in Figure 7.6 that the CCMC capacity increases proportionally to $\frac{Q}{T}$, as stated in Theorem 2.

The achievable DCMC capacity of LDCs having $M = 2$, $N = 2$, $T = 2$ and $Q = 1, 2, 3, 4, 5, 6$ using an ML detector is shown in Figure 7.7 as plotted according to Equation (7.23). Recall that when we have $Q \geq MT$, the CCMC MIMO channel capacity has already been achieved as seen in Figure 7.6. By contrast, Figure 7.7 demonstrates that the DCMC capacity calculated using Equation (7.23) increases with Q, even when we have $Q > MT$. Naturally, it is possible to further improve the throughput of the system by transmitting more bits per symbol, i.e. by using higher order modulation schemes.

Figure 7.8 shows the BER performance of a group of QPSK modulated LDCs having $M = 2$, $N = 2$, $T = 3$ and $Q = 1, 2, 3, 4, 5, 6$ using an ML detector. Again, a BER degradation is observed upon increasing the number of symbols transmitted per space-time block. Compared to the family of LDCs having $T = 2$ and characterized in Figure 7.5, the group of LDCs characterized in Figure 7.8 has the same spatial diversity order of $D = 4$. This observation is supported by Theorem 3, where the transmit diversity order is determined by $\min(M, T)$. However, it is still interesting to observe that the identical-rate LDC pairs of [LDC(2222), LDC(2233)] and [LDC(2224), LDC(2236)] characterized in Figures 7.5 and 7.8 exhibit the same BER performance.

Furthermore, Figure 7.9 characterizes the DCMC capacity achieved by the equal-rate LDC pairs of [LDC(2222), LDC(2233)] and [LDC(2224), LDC(2236)] using an ML detector in conjunction with

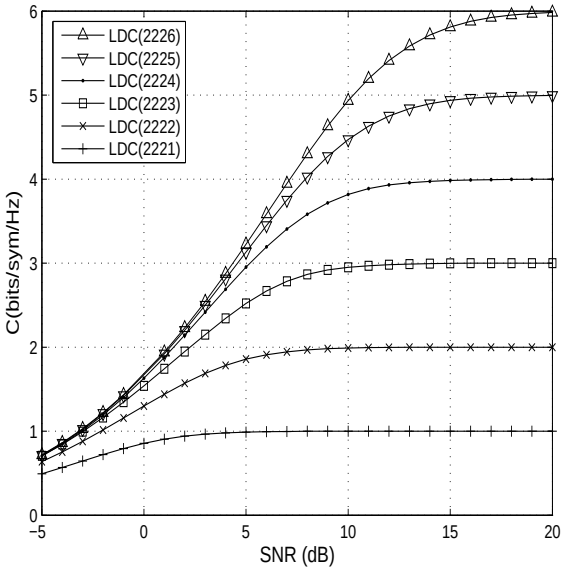

Figure 7.7: DCMC capacity comparison of LDCs obeying the structure of Figure 7.3 having $M = 2$, $N = 2$, $T = 2$ and $Q = 1, 2, 3, 4, 5, 6$ using an ML detector, as plotted from Equation (7.23), where QPSK modulation was employed.

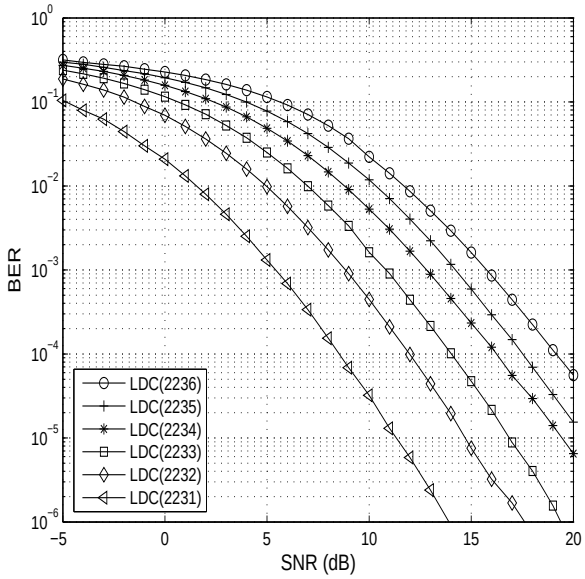

Figure 7.8: BER of a family of QPSK modulated LDCs obeying the structure of Figure 7.3 having $M = 2$, $N = 2$, $T = 3$ and $Q = 1, 2, 3, 4, 5, 6$ using an ML detector, when transmitting over i.i.d. Rayleigh-fading channels.

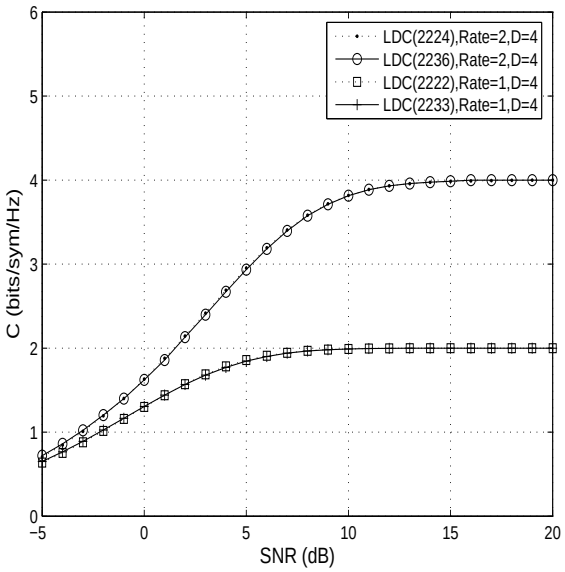

Figure 7.9: DCMC capacity comparison of QPSK modulated equal-rate LDC pairs [LDC(2222), LDC(2233)] and [LDC(2224), LDC(2236)] obeying the structure of Figure 7.3 using an ML detector, as evaluated from Equation (7.23).

QPSK modulation. Not surprisingly, according to Equation (7.23), these equal-rate equal-diversity-order LDCs achieve the same DCMC capacity. This implies that increasing T and maintaining $T > M$, while fixing the rate to $R_{LDC} = \frac{Q}{T}$, do not benefit the system in terms of an improved BER performance and increased achievable capacity. In fact, maintaining the minimum value of T is desirable due to the associated complexity considerations.

Figure 7.10 quantifies the achievable BER performance of the QPSK modulated equal-rate LDCs pairs [LDC(2212), LDC(2224)] obeying the structure of Figure 7.3 using an ML detector, when transmitting over i.i.d. Rayleigh-fading channels. According to Theorem 3, the LDC(2212) scheme achieves $D = 2$, whereas $D = 4$ diversity gain is achievable using the LDC(2224) scheme. The BER performance recorded in Figure 7.10 demonstrates a clear gap between these schemes in the high-SNR region.

The CCMC and DCMC capacity achieved by the LDC(2212) and LDC(2224) schemes plotted using Equations (7.9) and (7.23) are shown in Figure 7.11. According to Theorem 1, the only requirement for LDCs to achieve full MIMO channel's capacity is that the DCM χ has to be a unitary. Therefore, despite different diversity orders were achieved by the LDC(2212) and LDC(2224) schemes, they attain the same CCMC capacity. However, the LDC(2224) arrangement has a higher DCMC capacity characterized in Equation (7.23) in the SNR region of $5dB < \rho < 15dB$, since having a higher spatial diversity order provides a higher degree of protection, as shown in Figure 7.10.

Based on the discussions above as well as on Theorems $1, 2, 3$, our observations may be summarized as follows:

Corollary 1. *A group of LDCs ($MNTQ$) having M transmit and N receive antennas as well as a fixed rate of $\frac{Q}{T}$ ($T > M$), exhibits the same diversity order and the same capacity. Consequently, they have an identical rate and an identical BER performance.*

In Figure 7.12 we plot the BER performance of a group of QPSK modulated LDCs having the same fixed rate of $R_{LDC} = 2$, while using different MIMO antenna structures. Here, we used

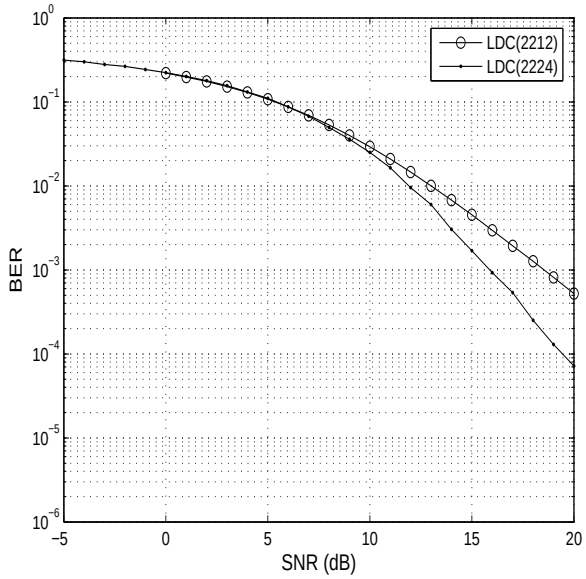

Figure 7.10: BER of QPSK modulated equal-rate LDC pairs [LDC(2212), LDC(2224)] obeying the structure of Figure 7.3 using an ML detector, when transmitting over i.i.d. Rayleigh-fading channels.

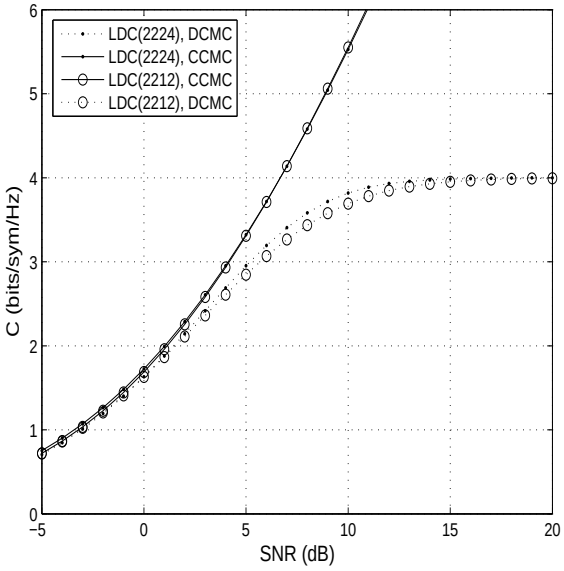

Figure 7.11: The CCMC and DCMC capacity of equal-rate LDC pairs [LDC(2212), LDC(2224)] obeying the structure of Figure 7.3 using an ML detector, as plotted using Equations (7.9) and (7.23). For plotting the DCMC capacity, QPSK modulation was employed.

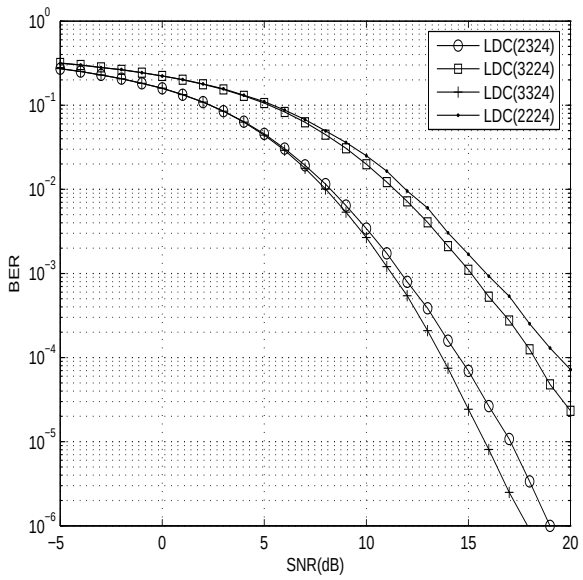

Figure 7.12: BER of a family of QPSK modulated LDCs obeying the structure of Figure 7.3 having $M = 2, 3$, $N = 2, 3$, $T = 2$ and $Q = 4$ using an ML detector, when transmitting over i.i.d. Rayleigh-fading channels.

the LDC(2224) scheme as our benchmarker. When increasing the number of transmit antennas to $M = 3$, according to Theorem 3, the LDC(3224) scheme exhibits the same diversity order of $D = 4$. However, the increased value of M enables the LDC(3224) arrangement to achieve a better coding gain, as shown in Figure 7.12. On the other hand, when increasing N to 3, the LDC(2324) arrangement achieved a diversity order of $D = 6$, which resulted in a significant SNR gain in Figure 7.12. Again, when an additional transmit antenna is employed compared to the LDC(2324) scheme, the resultant LDC(3324) arrangement demonstrated a better coding gain.

The capacity associated with changing the number of transmit and receive antennas is portrayed in Figure 7.13. Observe that the LDCs associated with $N = 3$, which have a higher diversity order also achieved a substantially higher CCMC/DCMC capacity, compared to the LDCs having $N = 2$. On the other hand, the effect of employing more transmit antennas ($M \geq T$), which results in an increased coding gain in Figure 7.12 is insignificant in terms of the increased achievable capacity, as quantified in Figure 7.13.

7.2.6 Summary

In this section, we characterize the performance of the LDCs presented in Section 7.2.5 in terms of the effective throughput and the coding gains, where the latter is defined as the SNR difference, expressed in dBs, at a BER of 10^{-4} between various LDCs and the identical throughput single-antenna-aided systems.

In Figure 7.14, we plot the effective throughput against the SNR required to achieve BER $= 10^{-4}$ for a group of LDCs having $N = 1, 2, 3, 4$ receive and $M = 2$ transmit antennas using $T = 2$ time slots to transmit $Q = 1$ symbols per space-time block. An increased effective throughput was achieved by employing high-order modulation schemes, rather than by increasing the value of Q. For this particular group of LDC($2N21$), 9.5dB is required for increasing the effective throughput from 0.5 to 2 (bits/sym/Hz).

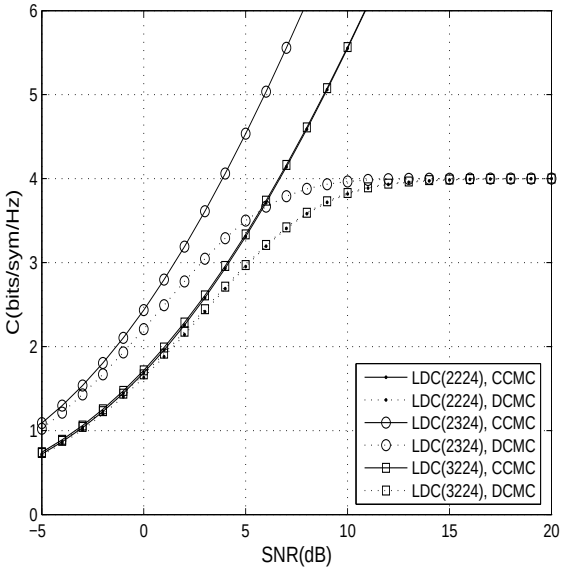

Figure 7.13: The CCMC and DCMC capacity of LDCs having $M = 2, 3$, $N = 2, 3$, $T = 2$ and $Q = 4$ obeying the structure of Figure 7.3 using an ML detector, as plotted using Equations (7.9) and (7.23). For plotting the DCMC capacity, QPSK modulation was employed.

Table 7.1: Coding gains of a family of LDCs have an effective throughput of 1 (bits/sym/Hz).

LDC	Diversity order	Modulation	Coding Gain
LDC(2211)	2	BPSK	17.5dB
LDC(2221)	4	QPSK	23.9dB
LDC(2222)	4	BPSK	23.65dB
LDC(2231)	4	8PSK	20.8dB
LDC(2233)	4	BPSK	23.7dB

Table 7.2: Coding gains of a family of LDCs have an effective throughput of 2 (bits/sym/Hz).

LDC	Diversity order	Modulation	Coding Gain
LDC(2211)	2	QPSK	17.7dB
LDC(2212)	2	BPSK	17.4dB
LDC(2221)	4	16QAM	19.9dB
LDC(2222)	4	QPSK	23.0dB
LDC(2224)	4	BPSK	23.3dB
LDC(2231)	4	64QAM	16.0dB
LDC(2232)	4	8PSK	20.7dB
LDC(2233)	4	QPSK	23.0dB

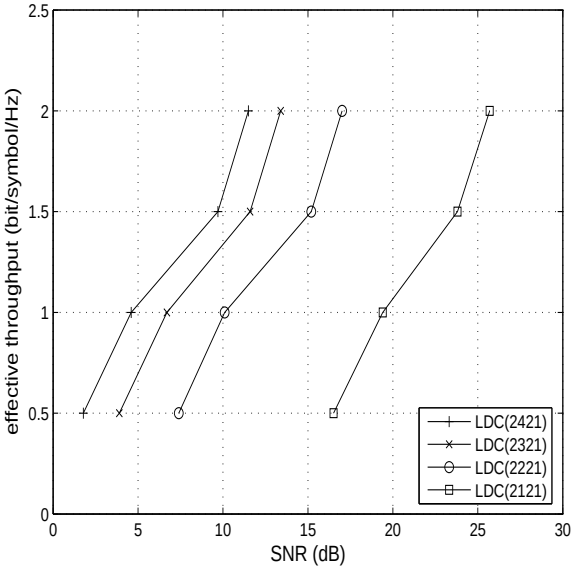

Figure 7.14: Effective throughput recorded at BER $= 10^{-4}$ of a family of LDCs obeying the structure of Figure 7.3 having $M = 2$, $N = 1, 2, 3, 4$, $T = 2$ and $Q = 1$ BER$= 10^{-4}$, when employing QPSK modulation in conjunction with an ML detector.

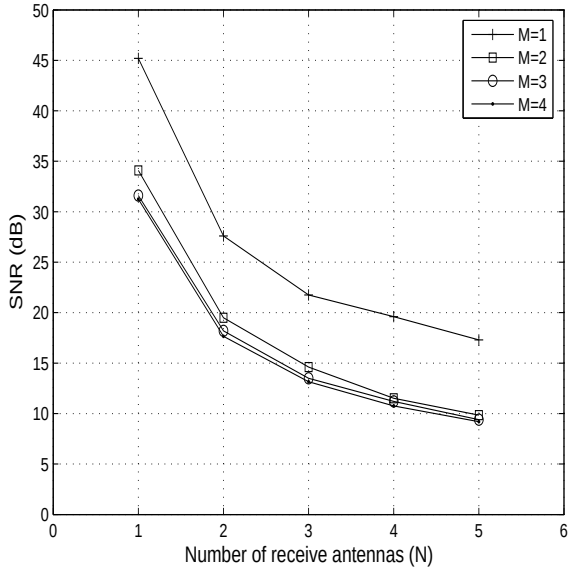

Figure 7.15: SNRs for a family of LDC schemes obeying the structure of Figure 7.3 having $M = 1, 2, 3, 4$, $N = 1, 2, 3, 4, 5$, $T = 2$ and $Q = 4$ to achieve BER $= 10^{-4}$, when employing QPSK modulation in conjunction with an ML detector.

Figure 7.15 plots the SNR requirement against the number of receive antennas N for a family of LDCs having $T = 2$, $Q = 4$ to achieve BER $= 10^{-4}$. For a given number of receive antennas N, the advantage of employing $M = 2, 3, 4$ transmit antennas is up to 6.5dB compared to that of the single antenna scheme, which increases gradually, as the total spatial diversity order is increased from $D = 2$ to $D = 4$. Also observe in Figure 7.15 that increasing N significantly reduces the SNR required to achieve BER $= 10^{-4}$, when we fix the number of transmit antennas M. In fact, the resultant SNR advantage of increasing N from 1 to 5 is about 25dB.

Furthermore, Tables 7.1 and 7.2 characterize the coding gains of a family of LDCs having an effective throughput of 1 and 2 (bits/sym/Hz) respectively, compared to the single antenna system having the identical effective throughput. The corresponding modulation schemes employed are also listed in Tables 7.1 and 7.2. More particularly, for schemes having an effective throughput of 1 (bits/sym/Hz), the largest coding gain is observed, when LDC(2233) was employed in conjunction with Binary Phase Shift Keying (BPSK) modulation, while the BPSK-modulated LDC(2224) arrangement is achieved the highest coding gain for an effective throughput of 2 (bits/sym/Hz).

7.3 Link Between STBCs and LDCs

In this section, we first continue our discourse by reviewing main results in the state-of-art literature related to STBCs, including the so-called *rank criterion* [54], the *determinant criterion* [54], the diversity versus multiplexing gain tradeoff [24] and the diversity versus rate tradeoff [27]. Secondly, we investigate the relationship between all the major representatives of STBCs reported in the open literature and LDCs from both mathematical and design concept perspectives.

7.3.1 Review of Existing STBC Knowledge

The PSEP of mistaking a space-time transmission matrix $\mathbf{S}$ of Equation (7.2) for another matrix $\bar{\mathbf{S}}$, denoted as $p(\bar{\mathbf{S}} \rightarrow \mathbf{S})$, depends only on the distance between the two matrices after transmission through the channel and the noise power, which is upper bounded by [54]:

$$p(\bar{\mathbf{S}} \rightarrow \mathbf{S}) \leq \frac{1}{(\nabla_1 \cdots \nabla_\eta)^N} \cdot (\frac{\rho}{4M})^{\eta N}. \tag{7.26}$$

- **Rank Criterion** [54]. Observe in Equation (7.26) that $(\frac{\rho}{4M})^{\eta N}$ dominates how fast the error decays with the SNR and the total diversity order is determined by ηN. More explicitly, the transmit diversity order of a STBC scheme equals to the minimum rank η of the difference matrix $\mathbf{S}_\triangle = (\mathbf{S} - \bar{\mathbf{S}})$. Accordingly, η has to be found by searching through all distinct codeword pairs $\mathbf{S}$ and $\bar{\mathbf{S}}$, where $\bar{\mathbf{S}} \neq \mathbf{S}$.

- **Determinant Criterion** [54]. Also observe in Equation (7.26) that $\frac{1}{(\nabla_1 \cdots \nabla_\eta)^N}$ has to be minimized, which determines the coding gain of a STBC scheme. Furthermore, the determinant criterion states the minimum of

$$(\nabla_1 \cdots \nabla_\eta) \tag{7.27}$$

  evaluated over all distinct ST codeword pairs determines the achievable coding gain and must be maximized, where the coefficients ∇_i are the non-zero eigenvalues of $\mathbf{S}_\triangle \mathbf{S}_\triangle^H$.

- **Full-diversity**. Using the average PSEP analysis technique of Equation (7.26), it follows that the maximum attainable diversity order of a STBC scheme designed for an $(M \times N)$-element MIMO system is [54] [11]

$$D_{full} = MN, \tag{7.28}$$

  which implies the ST difference matrix $\mathbf{S}_\triangle$ should have full rank.

- **Full-rate**.[1] Since it is possible to transmit up to one 'independent' symbol per antenna per time slot, the symbol rate could be

$$R_{full} = M. \tag{7.29}$$

  Note that LDCs obeying Equation (7.12) are capable of achieving a rate $R_{LDC} > M$, since the transmission matrix is the weighted sum of all the symbols as exemplified in Figures 7.5, 7.6 and 7.8. However, the terminology 'full-rate' remains useful in the discussion of a STBC scheme's CCMC capacity. For example, we have demonstrated in Equation (7.19) that when the LDC's rate $R_{LDC} \geq M$, there is no further improvement in terms of the achievable CCMC capacity. On the other hand, using the term 'full-rate' is inappropriate for quantifying the DCMC capacity, since the corresponding capacity increases upon increasing the rate, as seen in Figure 7.7.

- **Diversity Multiplexing Gain Tradeoff**. The authors of [24] showed that for a MIMO channel, there is a fundamental tradeoff between the achievable diversity gain and the attainable multiplexing gain. More explicitly, achieving a higher spatial multiplexing gain comes at the price of sacrificing diversity gain, when employing a continuous-valued signal alphabet that grows linearly with the logarithm of the SNR. In other words, the diversity and multiple gain tradeoff quantifies how rapidly the throughput of a STBC scheme can increase with the SNRs, while having a certain diversity order. Any transmission arrangement employing a fixed-throughput modulation scheme fails to approach the achievable capacity at high SNRs, because the capacity increases with the SNR, while the throughput of this fixed modem arrangement does not.

- **Rate Diversity Tradeoff**. In [27] [333], the authors argued that in MIMO systems, one can also increase the attainable transmission rate at the expense of a certain loss in the diversity gain, which reflects the associated rate versus diversity tradeoff. This tradeoff is characterized by $R_{STBC} \leq M - D_{tx} + 1$ [27], where D_{tx} denotes the spatial transmit diversity order. With the aid of recent advances in high-rate full-diversity STBCs [28] [320] [334], it has been shown that it is not necessary to sacrifice rate in order to achieve diversity and vice versa. However, considering the rate versus diversity tradeoff is still valuable for the analysis of STBCs obeying a certain structure, which is characterized by the so-called transmit symbol separability defined as follows.

Definition 1. *Transmit Symbol Separability (TSS) :*

- *If **all** the entries of the transmitted ST signal matrix $\boldsymbol{S}$ constitute a transformed version [2] of a single rather than several symbols from a specific modulated signal constellation, then this STBC is said to obey the property of full TSS.*

- *If **some** of the entries in the transmitted ST signal matrix $\boldsymbol{S}$ are constituted by a combination of several symbols from a specific modulated signal constellation, then the STBC is said to obey the property of partial TSS.*

- *If **all** the entries in the transmitted ST matrix $\boldsymbol{S}$ are constituted by a combination of several symbols from a specific modulated constellation, then the STBC is deemed to be non-separable.*

For example, the STBC scheme transmitting the signal $(\frac{1}{\sqrt{2}}s_1 + \frac{1}{\sqrt{2}}s_2)$ is non-separable, while Alamouti's scheme [10] transmits either $\pm s_1$ or $\pm s_1^*$ and hence exhibits full TSS. Let us now consider the family of STBCs from a TSS perspective in more detail.

[1] At this stage it is important to contrast the above-mentioned full-rate, full-diversity schemes, which were primarily conceived for providing transmit and receive diversity against the family of Spatial Division Multiplexing (SDM) MIMOs that were contrived for attaining a multiplexing gain, although they may also provide some diversity gain. The terminology of full-rate and full-diversity schemes is typically invoked in the context of STCs, although quantifying the throughput and diversity gain of SDM schemes would also be beneficial. Nonetheless to the best of our knowledge, no parallel terminology has been used in the context of SDM schemes.

[2] Transformation includes scalar multiplication, Hermitian transpose and conjugate operation.

Property 1. *If a STBC scheme exhibits full TSS, then there exists a tradeoff between the maximum rate and the maximum achievable spatial diversity. If a STBC scheme has the property of partial TSS or it is non-separable, it has the potential to achieve both high-rate and full-diversity at the same time.*

Discussion: When full TSS is maintained, each transmitted symbol only contains the information of its own. Therefore, there is a tradeoff between increasing the achievable rate by sending more independent symbols and increasing the diversity by transmitting redundant information. For example, Alamouti's STBC and the classic V-BLAST scheme achieve two extremes, respectively. On the other hand, even when partial TSS is maintained, some of the transmitted symbols may carry information related to multiple symbols, then it is possible to achieve some grade of diversity, despite operating at high-rate. Furthermore, the family of STBCs does not maintain TSS nonetheless has the potential of achieving high rate and full diversity.

7.3.2 Orthogonal STBCs

STBCs based on orthogonal designs in order to achieve full spatial diversity were first proposed in [10], and later were generalized in [26]. The philosophy behind Orthogonal STBCs (OSTBCs) is that each transmission space-time signal matrix $\mathbf{S}$ satisfies an orthogonality constraint. The orthogonality embedded in $\mathbf{S}$ enables the receiver to decouple the transmitted multi-antenna-coded symbol streams into independently symbols. Thus, simple ML detection can be carried out. Unfortunately, STBCs satisfying the orthogonality constraint exist for only a few specific choices of the parameters ($MNTQ$) and they do not achieve the ergodic capacity of Equation (7.10), especially not when multiple receive antennas are employed.

For example, given a symbol vector $\mathbf{K} = [s_1, s_2]^T$, the simple $\mathbf{G}_2$ space-time code of [26] can be written as

$$\begin{aligned}
\mathbf{G}_2 &= \begin{pmatrix} s_1 & s_2 \\ -s_2^* & s_1^* \end{pmatrix} \\
&= \begin{pmatrix} \alpha_1 & 0 \\ 0 & \alpha_1 \end{pmatrix} + j \begin{pmatrix} \beta_1 & 0 \\ 0 & -\beta_1 \end{pmatrix} + \begin{pmatrix} 0 & \alpha_2 \\ -\alpha_2 & 0 \end{pmatrix} + j \begin{pmatrix} 0 & \beta_2 \\ \beta_2 & 0 \end{pmatrix} \\
&= \begin{pmatrix} 1 & 0 \\ 0 & 1 \end{pmatrix} \alpha_1 + j \begin{pmatrix} 1 & 0 \\ 0 & -1 \end{pmatrix} \beta_1 + \begin{pmatrix} 0 & 1 \\ -1 & 0 \end{pmatrix} \alpha_2 + j \begin{pmatrix} 0 & 1 \\ 1 & 0 \end{pmatrix} \beta_2 \\
&= \mathbf{A}_1 \alpha_1 + j\mathbf{B}_1 \beta_1 + \mathbf{A}_2 \alpha_2 + j\mathbf{B}_2 \beta_2, \qquad (7.30)
\end{aligned}$$

where $s_1 = \alpha_1 + j\beta_1$ and $s_2 = \alpha_2 + j\beta_2$. Observe that Equation (7.30) is fully characterized by the LDC structure of Figure 7.2. Following the similar disassemble process of Equation (7.30), it may be readily shown that other OSTBCs such as the $\mathbf{G}_3$, $\mathbf{G}_4$, $\mathbf{H}_3$ and $\mathbf{H}_4$ schemes of [26] can also be fully specified by the dispersion structure of Figure 7.2.

From the perspective of LDCs, the family of OSTBCs disperses each multi-antenna ST symbol to specific spatial and temporal slots according to a certain pattern, as seen in Equation (7.30). The pattern is fully characterized by the orthogonality of the dispersion matrices. Hence, both full TSS as well as simple ML detection are guaranteed.

It is worth mentioning that the OSTBCs $\mathbf{H}_3$ and $\mathbf{H}_4$ [26] exhibit partial TSS, whereas their counterparts $\mathbf{G}_3$ and $\mathbf{G}_4$ [26] possess the property of full TSS. Therefore, $\mathbf{H}_3$ and $\mathbf{H}_4$ achieve a higher rate than the $\mathbf{G}_3$ and $\mathbf{G}_4$ codes, although none of them are capable of achieving a symbol rate higher than 1.

7.3.3 Quasi-Orthogonal Space-Time Block Codes

The main benefits of an orthogonal design are their simple decoding and full transmit diversity potential. When relaxing the simple separate decoding property of the multi-antenna streams, a potentially higher rate can be achieved. In [15], the family of the so-called Quasi-Orthogonal Space-Time Block Codes (QOSTBCs) was proposed for the sake of pursuing high-rate transmission, while maintaining a certain diversity order. The class of QOSTBCs is capable of decoupling the symbol streams into groups, where each decoding group contains two symbols rather than a single symbol. Hence, a higher ML decoding complexity is imposed compared to that of the OSTBCs.

The construction of QOSTBCs can be directly derived from that of OSTBCs. For example, a (4×4)-antenna QOSTBC codeword matrix is given by [15]:

$$\mathbf{S} = \begin{pmatrix} \mathbf{G}_2(s_1, s_2) & \mathbf{G}_2(s_3, s_4) \\ -\mathbf{G}_2(s_3, s_4)^* & \mathbf{G}_2(s_1, s_2)^* \end{pmatrix}. \tag{7.31}$$

Therefore, it is straight-forward to rewrite the QOSTBC transmission matrix of Equation (7.31) using the LDC structure of Figure 7.2 following the same procedure as in the context of Equation (7.30). Compared to the $\mathbf{G}_4$ OSTBC code of [26], the QOSTBC of Equation (7.31) achieves twice the symbol rate at the cost of sacrificing half of the transmit diversity order, which constitutes a manifestation of the rate versus diversity tradeoff formulated in the context of Property 1.

Clearly, the LDC structure of Figure 7.2 subsumes the family of QOSTBCs. Similarly to OSTBCs, QOSTBCs disperse each multi-antenna ST symbol to specific space-time slots obeying the relaxed orthogonality constraint. Observe from Equation (7.31) that full TSS is also ensured, which implies that the class of QOSTBCs obeys the rate versus diversity tradeoff.

In later works of [335] [336], the idea of constellation rotation was introduced in order to overcome the potential diversity loss. However, the associated diversity gain improvement accrued from modulation diversity [337], rather than from the spatial diversity addressed in this treatise.

7.3.4 Linear STBCs Based on Amicable Orthogonal Designs

Although QOSTBCs exhibit a higher design flexibility than OSTBCs, they are still unsuitable for MIMO systems having flexible $(MNTQ)$ parameter combinations and they are unable to achieve either full diversity or a symbol rate higher than 1. The further pursuit of high-diversity STBCs leads to the design of Linear Space-Time Block Codes (LSTBC) [338] [32] [339] [340], which are defined as:

$$\mathbf{S} = \sum_{q=1}^{Q} (\alpha_q \mathbf{A}_q + j\beta_q \mathbf{B}_q). \tag{7.32}$$

The philosophy behind LSTBCs is to find specific orthogonal dispersion matrices $\mathbf{A}_q$ and $\mathbf{B}_q$, which are capable of separating Q transmitted symbols at the receiver. In other words, Q symbols are mapped to M number of transmit antennas with the aid of a set of orthogonal matrices.

To accomplish this design goal, the dispersion matrices designed for real-valued symbols have to satisfy the following requirement [338]

$$\mathbf{A}_{i_1}\mathbf{A}_i^H = \mathbf{I} \qquad (i = i_1), \tag{7.33}$$

$$\mathbf{A}_{i_1}\mathbf{A}_i^H = -\mathbf{A}_i\mathbf{A}_{i_1}^H \qquad (i \neq i_1), \tag{7.34}$$

where $i, i_1 = 1, 2, \ldots, Q$. Full spatial diversity order is guaranteed by Equation (7.33), while Equation (7.34) ensures that the set of dispersion matrices are orthogonal to each other. For

complex-valued modulated symbols, the dispersion matrices $\mathbf{A}_q$ and $\mathbf{B}_q$ should satisfy [338]

$$\begin{aligned}
\mathbf{A}_{i_1}\mathbf{A}_i^H &= \mathbf{I}, \\
\mathbf{B}_{i_1}\mathbf{B}_i^H &= \mathbf{I}, \qquad (i = i_1), \qquad (7.35) \\
\mathbf{A}_{i_1}\mathbf{A}_i^H &= -\mathbf{A}_i\mathbf{A}_{i_1}^H, \\
\mathbf{B}_{i_1}\mathbf{B}_i^H &= -\mathbf{B}_i\mathbf{B}_{i_1}^H, \qquad (i \neq i_1), \qquad (7.36) \\
\mathbf{A}_{i_1}\mathbf{B}_i^H &= \mathbf{B}_i\mathbf{A}_{i_1}^H, \qquad (1 < i, i_1 < Q). \qquad (7.37)
\end{aligned}$$

Equation (7.35) ensures that full spatial transmit diversity order can be achieved and Equation (7.36) ensures the orthogonality within the dispersion matrices $\mathbf{A}_i$ and $\mathbf{B}_i$. The orthogonality between the dispersion matrices $\mathbf{A}_i$ and $\mathbf{B}_i$ is guaranteed by Equation (7.37).

Recall that the family of OSTBCs discussed in Section 7.3.2 obey the orthogonal constraint of

$$\mathbf{S}\mathbf{S}^H = \mathbf{I}. \qquad (7.38)$$

If the LSTBCs obeying the structure of Equation (7.32) satisfy the orthogonal constraint of Equation (7.38), it can be shown that the set dispersion matrices of $\mathbf{A}_q$ and $\mathbf{B}_q$ has to satisfy Equations (7.36), (7.36) and (7.37). The design of such set of matrices is referred to as *amicable orthogonal* design and more details can be found in [341]. In other words, LSTBCs constitute a family of LDCs obeying the structure of Figure 7.2 that satisfy the orthogonality constraint of Equation (7.38). Thus, it becomes clear that the LSTBCs have to obey the rate versus diversity tradeoff, owing to their full TSS property, as stated in Property 1.

7.3.5 Single-Symbol-Decodable STBCs Based on QOSTBCs

Observe in Equations (7.35), (7.36) and (7.37) that the orthogonality imposed enables the transmitted ST symbol streams to be separated by a set of dispersion matrices $\mathbf{A}_q$ and $\mathbf{B}_q$. However, ensuring the orthogonality for each of the Q transmitted symbols according to Equation (7.37) may not be necessary, if the real and imaginary parts of a transmitted ST symbol are jointly detected. If we eliminate this constraint, the requirement for the set of the dispersion matrices becomes [342]

$$\begin{aligned}
\mathbf{A}_{i_1}\mathbf{A}_i^H &= -\mathbf{A}_i\mathbf{A}_{i_1}^H, \quad \mathbf{B}_{i_1}\mathbf{B}_i^H = -\mathbf{B}_i\mathbf{B}_{i_1}^H \qquad (i \neq i_1), \qquad (7.39) \\
\mathbf{A}_{i_1}\mathbf{B}_i^H &= \mathbf{B}_i\mathbf{A}_{i_1}^H \qquad (i \neq i_1). \qquad (7.40)
\end{aligned}$$

Compared to Equation (7.37), Equation (7.40) excludes the scenarios, where $i = i_1$, which eliminates the orthogonality within each transmitted symbols of Figure 7.2. In the open literature, STBCs obeying Equations (7.39) and (7.40) are referred as Single-Symbol-Decodable Space-Time Block Codes (SSD-STBC) [341] [342].

From another point of view, SSD-STBCs constitute the class of LDCs having the structure of Figure 7.2 that obeys the constraints of Equations (7.39) and (7.40). Consequently, the full TSS property is maintained, which inevitably imposes the rate versus diversity tradeoff.

Note that the STBCs presented in Sections 7.3.2 to 7.3.5 can be characterized using the LDC structure of Figure 7.2, since they all possess some degrees of orthogonality. However, the orthogonality imposed not only restricts the design of STBCs, but imposed the rate versus diversity tradeoff [333] characterized by having the property of full TSS.

7.3.6 Space-Time Codes Using Time Varying Linear Transformation

For the sake of achieving high-rate and full diversity in the context of STBCs, the authors of [30] proposed a class of STBCs employing unitary Time Variant Linear Transformation (TVLT) TVLT.

A TVLT code can be represented using the notation of TVLT(M, N, T, MT), where the MT symbols mapped to the M antennas are transmitted using T time slots and received by N antennas. Hence, maintaining a symbol rate of $R = M$. More explicitly, a TVLT scheme firstly separates MT symbols into T sub-streams or layers, which contains M symbols. Then, each sub-stream is separately modulated by a specific vector for transmission in a single time slot. For example, a TVLT(2224) scheme disperses a sub-stream containing symbols s_1 and s_2 during the first time slot and disperses the other sub-stream containing symbols s_3 and s_4 during the second time slot. This process is expressed as follows:

$$\mathbf{S} = \begin{pmatrix} a_1^{11} & 0 \\ a_1^{21} & 0 \end{pmatrix} s_1 + \begin{pmatrix} a_2^{11} & 0 \\ a_2^{21} & 0 \end{pmatrix} s_2 + \begin{pmatrix} 0 & a_3^{12} \\ 0 & a_3^{32} \end{pmatrix} s_3 + \begin{pmatrix} 0 & a_4^{12} \\ 0 & a_4^{22} \end{pmatrix} s_4, \tag{7.41}$$

where $a_q^{i,j}$ denotes the entries of the dispersion matrices $\mathbf{A}_q$ of Equation (7.12). Furthermore, the rank criterion [54] discussed in Section 7.3.1 states that the minimum rank of the difference matrix $\mathbf{S}_\triangle = (\mathbf{S} - \bar{\mathbf{S}})$ equals to the transmit diversity order of a STBC scheme. For the TVLT(2224) example of Equation (7.41), the difference transmission matrix is given by:

$$\mathbf{S}_\triangle = \begin{pmatrix} a_1^{11} & 0 \\ a_1^{21} & 0 \end{pmatrix} s_{1\triangle} + \begin{pmatrix} a_2^{11} & 0 \\ a_2^{21} & 0 \end{pmatrix} s_{2\triangle} + \begin{pmatrix} 0 & a_3^{12} \\ 0 & a_3^{32} \end{pmatrix} s_{3\triangle} + \begin{pmatrix} 0 & a_4^{12} \\ 0 & a_4^{22} \end{pmatrix} s_{4\triangle}. \tag{7.42}$$

Observe in Equation (7.42) that maintaining full transmit diversity is guaranteed, as long as the non-zero columns of the dispersion matrices are independent of each other.

Clearly, the class of TVLT codes obeying similar structure as to Equation (7.41) constitute a subset of LDCs following the schematic of Figure 7.3. The TVLT codes can be obtained using the LDC model of Equation (7.12), under the constraint of dispersing each sub-stream to a single time slot. In other words, the different sub-streams are separated using time-division.

7.3.7 Threaded Algebraic Space-Time Codes

Recently, another family of STBCs has been proposed in order to achieve both high-rate and full diversity, which is referred as to Threaded Algebraic Space-Time Block Codes (TASTBC) [31] [319] [178]. The main rationale behind this framework is to partition the Q symbols into $\acute{L}$ ($\acute{L} \leq M$) sub-streams and disperse each sub-stream to a $(M \times 1)$-element vector with the aid of a set of dispersion matrices. The resultant vector is arranged diagonally into the space-time transmission matrix $\mathbf{S}$ of Figure 7.1 in order to span across the entire spatial and temporal domain encompassed by the TASTBC design. The $(M \times 1)$-element dispersed vector is referred as a 'thread' in [31]. The $\acute{L}$ number of dispersed vectors are designed to be 'orthogonal' to each other by employing an appropriately chosen scaling factor [31].

In order to expound a little further, we use the well-known $\mathbf{G}_2$ space-time matrix to demonstrate the philosophy of TASTBCs, where a $\mathbf{G}_2$ is given by

$$\mathbf{G}_2 = \begin{pmatrix} s_1 & s_2 \\ -s_2^* & s_1^* \end{pmatrix}. \tag{7.43}$$

With a small modification, Alamouti's scheme can be written as follows:

$$\mathbf{G}_2 = \begin{pmatrix} s_1 & \sqrt{-1} \cdot s_2 \\ \sqrt{-1} \cdot s_2^* & s_1^* \end{pmatrix}. \tag{7.44}$$

It is straightforward to verify that the modified representation seen in Equation (7.44) has the same properties as the original Alamouti scheme of Equation (7.43). However, the modified representation portrayed in Equation (7.44) falls within the scope of TASTBCs. More particularly, the first sub-stream containing the information symbol s_1 is dispersed by:

$$\acute{L}_1 \quad = \quad \begin{pmatrix} s_1 \\ s_1^* \end{pmatrix} = \begin{pmatrix} 1 \\ 1 \end{pmatrix} \alpha_1 + j \begin{pmatrix} 1 \\ -1 \end{pmatrix} \beta_1. \tag{7.45}$$

Table 7.3: Diversity, rate, complexity and design flexibility comparison for various STBCs.

STBC	Rate	Diversity	TSS	Complexity	Orthogonality	Flexibility
OSTBC [54]	≤ 1	MN	full	1	full	minimum
LSTBC [338]	≤ 1	MN	full	1	full	$\downarrow$
SSD-STBC [341]	1	$MN/2$	full	1	$\downarrow$	$\downarrow$
QOSTBC [15]	1	$MN/2$	full	2	$\downarrow$	$\downarrow$
TVLT [30]	M	MN	partial	M	$\downarrow$	$\downarrow$
TASTBC [31]	M	MN	partial	M	$\downarrow$	$\downarrow$
LDC [29] [28]	M	MN	non	Q	non	maximum

Similarly, the second sub-stream containing symbol s_2 is dispersed by:

$$\acute{L}_2 \quad = \quad \sqrt{-1} \cdot \begin{pmatrix} s_2 \\ s_2^* \end{pmatrix} = \sqrt{-1} \cdot \begin{pmatrix} 1 \\ 1 \end{pmatrix} \alpha_2 + j\sqrt{-1} \cdot \begin{pmatrix} 1 \\ -1 \end{pmatrix} \beta_2. \tag{7.46}$$

Note that in this case $\sqrt{-1}$ is the aforementioned scaling factor, which that guarantees the orthogonality between two threads.

The example of Equations (7.45) and (7.46) demonstrates that TASTBCs can be fully characterized by the general LDC structure of Figure 7.2. More explicitly, the orthogonality between the threads imposed on the space-time codeword **S** of Figure 7.2 restricts each sub-stream of TASTBC to only partially explore the ST recourses available. By contrast, LDC schemes disperse each information symbol to all the space-time dimensions available.

It also interesting to compare the TVLT and TASTBC schemes. They all share the same concept of dividing the Q symbols into sub-streams and then disperse each sub-stream independently. The separation of sub-streams is achieved by time division for TVLT schemes, whereas the TASTBC arrangements employ a unique scaling factor for differentiating and separating the sub-streams, which was $\sqrt{-1}$ in the explore of Equations (7.45) and (7.46).

7.3.8 Summary

We have argued in Sections 7.3.2 to 7.3.7 that the family of OSTBCs, QOSTBCs, LSTBCs, SSD-STBCs, TVLTs and TASTBCs can be described using the unified structure of LDCs provided in Figures 7.2 and 7.3, where LDC($MNTQ$) represents a MIMO system employing M transmit and N receive antennas, transmitting Q symbols using T time slots. All of the representatives of this LDC family imposed different degrees of 'orthogonality' on the general LDC framework of Figures 7.2 and 7.3. In this section, we compare the above-mentioned STBCs in terms of their diversity order, rate as well as complexity and characterize the evolution of STBCs.

Assuming that symbol-based ML decoding is used and the same modulation scheme is employed by all the STBCs considered, the decoding complexity ϖ imposed is associated with the number of symbols decoded at a time. The associated design flexibility can be quantified in terms of the number of practical MIMO solutions for a specific parameter combination of (M, N, T, Q).

In Table 7.3, we listed the rate, diversity and estimated decoding complexity of the diverse STBCs that have been discussed in Sections 7.3.2 to 7.3.7. Let us now continue with their brief characterization.

- Maintaining at least partial TSS constitutes a necessary condition for the design of high-rate, full-diversity STBCs. In simple physical terms, the TSS characterizes the degree of inter-dependence among the symbols within the transmitted space-time matrix **S**. If each

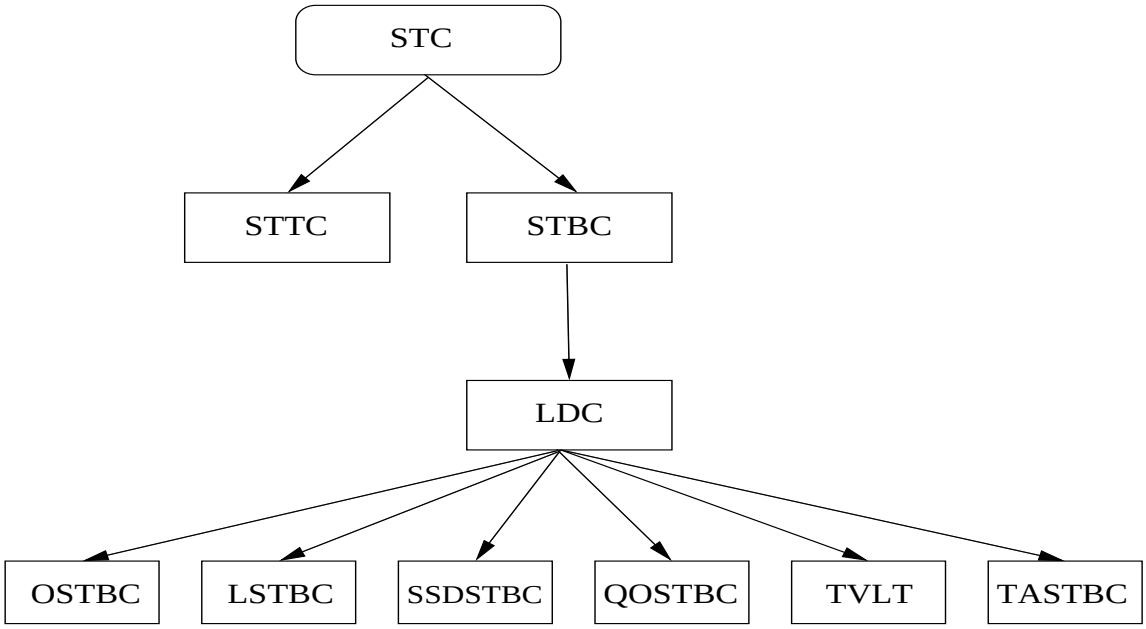

Figure 7.16: Classification of Space-Time Coding (STC) techniques.

transmitted signal encapsulates the information of more than one information symbol, then high-rate and full-diversity can be potentially achieved at the same time. By contrast, if each transmitted signal encapsulates a single original input symbol's information, then the corresponding STBCs can only achieve either full diversity or a rate $R_{STBC} \leq 1$, as shown in Table 7.3.

- When decreasing the degree of orthogonality embedded in the space-time matrix **S** of Figure 7.1, typically the degree of design flexibility is increased. For example, the OSTBC design of Section 7.3.2 enjoys simple single symbol ML decoding as a result of its full orthogonality. However, it has a very limited choice of dispersion matrices and the number of transmit antennas supported is limited. By contrast, LDCs' non-orthogonal structure of Figure 7.3 potentially facilitates an unlimited number of dispersion matrices for arbitrary MIMO antenna configurations, as shown in Equation (7.19).

- Observe from Table 7.3 that the degree of TSS is useful for characterizing the decoding complexity imposed. For example, high-rate full-diversity LDCs of [28] have to jointly decode Q symbols per space-time block. On the other hand, for example, the QOSTBCs of Section 7.3.3 is capable of separating the symbols into two-symbol decoding pairs, owing to their orthogonality.

- The flexibility of LDCs is also related to the number of space-time slots used by each symbol. For example, Equation (7.41) demonstrates the structure of TVLT [30] codes, which disperses each symbol merely to M out of the total MT number of space-time slots, whereas LDCs ensure that each space-time slot contains information related to all the information symbols, as characterized in Equation (7.12).

Finally, as illustrated in Figure 7.16, we portray the family of LDCs as a prominent class of space-time processing techniques, uniting the class STBCs [327]. More explicitly, the family of Space-Time Coding (STC) may be classified in two major categories, namely STBCs and Space-Time Trellis Codes (STTC) [54] [327] [52]. The general LDC structure of Figures 7.2 and 7.3 is capable of providing diverse solutions to meet the challenge of achieving both full-diversity

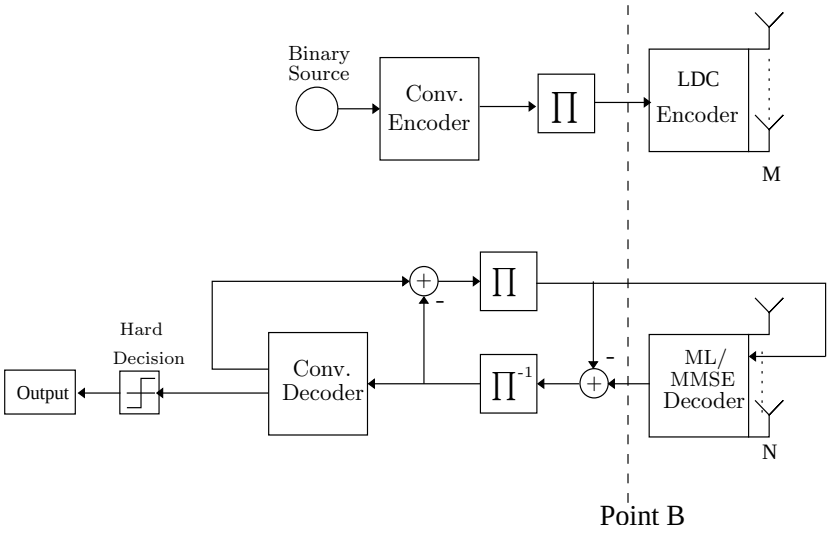

Figure 7.17: Schematic of a serial concatenated RSC-coded LDC system employing iterative decoding.

and high-rate. Hence, LDCs subsume many existing space-time block coding schemes, as seen in Figure 7.16.

7.4 EXIT Chart Based Design of LDCs

7.4.1 Analyzing Iteratively-Detected LDCs

In this section, we analyze a serial concatenated channel-coded LDC scheme using iterative decoding. The system design is approached from a capacity maximization perspective with the aid of EXIT charts. More explicitly, the EXIT chart analysis enables us to estimate the maximum achievable rate of the proposed channel-coded LDC scheme using both ML and MMSE detectors, when employing the LDCs optimized in Section 7.2.4. Provided the capacity results illustrated in Section 7.2.5, we will demonstrate how far the serial concatenated system operates from LDC's DCMC capacity.

Figure 7.17 plots the schematic of a serial concatenated RSC-encoded LDC system employing iterative decoding. The information bits are firstly encoded by a convolution code. Here a simple half-rate Recursive Systematic Convolutional (RSC) RSC(215) code was used. Then, the interleaved bits are fed into the LDC encoder of Figure 7.17. Here, the LDC block also incorporates bit-to-symbol mapping using Gray labelling. The dispersion operation maps each symbol vector $\mathbf{K}$ containing Q symbols to the space-time transmission matrix $\mathbf{S}$ defined in Equation (7.12). At the receiver, extrinsic information is exchanged between the SISO ML/MMSE and RSC detectors. More details about how the extrinsic information is calculated can be found in [343] and the references within. This simple SCC scheme employing iterative decoders has the advantage of exploring both the spatial diversity provided by the LDCs and the temporal diversity offered by the RSC code. To show the exchange of extrinsic information, the right hand side of Point B seen in Figure 7.17 is considered as the *inner* code and the left side is the *outer* code.

The EXIT chart of the half-rate RSC-coded LDC(2224) scheme of Figure 7.17 having a diversity order of $D = 4$ and using the ML decoder is shown in Figure 7.18. In this treatise, I_A denotes the *a-priori* information available for the *inner* code, which is provided by the extrinsic output of the *outer* code. By contrast, I_E denotes the extrinsic output of the *inner* code, which also contributes to the *a-priori* input for the *outer* code. Observe that the intersection points of the *inner* and

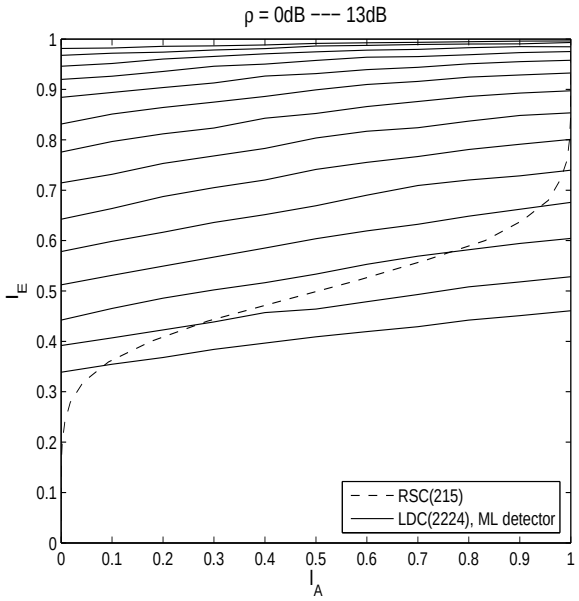

Figure 7.18: EXIT chart of the RSC(215)-coded LDC(2224) scheme of Figure 7.17 having a diversity order of D=4, when employing an **ML detector** as well as using QPSK modulation.

outer EXIT curves approach $I_A = 1.0$, as the SNR increases, where an infinitesimally low BER is expected.

Figure 7.19 shows the EXIT chart of the RSC(215)-coded LDC(2224) scheme having a diversity order of $D = 4$ and using an MMSE detector. Note that the area under the EXIT curves using the MMSE detector is smaller than that of its ML detection counterpart of Figure 7.18 for any given SNR.

The so-called 'area property' [303] [306] of EXIT charts may be formulated by stating that the area under the *outer* RSC code's EXIT curve is approximately equal to its code rate R_{out}. Thus, if we assume that the area under the EXIT curve of an *outer* code can be perfectly matched to the area under the *inner* code's EXIT curve at any SNR ρ, then it is possible to approximate the **maximum achievable rate** of a serial concatenated scheme by evaluating the area under the EXIT curves, given the rate of the *inner* block R_{in}, which is expressed as:

$$C(\rho) = log_2(L) \cdot R_{in} \cdot R_{out}, \tag{7.47}$$

where R_{out} is approximated by the area under the *inner* code's EXIT curve and L-PSK or L-QAM modulation is used.

Using Equation (7.47), we are able to plot the maximum achievable rates of the proposed serial concatenated RSC-coded LDC(2224) scheme using both ML and MMSE detectors in Figure 7.20. Observe that the system employing ML detection achieved a higher rate across the entire SNR region, since more decoding complexity was invested. Note that the achieved rate loss associated with employing an MMSE detector compared to the ML detector is not constant. The maximum rate loss was recorded at about $\rho = 7$dB. It is interesting to compare LDC(2224) scheme's maximum achievable rates employing the ML detector to its DCMC capacity curve plotted in Figure 7.7, where we observe that the two curves appear to be identical. This observation implies that it is feasible to achieving the MIMO channel's capacity using a SCC scheme under the assumption of using a variable-rate *outer* code.

To illustrate this a little further, Figure 7.21 quantifies the MMSE decoder's maximum achievable rate loss compared to that of the ML detector using the above-mentioned EXIT-aided method

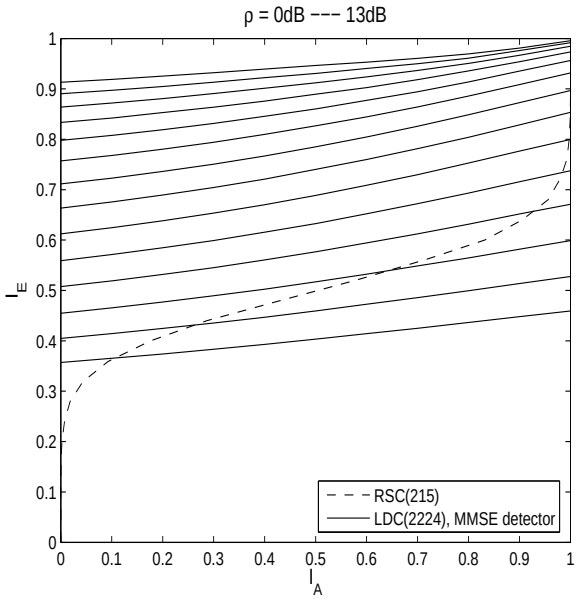

Figure 7.19: EXIT chart of the RSC(215)-coded LDC(2224) scheme of Figure 7.17 having a diversity order of D=4, when employing an **MMSE detector** as well as using QPSK modulation.

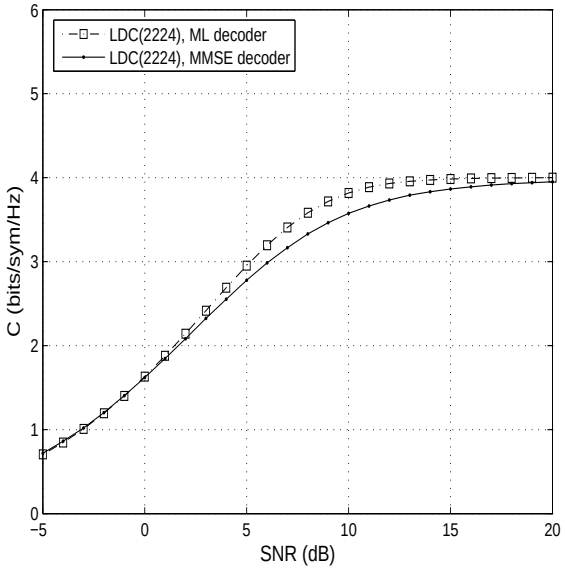

Figure 7.20: Maximum achievable rates comparison of half-rate RSC-coded LDC(2224) scheme of Figure 7.17 using QPSK modulation, when employing both ML and MMSE detectors.

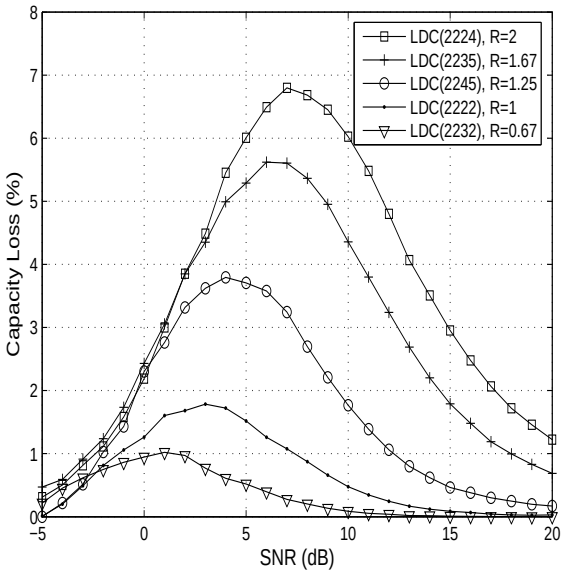

Figure 7.21: MMSE detector's maximum achievable rate loss for a group of RSC-coded LDC schemes of Figure 7.17 using QPSK modulation, when recorded at Point B of Figure 7.17.

as a function of the SNR. For the rate-two LDC(2224) scheme, the peak of the bell-shaped capacity loss curve appears at $\rho = 7$dB, where approximately 6.8% throughput is lost. When lower rate LDCs were employed, the rate loss was decreased and the peak of the curves gradually shifted to lower SNRs, as seen in Figure 7.21.

Ideally, in order to achieve an infinitesimally low BER, the *inner* and *outer* EXIT curves should only intersect at the $(I_A, I_E) = (1.0, 1.0)$ point. If this condition is satisfied, then a so-called convergence tunnel [344] appears in the EXIT chart. Even if there is no open tunnel in the EXIT chart leading to the $(1.0, 1.0)$ point, but the two curves intersect at a point close to $I_A = 1.0$, then a sufficiently low BER may still be achievable. Observe in Figure 7.19 that the intersection of *inner* and *outer* EXIT curves takes place before reaching the $I_A = 1.0$ point, unless the SNR is sufficiently high.

In Figure 7.22, we characterize the BER performance of the RSC(215)-coded LDC(2224) having a diversity order of D=4, while using QPSK modulation in conjunction with an MMSE decoder. Since the slope of the EXIT curves shown in Figure 7.19 is relatively low, the SCC scheme of Figure 7.17 reaches the best attainable performance after $k = 4$ iterations. The BER illustrated in Figure 7.22 gradually decreases upon increasing the SNRs, which corresponds to the fact that the *inner* and *outer* EXIT curves' intersection point shifts to $(1.0, 1.0)$ point on the EXIT chart with the SNRs, as seen in Figure 7.19.

Figure 7.23 compares the EXIT curves of RSC(215)-coded LDC schemes of Figure 7.17 having $M = 2$, $N = 2$, $T = 2$ and $Q = 1, 2, 3, 4$, when employing QPSK modulation in conjunction with an MMSE decoder. Observe that when Q increases, the area under the EXIT chart decreases. It is also interesting to observe in Figure 7.23 that the curves become more and more horizontal when Q is decreased. In fact, when we have $Q = 1$, the EXIT curve becomes a horizontal line. Recall that Gray mapping is employed for the information symbols, hence for the case of $Q = 1$, there is no extrinsic information induced improvement, as the *a-priori* information increases. However, when we have $Q > 1$, each transmitted symbol is subjected to independent fading, and hence Gray mapping may no longer guarantee the largest Euclidean distance in a $2Q-$dimensional space. Therefore, the resultant EXIT curves' slope is increased, as Q increases.

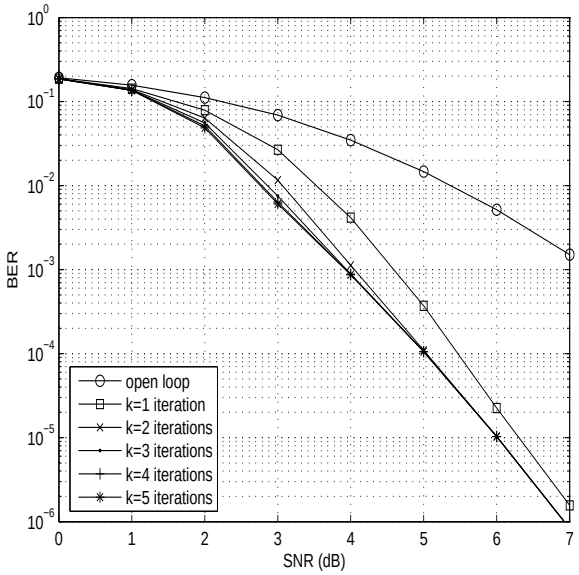

Figure 7.22: BER performance of the RSC(215)-coded LDC(2224) scheme of Figure 7.17 having a diversity order of D=4 using QPSK modulation in conjunction with an MMSE detector.

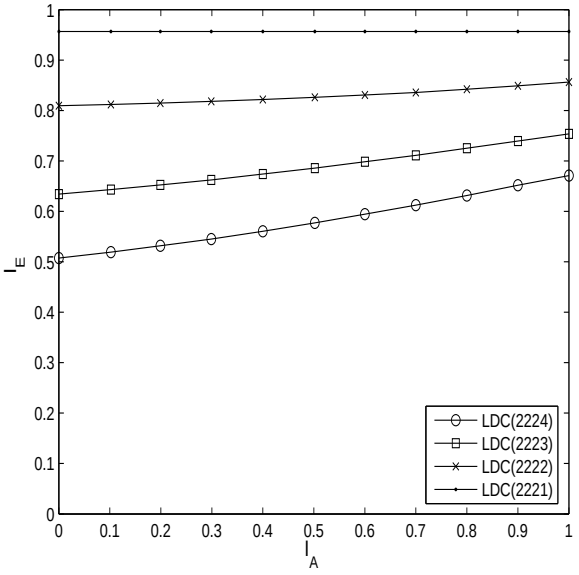

Figure 7.23: EXIT chart comparison for the QPSK modulated RSC(215)-coded LDC(222Q) schemes of Figure 7.17 at $\rho = 3$dB, where we have $Q = 1, 2, 3, 4$ and using an MMSE detector.

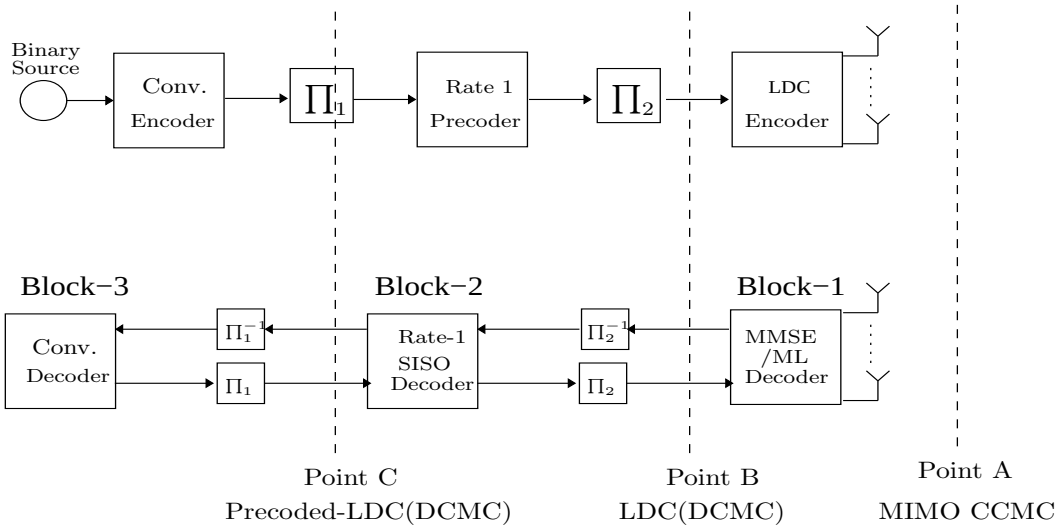

Figure 7.24: Schematic of a three-stage RSC-coded and precoder-aided LDCs using iterative decoding.

Despite its good BER performance, this simple convolutional coded LDC scheme of Figure 7.17 has a deficiency. More explicitly, the flatness of the EXIT curves seen in Figure 7.23 prevents the intersection from reaching the $(I_A, I_E) = (1.0, 1.0)$ point. Therefore an infinitesimally low BER can only be achieved at high SNRs. Driven by the desire of designing iterative decoding aided LDCs having an infinitesimally low BER, the family of convolutional-coded precoder-aided LDCs is proposed in the next section.

7.4.2 Analyzing Iteratively-Detected Precoded LDCs

The schematic of a RSC-coded and precoder-aided LDC system is shown in Figure 7.24. Compared to the non-precoded scheme of Figure 7.17, a rate-1 precoder is placed between the convolutional encoding block and the LDC encoder, complemented by a second interleaver. The resultant schematic constitutes a three-stage system, where the extrinsic information is passed through the three decoder blocks according to a pre-defined activation order. Block-1 of Figure 7.24, namely the MMSE/ML decoder, receives its input information from the MIMO channel and its feedback information from the precoder's decoder. The intermediate Block-2 of Figure 7.24 benefits from the information provided by both the convolutional decoder and the LDC decoder. Its two outputs are forward to the surrounding blocks at its both sides, respectively. An extrinsic information exchange cycle between Block-1 and Block-2 of Figure 7.24 is defined as an *inner* iteration. The third decoding block, namely the convolutional decoder exchanges information with the precoder. Hence, a single associated extrinsic information exchange cycle between the precoder's decoder and the convolutional decoder is referred to as an *outer* iteration.

Let us briefly discuss the features of the system structure of Figure 7.24. For example, if we split the system into two constituent parts at Point B of Figure 7.24, Block-1 has the same EXIT characteristics as the two-stage system of Figure 7.17, where the $(I_A, I_E) = (1.0, 1.0)$ point cannot be reached at all, unless the associated SNR is sufficiently high. However, if we split the system at Point C of Figure 7.24, we will demonstrate at a later stage that the *inner* Precoded Linear Dispersion Codes (PLDC) become capable of reaching the $(I_A, I_E) = (1.0, 1.0)$ point. Observe furthermore in Figure 7.24 that the equivalent channel at Point C is recursive i.e. has an Infinite Impulse Response (IIR) as a benefit of using the precoder, whereas the equivalent channel at Point B is non-recursive.

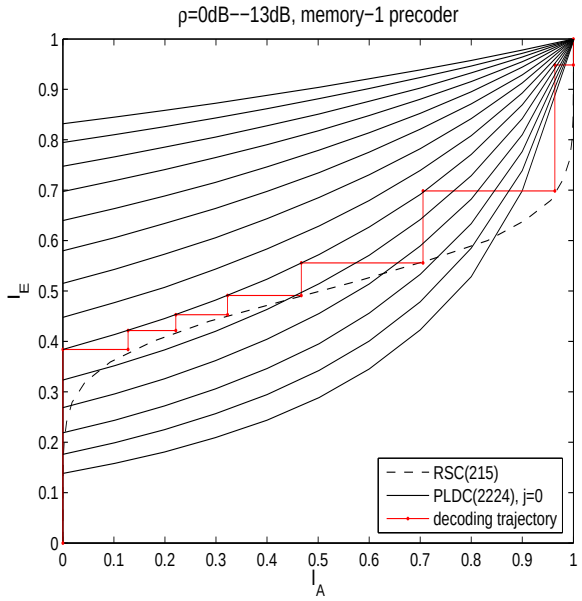

Figure 7.25: EXIT chart of the RSC(215)-coded memory-one precoder-aided LDC(2224) scheme of Figure 7.24 using QPSK modulation in conjunction with an MMSE detector, when using $j = 0$ inner iterations and the decoding trajectory was recorded at $\rho = 5$dB.

It was argued for example in [345] that the activation order of the decoding blocks of a three-stage system substantially affects both the achievable performance as well as the detection complexity imposed at the receiver. The decoding activation order of the proposed three-stage system of Figure 7.24 is set to $[(\text{Block-1, Block-2})^{j+1}, \text{Block-3}]^{k+1}$, where j and k are the number of *inner* and *outer* iterations, respectively. More explicitly, $(j + 1)$ iterations are invoked between Block-1 and Block-2 of Figure 7.24, followed by exchanging their joint extrinsic information with Block-3 $(k+1)$ times. We propose to answer the question of how many *inner* iterations per *outer* iteration are necessary, from the capacity approaching perspective. Ideally, a small value of j is desirable in the interest of minimizing the overall decoding complexity. In order to carry out a comparison between the non-precoded scheme of Figure 7.17 and the precoded schemes of Figure 7.24, in our forthcoming investigations a half-rate RSC(215) code is employed as the *outer* code and the length of the interleaver is set to 10^6 bits.

Figure 7.25 plots the EXIT chart of the three-stage RSC(215)-coded PLDC(2224) scheme of Figure 7.24, when using $j = 0$ *inner* iterations and the associated decoding trajectory was recorded at $\rho = 5$dB. Observe that the employment of the precoder facilitates the converge of all the *inner* EXIT curves to the $(I_A, I_E) = (1.0, 1.0)$ point, since the precoder is capable of gleaning extrinsic information from all the bits within a frame. By contrast, for the non-precoded scheme of Figure 7.17, the extrinsic information can only be extracted from the bits within one information symbol. The decoding trajectory shown at $\rho = 5$dB required $k = 6$ *outer* iterations to achieve an infinitesimally low BER.

When $j = 1$ *inner* iteration is employed in the three-stage RSC(215)-coded PLDC (2224) scheme of Figure 7.24, the corresponding EXIT chart is plotted in Figure 7.26. We observe that the area under the EXIT curves is higher than that of the system employing $j = 0$ *inner* iterations, as characterized previously in Figure 7.25, which implies having potentially increased maximum achievable rates. Note that the increased-area open EXIT tunnel between the *inner* and *outer* code's EXIT curves benefits the decoding trajectory recorded at $\rho = 5$dB, since only $k = 4$ *outer* iterations are necessary to converge to the $(I_A, I_E) = (1.0, 1.0)$ point.

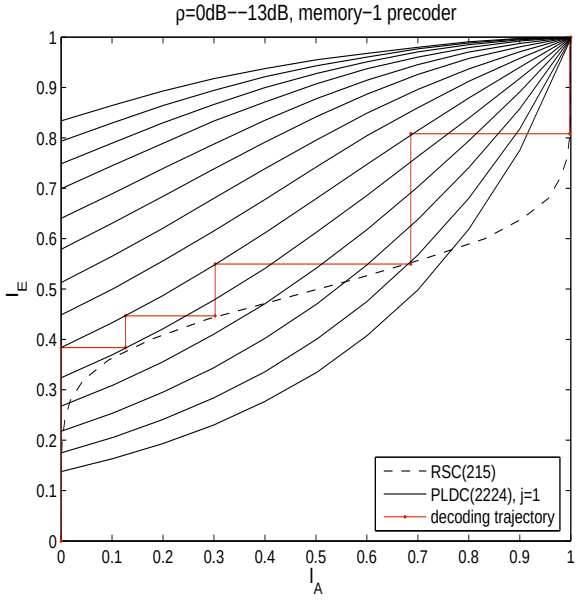

Figure 7.26: EXIT chart of the RSC(215)-coded memory-one precoder-aided LDC(2224) scheme of Figure 7.24 using QPSK modulation in conjunction with an MMSE detector, when using $j = 1$ inner iterations and the decoding trajectory was recorded at $\rho = 5$dB.

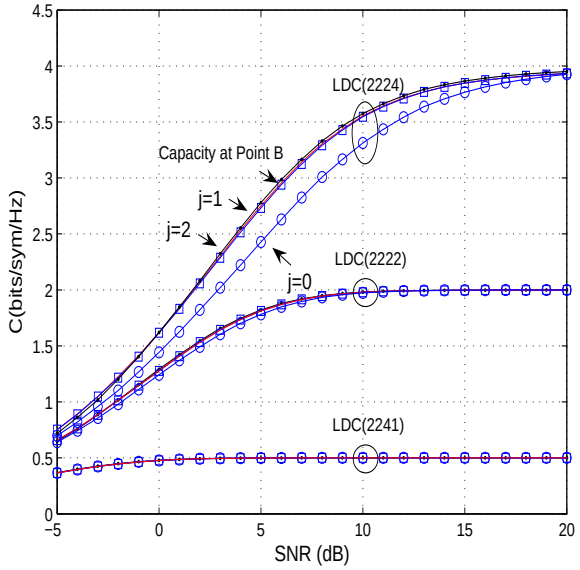

Figure 7.27: Comparison of the maximum achievable rates recorded at Point C of Figure 7.24 for the various PLDC schemes having $j = 0, 1, 2$ inner iterations, when using QPSK modulation in conjunction with an MMSE detector.

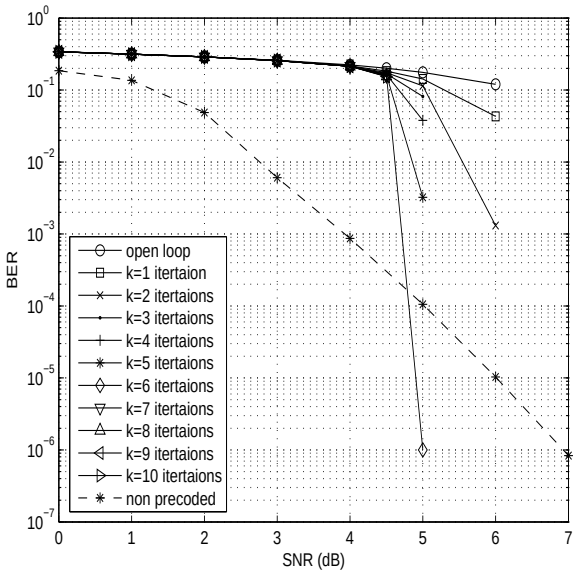

Figure 7.28: BER performance of the three-stage RSC(215)-coded PLDC(2224) scheme of Figure 7.24, employing $j = 0$ inner iterations using MMSE detection in conjunction with QPSK modulation.

Figure 7.27 quantifies the maximum achievable rates for the three-stage memory-one precoder-aided LDC (PLDC) schemes of Figure 7.24 having different rates in conjunction with different number of *inner* iterations j. For each set of comparisons, the LDC's capacity measured at Point B of Figure 7.24 is plotted as the benchmarker. For the rate $R_{2224} = 2$ scheme, a substantial maximum achievable rate gap is observed between the LDC scheme measured at Point B of Figure 7.24 and the corresponding PLDC scheme recorded at Point C of Figure 7.24, when the number of *inner* iterations is $j = 0$. However, when we have $j = 1$, the aforementioned rate loss is eliminated and a further increase of j has only a modest additional rate improvement. In fact, the maximum achievable rate loss is less than 1%, when we have $j = 1$. For the PLDC(2222) scheme having a rate of $R_{2222} = 1$, we observe in Figure 7.27 that although the aforementioned maximum achievable rate loss compared to the associated LDC's achievable capacity is still present, when employing $j = 0$ *inner* iterations, the associated discrepancy is narrower than that seen for the PLDC(2224) scheme. Observe in Figure 7.27 for the PLDC(2241) scheme having a rate of $R_{2241} = 0.25$ that there is no maximum achievable rate loss even in the absence of *inner* iterations.

The above observations are related to the EXIT characteristics of the LDC's MMSE decoding block, which is shown in Figure 7.23. When a single symbol is transmitted, i.e. we have $Q = 1$, the EXIT curve is a horizontal line. Therefore, regardless of the number of *inner* iteration employed, Block-1 of Figure 7.24 always outputs the identical extrinsic information. When Q is increased, the EXIT curves of Block-1 seen in Figure 7.23 become more steep, therefore higher extrinsic information can be obtained upon increasing the *a-priori* information by using a higher number of *inner* iterations. Therefore, the resultant maximum achievable rate observed in Figure 7.27 at Point C of Figure 7.24 has an increasing gap with respect to the one observed at Point B, when a higher number of symbols Q is transmitted by each LDC block.

In Figure 7.28, we characterize the achievable BER performance of the three-stage RSC(215)-coded memory-1 precoder-aided LDC(2224) scheme using $j = 0$ *inner* iteration. The EXIT chart of Figure 7.25 predicted that an open convergence tunnel will be formed at $\rho = 5$dB, which is evidenced by the BER performance of Figure 7.28, where $k = 6$ *outer* iterations were required to achieve an infinitesimally low BER. The comparison of Figures 7.22 and 7.28 reveals that

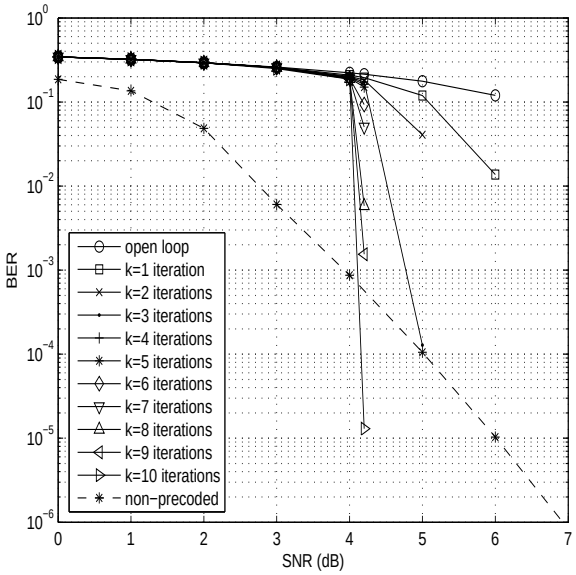

Figure 7.29: BER performance of the three-stage RSC(215)-coded PLDC(2224) scheme of Figure 7.24, employing $j = 1$ inner iterations using MMSE detection in conjunction with QPSK modulation.

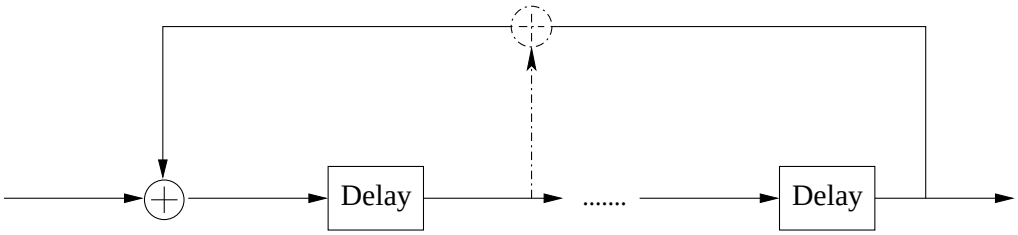

Figure 7.30: Schematic of the unity-rate precoder having different memories.

the precoded scheme is capable of achieving a lower BER in the high-SNR region, compared to its non-precoded counterpart. When employing $j = 1$ *inner* iterations, the corresponding BER performance is plotted in Figure 7.29. This scheme reached the so-called turbo-cliff associated with an infinitesimally low BER at about $\rho = 4.2$dB using $k = 10$ iterations, where a 0.8dB SNR gain is achieved compared to the scheme employing $j = 0$ *inner* iteration.

Another advantage of employing a precoder is that by changing the generator polynomial and/or the precoder's memory size, it is possible to shape the EXIT curves without changing the area below them. The schematic of the unity-rate precoder having different memories is portrayed in Figure 7.30. The generator polynomial characterized in octal form determines the portion of the connections in Figure 7.30.

Figure 7.31 portrays the EXIT curves of the three-stage unity-rate precoder-aided LDC(2221) scheme having various precoder memories and polynomials at $\rho = -1$dB. Observe that the area under the EXIT curve is constant to 0.79 for all the curves, although their shapes are different. Note that the memory-one precoder has the highest I_E starting point at the left on the ordinate axis of Figure 7.31 , when we have $I_A = 0$. Higher-memory precoded systems have an EXIT curve starting at a significantly lower I_E value, although they are capable of benefiting from the extrinsic information more substantially in the middle range of I_A, as seen in Figure 7.31.

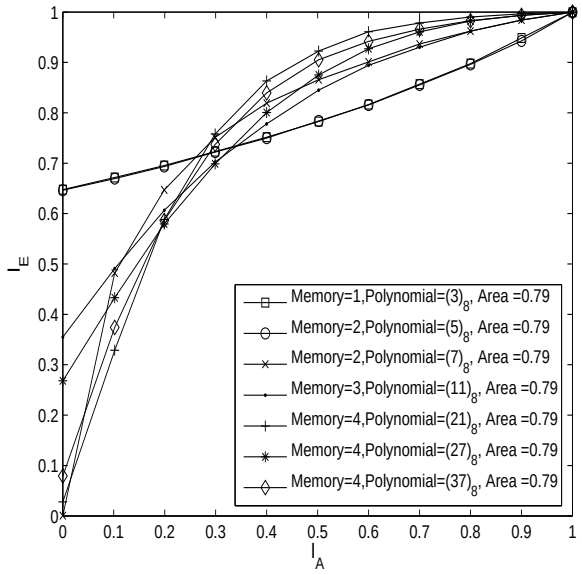

Figure 7.31: EXIT chart comparison of the three-stage RSC(215)-coded PLDC(2221) scheme of Figure 7.24, having different precoder memories and polynomials of Figure 7.30 at $\rho = -1$dB, when using an MMSE detector in conjunction with QPSK modulation.

Table 7.4: Coding gains of the RSC(215)-coded LDC(2224) scheme with/without a memory-1 precoder having an effective throughput of 1 (bits/sym/Hz).

	Number of *inner* iterations (j)	**Number of *outer* iterations** (k)	**at BER of** 10^{-4}	**at BER of** 10^{-5}
Two-stage system of Figure 7.17	0	5	9.3dB	11.8dB
Three-stage system of Figure 7.24	0	10	9.5dB	12.9dB
Three-stage system of Figure 7.24	1	10	10.1dB	13.5dB

7.4.3 Summary

In this section, we summarize the coding advantage of the proposed serial concatenated schemes operating with/without the memory-1 precoders, as portrayed in Figures 7.17 and 7.24, respectively. For the half-rate RSC(215)-coded schemes of Figures 7.17 and 7.24, the LDC(2224) scheme using QPSK modulation in conjunction with an MMSE detector was employed. Therefore, the resultant effective throughput is 1 (bits/sym/Hz). The uncoded LDC(2224) scheme using BPSK modulation having the identical throughput was used as a benchmarker. The coding gain was recorded between the uncoded scheme and the RSC(215)-coded LDC scheme at both BER $= 10^{-4}$ and 10^{-5} from Figures 7.22, 7.28 and 7.29.

Table 7.4 summarizes the coding gains of the two-stage non-precoded system of Figure 7.17 and three-stage precoded LDC(2224) scheme of Figure 7.24 as well as the number of *inner* and *outer* iterations required to achieve the target BER. At BER of 10^{-4}, an increased coding gain is observed, when a higher decoding complexity was invested in terms of employing precoders and increasing the number of *inner* iterations. Note that the advantage of employing a memory-1 precoder having a single *inner* iteration over the non-precoded scheme is 0.8dB. By contrast, the precoding advantage increased to 1.7dB, when the coding gain was quantified at BER of 10^{-5}. In conclusion, the RSC-coded precoder-aided LDC scheme of Figure 7.24 outperforms the non-

precoded scheme of Figure 7.17 in the low-BER region.

7.5 EXIT Chart Based Design of IrRegular Precoded LDCs

In this section, we propose the novel IrRegular Precoded Linear Dispersion Codes (IR-PLDCs) as the *inner* code of a SCC scheme. The throughput of the SCC system is determined by the rate R_{out} of the *outer* channel code, the rate R_{in} of the IR-PLDC and the modulation scheme employed. Since unity-rate precoders are used, R_{in} is purely determined by the rate of the LDCs employed. The SCC scheme employing the IR-PLDC as the *inner* code is designed under the following assumptions:

- QPSK modulation is employed by all the component codes of the proposed IR-PLDC scheme, although employing different modulation schemes is equally feasible;
- Rate-1 precoders are employed by all the component codes of the IR-PLDC, since lower-rate precoders introduce a capacity loss;
- The receiver has the knowledge of the DCMs as well as the weighting coefficients $\boldsymbol{\lambda}$ and knows when to activate a specific dispersion matrix;

Before proceeding to the detailed description of the proposed serial concatenated IR-PLDC scheme, we summarize the salient results of previous Sections. Firstly, the LDCs optimized according to Equation (7.24) achieve the maximum possible rate. Secondly, the number of *inner* iterations j required to attain the maximum achievable rate is $j = 1$ for $Q > 1$ or $j = 0$ for $Q = 1$, for the precoder-aided LDCs.

7.5.1 RSC-coded IR-PLDC Scheme

Figure 7.32 portrays the system model of the proposed serially concatenated RSC-coded IR-PLDC scheme. At the transmitter, a frame of information bits u_1 is encoded by a simple RSC encoder. Then the encoded bits c_1 are interleaved by a random interleaver, yielding the *outer* encoded bits u_2. Then the 'irregular partitioner' of Figure 7.32 feeds the appropriately selected fraction of u_2 into the various PLDC component codes according to a predefined weighting coefficient vector $\boldsymbol{\lambda}$. The *inner* IR-PLDC contains P_{in} number of component codes. The unity-rate precoders may exhibit different EXIT characteristics by employing different memories and generator polynomials, as seen in Figure 7.30. However, for the proposed system of Figure 7.32, memory-1 precoders are employed for all the PLDC components. More explicitly, within each PLDC encoder, the resultant precoded bits c_2 are interleaved by a second interleaver, yielding the interleaved bits u_3, which are fed to the bit-to-symbol mapper inside the LDC block of Figure 7.32. After QPSK modulation and space-time dispersion, the space-time transmission matrix $\mathbf{S}$ of Equation (7.12) is mapped to the $(M \times T)$ spatial and temporal dimensions by the 'ST mapper' and transmitted over the uncorrelated Rayleigh fading channel contaminated by AWGN at each receive antenna.

At the receiver of Figure 7.32, again the 'irregular partitioner' determines the portion of the received signal matrices $\mathbf{Y}$ and the *a-priori* information to each PLDC decoders, according to the weighting coefficient vector $\boldsymbol{\lambda}$. Then, an iterative decoding structure is employed, where extrinsic information is exchanged between three SISO modules, namely the MMSE detector, the precoder and the *outer* RSC decoder in a number of consecutive iterations. To be specific, in Figure 7.32, I_A denotes the *a-priori* information for the IR-PLDC represented in terms of Log-Likelihood Ratio (LLR) , where I_E denotes the extrinsic information output of the *inner* code also expressed in terms of LLR. We use $\bar{I}_A$ and $\bar{I}_E$ to represent the *a-priori* input and extrinsic output of the *outer* RSC decoder, respectively. Note that the intermediate rate-1 precoder processes two *a-priori* inputs

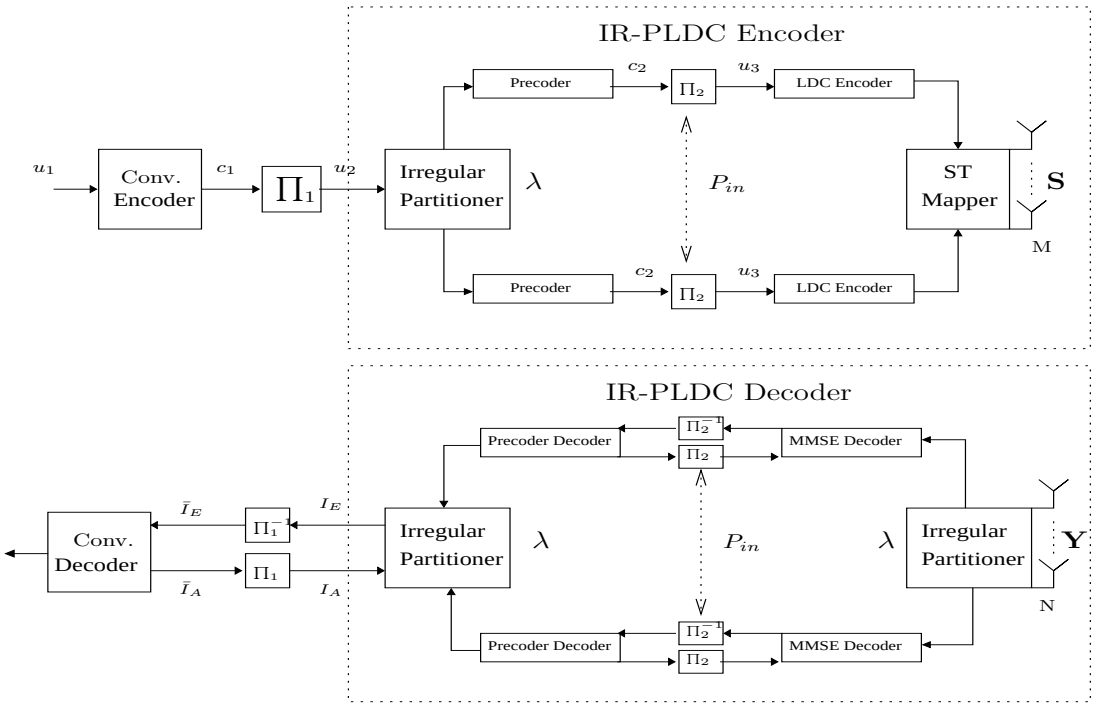

Figure 7.32: Schematic of the serial concatenated RSC-coded IR-PLDC system using iterative decoding.

arriving from the MMSE detector and the *outer* decoder and generates two extrinsic outputs as well. Since the activation of different PLDC components is implemented by employing different dispersion matrices, the hardware cost is modest low.

In our forthcoming EXIT chart analysis, the precoders' decoders and the MMSE decoders are considered as a single *inner* decoding block, namely the IR-PLDC's decoder of Figure 7.32. The advantage of this representation is that the IR-PLDC's extrinsic information output I_E is only determined by the received signal matrix $\mathbf{Y}$ and the *a-priori* input I_A, but remains unaffected by the extrinsic information exchange between the precoder's decoder and the MMSE detector. Thus, we can project the three-stage system into a two-stage system and hence the conventional two-dimensional EXIT chart analysis [344] [303] is applicable.

Following the approach of [184], we now carry out the EXIT chart analysis of the proposed RSC-coded IR-PLDC system. The *inner* IR-PLDC block has an *a-priori* input given by I_A and the channel output $\mathbf{Y}$ of Figure 7.32. Thus the corresponding EXIT functions are:

$$I_E = \Gamma_{u_2}[I_A, \rho], \tag{7.48}$$

and for the *outer* RSC code the EXIT function is:

$$\bar{I}_E = \Gamma_{c_1}[\bar{I}_A]. \tag{7.49}$$

According to the area properties [346] of EXIT charts introduced in Section 7.4.1, the area under the EXIT curve of an *outer* code is approximately equal to $(1 - R_{out})$. More explicitly, we have

$$R_{out} \approx 1 - \int_0^1 \Gamma_{c_1}(i)di, \tag{7.50}$$

suggesting that a higher rate code has a lower area under its EXIT curve. This observation is the rationale behind the design of IRCCs proposed in [204], where the aim is to minimize the

area of the open EXIT tunnel, because this facilitates a near-capacity operation. However, we will demonstrate in Section 7.5.1.1 that in contrast to IRCCs, the area under the *inner* IR-PLDC code's EXIT curve does not have a linear relationship with its code rate. This property results in a different design procedure and objective of the IR-PLDCs in comparison to the IRCCs.

7.5.1.1 Generating Component Codes for IR-PLDCs

The employment of irregular codes was proposed by Tüchler and Hagenauer [204] [182], where IRCCs were used as an *outer* channel code. IRCCs are constituted by a family of convolutional codes having different code rates. They were specifically designed with the aid of EXIT charts [177], for the sake of improving the convergence behaviour of iteratively decoded systems. In [204], the authors have proved that the aggregate EXIT function of an irregular code containing P component codes can be obtained from the linear combination of that of its component codes, under the assumption that the PDF of the LLRs is symmetric and continuous. More explicitly, the EXIT function of an irregular code is given by

$$\Gamma_{ir} = \sum_{i=1}^{P} \lambda_i \Gamma_i(I_{input}), \tag{7.51}$$

where λ_i represents the weighting coefficients of the i-th component having transfer function Γ_i.

Inspired by the above-mentioned beneficial properties of an irregular system, in this section, we propose an IR-PLDC scheme for employment as our *inner* rather than *outer* code for the SCC system. The EXIT function of the proposed IR-PLDC scheme is constituted by the superimposed combination of its component codes' EXIT functions determined by Equation (7.51). Clearly, each PLDC component's EXIT curve as well as the corresponding weighting coefficient vector $\boldsymbol{\lambda}$ play a crucial role in shaping the resultant aggregate EXIT function. Each component PLDC of the proposed IR-PLDC scheme of Figure 7.32 is constituted by an independent LDC combined with a unity-rate precoder. Different PLDC rates can be obtained by varying the number of transmitted symbols Q and the number of time slots T used per space-time block. Naturally, maintaining low values of Q and T is desirable for the sake of maintaining a low encoding/decoding complexity.

For example, in order to design an *inner* IR-PLDC coding scheme containing $P_{in} = 11$ components for a MIMO configuration having $M = 2$ transmit and $N = 2$ receive antennas, we commence by setting $T = 2$. Hence, all the components have the potential of achieving the maximum diversity order of $D = 4$ according to Theorem 3. By setting $Q = 1$, we are able to optimize the DCMC capacity of LDC(2221) using Equation (7.24). Consequently, we can obtain more components by gradually increasing the Q value to increase the rate. We impose the limit of $Q \leq MT$ for the sake of maintaining a low complexity, although employing a higher value of Q is equally feasible. Hence, by increasing the value of T and maximizing the corresponding DCMC capacity of each LDC, we can generate a set of beneficial LDCs. Again, low Q and T values are desirable for the sake of maintaining a low complexity. The resultant $P_{in} = 11$ component codes designed for our IR-PLDC scheme are listed in Table 7.5.

Hence, for a MIMO system associated with M transmit and N receive antennas, the universal algorithm of generating P_{in} component codes for an IR-PLDC scheme can be formulated as follows:

- Step 1. Set the number of time slots to $T = M$ in order to ensure that all the resultant component LDCs have the same maximum achievable diversity order of $N \cdot \min(M, T)$, as argued in Theorem 3;
- Step 2. Set $Q = 1$ and find the specific LDCs by searching through the entire set of legitimate codes, which maximize the DCMC capacity of Equation (7.24);
- Step 3. Set $Q := Q + 1$ for the sake of increasing the attainable throughput and repeat

Table 7.5: The $P_{in} = 11$ number of LDC component codes of the IR-PLDC scheme of Figure 7.32 generated for a MIMO system having $M = 2$ and $N = 2$ antennas and employing QPSK modulation and an MMSE detector.

Index	M	N	T	Q	R_{LDC}	**Inner Iteration**	**Complexity**
0	2	2	2	1	0.5	0	1571
1	⋮	⋮	⋮	2	1	1	4086
2	⋮	⋮	⋮	3	1.5	1	5030
3	⋮	⋮	⋮	4	2	1	5974
4	⋮	⋮	3	1	0.33	0	3285
5	⋮	⋮	⋮	2	0.67	1	8562
6	⋮	⋮	⋮	4	1.33	1	12546
7	⋮	⋮	⋮	5	1.67	1	14538
8	⋮	⋮	4	1	0.25	0	5639
9	⋮	⋮	⋮	3	0.75	1	18126
10	⋮	⋮	⋮	5	1.25	1	24974

the above optimization procedure using Equation (7.24), until the maximum number of transmitted symbols reaches $Q = MT$;

- Step 4. If the LDC having a rate of $R_{LDC} = \frac{Q}{T}$ existed, discard the current code having the same rate but a larger value of Q and T, for the sake of minimizing the complexity according to Corollary 1;
- Step 5. If the number of component codes found is less than P_{in}, then set $T := T + 1$ and proceed to Step 2. Otherwise, terminate the search process.

Naturally, the resultant code rates may not be expected to be evenly distributed, owing to having a limited number of legitimate combinations of T and Q.

Since unity-rate precoders are employed, the rate of each PLDC block is equal to the component LDC's rate. The number of *inner* iterations listed in Table 7.5 quantifies the number of iterations carried out between the precoder and the MMSE detector, which was optimized from the capacity approaching perspective, as detailed explained in Figure 7.27. The component codes generated from the above-mentioned algorithm ensure that the resultant P_{in} number of component codes have the lowest possible complexity. More explicitly, the complexity of each PLDC component code is jointly determined by the precoder's complexity, the MMSE detector's complexity and the number of *inner* iterations. In order to quantify the complexity in a unified manner, we count the number of addition and multiplication operations required to calculate a single LLR value in the logarithmic domain. Since the number of addition and multiplication operations can be quantified in terms of the so-called Add-Compare-Select (ACS) arithmetic operations, the complexity of each PLDC component is quantified by the ACS operations per LLR computation. Observe in Table 7.5 that when the value of T is fixed, the complexity is increased by increasing the value of Q. Furthermore, increasing the value of T typically resulted in a substantially increased complexity.

Figure 7.33 shows the EXIT charts of the above-mentioned $P_{in} = 11$ component PLDCs of Table 7.5 at $\rho = 0$dB using memory one precoders, which are used as component codes for the proposed IR-PLDC scheme of Figure 7.32. The shape of all the EXIT curves is similar, since they

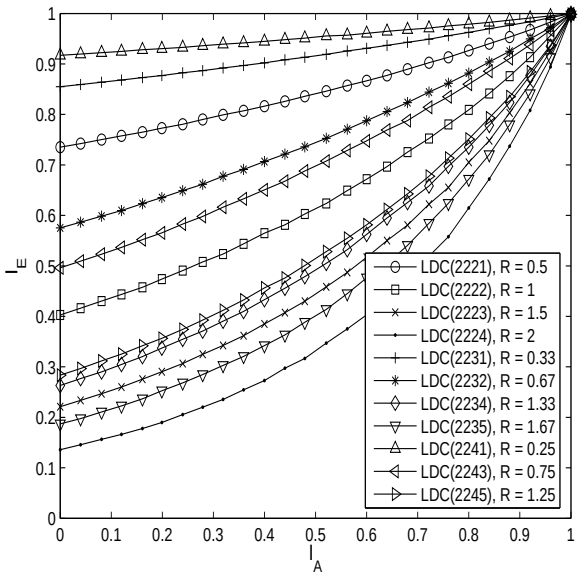

Figure 7.33: EXIT chart of the $P_{in} = 11$ PLDCs of Table 7.5 at $\rho = 0$dB using memory **one** precoders, which are used as component codes for the proposed IR-PLDC scheme of Figure 7.32.

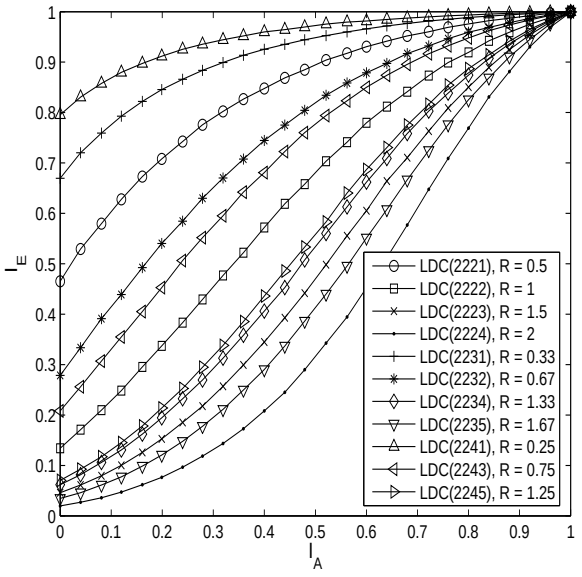

Figure 7.34: EXIT chart of the $P_{in} = 11$ PLDCs of Table 7.5 at $\rho = 0$dB using memory **three** precoders, which are used as component codes for the proposed IR-PLDC scheme of Figure 7.32.

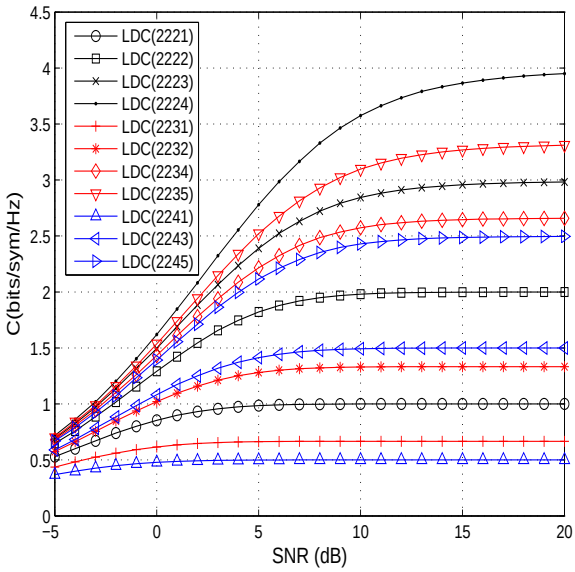

Figure 7.35: Maximum achievable rates of the $P_{in} = 11$ PLDCs listed in Table 7.5 as the component codes for the proposed IR-PLDC scheme of Figure 7.32, when employing QPSK modulation as well as an MMSE detector.

are all combined with the memory one precoders. Furthermore, Figure 7.34 portrays the EXIT curves of the same set of LDC component codes of Table 7.5 in conjunction with memory three precoders. Clearly, although changing the size of the precoder's memory does not affect the area under the curves, it has a substantial impact on the shape of the curves. It is worth mentioning at this stage that a sufficiently diverse set of curves is necessary for employment in a flexible IR-PLDC scheme for the sake of maximizing the achievable rates as well as minimizing the detector's complexity.

Figure 7.35 quantifies the maximum achievable rates of the *inner* IR-PLDC scheme of Figure 7.32 using the EXIT charts of the $P_{in} = 11$ memory-1 precoder-aided LDC component codes listed in Table 7.5. Recall from Section 7.4.1 that the maximum achievable rate is attained using Equation (7.47) under the assumption of having perfectly matched *inner* and *outer* EXIT curves, which results in an infinitesimally low EXIT tunnel area. Observe in Figure 7.35 that a high-rate PLDC component code is capable of attaining a high maximum achievable rate. However, this does not necessarily imply imposing a higher complexity. For example, Table 7.5 shows that the high-rate PLDC(2224) scheme imposes a substantially lower complexity than that of the PLDC(2235) arrangement, since the former scheme maintains lower T and Q values.

Let us use λ_i, $i = (1, 2, \ldots, P_{in})$ represents the specific fraction of I_E conveying the corresponding extrinsic information, which are fed into the IR-PLDC encoders/decoders of Figure 7.32. Therefore, the weighting coefficients $\boldsymbol{\lambda}$= $[\lambda_1, \ldots, \lambda_{P_{in}}]$ have to satisfy

$$\sum_{i=1}^{P_{in}} \lambda_i = 1 \qquad \lambda_i \in [0, 1], \tag{7.52}$$

and the aggregate rate R_{in} of the *inner* IR-PLDC scheme is given by:

$$\frac{1}{R_{in}} = \sum_{i=1}^{P_{in}} \lambda_i \frac{1}{R_{(i,LDC)}}. \tag{7.53}$$

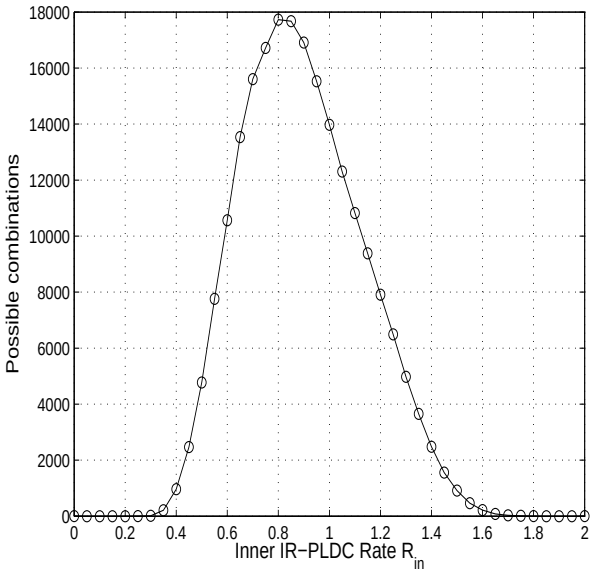

Figure 7.36: The number of possible combinations for the IR-PLDC scheme of Figure 7.32 against its rate using the $P_{in} = 11$ component codes listed in Table 7.5, where $\lambda_i \in [0, 0.1, 0.2, \ldots, 1]$.

In order to further illustrate the flexibility provided by the IR-PLDCs using the weighting coefficient vector $\boldsymbol{\lambda}$, Figure 7.36 plots the possible number of combinations against the *inner* IR-PLDC scheme's rate R_{in} given in Equation (7.53), under the assumption that we have $\lambda_i \in [0, 0.1, 0.2, \ldots, 0.9, 1]$. The bell-shaped distribution of Figure 7.36 exhibits a peak at approximately $R_{in} = 0.8$. At extremely low and high rates in the vicinity of $R_{in} = 0.25$ and $R_{in} = 2$, respectively, the number of legitimate combinations gradually reduced, owing to the lack of irregularity. Again, Figure 7.36 was generated using an exhaustive search for the weighting coefficient vector $\boldsymbol{\lambda}$ having a step size of 0.1 under the constraint of Equation (7.52).

Figure 7.37 attempts to characterize the flexibility of the IR-PLDC scheme of Figure 7.32 in terms of the associated area under the EXIT curves at $\rho = -1$dB by plotting a group of IR-PLDC's EXIT charts having different weighting coefficient vectors. Note that all the IR-PLDCs' EXIT curves plotted in Figure 7.37 maintain an identical aggregate rate of $R_{in} = 0.85$. Figure 7.36 has revealed that there are around $17,500$ possibilities, given the weighting coefficients $\lambda_i \in [0, 0.1, 0.2, \ldots, 0.9, 1]$. Figure 7.37 merely illustrates 12 EXIT curves out of the total $17,500$ possible combinations. Observe in Figure 7.37 that the area under the curves exhibits a significant variation, which implies that the MIMO channel's capacity achieved by the IR-PLDC using different weighting coefficient vector $\boldsymbol{\lambda}$ is different, despite the fact that they share the same aggregate rate $R_{in} = 0.85$.

In conclusion, the *outer* code's 'area property' of Equation (7.50) reflects a linear relationship between its rate R_{out} and the area under the EXIT curve, hence the area under the EXIT curves of the IRCC scheme [204] is equal to the aggregate rate, regardless of the shape of the curves. By contrast, the proposed *inner* IR-PLDC scheme of Figure 7.32 does not obey the linear property, since the area under the EXIT curve quantifies the MIMO channel's capacity achieved using an IR-PLDC scheme and its rate is given by Equation (7.53). Our arguments are further justified by Figure 7.37.

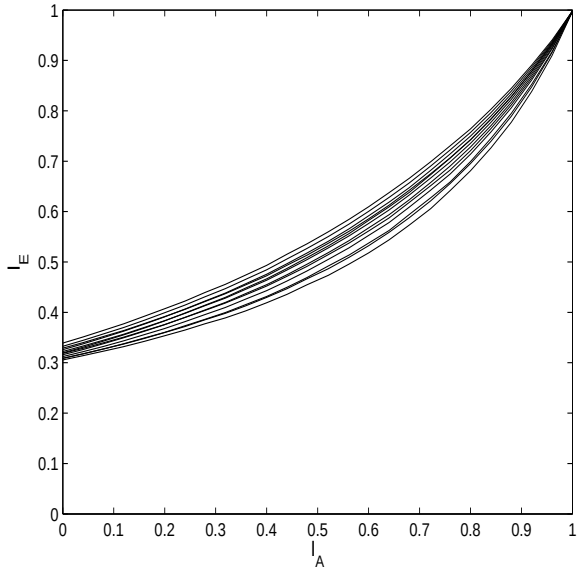

Figure 7.37: A group of EXIT charts of the IR-PLDC scheme of Figure 7.32 using the component codes of Table 7.5 at $\rho = -1$dB, while having a fixed rate $\boldsymbol{R_{in} = 0.85}$ achieved by employing different weighting coefficient vectors $\boldsymbol{\lambda}$.

7.5.1.2 Maximum-Rate RSC-Coded IR-PLDCs

The channel-coded IR-PLDC system of Figure 7.32 employs a simple RSC code ($P_{out} = 1$) as the *outer* code, while using the $P_{in} = 11$ component codes characterized in Table 7.5 as the *inner* code. Hence, we have a total number of $P = P_{in} + P_{out} = 12$ component codes. Each PLDC component processes a fraction of the input information according to its weighting coefficient λ_i, which has to satisfy Equation (7.52) and the resultant aggregate *inner* code rate R_{in} is given by Equation (7.53).

In order to achieve an infinitesimally low BER at a specific SNR, an open EXIT tunnel should exist in the EXIT chart. Assuming that each component code's EXIT curve is represented by l points, the EXIT function Γ_{irr} at SNR ρ of the IR-PLDC should be optimized by 'maximizing' the square of the EXIT chart matching error function given by:

$$J(\lambda_1, \ldots, \lambda_{P_{in}}) = \int_0^1 e(\rho)^2 di, \tag{7.54}$$

where the error function is given by:

$$\mathbf{e}(\rho) = \underbrace{\begin{bmatrix} \Gamma_1(I_{A,1}), & \Gamma_2(I_{A,1}), & \cdots & \Gamma_P(I_{A,1}) \\ \Gamma_1(I_{A,2}), & \Gamma_2(I_{A,2}), & \cdots & \Gamma_P(I_{A,2}) \\ \vdots & \vdots & \ddots & \vdots \\ \Gamma_1(I_{A,l}), & \Gamma_2(I_{A,l}), & \cdots & \Gamma_P(I_{A,l}) \end{bmatrix} \begin{bmatrix} \lambda_1 \\ \lambda_2 \\ \vdots \\ \lambda_{P_{in}} \end{bmatrix}}_{\Gamma_{irr}} - \underbrace{\begin{bmatrix} \Gamma_{rsc}^{-1}(I_{A,1}) \\ \Gamma_{rsc}^{-1}(I_{A,2}) \\ \vdots \\ \Gamma_{rsc}^{-1}(I_{A,l}) \end{bmatrix}}_{\Gamma_{rsc}}, \tag{7.55}$$

subject to the constraints imposed by Equation (7.52), where $I_{A,l}$ denotes the l-th *a-priori* information input of the PLDC components.

The gradient search method of maximizing $J(\lambda_1, \ldots, \lambda_P)$ of Equation (7.54) is similar to the algorithm proposed in [204]. More explicitly, the algorithm starts by setting the *inner* code rate

Table 7.6: Design comparison of irregular schemes using either IRCCs having $\boldsymbol{\gamma} = [\gamma_1, \ldots, \gamma_{P_{out}}]$ or IR-PLDCs having $\boldsymbol{\lambda} = [\lambda_1, \ldots, \lambda_{P_{in}}]$, where the weighting coefficient vectors $\boldsymbol{\gamma}$ and $\boldsymbol{\lambda}$ quantify the fraction of bits encoded by each component code.

	IRCC	**IR-PLDC**
Design objective	Maximizing the achievable rates	
Component codes generated by	Puncturing a mother code	Varying T and Q
Area and rate relationship	Unique	Non-unique
Interleaver length requirement	High	Modest
Error function of Equation (7.54)	Minimizing	Maximizing
Aggregate code rate	$\frac{1}{R_{out}} = \sum_{i=1}^{P_{out}} \gamma_i \frac{1}{R_{i,ircc}}$	$\frac{1}{R_{in}} = \sum_{i=1}^{P_{in}} \lambda_i \frac{1}{R_{i,ldc}}$

R_{in} to the minimum value. If the set of weighting coefficients maximizing the area expression of Equation (7.54) is generated using the gradient search method of [204] and an open EXIT tunnel exists, R_{in} is increased by a small amount. The algorithm terminates at the highest possible R_{in} value, where an open convergence tunnel may no longer be found.

The reason that our proposed *inner* IR-PLDC scheme is seeking the solutions 'maximizing' the area expression of $J(\lambda_1, \ldots, \lambda_P)$ is justified as follows. The benefit of employing irregular *inner* or *outer* codes for an iteratively-detected scheme is to maximize the achievable rates. When using IRCCs as an *outer* code, minimizing the EXIT tunnel area corresponds to maximizing the achievable rate, owing to the area property discussed in Section 7.4.1. In other words, IRCCs are designed to find an *outer* EXIT curve that matches a given *inner* EXIT curve as close as possible by maximizing the area under the EXIT curve. However, there is no one-to-one relationship between the *inner* aggregate rate R_{in} and the associated area under the EXIT curves. Consequently, the IR-PLDC scheme offers multiple area values under its EXIT curves for a given rate, as illustrated in Figure 7.37. Larger EXIT tunnel area potentially requires less *outer* iterations to achieve an infinitesimally low BER. Therefore, given an *outer* code, the design criterion for the *inner* IR-PLDC is to maximize the achievable rate, while having an infinitesimally low BER, which corresponds to **maximizing the inner code rate R_{in} and simultaneously maximizing the EXIT tunnel area according to Equation (7.54)**, since the latter minimizes the number of iterations required. A detailed comparison of designing the proposed *inner* IR-PLDC and the IRCC of [204] as an *outer* code is provided in Table 7.6.

In the previous iteratively detected schemes in Sections 7.4.1 and 7.4.2, half-rate RSC(215) code is employed. It is natural to ask the question whether it is possible to employ an even simpler RSC code to reduce the decoding complexity, while operating near MIMO channel's capacity. Hence, we designed our IR-PLDC system for a half-rate RSC(213) code, which has a decoding complexity of 217 ACS operations per LLR value compared to the 841 ACS operations imposed by the RSC(215) code. It is also worth mentioning that when plotting the EXIT chart, it is often assumed that the distribution of the LLRs is Gaussian, which is only sufficiently accurate, when a high interleaver length is used in the schematic of Figure 7.32. In the context of the RSC(213) code, the Gaussian assumption of the EXIT chart becomes easier to satisfy in conjunction with a shorter interleaver, since the RSC(213) code imposes correlation over a factor of $\frac{3}{5}$ shorter segment of the encoded bit stream.

Figure 7.38 presents the EXIT charts and the corresponding decoding trajectory of the RSC(213)-coded IR-PLDC scheme of Figure 7.32 designed for operating at $\rho = 0$dB, when using QPSK modulation in conjunction with an MMSE detector. The dotted lines are the EXIT curves of the $P_{in} = 11$ component codes of Table 7.5 and the solid line represents the EXIT curve of the *inner* IR-PLDC having the weighting coefficients given in Table G.1 of Appendix G. The resultant throughput of the system is $C(0dB) = 1.1392$ (bits/sym/Hz), according to Equation (7.47). By

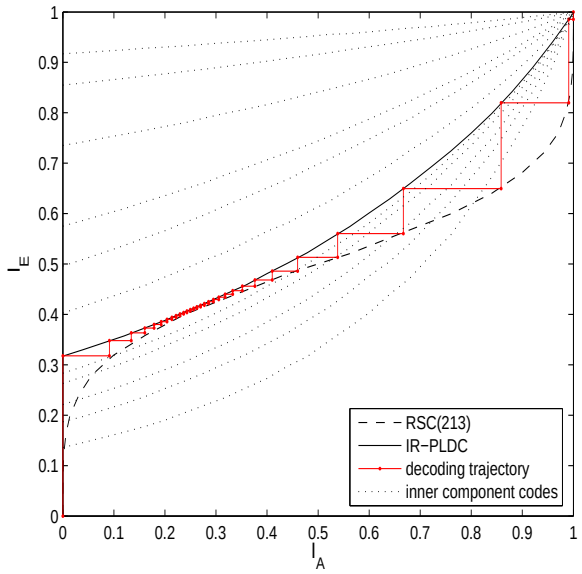

Figure 7.38: EXIT chart and the decoding trajectory of the RSC(213)-coded IR-PLDC scheme of Figure 7.32 recorded at $\rho = 0$dB using QPSK modulation, when an MMSE detector was employed.

maximizing R_{in} as well as maximizing the open EXIT tunnel area of Equation (7.54), the optimized EXIT curves of Figure 7.38 exhibit a significant tunnel area, where the decoding trajectory of Figure 7.38 shows that $k = 29$ *outer* iterations were required.

The corresponding BER of the RSC(213)-coded IR-PLDC system of Figure 7.32 designed for achieving an infinitesimally low BER at $\rho = 0$dB using QPSK modulation is shown in Figure 7.39. There is a turbo cliff at $\rho = 0$dB, when $k = 29$ *outer* iterations were carried out between the RSC(213) decoder and the IR-PLDC decoder. Note that the complexity required for achieving an infinitesimally low BER at $\rho = 0$dB is quantified in terms of the number of ACS operations per LLR value. Given the number of *outer* iterations and the complexity of each PLDC component of Table 7.5 combined with the RSC(213) decoder requires 217 ACS operations, the total decoding complexity per LLR value was evaluated by considering the number of iterations as well as each component's complexity as follows:

$$\varpi(0dB) = 29 \cdot (0.146 \cdot 8562 + 0.034 \cdot 18126 + 0.82 \cdot 12546 + 217) = 3.5876 \times 10^5. \quad (7.56)$$

Naturally, the same design process can be extended to other SNR values. Figure 7.40 plots the maximum rates achieved by the proposed IR-PLDC scheme of Figure 7.32, when half-rate RSC(213) and RSC(215) codes were employed. Each point in Figure 7.40 was designed to achieve the maximum rate with the aid of specific weighting coefficients, which are listed in Tables G.1 and G.2 of Appendix G. The dotted lines of Figure 7.40 quantify the maximum achievable rates of the $P_{in} = 11$ component codes of Table 7.5. By simply adjusting the fraction of information fed into each components, as seen in Tables G.1 and G.2, the proposed system of Figure 7.32 employing irregular *inner* codes becomes capable of operating across a wide range of SNRs. Figure 7.40 clearly demonstrates the variation of the maximum rate, when encounters different-SNR scenarios.

Also observe in Figure 7.40 that the IR-PLDC scheme employing the RSC(213) code is capable of achieving a higher maximum rate compared to the system employing the RSC(215) code, which is about 2.5dB away from MIMO channel's capacity. Compared to the EXIT curve of the RSC(215) code seen in Figure 7.17, the RSC(213) code's EXIT curve of Figure 7.38 has a lower I_E value for

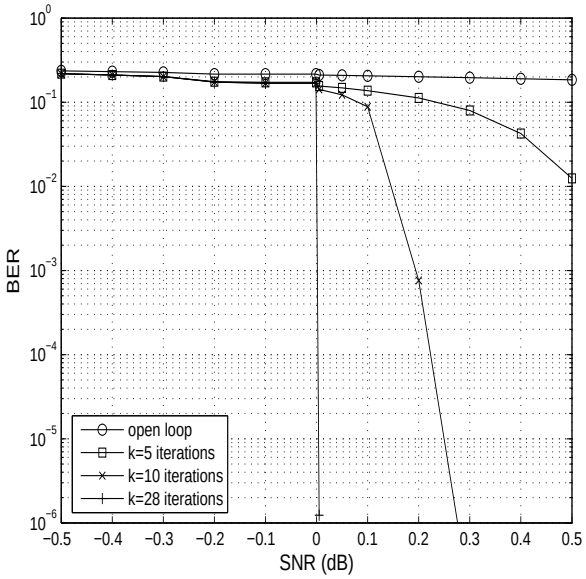

Figure 7.39: BER of the RSC(213)-coded IR-PLDC scheme of Figure 7.32 that designed to achieve an infinitesimally low BER at $\rho = 0$dB using QPSK modulation, when an MMSE detector was employed.

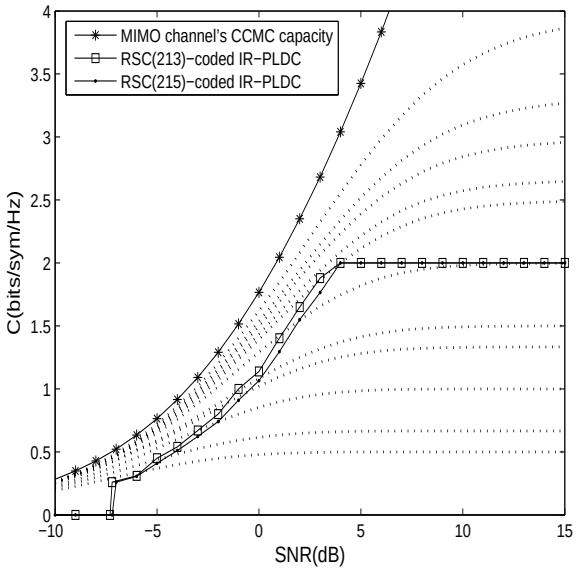

Figure 7.40: The maximum rates achieved by the IR-PLDC schemes of Figure 7.32 using RSC(213) and RSC(215) codes according to Tables G.1 and G.2, when QPSK modulation in conjunction with an MMSE detector were employed.

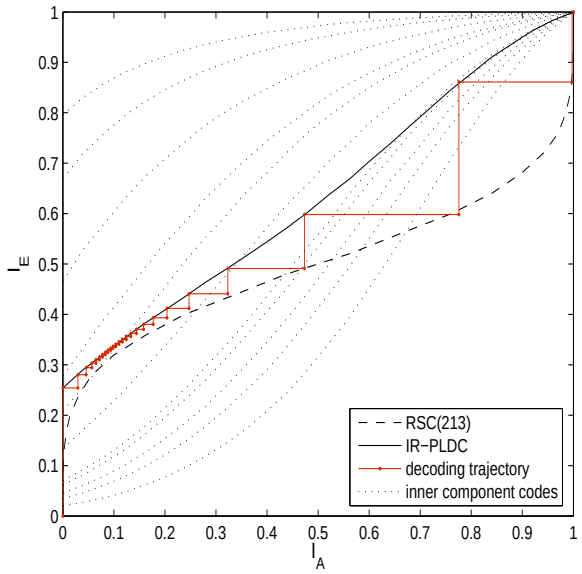

Figure 7.41: EXIT chart and the decoding trajectory of the RSC(213)-code IR-PLDC scheme of Figure 7.32 having a precoder memory of **three** recorded at $\rho = 0$dB using QPSK modulation, when an MMSE detector was employed.

abscissa values of $I_A < 0.5$ and a higher I_E value in the rest of the abscissa range. The resultant shape of the *outer* EXIT curve forms a larger open EXIT tunnel area and hence enables the *inner* IR-PLDC code to provide a higher aggregate rate for the serial concatenated system. This implies that having a beneficial shape for the EXIT curves plays a more influential role in determining the achievable rates of the system, than having a larger minimum distance, as it becomes explicit by comparing the performance of the RSC(213) and RSC(215) coded systems.

Tables G.1 and G.2 in Appendix G list the weighting coefficient vector $\boldsymbol{\lambda}$ for the IR-PLDC scheme of Figure 7.24 required for achieving maximum rates ranging from $\rho = -7$dB to $\rho = 4$dB, when the RSC(213) and RSC(215) codes were employed, respectively. The $P_{in} = 11$ component codes are listed from low-rate to high-rate components, where an entry of '0' implies that the specific PLDC component is inactivated during the transmission process. Observe further in Tables G.1 and G.2 that increasing the system's maximum rate upon increasing the SNR is achieved by appropriately adjusting the weighting coefficient vector $\boldsymbol{\lambda}$. However, when we have $\rho = 4$dB in Table G.1, the maximum-rate PLDC component having a rate of $R_{3,LDC} = 2$ has already fully activated, which means that it has a weighting coefficient of $\lambda_3 = 1$. Therefore, no more rate increase is observed in Figure 7.40, when we have $\rho > 4$dB. Naturally, further rate improvements can be achieved, if higher-rate PLDC components are employed.

An alternative way of changing the shape of the EXIT curves is constituted by changing the precoder's memory size and/or the generator polynomials for the system of Figure 7.32. Previously, Figure 7.31 has indicated that changing the rate-1 precoder's memory and generator polynomial does not change the area under the corresponding EXIT curves. Hence, Figure 7.41 portrays both the EXIT curves and the decoding trajectory of the IR-PLDC scheme of Figure 7.32 at $\rho = 0$dB using the RSC(213) code, when the precoder's memory size was increased to three. Compared to Figure 7.38, the EXIT curves of Figure 7.41 are more steep. However, in this particular case, increasing the precoder's memory size does not benefit the system in terms of its maximum achievable rate, which is $C(0dB) = 0.7908$ (bits/sym/Hz), while $C(0dB) = 1.1392$ (bits/sym/Hz) was achieved for the IR-PLDC schemes having precoder memory size of one. Again, Figure 7.41 demonstrate that the shape of the *inner* and *outer* EXIT curves exhibits an influential

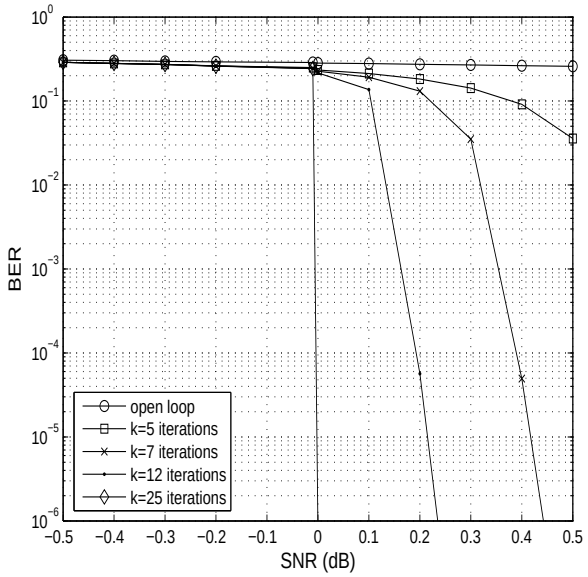

Figure 7.42: BER of the RSC(213)-coded IR-PLDC scheme of Figure 7.32 having a precoder memory of **three** that designed to achieve an infinitesimally low BER at $\rho = 0$dB using QPSK modulation, when an MMSE detector was employed.

role in the EXIT chart based design. The corresponding BER performance is shown in Figure 7.42.

7.5.1.3 Complexity-Constrained RSC-Coded IR-PLDCs

In Figures 7.38 and 7.41, we have characterized a number of IR-PLDC designs contrived for achieving the maximum rate at a certain SNR. Observe from Equation (7.56) that an excessive amount of complexity is required to decode each information bit. However, the mobile handsets normally can not afford such high complexity. Therefore, in this section, we investigate the IR-PLDC designs of Figure 7.32 that are capable of achieving the maximum possible rate under a certain complexity constraint.

The total decoding complexity is constituted by two contributions. Firstly, the particular fraction of bits λ_i fed into each component code as well as each component's own complexity quantified in Table 7.5. Secondly, the number of *outer* iterations k required for reaching the $(1.0, 1.0)$ point on the EXIT chart constitutes a linear complexity factor. Observe from Figure 7.38 that the IR-PLDC schemes designed for maximizing the achievable rate often result in a high decoding complexity, which is associated with a narrow EXIT tunnel. These high-complexity designs may be suitable for the base station. The flexibility of the IR-PLDCs also allows us to derive designs for mobile handsets, where the affordable complexity is more limited. We refer to this as a 'complexity-constrained' design.

For the above-mentioned 'maximum-rate' schemes, the design problem was formulated in Equation (7.54) and a gradient search [204] can be performed to find the most suitable weighting coefficient vector $\boldsymbol{\lambda}$. However, for the 'complexity-constrained' scheme, we are looking for the maximum achievable rate under a specific complexity constraint, which requires an extended search for the weighting coefficient vector $\boldsymbol{\lambda}$. More specifically, the complexity of an IR-PLDC scheme employing an RSC code at SNR ρ is restricted by:

$$k \cdot (\varpi_1\lambda_1 + \varpi_2\lambda_2 \ldots + \varpi_P\lambda_P + \varpi_{RSC}) \leq \varpi_{target}, \tag{7.57}$$

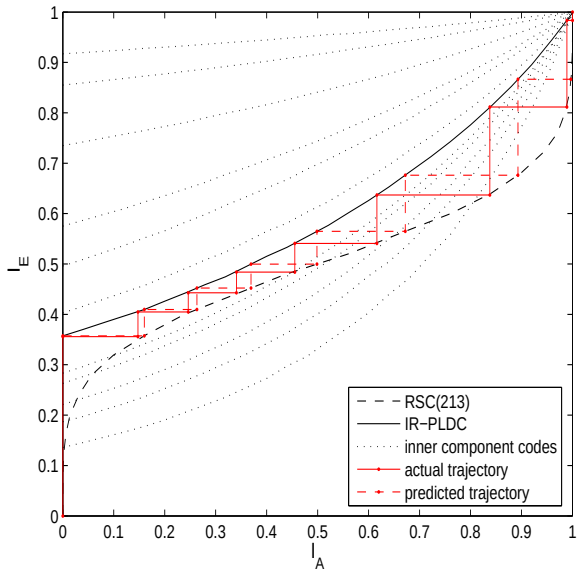

Figure 7.43: EXIT chart and the (predicted) decoding trajectory of the 'complexity-constrained' RSC(213)-coded IR-PLDC scheme of Figure 7.32 at ρ = 0dB, when using QPSK modulation and an MMSE detector.

where ϖ_i is the complexity of the i-th component code quantified in Table 7.5. The number of decoding iterations k required to achieve an infinitesimally low BER is predicted using a predicted decoding trajectory illustrated in Figure 7.43.

In the following design example, we optimize the IR-PLDC scheme of Figure 7.32 employing a half-rate RSC(213) code as our *outer* code at $\rho = 0$dB. The complexity imposed at the receiver is restricted by $\varpi_{213,c}(0dB) \leq \frac{1}{10}\varpi_{213}(0dB) = 0.35876 \times 10^5$ ACS operations per LLR value.

Figure 7.43 shows the EXIT curves of our 'complexity-constrained' IR-PLDC scheme as well as the predicted decoding trajectory using interpolation and the actual decoding trajectory recorded using simulation. Firstly, a wider convergence tunnel is observed in Figure 7.43 compared to that of Figure 7.38, hence the number of decoding iterations can be effectively reduced. Furthermore, there is a difference between the predicted decoding trajectory generated using interpolation and the actual trajectory recorded using simulation. The accuracy of the match between the decoding trajectory and the EXIT chart is dependent on the validity of the assumption of the LLRs' Gaussian distribution, which requires a large interleaver length. If the assumption has a limited accuracy, the actual decoding trajectory may exhibit an 'overshoot' problem. In this design example, the first interleaver Π_1 of Figure 7.32 is set to have a length of 10^6 bits and the length of the second interleaver Π_2 is equal to the corresponding number of bits fed into each component code. Note in Figure 7.43 that although no substantial 'overshoot' is visible, the resultant predicted and the actually encountered decoding trajectories exhibit an obvious difference after a few iterations. However, we may state that the number of decoding iterations predicted k using interpolation is sufficiently accurate. The results of our further investigations included here suggest that unless encountering narrow EXIT tunnels, where more than $k = 15$ iterations are necessary, the predicted number of iterations using EXIT chart based interpolation is typically quite accurate. On the other hand, when aiming for low-complexity designs, the 'wide EXIT tunnel assumption' is usually satisfied and hence the aforementioned inaccurate prediction is not encountered.

Furthermore, a rate of $C(0dB)$=1.10929 (bits/sym/Hz) is achieved in Figure 7.43, where the rate loss recorded is insignificant, compared to the maximum achievable rate of $C(0dB) = 1.1392$

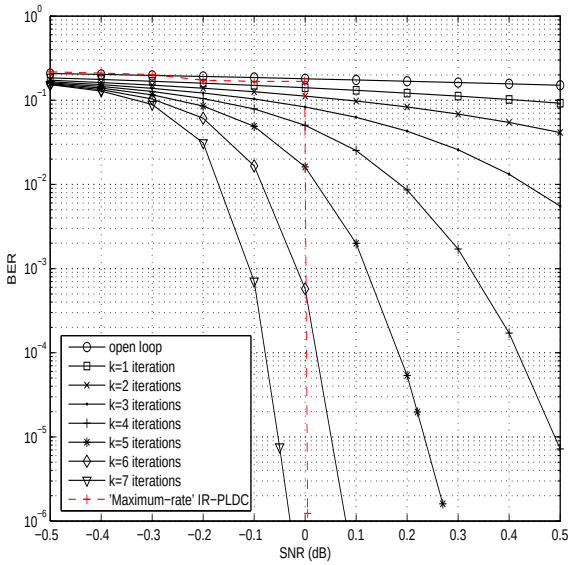

Figure 7.44: BER of the 'complexity-constrained' RSC(213)-coded IR-PLDC scheme of Figure 7.32 designed for achieving an infinitesimally low BER at $\rho = 0$dB, when using QPSK modulation and an MMSE detector.

(bits/sym/Hz) recorded for the previous 'maximum-rate' design at $\rho = 0$dB. As a benefit of this 'complexity-constrained' design, only about 10% of the decoding complexity of the 'maximum-rate' design is imposed. The actual decoding complexity is:

$$\begin{aligned} \varpi_{213,c}(0dB) &= 7 \cdot (0.83 \cdot 4086 + 0.17 \cdot 5974 + 217) \\ &= 0.3237 \times 10^5 < 0.35876 \times 10^5, \end{aligned} \tag{7.58}$$

where the weighting coefficient vector is given by $\boldsymbol{\lambda} = [0, 0.83, 0, 0.17, 0, 0, 0, 0, 0, 0, 0]$.

Figure 7.44 portrays the BER performance of the RSC(213)-coded IR-PLDC scheme designed for satisfying the complexity constraint of Equation (7.57), when using QPSK modulation in conjunction with an MMSE detector. Recall that this system was designed for maintaining an infinitesimally low BER at $\rho = 0$dB and $k = 7$ *outer* iterations were required by the system to achieve an infinitesimally low BER. In contrast to the previous 'maximum-rate' design of Figure 7.39, where a sharp turbo-cliff BER was observed, the BER of the complexity-constrained schemes dropped more gradually, owing to having a wider EXIT tunnel.

In order to elaborate a little further, Figure 7.45 quantifies the maximum achievable rate of the 'complexity-constrained' RSC-coded IR-PLDC scheme of Figure 7.32 having various complexity constrains. The minimum complexity required to enable the system to operate at $\rho = -2, -1$ and 0dB is about 3576 ACS arithmetic operations, where a throughput of 0.5 was achieved in Figure 7.45. At the minimum decoding complexity point, the *inner* IR-PLDC only activates the minimum-complexity PLDC component of PLDC(2221) with a weighting coefficient $\lambda_0 = 1$. As a result of investing more complexity, a higher rate becomes achievable in conjunction with more complex PLDC components, while operating at a certain SNR ρ. Note that in the vicinity of the cliff region, the system becomes capable of approaching the performance of the maximum-rate design at a significant complexity reduction, as evidenced in Figures 7.43 and 7.44.

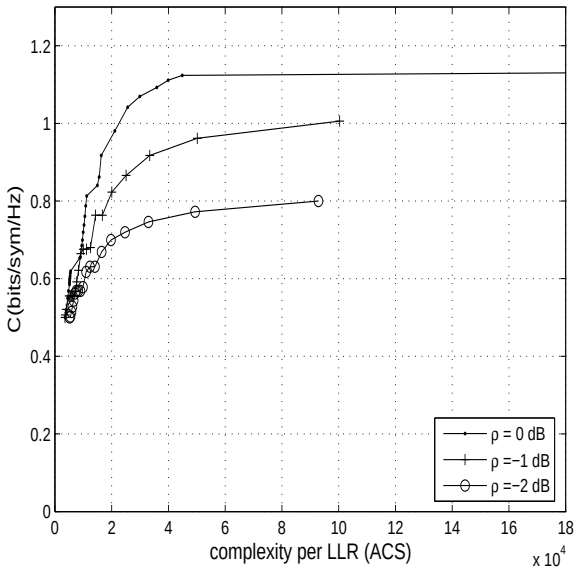

Figure 7.45: Maximum achievable rates against the required decoding complexity of the RSC(213)-coded IR-PLDC schemes of Figure 7.32 at $\rho = -2, -1, 0$dB, when using QPSK modulation and an MMSE detector.

7.5.2 IR-PLDCs Vs. IRCCs

Since both irregular *inner* schemes, such as IR-PLDCs and irregular *outer* schemes, i.e. IRCCs have the ability of providing flexible EXIT curves, it is natural to investigate further in order to explore the difference between these two approaches.

In this section, we provide a detailed comparison of the IRCCs and IR-PLDCs in terms of the maximum achievable rates and the working SNR region. We adopt the RSC(213)-coded IR-PLDC scheme having a total number of $P = P_{in} + P_{out} = 11 + 1 = 12$ components, which has been extensively demonstrated in Section 7.5.1.2. Since the IR-PLDC component codes have a maximum rate of $R_{3,LDC} = 2$, the resultant maximum rate of the RSC(213)-coded IR-PLDC scheme of Figure 7.32 is limited to 2 (bits/sym/Hz) using QPSK modulation, as seen in Figure 7.40.

For a fair comparison, we also set the maximum rate of the a IRCC-coded PLDC scheme to 2 (bits/sym/Hz), when QPSK modulation is employed. Furthermore, an IRCC scheme constituted by a set of $P_{out} = 11$ component codes was constructed in [182] from a systematic half-rate memory-4 mother code defined by the octally represented generator polynomials of $(23, 35)_8$. Hence, we have a total number of $P = P_{in} + P_{out} = 1 + 11 = 12$ components. The EXIT chart characteristic of the resultant $P_{out} = 11$ IRCC component codes is shown in Figure 7.46, where the rates of the codes are $R_{i,IRCC} = [0.1, 0.15, 0.25, 0.4, 0.45, 0.55, 0.6, 0.7, 0.75, 0.85, 0.9]$, respectively. Each component encodes a specific fraction of the incoming bit stream, as quantified by the weighting coefficient vector $\boldsymbol{\gamma} = [\gamma_1, \ldots, \gamma_{P_{out}}]$. Hence, the weighting coefficient vector $\boldsymbol{\gamma}$ is optimized with the aid of the iterative algorithm in [204], so that the EXIT curve of the resultant IRCC closely matches that of the *inner* code.

Figure 7.47 portrays the maximum achievable rates achieved by the IRCC-coded schemes using PLDC(2224) or PLDC(2221) as the *inner* codes according to Tables G.3 and G.4 in Appendix G, when employing QPSK modulation as well as an MMSE detector. The maximum achievable rates of the corresponding RSC(213)-coded IR-PLDC scheme configured according to Table G.1 is also plotted as the benchmarker. When a rate-two PLDC(2224) code is employed, the resultant IRCC-

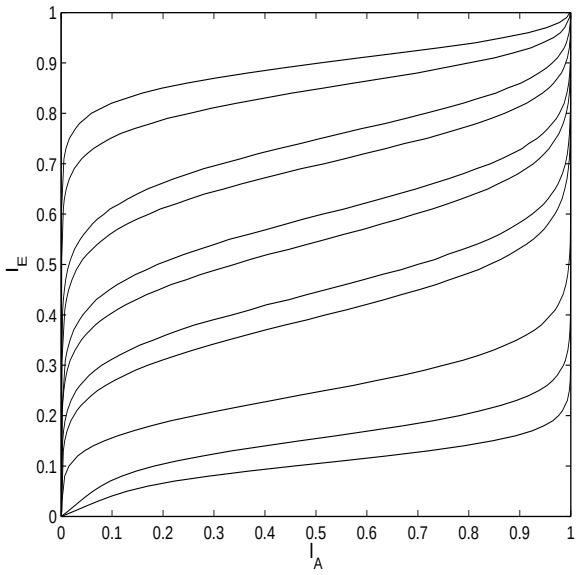

Figure 7.46: EXIT charts of the IRCC scheme having $P_{out} = 11$ component codes.

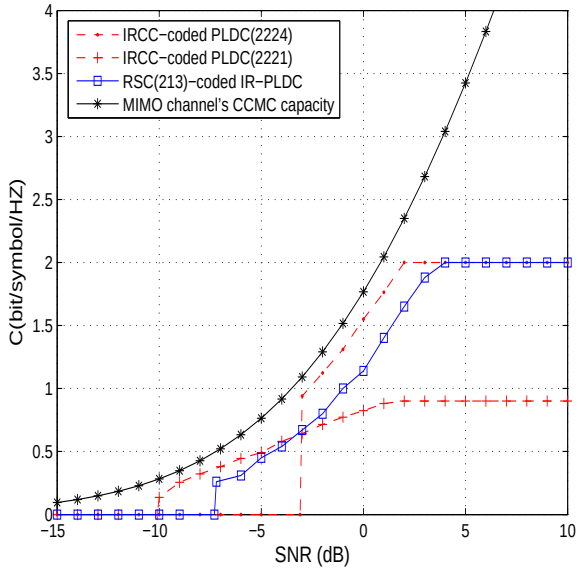

Figure 7.47: Maximum achievable rates plotted according to Tables G.3 and G.4 for the IRCC-coded schemes using PLDC(2224) and PLDC(2221) as the inner codes, when QPSK modulation in conjunction with an MMSE detector were employed.

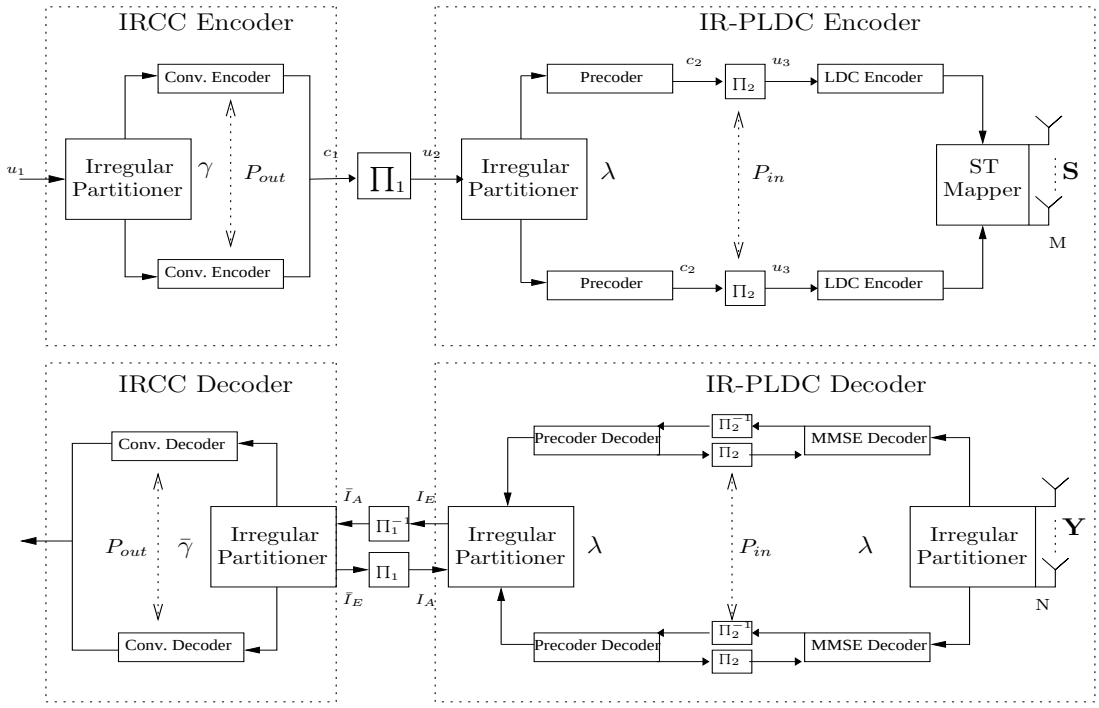

Figure 7.48: Schematic of the serial concatenated IRCC-coded IR-PLDC using iterative decoding.

coded scheme becomes capable of operating about 0.9dB away from the MIMO channel's capacity of Equation (7.10), but no open EXIT tunnel is formed until we have $\rho \geq -3$dB, which implies that it fails to function adequately in the low SNR region. By contrast, when we use the half-rate PLDC(2221) arrangement as our *inner* code, the system performs adequately for SNRs in excess of $\rho = -10$dB, as seen in Figure 7.47. However, this scheme suffers from a rate loss in the high SNR region, because the *inner* PLDC(2221) code fails to operate near the MIMO capacity. By contrast, the RSC(213)-coded IR-PLDC scheme operates about 2.5dB way from the MIMO channel's capacity for SNRs spanning from $\rho = -7$dB to $\rho = 4$dB.

In conclusion, the IRCC-coded schemes are capable of operating about 0.9dB away from the MIMO channel's capacity in either high-SNR or low-SNR region, but fail to operate across a number of SNRs. On the other hand, although the IR-PLDC aided scheme operates about 2.5dB away from the MIMO channel's capacity, it can work in a wider SNR region.

7.5.3 IRCC-Coded IR-PLDC Scheme

It is desirable to have a flexible system that is capable of working close to the MIMO channel's capacity and at the same time operating across a wide SNR region. We have demonstrated in Figure 7.47 that either IRCCs or IR-PLDCs are only capable of satisfying one of these design objectives. In this section, we will demonstrate that by serially concatenating the IRCCs [204] and the proposed IR-PLDCs, such ambitious design objectives can be fulfilled at the same time.

Figure 7.48 portrays the schematic of the proposed IRCC-coded IR-PLDC scheme. The receiver is assumed to have the knowledge of the weighting coefficient vectors $\boldsymbol{\gamma}$ and $\boldsymbol{\lambda}$, as well as that of the set of DCMs. The 'irregular partitioner' of Figure 7.48 feeds the required fraction of bits into the relevant component codes, according to the corresponding weighting coefficient vectors. For the sake of having a fair comparison to the schemes illustrated in Section 7.5.2, in the following design example, we consider a MIMO system equipped with $M = 2$ transmit as well as $N = 2$ receive

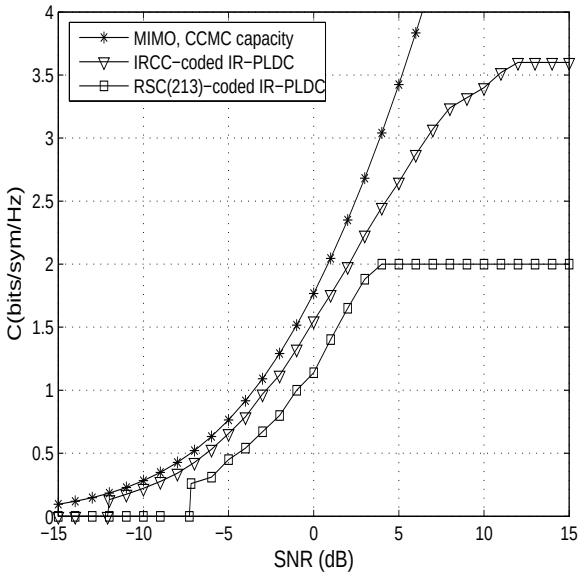

Figure 7.49: Maximum achievable rates plotted according to Tables G.5 and G.6 for the IRCC-coded IR-PLDC schemes of Figure 7.48, when QPSK modulation in conjunction with an MMSE detector were employed.

antennas and a total number of $P = 12$ component codes are used, where we have $P_{out} = 6$ IRCC component codes and $P_{in} = 6$ IR-PLDC component codes. More specifically, the IRCC component codes of Figure 7.46 having a rate of $R_{i,IRCC} = [0.1, 0.25, 0.4, 0.55, 0.7, 0.9]$ and the IR-PLDC component codes having a rate of $R_{i,LDC} =[\ 0.33, 0.5, 0.67, 1, 1.5, 2]$ in Table 7.5 were employed. Note that IRCC encoder's 'irregular partitioner' of Figure 7.48 is based on the weighting coefficient vector $\boldsymbol{\gamma} = [\gamma_1, \ldots, \gamma_{P_{out}}]$, whereas the 'irregular partitioner' of IRCC's decoder is determined by another vector $\bar{\boldsymbol{\gamma}} = [\bar{\gamma}_1, \ldots, \bar{\gamma}_{P_{out}}]$. That is because $\boldsymbol{\gamma}$ quantifies the fraction of incoming information bits, while $\bar{\boldsymbol{\gamma}}$ quantifies the fraction of incoming LLRs and they are related by:

$$\bar{\gamma}_i = \frac{\gamma_i \times R_{out}}{R_{i,IRCC}}. \qquad i = 1, \ldots, P_{out} \tag{7.59}$$

We run an exhaustive search operation for all the possible combinations of $\boldsymbol{\gamma}$ and $\boldsymbol{\lambda}$ under the following constraints:

- An open convergence tunnel must exist between the *inner* and *outer* EXIT curves in order to achieve an infinitesimally BER, provided that the aid of the decoding trajectory arrives at the top right corner of the EXIT chart;
- The throughput $C(\rho) = log_2(L) \cdot R_{in} \cdot R_{out}$ has to be maximized;
- The resultant open EXIT tunnel area has to be maximized, for the sake of minimizing the number iterations required;
- $\gamma_1 + \gamma_2 + \cdots + \gamma_{P_{out}} = 1$ and $\lambda_1 + \lambda_2 + \cdots + \lambda_{P_{in}} = 1$.

The exhaustive search is set to have a step-size of 0.05.

In Figure 7.49, we plotted the maximum rates achieved by the IRCC-coded IR-PLDC scheme of Figure 7.48 according to Tables G.5 and G.6, when QPSK modulation in conjunction with an

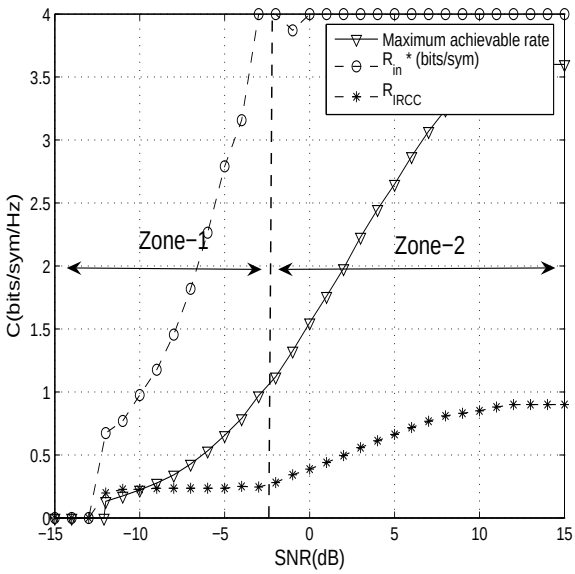

Figure 7.50: Inner throughput $log_2(L) \cdot R_{in}$ and outer rate R_{out} for the IRCC-coded IR-PLDC scheme of Figure 7.48 to achieve maximum rate according to Tables G.5 and G.6, when QPSK modulation and an MMSE detector were employed.

MMSE detector were employed. The corresponding maximum achievable rates of the RSC(213)-coded IR-PLDC scheme of Figure 7.32 was also presented as the benchmarker, which also employed $P = 12$ component codes. Observe in Figure 7.49 that employing an irregular design at both the *inner* and the *outer* codes enables the system to achieve an infinitesimally low BER for SNR starting from as low as $\rho = -12$dB. Furthermore, the double-side EXIT matching based scheme is capable of operating about 0.9dB from the MIMO channel's CCMC capacity quantified in Equation (7.10). Note that when we have $\rho > 2$dB, the IRCC-coded IR-PLDC scheme of Figure 7.48 begins to gradually deviate from the MIMO capacity, owing to lack of high-rate IR-PLDC components. Naturally, the dispense observed in the high-SNR region can be eliminated, when adopting high-rate PLDCs as the component codes.

In order to illustrate this phenomenon a little further, Figure 7.50 characterizes the effect of the *inner* throughput $log_2(L) \cdot R_{in}$ and the *outer* rate R_{out} of the IRCC-coded IR-PLDC scheme of Figure 7.48 designed for achieving the maximum rate according to Tables G.5 and G.6, when QPSK modulation and an MMSE detector were employed. The operating SNR range may be divided into two zones around $\rho = 3$dB. Observe in Figure 7.50 that in the low-SNR region, namely in Zone-1, the proposed scheme achieved a near-capacity throughput owing to the flexibility provided by the IR-PLDCs. By contrast, when we have high SNRs, i.e. in Zone-2, the maximum rate is achieved by increasing the rate of the IRCC scheme. This observation further justifies the results presented in Figure 7.47.

As far as the decoding complexity is concerned, the original IRCC scheme of [182] imposed a potentially excessive complexity in the low-rate region, owing to the additional generator polynomials. However, flexible rates of the IRCC-coded IR-PLDC scheme of Figure 7.48 in the low-SNR region are achieved by adjusting the IR-PLDC's rate, where the associated complexity is low, as seen in Figure 7.50. In Zone-2, since high-rate IRCC components are activated, the overall decoding complexity is still manageable, despite the fact that the IR-PLDC scheme's complexity is increased.

The weighting coefficient vectors $\boldsymbol{\gamma}$ and $\boldsymbol{\lambda}$ of the IRCC and IR-PLDC schemes optimized for

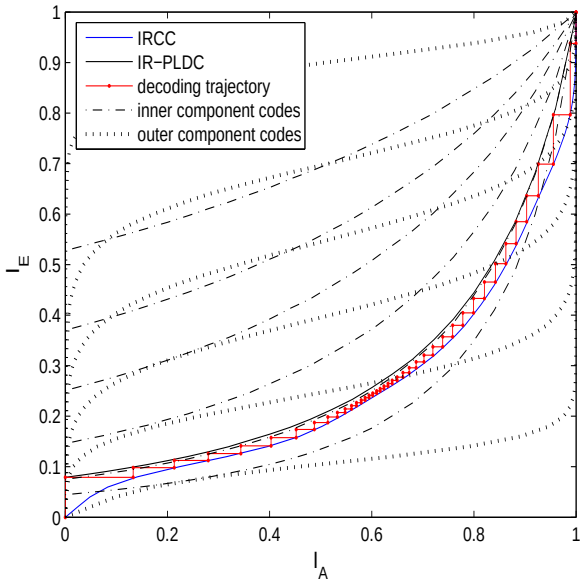

Figure 7.51: EXIT chart and the decoding trajectory of the IRCC-coded IR-PLDC scheme of Figure 7.48 at $\rho = -4$dB according to Tables G.5 and G.6, when using QPSK modulation in conjunction with an MMSE detector.

achieving the maximum aggregate rates are listed in Tables G.5 and G.6 of Appendix G. Observe in Table G.6 that typically only two components of the *inner* IR-PLDC are activated, while a number of IRCC components are required for the sake of minimizing the open EXIT tunnel area according to Table G.5. For example, when we have $\rho = 6$dB, only $P_{out} + P_{in} = 2 + 2 = 4$ out of the total of $P = 12$ components were activated. As a result of having a limited range of EXIT curve shapes, the superimposed EXIT curves cannot be accurately matched, thus we observe that the system is operating about 1.6dB away from the MIMO capacity at $\rho = 6$dB. By contrast, in the low-SNR region, i.e. when we have $\rho = -4$dB, $P_{out} + P_{in} = 5 + 2 = 7$ component codes were activated. Hence, a more accurate EXIT curve matching becomes possible. The resultant system operates 0.9dB away from the MIMO capacity, as seen in Figure 7.49.

In Figure 7.51 we portray both the EXIT curves and the decoding trajectory of the IRCC-coded IR-PLDC scheme of Figure 7.48 recorded at $\rho = -4$dB using QPSK modulation, when an MMSE detector was employed. The corresponding weighting coefficients are given in Tables G.5 and G.6. Observe in Figure 7.51 that an extremely narrow EXIT tunnel was formed, which required $k = 39$ *outer* iterations to reach the $(I_A, I_E) = (1.0, 1.0)$ point. The associated BER curve is plotted in Figure 7.52.

7.5.4 Summary

In order to pursue the design objective of operating in the vicinity of the MIMO channel's capacity across a wide range of SNRs, irregular system designs are necessary. In Sections 7.5.1 to 7.5.3, we have demonstrated the design process of irregular systems using IR-PLDCs and/or IRCCs. The factors affecting the design of near-capacity schemes using the irregular approach are summarized in Figure 7.53, where the decoding complexity and the EXIT matching accuracy of *inner* and *outer* EXIT curves are two main design factors. More specifically, the matching of the *inner* and *outer* code's EXIT curves quantifies the maximum achievable rate, which is dependent on the affordable complexity. The specific shape of the EXIT curves is also related to the decoding complexity. For

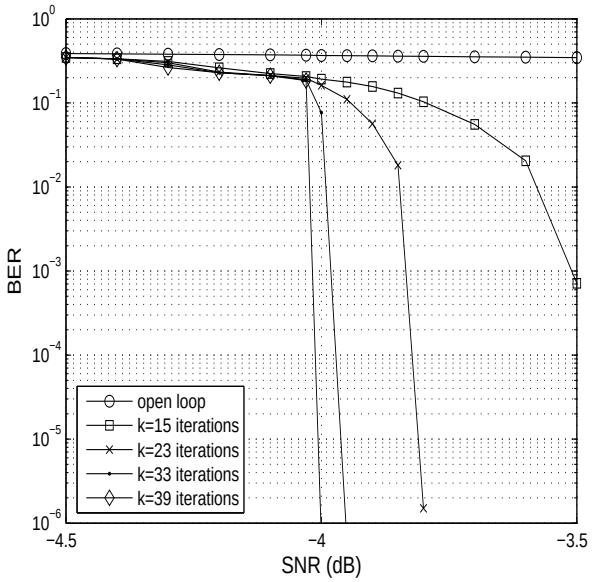

Figure 7.52: BER of the IRCC-coded IR-PLDC scheme of Figure 7.48 that designed to achieve an infinitesimally low BER at $\rho = -4$dB according to Tables G.5 and G.6, when using QPSK modulation in conjunction with an MMSE detector.

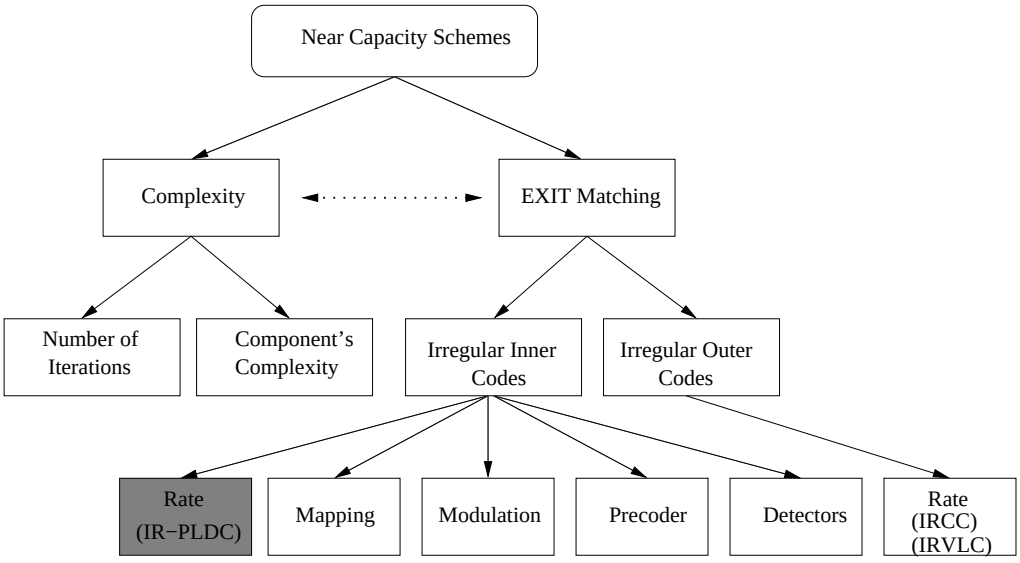

Figure 7.53: Factors affecting the design of near-capacity schemes using irregular principle.

example, if the *inner* and *outer* EXIT curves are matched while having a high gradient, a large number of iterations are required to achieve an infinitesimally low BER. On the other hand, if the matched pair of EXIT curves are near-horizonal, a low number of iterations is required. The relationship between "EXIT Matching" and "Complexity" is represented by the dotted line in Figure 7.53.

Irregular schemes are suitable for accurate EXIT curve matching, since they are capable of providing EXIT curves with flexible characteristics. The design of irregular *outer* codes can be accomplished for example by using IRCCs [204] [182] or IrRegular Variable Length Codes (IR-VLCs) [347], where irregularity is achieved by employing various code rates. The area property quantified in Equation (7.50) suggests that maximizing the achievable rate corresponds to minimizing the open EXIT tunnel area. By contrast, the irregularity of the *inner* code can be created in various ways, as seen in Figure 7.53. The IR-PLDC approach proposed in this chapter creates a diverse set of EXIT curves using different rates, as exemplified in Figures 7.33 and 7.34. There are two main differences between the irregular *inner* and *outer* schemes. Firstly, the *inner* code's EXIT curves are affected by the SNR encountered. In other words, there is a different set of *inner* EXIT curves for each SNR. This property further explains the reason that IRCC schemes may facilitate operation closer to the MIMO channel's capacity than IR-PLDCs within a certain SNR region, as evidenced in Figure 7.47. Secondly, the IR-PLDC schemes has a non-unique relationship between its aggregate rate R_{in} of Equation (7.53) and the area under the EXIT curves, which was demonstrated in Figure 7.37. Hence, our optimization objective is to maximize the achievable rate as well as maximize the open EXIT tunnel area. However, the employment of the IR-PLDCs potentially facilitates the resultant scheme to operate across a wide SNR range, as seen in Figure 7.49.

Figure 7.53 also lists other techniques of creating a diverse set of EXIT curves in the context of irregular *inner* codes. For example, changing the precoder's memories and/or the generator polynomials is capable of effectively changing the shape of the EXIT curves without affecting the area under them, as illustrated in Figure 7.31. Another possible approach of changing the EXIT curves' shape, while maintaining the same area is to employ different mapping schemes for each component [343] [48]. Obviously, employing different modulation schemes for each component code can also adjust the effective throughput of the system. Hence, a diverse set of EXIT curve shapes can be generated. When the decoding complexity is taken into account, the *inner* code's irregularity can be complemented by using various detectors, such as ML, MMSE, Serial Interference Cancellation (SIC) and Parallel Interference Cancellation (PIC) detectors. Finally, it is important to point out the set of the techniques seen in Figure 7.53 can be jointly employed to create an even more diverse *inner* irregularity.

7.6 Conclusion

In this chapter, after illustrating the design of STBCs, we have demonstrated that the family of LDCs constitutes a general framework, which accommodates the entire set of STBCs having different design objectives. Furthermore, we proposed a novel method of optimizing the LDCs based on their DCMC capacity, as seen in Section 7.2.4. More particularly, in Section 7.3 we demonstrated the linkage between the existing STBC schemes and LDCs by characterizing their mathematical representations and the design philosophy under LDC's general framework. In Sections 7.4.1 we investigated the performance of two-stage serial concatenated LDCs, with the aid of EXIT charts. The employment of precoders for the sake of achieving an infinitesimally low BER was investigated in Section 7.4.2, while approaching the maximum achievable rate.

Motivated by the flexibility of the LDC structure complied with its near-capacity performance potential, in Section 7.5.1.2 we proposed a novel IR-PLDC scheme that is capable of approaching the maximum attainable rate across a wide range of SNRs, as demonstrated from Figures 7.38 to 7.42, when combined with a simple *outer* channel coder. In Figure 7.40, we showed that

the proposed RSC(213)-coded IR-PLDC scheme is capable of operating about 2.5dB from the MIMO channel's capacity. In the situation where the affordable decoding complexity is limited, in Section 7.5.1.3 we proposed a 'complexity-constrained' IR-PLDC scheme, which was designed with the aid of EXIT charts and maximizing the attainable rate under a specific complexity constraint. After the detailed examination of the advantages and drawbacks of irregular *inner* and *outer* encoding schemes in Section 7.5.2, in Section 7.5.3 we proposed an IRCC-coded IR-PLDC scheme, which is capable of operating about 0.9dB from the MIMO channel's capacity for a wide range of SNRs, while achieving an infinitesimally low BER.

Chapter 9

Cooperative Space-Time Block Codes

9.1 Introduction and Outline

The space time block coding techniques detailed in Chapters 7 and 8 provide promising solutions in the context of co-located MIMO systems requiring reliable wireless communications at high rates. However, it may not always be practical to accommodate multiple antennas at the mobile stations, owing to cost, size and other hardware limitations. A further limitation of co-located MIMO elements is that even at relatively large element separations their elements may not benefit from independent fading, when subjected to shadow-fading imposed for example by large-bodied vehicles or other shadowing local paraphernalia. As a remedy, High Speed Downlink Packet Access (HSDPA) style adaptive modulations [370] as well as the concept of cooperative MIMOs [371] have been proposed for cellular systems as an attempt to attain a better communication efficiency beyond that permitted by a single node's local resources. More specifically, a group of mobile nodes, known as relays, 'shares' their antennas with other users to create a virtual antenna array to provide spatial diversity gain. In order to deepen our discussion, Figure 9.1 illustrates the relay concept as well as potential applications of various cooperative MIMO systems in a cellular network. For example, when a user is behind buildings or underground, as seen in Figure 9.1, direct communication with the Base Station (BS) becomes unreliable, owing to severe shadow fading and path loss. In order to maintain reliable wireless communications, a group of users in each others' vicinity may form a virtual antenna array in order to reliably forward the data between the source node and the BS.

A ground-breaking paper of Cover and El Gamal [121] proposed several cooperation strategies for the relays and extensively investigated the information-theoretic properties based on the assumption of encountering Line-Of-Sight (LOS) Gaussian channels. More recent studies have focused on the more realistic assumptions of encountering fading channels [118] [119] and applied the relay-aided cooperation concept to wireless sensor networks [372]. It has been shown by several researchers [119] [373] that considerable benefits can be achieved as a result of relay-aided cooperation, including the reduction of the outage probability and a substantial diversity gain as well as throughput improvement.

Generally speaking, there are three types of cooperations [121], Amplify-and-Forward (AF) , Decode-and-Forward (DF) as well as Compress-and-Forward (CF) . When using the AF cooperation scheme, the relay nodes simply amplify the received signal waveforms, but they amplify the

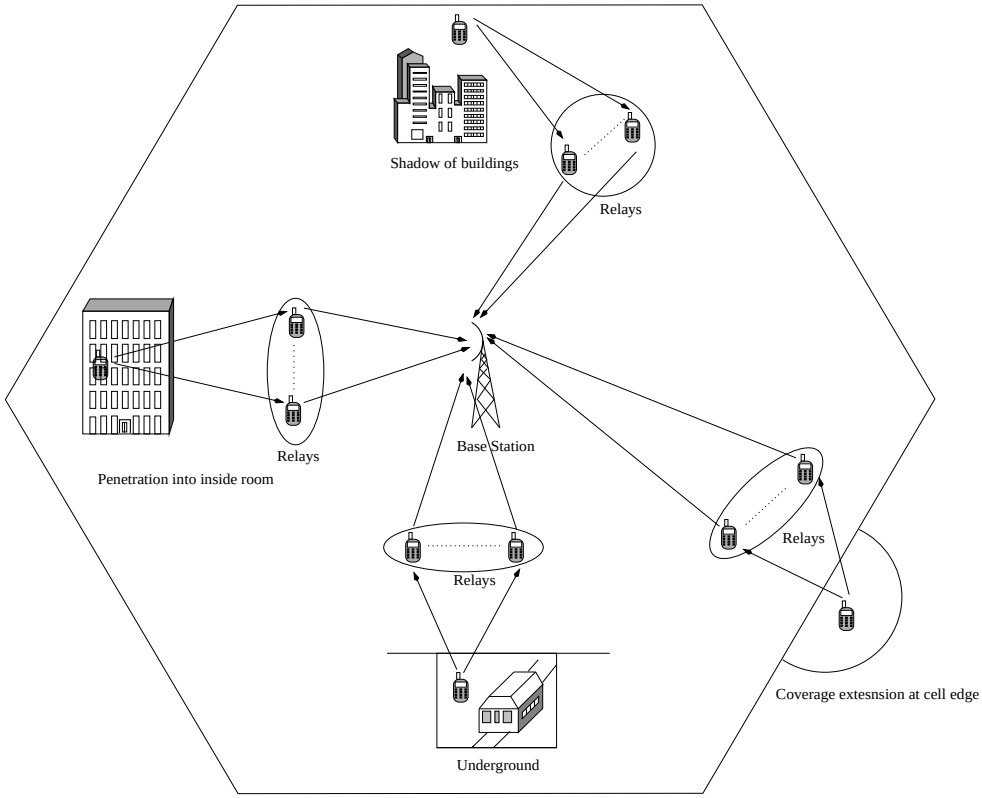

Figure 9.1: Cooperative MIMO systems in a cellular network.

signal and noise jointly and hence are unable to improve the SNR. On the other hand, in the DF strategy, the signals received at the relays are decoded and possibly re-encoded using different Forward Error Correction (FEC) codes, before being forwarded to the destination. Finally, the CF arrangement is also referred to as an observe-forward or quantize-forward technique by some researchers [373]. In its original form [121], the relay compresses, estimates or quantizes its observations without decoding the information.

Owing to the philosophical similarities between the cooperative MIMO and the co-located MIMO systems, numerous space-time block coding techniques have been 'transplanted' into relay-aided schemes in order to achieve cooperative diversity, based on either AF strategies [25] [130] or DF arrangements [118] [119]. It was Laneman and Wornell [25] who first proposed to employ orthogonal STBCs for cooperative MIMO systems, where each relay transmits according to a different column of the orthogonal STBC matrix. As argued in Chapter 7, the family of LDCs [29] becomes a more powerful design alternative to provide cooperative diversity gain for various relay-aided systems [374] [375] [376], owing to its remarkable design flexibility guaranteed by its linear structure. Furthermore, the authors of [377] [133] [378] exploited the diversity-multiplexing gain tradeoff as a means of evaluating the fundamental limitations of different cooperation strategies. In a similar manner, the same tradeoff was capitalized on by Zheng and Tse in the context of the co-located MIMO systems [24].

In an effort to introduce channel coding schemes into cooperative MIMO systems for the sake of attaining near error-free transmission, the authors of [131] [128] developed the so-called 'coded-cooperative' schemes, where each relay contributes extrinsic information in a manner similar to the 'parallel-concatenated' component of classic turbo codes [327]. More explicitly, after receiving the channel-coded signals broadcast by the source node, the relays decode and interleave the information, before it is re-encoded by another channel encoder. Hence, the BS becomes capable

of exploiting the extrinsic information gleaned from various interleaved replicas of the transmitted information by employing a conventional turbo detector [327]. In [139] [379], the coded-cooperative aided schemes have been further improved by forwarding the soft estimates of the transmitted bits from the relays, rather than forwarding the hard decoded bits. However, this family of coded-cooperative schemes inevitably imposes both a high complexity as well as a high delay at the relays. Furthermore, it increases the power consumption of the relays despite transmitting no source-data from themselves.

In order to attain cooperative diversity as well as to eliminate high-complexity operations at the relays, in this chapter we propose a novel family of twin-layer Cooperative Linear Dispersion Codes (CLDCs) based on the AF protocol. Since the AF strategy typically relies on twin-phase transmissions, namely the broadcast interval and the cooperation interval, the proposed CLDC schemes also have a twin-layer structure, which allows us to explore each transmission interval's specific characteristics as discussed in more detail in Section 9.2.3. Furthermore, the novel class of twin-layer CLDCs inherits the LDCs' flexible yet powerful linear structure, where similar properties can be observed. We also propose a novel serial concatenated coded-cooperative system, and highlight its benefits in contrast to the coded-cooperative schemes of [131] [128] based on parallel concatenated philosophies. More explicitly, the novel features of the schemes proposed in this chapter are listed as follows:

- The proposed twin-layer CLDC schemes may be readily integrated with next-generation systems, such as the Third Generation Partnership Project's Long Term Evolution (3GPP-LTE) proposals;
- The twin-layer CLDC schemes advocated are capable of supporting an arbitrary number of relays equipped with single or multiple antennas, while adopting various modulation schemes;
- The power consumption as well as the complexity imposed by cooperation at the relays are insignificant, since only simple linear combination operations are performed;
- We propose a novel IRCC aided IrRegular Precoded Cooperative Linear Dispersion Code (IR-PCLDC) using iterative decoding, which is designed based on EXIT charts [380];
- The proposed IRCC-coded IR-PCLDC scheme becomes capable of providing flexible rates, which may be harmonized with the SNR encountered.

The rest of this chapter is structured in two parts. In the first part, we commence by presenting a general system model for the CLDCs based on the AF protocol in Section 9.2.1 and outline the associated assumptions in Section 9.2.2, followed by the mathematical characterization of the twin-layer CLDC scheme. Hence, the linkage between LDCs designed for co-located MIMO systems and CLDCs designed for cooperative MIMO systems is outlined in Section 9.2.4. In the second part of our investigations, Section 9.3 introduces the irregular design philosophy in the context of cooperative systems and proposes a novel IRCC-coded IR-PCLDC scheme in order to maintain high rates across a wide SNR range, while maintaining an infinitesimally low BER. We focus our attention on the irregular system's distinctive features in the context of the cooperative MIMO systems. The corresponding irregular co-located MIMO system detailed in Section 7.5.3 will be used as the benchmarker. Finally, we summarize the findings of this chapter and provide our concluding remarks in Section 9.4.

9.2 Twin-Layer Cooperative Linear Dispersion Codes

9.2.1 System Model

In this section, we commence our discourse with the detailed description of the proposed twin-layer CLDCs based on the AF cooperation protocol, noting that this philosophy may be readily

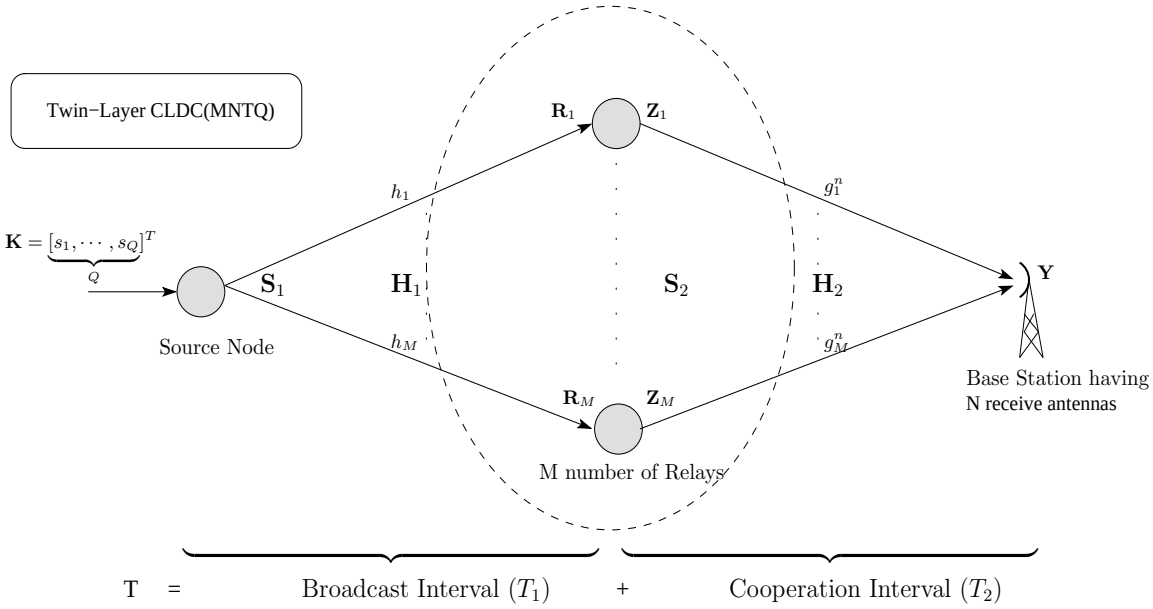

Figure 9.2: Schematic of the cooperation-aided uplink system employing the twin-layer Cooperative Linear Dispersion Codes (CLDCs).

extended to DF and CF strategies. An UpLink (UL) scenario in a cellular network is considered, as exemplified in Figure 9.1, where a source node communicates with the BS having N receive antennas with the aid of M independent relays. For simplicity, each cooperating node is assumed to equip with a single transmit antenna, although multiple antenna aided nodes may also be incorporated into the proposed CLDCs.

Figure 9.2 portrays the schematic of the cooperation-aided uplink system based on the proposed twin-layer CLDCs. As seen in Figure 9.2, each transmission block consists of two intervals, namely the broadcast interval and the cooperation interval. During the broadcast interval T_1, the source broadcasts an UL information bearing vector $\mathbf{K} = [s_1, \ldots, s_Q]^T$ containing Q L-PSK symbols to the relay nodes using CLDC's the first-layer dispersion matrix, which will be detailed in Section 9.2.3. During the cooperation interval T_2, the relays form a virtual antenna array and cooperatively transmit a space-time codeword $\mathbf{S}_2$ of Figure 9.2 to the BS based on CLDC's second-layer dispersion matrices. Hence, the twin-layer CLDC scheme of Figure 9.2 based on the AF strategy can be fully specified by the parameters $(MNTQ)$, provided that the total number of channel uses T obeys $T = T_1 + T_2$. Throughout our investigations, a side-by-side comparison of the twin-layer cooperative CLDC$(MNTQ)$ scheme and the corresponding co-located LDC$(MNTQ)$ arrangement of Figure 9.3 is provided.

9.2.2 System Assumptions

In this section, we outline our assumptions stipulated, in order to make the twin-layer CLDC scheme of Figure 9.2 as practical as possible. The assumptions and their rationale are summarized as follows:

- All the relays of Figure 9.2 are assumed to transmit synchronously. Time-synchronous transmissions can be accomplished, when the relative delays between the relays are significantly shorter than the symbol duration. Solutions designed for asynchronous cooperations have been proposed by a number authors [381] [382], but this issue is beyond the scope of our discussions;

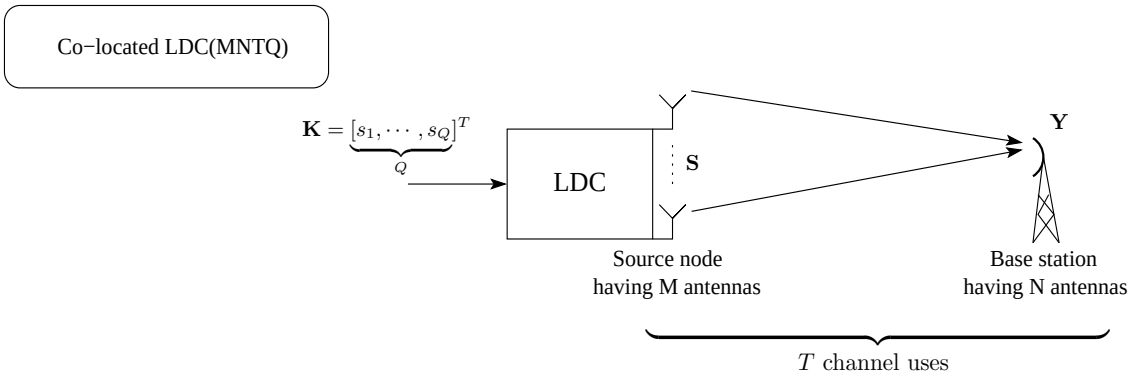

Figure 9.3: Schematic of a co-located uplink MIMO system using Linear Dispersion Codes (LDCs).

- All the nodes of Figure 9.2 are assumed to have a single antenna and hence operate in half-duplex mode, i.e. at any point of time, a node can either transmit or receive. This constraint is imposed, in order to prevent the high-power transmit signal from contaminating the low-power received signal, for example, by the non-linear distortion-induced out-of-bound emissions routinely encountered at the transmitter. This may even potentially mislead the Automatic Gain Control (AGC) AGC of the receiver into believing that a high-level signal was received, which would block the useful received signal arriving at a low power;

- All the relays of Figure 9.2 transmit and receive on the same frequency as the source node, in order to avoid wasting or occupying additional bandwidth;

- No communication is permitted between the relays, in an effort to minimize the total network traffic. The relays may use the same unallocated time-slot for their reception and transmission;

- Since the simple AF strategy is adopted, only linear combination operations are performed at the relays before retransmitting the signals dispersed to the cooperating MIMO elements to the BS, which will be explicitly shown in the context of Equation (9.13);

- The BS seen in Figure 9.2 is equipped with N receive antennas. Moreover, the BS is assumed to have the knowledge of perfect CSI for all the wireless links, i.e. it knows $\mathbf{H}_1$ and $\mathbf{H}_2$ of Figure 9.2 in order to facilitate coherent detection. More particularly, $\mathbf{H}_1$ and $\mathbf{H}_2$ are given by

$$\mathbf{H}_1 = [h_1, \ldots, h_M]^T, \qquad \mathbf{H}_2 = \begin{pmatrix} g_1^1 & \cdots & g_m^1 \\ \vdots & \ddots & \vdots \\ g_1^N & \cdots & g_m^N \end{pmatrix}, \tag{9.1}$$

  where h_m denotes the CIR between the source and the m-th relay of the broadcast interval and g_m^n denotes the CIR between the m-th relay and the n-th receive antenna of the BS during the cooperation interval, and we have $m = (1, \ldots, M)$ and $n = (1, \ldots, N)$;

- All the channel matrices $\mathbf{H}_1$ and $\mathbf{H}_2$ of Figure 9.2 are assumed to be representing quasi-static Rayleigh-fading, i.e. the channel gains remain constant during T time slots and change independently at the beginning of the next. Furthermore, the channels gains are assumed to be spatially independent, while having a unit variance. Therefore, the resultant virtual antenna array elements can be considered to be subjected to perfectly independent fading. By contrast, the co-located MIMO elements of Figure 9.3 typically suffer from a certain degree of spatial correlation, owing to their insufficient spatial separation;

- We confine the total number of channel uses of the twin-layer CLDC scheme of Figure 9.2 to T, where $T = T_1 + T_2$. Hence, by appropriately adjusting the parameters T_1 or T_2, different degrees of freedom can be provided for the broadcast interval as well as for the cooperation interval;
- At any given time, the total transmit power of the twin-layer CLDC scheme of Figure 9.2 is normalized to unity. More explicitly, the source transmits at unit power during the broadcast interval, but keeps silent during the cooperation interval. On the other hand, after listening for T_1 time slots, each relay transmits a signal vector with the power of $\frac{1}{M}$ in order to exploit the next unallocated T_2 time slots. Since M number of relays are involved in the cooperation, the total power remains unity during the cooperation interval.

9.2.3 Mathematical Representations

Based on the assumptions outlined in Section 9.2.2, we are now ready to provide a more insightful description of the twin-layer CLDC model of Figure 9.2. When a user intends to transmit data, the BS firstly functions as a control unit and selects a group of nearby users in order to assist the source node's UL transmission. More specifically, the BS assigns a dispersion matrix χ_1 obeying Equation (9.4) to the source node in order to enable its UL transmission during the broadcast interval. Each relay also receives a different dispersion matrix $\mathbf{B}_m$ obeying Equation (9.13) from the BS in order to attain diversity during the cooperation interval. These control information transmissions are necessary for initializing the cooperation-aided UL transmission of the source node.

Since the distance between the relays is typically far lower than the distance to the source, we could reasonably assume that the SNR between the source and the relays becomes:

$$\rho_{SR} = \frac{1}{\sigma_{SR}}, \tag{9.2}$$

where σ_{SR} denotes the corresponding noise variance at the relays. During the cooperation interval, each relay transmits at a power of $\frac{1}{M}$, which implies that the total transmit power is evenly distributed across the M relays of Figure 9.2. Hence, the SNR at the BS can be written as:

$$\rho_{RB} = \frac{1}{\sigma_{RB}}, \tag{9.3}$$

where σ_{RB} is the noise variance at the BS.

In the first stage of the cooperation-aided communication, namely the broadcast interval occupying T_1 time slots, the source node encodes each L-PSK modulated information vector $\mathbf{K} = [s_1, \ldots, s_Q]^T$ to a transmission vector $\mathbf{S}_1 \in \zeta^{T_1 \times 1}$ based on

$$\underbrace{\begin{pmatrix} t^1 \\ \vdots \\ t^{T_1} \end{pmatrix}}_{\mathbf{S}_1} = \underbrace{\begin{pmatrix} x^{1,1} & \cdots & x^{1,Q} \\ \vdots & \ddots & \vdots \\ x^{T_1,1} & \cdots & x^{T_1,Q} \end{pmatrix}}_{\chi_1} \underbrace{\begin{pmatrix} s_1 \\ \vdots \\ s_Q \end{pmatrix}}_{\mathbf{K}}, \tag{9.4}$$

where the first-layer dispersion matrix $\chi_1 \in \zeta^{T_1 \times Q}$ is responsible for dispersing the information vector $\mathbf{K}$ to all the T_1 temporal dimensions. According to the power constraint, the transmission vector is normalized to $E\{tr(\mathbf{S}_1^H \mathbf{S}_1)\} = T_1$, which requires the dispersion matrix χ_1 to satisfy

$$tr(\chi_1^H \chi_1) = T_1. \tag{9.5}$$

At the m-th relay, the corresponding receive vector $\mathbf{R}_m = [r_m^1, \ldots, r_m^{T_1}]^T$ becomes

$$\mathbf{R}_m = h_m \mathbf{S}_1 + \mathbf{V}_m. \tag{9.6}$$

By stacking the received signals from M relays, we arrive at

$$\begin{array}{ccccc} \underbrace{\begin{pmatrix} \mathbf{R}_1 \\ \vdots \\ \mathbf{R}_M \end{pmatrix}} & = & \underbrace{\begin{pmatrix} h_1\mathbf{I} \\ \vdots \\ h_M\mathbf{I} \end{pmatrix}} \mathbf{S}_1 + & \underbrace{\begin{pmatrix} \mathbf{V}_1 \\ \vdots \\ \mathbf{V}_M \end{pmatrix}} & \\ \mathbf{R} & = & \bar{\mathbf{H}}_1 \mathbf{S}_1 & + & \bar{\mathbf{V}}_1, \end{array} \tag{9.7}$$

where $\mathbf{R} = [\mathbf{R}_1, \ldots, \mathbf{R}_M]^T$ and $\bar{\mathbf{V}}_1 \in \zeta^{MT_1 \times 1}$ denotes the combined noise vector having a variance of σ_{SR}. The equivalent channel matrix $\bar{\mathbf{H}}_1 \in \zeta^{MT_1 \times T_1}$ of Equation (9.7) can be represented by

$$\bar{\mathbf{H}}_1 = \mathbf{H}_1 \otimes \mathbf{I}, \tag{9.8}$$

where $\mathbf{I}$ denotes an identity matrix having a size of $(T_1 \times T_1)$. Furthermore, by combining Equations (9.4) and (9.7), we have

$$\mathbf{R} = \bar{\mathbf{H}}_1 \chi_1 \mathbf{K} + \bar{\mathbf{V}}_1. \tag{9.9}$$

During the cooperation interval of Figure 9.2, the relays cooperatively construct a space-time codeword based on the pre-assigned dispersion matrices $\mathbf{B}_m$ of Equation (9.13) using the received signal vectors $\mathbf{R}_m$ of Equation (9.6). Firstly, the energy of the received signals has to be normalized during the broadcast interval. From Equation (9.6), we have

$$E\{\mathbf{R}_m^H \mathbf{R}_m\} = (1 + \sigma_{SR})T_1. \tag{9.10}$$

Thus, before performing the second-layer dispersion operations, we multiply $\mathbf{R}_m$ of Equation (9.6) by the normalization factor

$$\theta = \sqrt{\frac{T_1}{E\{\mathbf{R}_m^H \mathbf{R}_m\}}} = \sqrt{\frac{1}{1 + \sigma_{SR}}}, \tag{9.11}$$

so that we arrive at

$$\theta^2 E\{\mathbf{R}_m^H \mathbf{R}_m\} = T_1. \tag{9.12}$$

At the m-th relay, the second-layer dispersion matrices $\mathbf{B}_m \in \zeta^{T_2 \times T_1}$ are employed to disperse the normalized received vector $\theta \mathbf{R}_m$ to the T_2 available number of time slots. Hence, the m-th relay's transmitted vector is given by

$$\begin{array}{ccccc} \underbrace{\begin{pmatrix} z_m^1 \\ \vdots \\ z_m^{T_2} \end{pmatrix}} & = & \theta \underbrace{\begin{pmatrix} b_m^{1,1} & \cdots & b_m^{1,T_1} \\ \vdots & \ddots & \vdots \\ b_m^{T_2,1} & \cdots & b_m^{T_2,T_1} \end{pmatrix}} & \underbrace{\begin{pmatrix} r_m^1 \\ \vdots \\ r_m^{T_1} \end{pmatrix}} & \\ \mathbf{Z}_m & = & \theta \cdot \mathbf{B}_m & \mathbf{R}_m, & \end{array} \tag{9.13}$$

which should satisfy the power constraint of $E\{tr(\mathbf{Z}_m^H \mathbf{Z}_m)\} = \dfrac{T_2}{M}$ and z_m^i $(i = 1, \ldots, T_2)$ denotes the m-th relay's transmit signal of the i-th slot. Thus, the set of second-layer matrices $\mathbf{B}_m$ should obey

$$tr(\mathbf{B}_m^H \mathbf{B}_m) = \frac{T_2}{M}. \tag{9.14}$$

Therefore, the 'virtual' space-time codeword $\mathbf{S}_2 \in \zeta^{M \times T_2}$ of Figure 9.2 can be formed by concatenating the dispersed vectors from all the relays, which is given by

$$\mathbf{S}_2 = \begin{pmatrix} \mathbf{Z}_1^T \\ \vdots \\ \mathbf{Z}_M^T \end{pmatrix} = \theta \begin{pmatrix} (\mathbf{B}_1 \mathbf{R}_1)^T \\ \vdots \\ (\mathbf{B}_M \mathbf{R}_M)^T \end{pmatrix}. \tag{9.15}$$

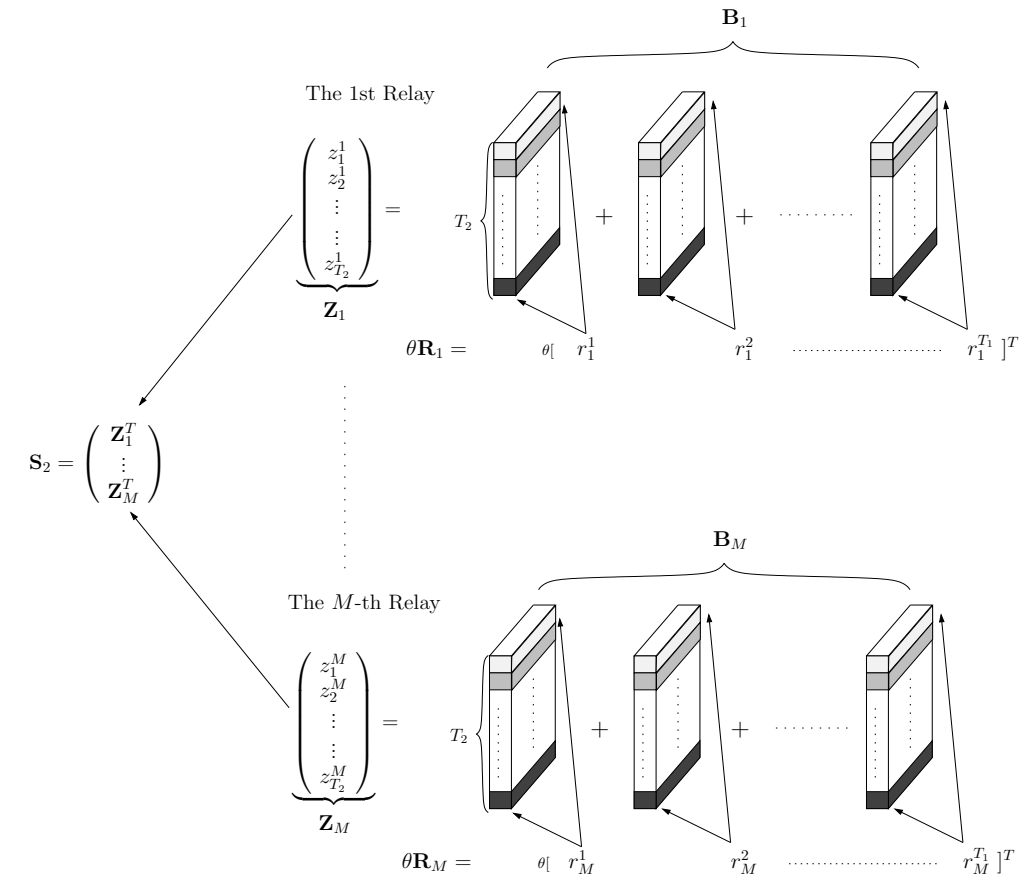

Figure 9.4: The cooperative space-time codeword $\mathbf{S}_2$ formulated based on Equations (9.13) and (9.15).

Observe in Equation (9.15) that each relay contributes one row of the second-layer space-time codeword $\mathbf{S}_2$. Also note that each relay's received signal $\mathbf{R}_m$ formulated in Equation (9.6) may experience quite different channel conditions, owing to experiencing i.i.d. Rayleigh fading. Furthermore, the process of forming the cooperative space-time codeword $\mathbf{S}_2$ for the cooperation interval is visualized in Figure 9.4. More explicitly, the m-th relay disperses the corresponding normalized received signal vector $\theta\mathbf{R}_m = \theta[r_m^1, \ldots, r_m^{T_1}]^T$ to the T_2 temporal slots using the assigned dispersion matrix $\mathbf{B}_m$ obeying Equation (9.13), as seen in Figure 9.4. The resultant signal vector $\mathbf{Z}_m$ contributes one row the space-time codeword $\mathbf{S}_2$ of Equation (9.15).

At the BS, the received signal matrix $\mathbf{Y} \in \zeta^{N \times M}$ of Figure 9.2 becomes

$$\mathbf{Y} = \mathbf{H}_2\mathbf{S}_2 + \mathbf{V}_2. \tag{9.16}$$

Define the $row()$ operation as the vertical stacking of the rows of an arbitrary matrix. Subjecting both sides of Equation (9.16) to the $row()$ operation gives the equivalent system matrix:

$$\bar{\mathbf{Y}} = \bar{\mathbf{H}}_2\mathbf{Z} + \bar{\mathbf{V}}_2, \tag{9.17}$$

where $\bar{\mathbf{Y}} \in \zeta^{NT_2 \times 1}$ and $\bar{\mathbf{V}}_2 \in \zeta^{NT_2 \times 1}$ denotes the noise vector having a variance of σ_{RB}. The equivalent channel matrix $\bar{\mathbf{H}}_2 \in \zeta^{NT_2 \times MT_2}$ of Equation (9.17) is given by

$$\bar{\mathbf{H}}_2 = \mathbf{H}_2 \otimes \mathbf{I}, \tag{9.18}$$

and the equivalent transmission matrix $\mathbf{Z} \in \zeta^{MT_2 \times 1}$ of Equation (9.17) becomes

$$\begin{aligned} \underbrace{\begin{pmatrix} \mathbf{Z}_1 \\ \vdots \\ \vdots \\ \mathbf{Z}_M \end{pmatrix}}_{\mathbf{Z}} &= \underbrace{\begin{pmatrix} \mathbf{B}_1 & \mathbf{0} & \cdots & \mathbf{0} \\ \mathbf{0} & \mathbf{B}_m & \cdots & \mathbf{0} \\ \mathbf{0} & \mathbf{0} & \ddots & \mathbf{0} \\ \mathbf{0} & \cdots & \cdots & \mathbf{B}_M \end{pmatrix}}_{\chi_2} \cdot \theta\mathbf{R}, \\ \mathbf{Z} &= \chi_2 \cdot \theta\mathbf{R}, \end{aligned} \tag{9.19}$$

where $\mathbf{0} \in \zeta^{T_2 \times T_1}$ denotes a zero matrix. The equivalent second-layer Dispersion Character Matrix (DCM) $\chi_2 \in \zeta^{MT_2 \times MT_1}$ defined in Equation (9.19) fully characterizes the transmissions during the cooperation interval.

Further combining Equations (9.9), (9.17) and (9.19) we arrive at

$$\begin{aligned} \bar{\mathbf{Y}} &= \bar{\mathbf{H}}_2\mathbf{Z} + \bar{\mathbf{V}}_2 \\ &= \theta\bar{\mathbf{H}}_2\chi_2\mathbf{R} + \bar{\mathbf{V}}_2 \\ &= \theta\bar{\mathbf{H}}_2\chi_2(\bar{\mathbf{H}}_1\chi_1\mathbf{K} + \bar{\mathbf{V}}_1) + \bar{\mathbf{V}}_2 \\ &= \theta\underbrace{\bar{\mathbf{H}}_2\chi_2\bar{\mathbf{H}}_1\chi_1}\mathbf{K} + \underbrace{\theta\bar{\mathbf{H}}_2\chi_2\bar{\mathbf{V}}_1 + \bar{\mathbf{V}}_2} \\ &= \quad\bar{\mathbf{H}}\mathbf{K} \quad + \quad \bar{\mathbf{V}}. \end{aligned} \tag{9.20}$$

The combined noise $\bar{\mathbf{V}}$ becomes colored, with a covariance of $\sigma_0 = (\mathbf{I}_{T_2}\sigma_{RB} + \theta^2\bar{\mathbf{H}}_2\chi_2\chi_2^H\bar{\mathbf{H}}_2^H\sigma_{SR})$, owing to the noise amplification and recombination experienced at the relays. The equivalent channel matrix $\bar{\mathbf{H}} \in \zeta^{NT_2 \times Q}$ of Equation (9.20) is known to the BS, since the BS has the knowledge of the CIR matrices $\mathbf{H}_1$ as well as $\mathbf{H}_2$ of Figure 9.2 and that of the DCM pair $\{\chi_1, \chi_2\}$. Most importantly, Equation (9.20) demonstrates that the twin-layer CLDC structure originally formulated in Equations (9.4) and (9.13) can be merged into a 'single' equivalent channel matrix.

In order to perform ML detection, we have to whiten the noise, which is achieved by multiply with $\sigma_0^{-\frac{1}{2}}$ on both sides of Equation (9.20). Hence, the ML estimation of the transmitted symbol vector $\mathbf{K} = [s_1, \ldots, s_Q]^T$ can be written as

$$\bar{\mathbf{K}} = arg\{\min(||\sigma_0^{-\frac{1}{2}}\mathbf{Y} - \sigma_0^{-\frac{1}{2}}\bar{\mathbf{H}}\mathbf{K}_f||^2)\}, \tag{9.21}$$

where $\mathbf{K}_f$ denotes all the possible combinations of the Q transmitted symbols.

9.2.4 Link Between CLDCs and LDCs

This section aims for characterizing the fundamental link between the LDCs designed for the co-located MIMO systems of Figure 9.3 and the CLDCs contrived for the cooperative MIMO systems of Figure 9.2. The similarities as well as the differences between the LDCs and the CLDCs are summarized in Table 9.1 and a range of remarks is offered as follows.

- The LDCs of Figure 9.3 employ M number of transmit antennas, whereas the CLDCs of Figure 9.2 form an identical-size virtual antenna array with the aid of M relays selected by the BS;
- In both scenarios, the UL receiver of the BS is assumed to have N receive antennas;
- The LDCs of Figure 9.3 occupy a total of T channel slots per space-time block. For the sake of a fair comparison, the twin-layer CLDCs also span $T = T_1 + T_2$ time slots per block. More explicitly, the broadcast interval having T_1 slots is employed for the relays to receive the source information, whereas T_2 time slots are used for the cooperation phase;

Table 9.1: Comparison of the LDCs of Figure 9.3 and the CLDCs of Figure 9.2.

	LDCs of Figure 9.3	**CLDCs of Figure 9.2**
M	Number of transmit antennas	Number of relays
N	Number of receive antennas	Number of receive antennas
T	Time slots per LDC block	$T = T_1 + T_2$
Q	Number of symbols	Number of symbols
R	$R_{LDC} = Q/T$	$R_{CLDC} = Q/T$
$\mathbf{K}$	Perfect knowledge	Obtained using Equation (9.6)
DCM	χ	$\{\chi_1, \chi_2\}$
Equivalent channel matrix	$\mathbf{H}\chi$ of Equation (7.15)	$\mathbf{H}_2\chi_2\mathbf{H}_1\chi_1$ of Equation (9.20)

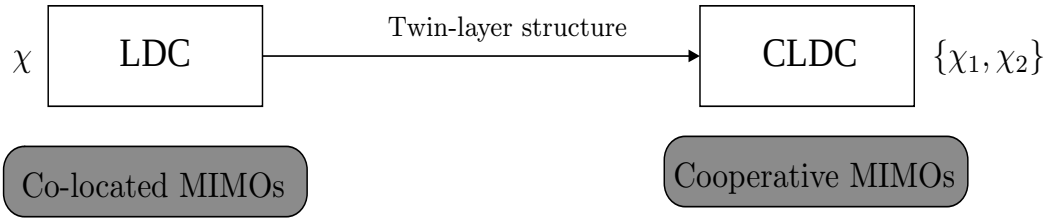

Figure 9.5: Link between LDCs designed for co-located MIMO systems and twin-layer CLDCs designed for cooperative MIMO systems.

- The symbol rate of both the LDCs and CLDCs is defined as $R = \frac{Q}{T}$, where Q is the number of L-PSK symbols transmitted per space-time block;
- When constructing the symbol vector $\mathbf{K} = [s_1, \ldots, s_Q]^T$, each transmit antenna element of the LDCs of Figure 9.3 has direct access to the Q number of L-PSK symbols. In contrast, the CLDCs of Figure 9.2 only have access to the potentially channel-contaminated version of $\mathbf{K}$ received during the broadcast interval using Equation (9.6). We will characterize the CLDCs' BER performance in Figure 9.7, when the relays have differently contaminated information vectors of $\mathbf{K}$;
- LDCs can be fully characterized by a single DCM χ, as extensively demonstrated in Chapter 7. By contrast, the CLDCs are characterized by a DCM pair $\{\chi_1, \chi_2\}$, which was given in Equations (9.4) and (9.19), respectively, owing to the twin-layer structure shown in Figure 9.2. The twin-layer structure portrays the fundamental design difference between LDCs and CLDCs, and this relationship is explicitly shown in Figure 9.5;
- The LDCs' equivalent channel model of Equation (7.15) implies transmitting the symbol vector $\mathbf{K}$ through the channel characterized by the equivalent channel matrix $\bar{\mathbf{H}}\chi$. Similarly, Equation (9.20) indicates that the CLDCs transmit the symbol vector $\mathbf{K}$ through the channel characterized by the equivalent channel matrix $\bar{\mathbf{H}}_2\chi_2\bar{\mathbf{H}}_1\chi_1$. More explicitly, the DCM χ_1 of Equation (9.4) together with the CIR matrix $\bar{\mathbf{H}}_1$ of Equation (9.8) characterizes the transmission during the broadcast interval, while the cooperation interval is characterized by the DCM χ_2 of Equation (9.19) as well as by $\bar{\mathbf{H}}_2$ of Equation (9.18).

Observe furthermore in Equations (7.15) and (9.20) that both LDCs and CLDCs obey a similar equivalent system structure, where the equivalent CIR matrix is determined by the channel CIR experienced and the specific DCM employed. Recall from Section 7.2.4 that we optimized the LDCs' DCM χ based on the DCMC capacity of Equation (7.23) using the corresponding equivalent

Table 9.2: System parameters for the CLDC schemes of Figure 9.2.

Number of relays	M
Number of antenna per relay	1
Number of antennas at BS	N
Total channel uses	$T = T_1 + T_2$
Number of symbols per CLDC block	Q
SNR (dB)	$\rho_{SR} = \rho_{RB}$
Modulation	BPSK
Mapping	Gray mapping
Detector	ML of Equation (9.21)

channel matrix of Equation (7.15). Similarly, for a CLDC scheme, we are looking for the particular pair of DCMs $\{\chi_1, \chi_2\}$ that maximizes the DCMC capacity of Equation (7.23). Accordingly, all the DCM pairs $\{\chi_1, \chi_2\}$ used in this chapter are listed in Appendix F.

9.2.5 Performance Results

In this section, we present our simulation results for a number of CLDC schemes obeying the structure of Figure 9.2, which are associated with parameters $(MNTQ)$. In most of our simulations, we set the SNR ρ_{SR} experienced at the relays to the SNR ρ_{RB} recorded at the BS and the resultant BER performance is plotted against ρ_{RB}. However, the scenarios where $\rho_{SR} \neq \rho_{RB}$ are also characterized in Figure 9.9. All the system parameters are listed in Table 9.2, unless otherwise stated.

Figure 9.6 characterizes the BER of a family of CLDCs having $M = 4$, $N = 1$, $T = 8$ and $T = 3$ as well as using different T_1 and T_2 values, when transmitting over uncorrelated i.i.d. Rayleigh-fading channels. Since we set the total number of channel uses per CLDC block to a relatively high value of $T = 8$, we are able to vary the resource allocation by employing different T_1 and T_2 values during the broadcast and cooperation intervals. Observe in Figure 9.6 that the best achievable BER performance was recorded, when we have $T_1 = 2$ and $T_2 = 6$. This phenomenon is related to the achievable cooperative diversity gain of the CLDC schemes of Figure 9.2.

More explicitly, observe in Figure 9.2 that during the broadcast interval, only first-order diversity can be achieved, because each cooperating node is equipped with a single antenna. During the cooperation interval, the space-time transmission matrix $\mathbf{S}_2$ of Equation (9.15) is formed across the relays, which potentially facilitates a spatial diversity order of $N \cdot \min(M, T_2)$ according to Theorem 3 of Chapter 7. Observe in Figure 9.6 that when we have $T_2 \geq (M = 4)$, the CLDCs achieve a cooperative diversity order of $D \approx 4$. The achievable performance is not exactly identical to that of fourth-order diversity, since the relays only have access to the noisy version of the transmitted information. When we have $(T_2 = 1, 2, 3) < M$, $D \approx 1, 2, 3$ can be observed from Figure 9.6, respectively. Again, observe in Figure 9.6 that the CLDC(4183) scheme having $T_1 = 2$ and $T_2 = 6$ exhibits the best BER performance, since it guaranteed the maximum achievable cooperative diversity order provided by the cooperation interval as well as protected the signals received by the relays during the broadcast interval. Figure 9.6 also plots the BER of the LDC(4183) scheme of Figure 9.3 designed for the co-located MIMO system as our benchmarker. Observe in Figure 9.6 that an SNR gap of 8.3dB is recorded at BER$= 10^{-4}$ between the BER curves of the LDC(4183) scheme and the CLDC(4183) arrangement having $T_1 = 2$ and $T_2 = 6$. The non-cooperative LDC scheme outperformed its cooperative counterpart, which is predominantly owing to the imperfect reception of the source data by the relays during the broadcast phase. A further reason is that only a reduced number of slots is available for increasing the diversity gain during the cooperation phase

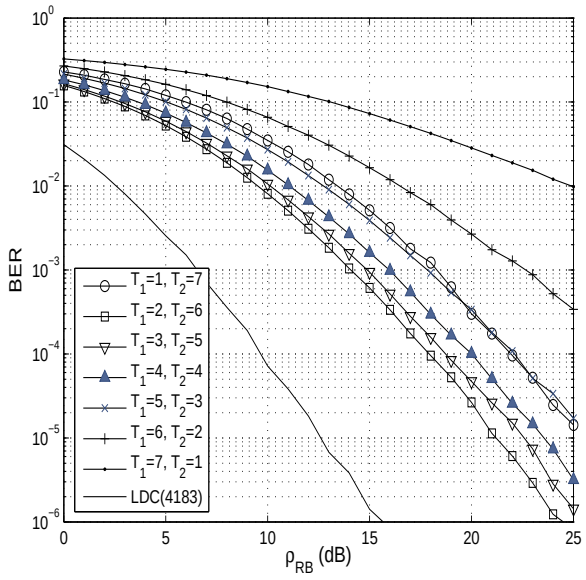

Figure 9.6: BER comparison of a group of CLDCs obeying the architecture of Figure 9.2 having $M = 4$, $N = 1$, $T = 8$ and $Q = 3$ while using different T_1 and T_2 values, when transmitting over uncorrelated i.i.d. Rayleigh-fading channels. All the system parameters were summarized in Table 9.2.

owing to dedicating $T_1 = 2$ slots to the broadcast phase, which imposes further SNR penalties.

In order to further explain this SNR gap in more quantitative terms, in Figure 9.7 we plot the BER performance of the CLDC(4183) scheme having $T_1 = 2$ and $T_2 = 6$, when transmitting over perfect broadcast channels or AWGN as well as over noisy Rayleigh-faded source-to-relay channels. The channels between the relays and the BS are assumed to be uncorrelated i.i.d. Rayleigh-fading channels. When we have perfect source-to-relay links, namely the relays have access to the perfect source information, the CLDC(4183) scheme suffers about 1.8dB SNR penalty in comparison to the LDC(4183) benchmarker, since only $T_2 = 6$ time slots are employed for the cooperative transmission scenario compared to $T = 8$ slots available for the co-located MIMO systems. When the source-to-relay links are LOS AWGN channels, the associated SNR penalty in comparison to the LDC(4183) benchmarker increases only modestly to 3.3dB. Finally, when each relay's received signals $\mathbf{R}_m$ formulated in Equation (9.6) suffers further, owing to experiencing independent Rayleigh fading, the SNR gap widens more dramatically to 8.3dB. It worth noting at this stage that owing to the crucial impact of the broadcast phase integrity on the overall BER performance, it is anticipated that the best combination of T_1 and T_2 has the potential of improving the overall BER performance.

The BER performance gap between the CLDCs and the corresponding LDCs illustrated in Figure 9.6 was investigated under small-scale Rayleigh fading conditions. However, when the transmitted signals are subjected to large-scale fading effects, i.e. shadow fading, the cooperative MIMO system has the potential to outperform its co-located MIMO system counterpart. More particularly, Figure 9.8 characterizes the BER performance of the LDC(4183) scheme following the schematic of Figure 9.3, when communicating over uncorrelated i.i.d. Rayleigh faded channels contaminated by large-scale shadow fading. The shadow fading effect is modelled to have log-normal distribution [383], which can be written as:

$$h_{slow} = 10^{\bar{h}_s/10}, \tag{9.22}$$

where $\bar{h}_s$ is a random Gaussian variable with zero mean and standard deviation Ω (dB).

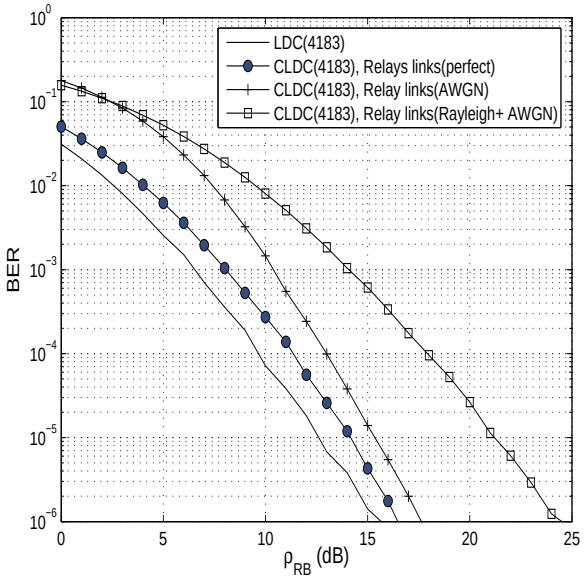

Figure 9.7: BER of the CLDC(4183) scheme of Figure 9.2 having $T_1 = 2$ and $T_2 = 6$. The source-to-relay channels were assumed to be either perfect, or a LOS AWGN or worse-case Rayleigh channels. The relay-to-BS channels remain uncorrelated i.i.d. Rayleigh-fading channels. All the system parameters were summarized in Table 9.2.

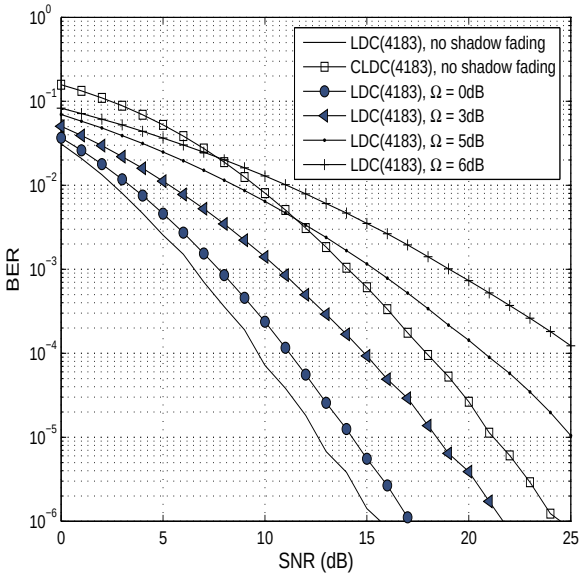

Figure 9.8: BER of the LDC(4183) scheme following the schematic of Figure 9.3, when communicating over uncorrelated i.i.d. Rayleigh faded channels contaminated by large-scale shadow fading governed by Ω.

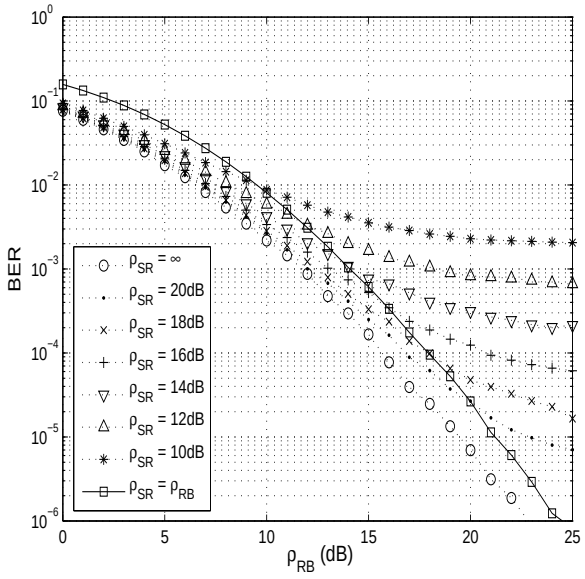

Figure 9.9: BER of the CLDC(4183) scheme of Figure 9.2 having $T_1 = 2$ and $T_2 = 6$, when communicating over uncorrelated i.i.d. Rayleigh faded channels at an SNR of ρ_{SR} and ρ_{RB}, respectively. All the system parameters were summarized in Table 9.2.

Observe in Figure 9.8 that when the shadow fading is insignificant, i.e. we have $\Omega = 0$dB, the LDC(4183) scheme maintains the diversity order of $D \approx 4$, although suffering approximately 1.4dB SNR penalty compared to the scenario in the absence of shadowing. When we have $\Omega = 6$dB, the achievable diversity order is reduced to $D = 1$, since all the communication channels tend to experience the same shadow fading. By contrast, the cooperative MIMO systems can eliminate the shadow fading effect by appropriately choosing a group of relays to assist their transmissions, as illustrated in Figure 9.1. Hence, Figure 9.8 demonstrates that the CLDC(4183) scheme is capable of offering more reliable transmissions than its co-located counterpart, when large-scale fading effects dominate the BER performance.

Figure 9.9 shows the BER performance of the CLDC(4183) scheme of Figure 9.2 having $T_1 = 2$ and $T_2 = 6$, when the source-to-relay Rayleigh fading channels have an SNR of ρ_{SR}, while the relay-to-BS Rayleigh fading channels have an SNR of ρ_{RB}. We use the BER curve of the CLDC(4183) scheme having $\rho_{SR} = \rho_{RB}$ as the benchmarker, which was previously recorded in Figure 9.6. When we have $\rho_{SR} = \infty$, namely the source-to-relay links are Rayleigh fading channels without AWGN, the resultant BER curve exhibits 1.2dB SNR gain over the benchmarker. When we gradually decrease the value of ρ_{SR}, an error floor begins to emerge, owing to the noise of the broadcast interval formulated in Equation (9.20). Again, Figure 9.9 evidences the importance of the received signals' integrity at relays.

Figure 9.10 quantifies the BER performance of a group of CLDCs having $M = 4$, $N = 1$, $T = 8$ and $Q = 1, 2, 3, 4, 5$, when transmitting over uncorrelated i.i.d. Rayleigh-fading channels. Previously, Figure 9.6 has demonstrated that the achievable BER performance is seriously affected by the integrity of the source-to-relay channels, depending on the specific choice of T_1 and T_2 values. Similar to Figure 9.6, we are capable of appropriately configuring a specific CLDC(418Q) scheme by characterizing all the possible T_1 and T_2 combinations and then choosing the particular configuration exhibiting the best achievable BER performance. A group of CLDCs configured using this method is listed in Table 9.3, while their BER performance is shown in Figure 9.10. Furthermore, observe in Table 9.3 that all the CLDCs maintain $T_2 > M$, which potentially enables the CLDCs to achieve the maximum cooperative diversity order. When the value of Q is gradually

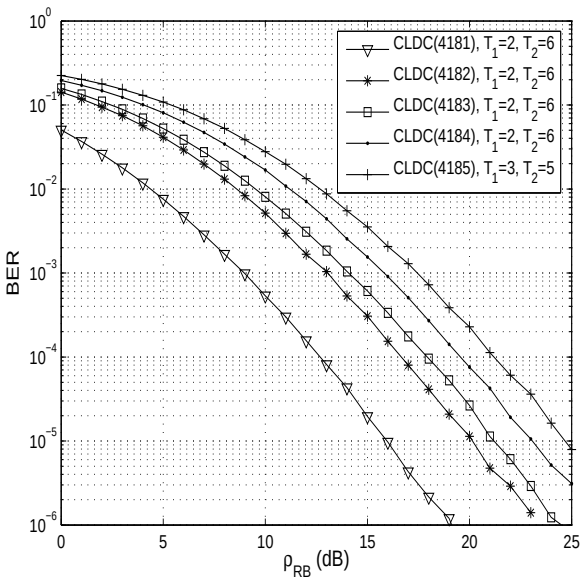

Figure 9.10: BER comparison of a group of CLDCs obeying the structure of Figure 9.2 having $M = 4$, $N = 1$, $T = 8$ and $Q = 1, 2, 3, 4, 5$, when transmitting over uncorrelated i.i.d. Rayleigh-fading channels. All the system parameters were summarized in Table 9.2.

Table 9.3: The best combination of T_1 and T_2 values for a group of CLDCs obeying the structure of Figure 9.2 having $M = 4$, $N = 1$, $T = 8$ and $Q = 1, 2, 3, 4, 5$.

	T	T_1	T_2	Diversity
CLDC(4181)	8	2	6	≈ 4
CLDC(4182)	8	2	6	≈ 4
CLDC(4183)	8	2	6	≈ 4
CLDC(4184)	8	2	6	≈ 4
CLDC(4185)	8	3	5	≈ 4

increased, more time slots are necessary for the broadcast interval T_1 in order to increase the level of protection provided for the symbols received at the relays.

Figure 9.11 characterizes a group of CLDCs obeying the structure of Figure 9.2 having $M = 4$, $N = 1$, $T = 2, 4, 6, 8$ and $Q = 3$, when transmitting over uncorrelated i.i.d. Rayleigh-fading channels. Observe in Figure 9.11 that when the total number of slots available decreased from $T = 8$ to 4, the CLDC(4143) scheme having $T_1 = 1$ and $T_2 = 3$ exhibits a maximum diversity order of $D \approx 3$, since the cooperative diversity order is bounded by $N \cdot \min(M, T_2)$. When we have $T_1 = 1$ and $T_2 = 1$ corresponding to $T = 2$, the resultant CLDC(4123) scheme can only attain a cooperative diversity order of $D = 1$, despite the fact that $M = 4$ relays were employed to assist the cooperation-aided transmission. Again, Figure 9.11 demonstrates that the maximum achievable cooperative diversity order of a CLDC($MNTQ$) scheme is determined by both the total number of time slots T available and the number of relays M.

Figure 9.12 characterizes a group of CLDCs obeying the structure of Figure 9.2 having $M = 4$, $N = 1, 2, 3$, $T = 8$ and $Q = 3$ using $T_1 = 2$ as well as $T_2 = 6$, when communicating over uncorrelated i.i.d. Rayleigh-fading channels. As expected, when the BS employs more receive antennas, the maximum achievable diversity order can be significantly improved as a benefit of the well-known

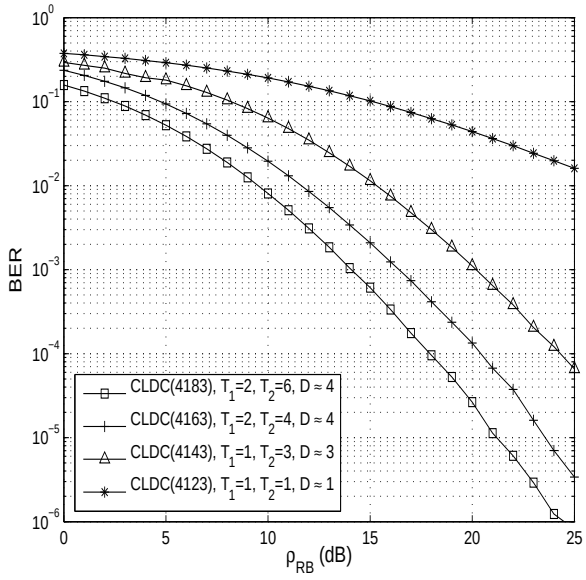

Figure 9.11: BER comparison of a group of CLDCs obeying the structure of Figure 9.2 and using $M = 4$, $N = 1$, $T = 2, 4, 6, 8$ and $Q = 3$, when transmitting over uncorrelated i.i.d. Rayleigh-fading channels. All the system parameters were summarized in Table 9.2.

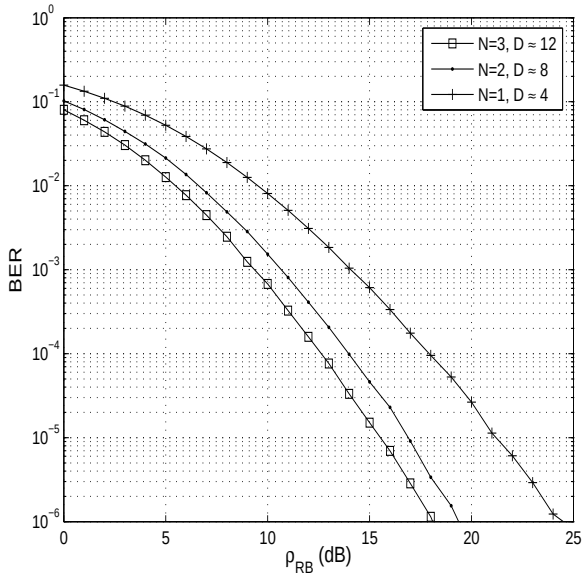

Figure 9.12: BER comparison of a group of CLDCs following the schematic of Figure 9.2 having $M = 4$, $N = 1, 2, 3$, $T = 8$ and $Q = 3$ using $T_1 = 2$ as well as $T_2 = 6$, when transmitting over uncorrelated i.i.d. Rayleigh-fading channels. All the system parameters were summarized in Table 9.2.

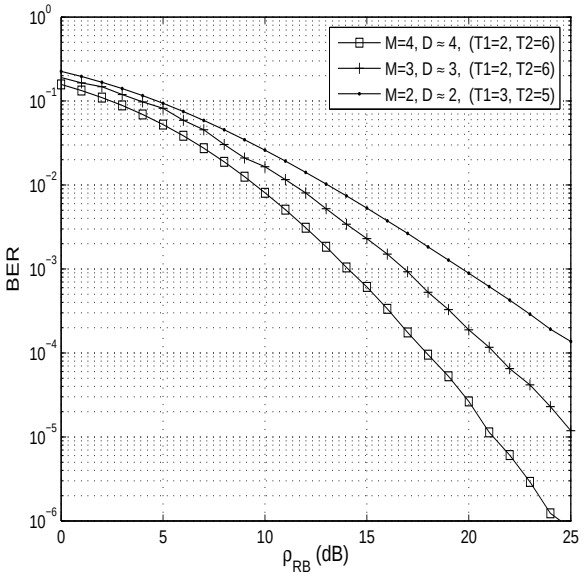

Figure 9.13: BER comparison of a group of CLDCs obeying the structure of Figure 9.2 having $M = 2, 3, 4$, $N = 1$, $T = 8$ and $Q = 3$, when transmitting over uncorrelated i.i.d. Rayleigh-fading channels. All the system parameters were summarized in Table 9.2.

receive diversity gain. In fact, for this family of CLDCs, Figure 9.12 suggests that a cooperative diversity order of $D \approx 4, 8, 12$ can be achieved, when increase the value of N from 1 to 3.

Figure 9.13 attempts to characterize CLDCs' ability to provide cooperative diversity for the configuration of $M = 2, 3, 4$, $N = 1$, $T = 8$ and $Q = 3$, when transmitting over uncorrelated i.i.d. Rayleigh-fading channels. Observe in Figure 9.13 that a diversity order of $D \approx 2, 3, 4$ can be achieved with the aid of $M = 2, 3, 4$ relays, respectively, provided that maintaining $T_2 > M$ is guaranteed. Recall from Figure 9.6 that the CLDC(4183) scheme of Table 9.3 constitutes the best configuration, when we have $T_1 = 2$ and $T_2 = 6$. On the other hand, observe in Figure 9.13 that the CLDC(2183) scheme achieves the best performance, when we have $T_1 = 3$ and $T_2 = 5$.

In Figure 9.14, we characterize the effective throughput of a family of CLDCs employing the parameter of $M = 2, 3, 4$, $N = 1$, $T = 8$ and $Q = 1, 2, 3, 4$ recorded at BER $= 10^{-4}$, when transmitting over uncorrelated i.i.d. Rayleigh-fading channels, where the throughput is calculated as $C = log_2(L) \cdot R_{CLDC}$. The increase of the effective throughput was achieved by transmitting more symbols Q per CLDC block and BPSK modulation was employed by all the schemes. The effective throughput achieved by the corresponding group of LDCs with/without shadowing is also shown as the benchmarker. Similarly, the effective throughput achieved by a group of CLDCs employing different number of receive antennas $N = 1, 2, 3$, while having the parameter of $M = 4$, $T = 8$ and $Q = 1, 2, 3, 4$ is quantified in Figure 9.15. Observe in Figures 9.14 and 9.15 that CLDCs outperform the corresponding LDCs, when encountering large-scale shadowing governed by $\Omega = 6$dB.

Finally, Table 9.4 lists the coding gains of a family of CLDCs obeying the structure of Figure 9.2 and the corresponding LDCs having the structure of Figure 9.3, when having an effective throughput of 0.5 (bits/sym/Hz) as well as using BPSK modulation. The coding gain was defined as the SNR difference, at a BER of 10^{-4} between various LDCs/CLDCs and a single-antenna aided system having the same effective throughput. Observe in Table 9.4 that the achieve coding gains gradually increase with the number of relays and the family of LDCs having co-located MIMO elements suffers a substantial SNR penalty in the presence of shadowing.

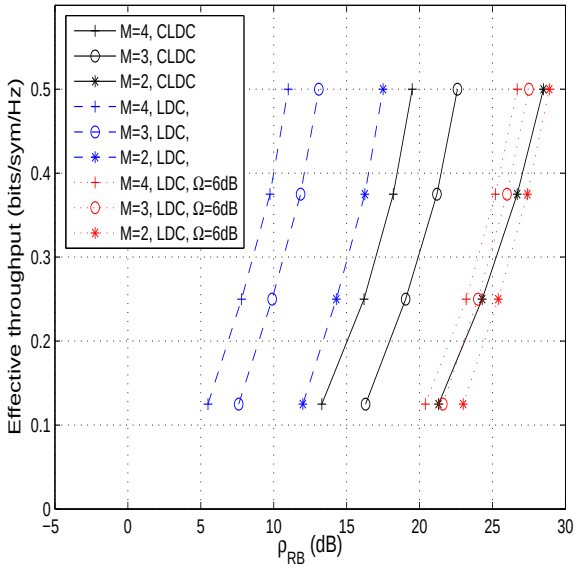

Figure 9.14: Effective throughput of a family of CLDCs obeying the structure of Figure 9.2 having $M = 2, 3, 4$, $N = 1$, $T = 8$ and $Q = 1, 2, 3, 4$ and the corresponding LDCs with/without shadowing, when transmitting over uncorrelated i.i.d. Rayleigh-fading channels. All the system parameters were summarized in Table 9.2.

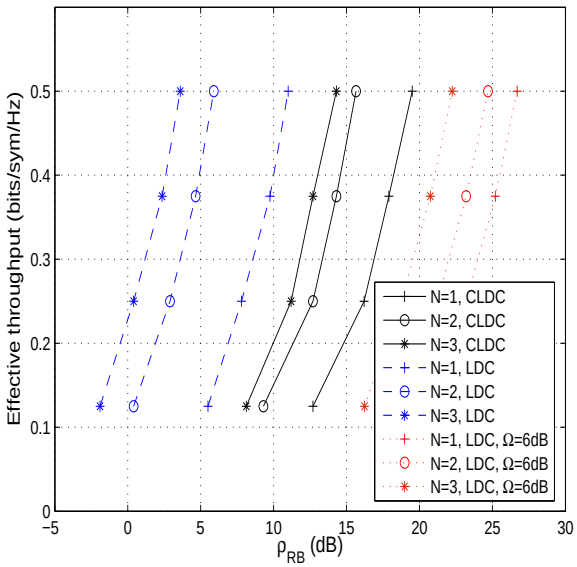

Figure 9.15: Effective throughput of a family of CLDCs obeying the structure of Figure 9.2 having $M = 4$, $N = 1, 2, 3$, $T = 8$ and $Q = 1, 2, 3, 4$ and the corresponding LDCs with/without shadowing, when transmitting over uncorrelated i.i.d. Rayleigh-fading channels. All the system parameters were summarized in Table 9.2.

Table 9.4: Coding gain comparison of a family of CLDCs obeying the structure of Figure 9.2 and the corresponding LDCs having the structure of Figure 9.3, which are extracted from Figures 9.14 and 9.15, when having an effective throughput of 0.5 (bits/sym/Hz) as well as using BPSK modulation.

CLDC				**Coding**	**LDC**				**Coding Gain**	**Coding Gain**
M	N	T	Q	**Gain**	M	N	T	Q	**no shadowing**	$\Omega = 6$dB
2	1	8	4	2.7dB	2	1	8	4	13.5dB	2.1dB
3	⋮	⋮	⋮	8.4dB	3	⋮	⋮	⋮	17.9dB	3.5dB
4	⋮	⋮	⋮	11.5dB	4	⋮	⋮	⋮	20.0dB	4.3dB
4	2	8	4	15.3dB	4	2	8	4	25.1dB	8.5dB
⋮	3	⋮	⋮	16.7dB	⋮	3	⋮	⋮	27.5dB	11.0dB

9.3 IRCC-coded Precoder-Aided CLDCs

The 'coded-cooperative' schemes proposed in [131] and [139] were based on the DF cooperation strategy, which requires the relays to perform either hard or soft decoding. However, the DF-based coded-cooperative schemes have two impediments. Firstly, the power consumption of the relays used for the decoding as well as for transmitting the re-encoded data may be quite significant. Secondly, the resultant overall delay at the final destination may become excessive, which renders the support of delay-sensitive real-time interactive applications, such as video telephony infeasible.

In this section, we propose a novel IRCC aided IrRegular Precoded Cooperative Linear Dispersion Code (IR-PCLDC) scheme based on the AF protocol [121]. The proposed scheme becomes capable of operating at reduced SNRs as a benefit of adopting the sophisticated irregular near-capacity code-design principles of Section 7.5. More explicitly, we have demonstrated in Section 7.5.2 that the irregular design principles are applicable to both the *inner* and *outer* code. However, if only the *inner* code employs the irregular design, the resultant scheme may fail to closely approach the achievable capacity. Hence, we argued in the context of Figures 7.48 and 8.25 that irregularity should be imposed on both the *inner* code and the *outer* code, in order to achieve the best possible performance at an acceptable complexity.

The proposed scheme only requires the relays to perform low-complexity, low-delay linear combining according to Equation (9.13), rather than DF operations. Figure 9.16 portrays the schematic of the proposed IRCC-coded IR-PCLDC scheme using iterative decoding, where memory-1 unit-rate precoders are employed. Compared to the IRCC-coded IR-PLDC scheme of Figure 7.48 designed for co-located MIMO systems, the schematic of Figure 9.16 employs a group of CLDCs for the relay-aided system's twin-phase transmissions. Owing to the striking similarity observed in Figures 9.16 and 7.48, our design methodology will be similar to that described in Section 7.5.3, which is appropriately adopted for the IRCC-coded IR-PCLDCs employing in a cooperative MIMO system. Hence, in this section we will focus our attention on the proposed irregular system's features imposed by the twin-layer structure, rather than on the similarities with respect to the irregular co-located MIMO systems.

9.3.1 EXIT Chart Based IR-PCLDC Design

In this section, we will describe the BPSK-modulated IRCC-coded IR-PCLDC scheme of Figure 9.16 having $P = 10$ component codes, where the IRCC employs $P_{out} = 6$ *outer* and the IR-PCLDC has $P_{in} = 4$ *inner* component codes, respectively. More explicitly, an IRCC scheme having a component rate of $R_{i,IRCC} = [0.1, 0.25, 0.4, 0.55, 0.7, 0.9]$ is adopted, where the corre-

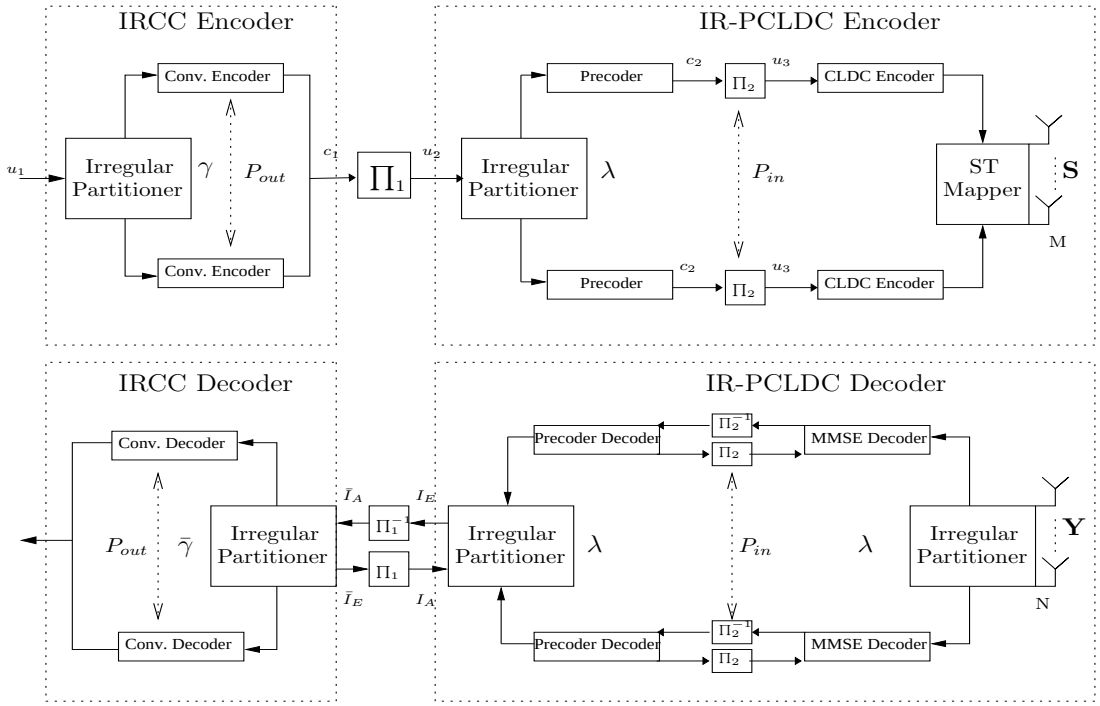

Figure 9.16: Schematic of the IRCC-coded IR-PCLDC scheme using iterative decoding.

Table 9.5: The $P_{in} = 4$ component codes of the BPSK modulated IR-PCLDC scheme of Figure 9.16 generated for the cooperative MIMO system of Figure 9.2 having $M = 4$ and $N = 1$.

Index	M	N	T	T_1	T_2	Q	**Rate**	D	**Inner Iterations** (j)
0	4	1	8	2	6	1	0.125	≈ 4	0
1	⋮	⋮	8	2	6	2	0.25	≈ 4	1
2	⋮	⋮	8	2	6	3	0.375	≈ 4	1
3	⋮	⋮	8	2	6	4	0.5	≈ 4	2

Table 9.6: The $P_{in} = 4$ component codes of the BPSK modulated IR-PLDC scheme of Figure 7.48 generated for the co-located MIMO system of Figure 9.3 having $M = 4$ and $N = 1$ antennas.

Index	M	N	T	Q	**Rate**	D	**Inner Iterations** (j)
0	4	1	8	1	0.125	4	0
1	⋮	⋮	⋮	2	0.25	4	1
2	⋮	⋮	⋮	3	0.375	4	1
3	⋮	⋮	⋮	4	0.5	4	2

Table 9.7: System parameters of the IRCC-coded IR-PCLDC scheme of Figure 9.16.

Number of relays	$M = 4$
Number of antennas per relay	1
Number of antennas at the BS	$N = 1$
Total number of slots	$T_1 + T_2 = 8$
Number of symbols per CLDC block	Q
SNR at the relays (dB)	$\rho_{SR} = 20$
SNR at the BS (dB)	ρ_{RB}
Modulation	BPSK
Mapping	Gray mapping
Detector	MMSE

sponding EXIT characteristics have been shown in Figure 7.46. The BS is assumed to have $M = 4$ relays to assist the source node and it employs $N = 1$ receive antennas, as seen in Figure 9.2. All the system parameters are listed in Table 9.7. As usual in irregular code design, we have to determine the specific fraction of the input bits to be encoded by each of the component codes, so that the corresponding *inner* and *outer* code's EXIT curves match each other as closely as possible. This design philosophy was detailed in the context of Figures 7.49 of Section 7.5.2.

Table 9.5 lists the group of CLDCs used as the component codes of the IR-PCLDC scheme obeying the structure of Figure 9.16. The number of *inner* iterations (j) listed in Table 9.5 refers to the iterations carried out between the unity-rate precoder's decoder and the MMSE detector of Figure 9.16. Accordingly, Precoded Cooperative Linear Dispersion Codes (PCLDCs) of Figure 9.16 are constituted by memory-1 unity-rate precoders and CLDCs having parameters $(MNTQ)$. Furthermore, Table 9.6 constructs a group of LDCs having identical parameters to the CLDCs of Table 9.5, which will be employed as the component codes of the IRCC-coded IR-PLDC scheme of Figure 7.48. Hence, we are able to carry out a fair comparison between the irregular system of Figure 9.16 invoked in cooperative MIMO systems and the corresponding irregular system of Figure 7.48 designed for co-located MIMO systems.

Figure 9.17 characterizes the EXIT charts of the BPSK-modulated PCLDC(4183) scheme of Table 9.5 obeying the structure of Figure 9.2, when communicating over i.i.d. Rayleigh fading channels. Assume that the *inner* code's EXIT curves can be perfectly matched by the EXIT curves of an *outer* code at any SNR ρ_{RB}, then the **maximum achievable rate** of a serial concatenated scheme can be approximated by evaluating the area under the EXIT curves. Given the rate of the *inner* block R_{in}, the maximum achievable rate is expressed as:

$$C(\rho_{RB}) = log_2(L) \cdot R_{in} \cdot R_{out}, \tag{9.23}$$

where R_{out} is approximated by the area under the *inner* code's EXIT curve [303] and L-PSK modulation is used. Note that in Sections 7.4.2 and 8.6.1, we have explicitly shown that there may be a potential maximum achievable rate gap, when it is measured before and after the unit-rate precoder. The associated gap can be closed by employing *inner* iterations (j), which has been shown in Figures 7.27 and 8.26. Similarly, there may be a potential gap between the maximum achievable rates recorded for CLDCs and PCLDCs based on each component code's EXIT characteristic and the associated gap can be eliminated by increasing the value of j, which will be discussed in more detail below.

Figure 9.18 plots the maximum achievable rates of the CLDCs of Table 9.5 and the corresponding PCLDCs having different number of *inner* iterations j, when communicating over i.i.d. Rayleigh fading channels. The maximum achievable rates are measured based on the EXIT charts using Equation (9.23). When we use the PCLDC(4181) scheme, the employment of the precoder

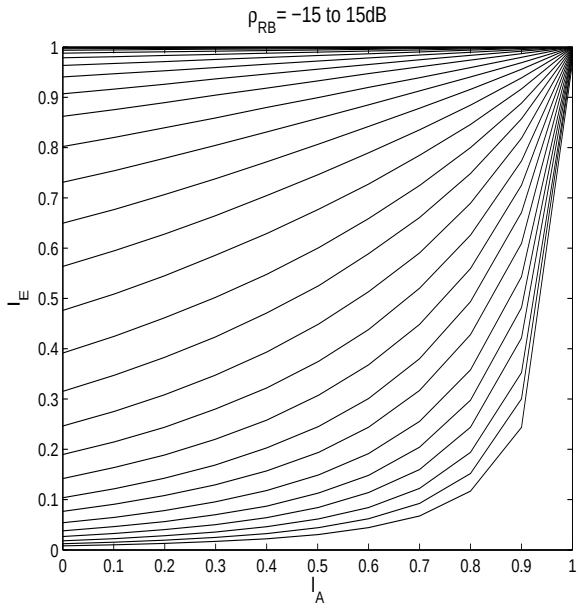

Figure 9.17: EXIT charts of the PCLDC(4183) scheme of Table 9.5 obeying the structure of Figure 9.2, when communicating over i.i.d. Rayleigh fading channels. All the system parameters were summarized in Table 9.7

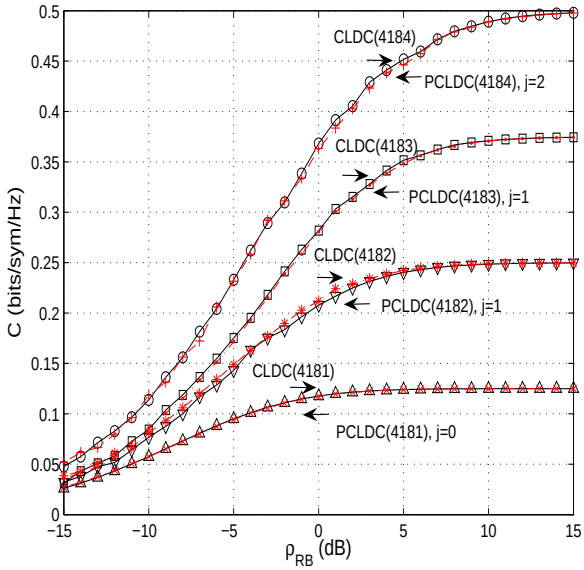

Figure 9.18: Maximum achievable rates of the CLDC and PCLDC schemes of Table 9.5 having different number of inner iterations j using an MMSE detector, when communicating over i.i.d. Rayleigh fading channels. All the system parameters were summarized in Table 9.7.

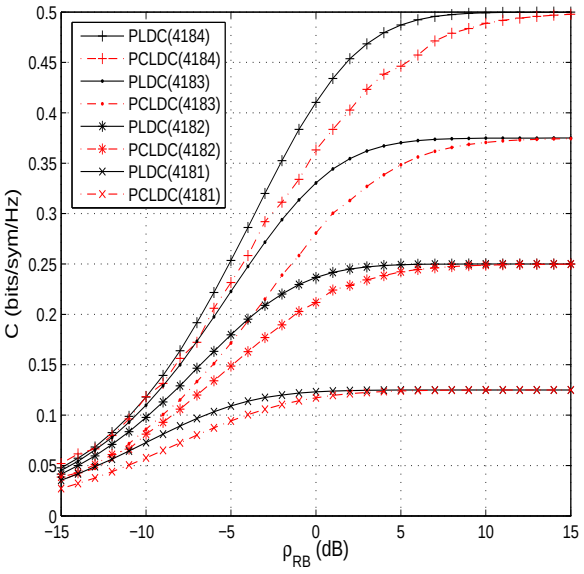

Figure 9.19: Maximum achievable rates of the PCLDC schemes of Table 9.5 and PLDC schemes of Table 9.6 using an MMSE detector, when communicating over i.i.d. Rayleigh fading channels. All the system parameters were summarized in Table 9.7.

does not decrease the maximum achievable rates compared to the CLDC(4181) scheme even without *inner* iterations, i.e. at $j = 0$. When more symbols have to be transmitted per CLDC block, i.e. when Q is increased, more *inner* iterations are necessary for the PCLDCs to approach the maximum achievable rates of the corresponding CLDCs. More particularly, we found from Figure 9.18 that $j = 1$ is adequate for both the PCLDC(4182) as well as for the PCLDC(4183) schemes and $j = 2$ is suitable for the PCLDC(4183) scheme. Again, the number of *inner* iterations necessary to close the maximum achievable rate gap is listed in Table 9.5.

Figure 9.19 characterizes the maximum achievable rates of the PCLDCs of Table 9.5 and the PLDC schemes of Table 9.6, when communicating over i.i.d. Rayleigh fading channels. Observe in Figure 9.19 that the family of PCLDCs summarized in Table 9.5 suffers from a substantial maximum rate loss compared to the class of its PLDC aided counterparts. Recall that the CLDC's equivalent system model of Equation (9.20) suggests that the combined noise term $\bar{\mathbf{V}}$ consists of the noise variance σ_{SR} of the broadcast phase and that of the cooperation interval, namely σ_{RB}. In contrast, the PLDC scheme using identical parameters is only affected by the noise encountered at the BS. Again, it is the linear combination and amplification operations of Equation (9.13) carried out at the relays, which impose the additional noise encountered during the broadcast interval. Naturally, the degradation imposed during the broadcast phase as characterized by σ_{SR} can be eliminated by adopting DF related cooperation strategies, which may be able to ensure that the relays will have access to the perfect source information.

In order to elaborate a little further, Figure 9.20 characterizes the maximum achievable rates of the PCLDC(4183) schemes of Table 9.5, when transmitting over perfect broadcast channels, over noisy AWGN or Rayleigh-faded source-to-relay channels having an SNR of ρ_{SR}. The relay-to-BS channels are modelled as uncorrelated i.i.d. Rayleigh-fading channels. More explicitly, even when the source-to-relay channels are perfect, which implies that the relays have perfect source information, there exist a maximum achievable rate gap between the PCLDC(4183) schemes of Table 9.5 and the PLDC(4183) arrangements of Table 9.6. This is because the PCLDC(4183) scheme has to employ $T_1 = 2$ time slots to broadcast the source information to the relays. In other words, only $T_2 = 6$ slots or channel uses are available for the effective transmission of the data,

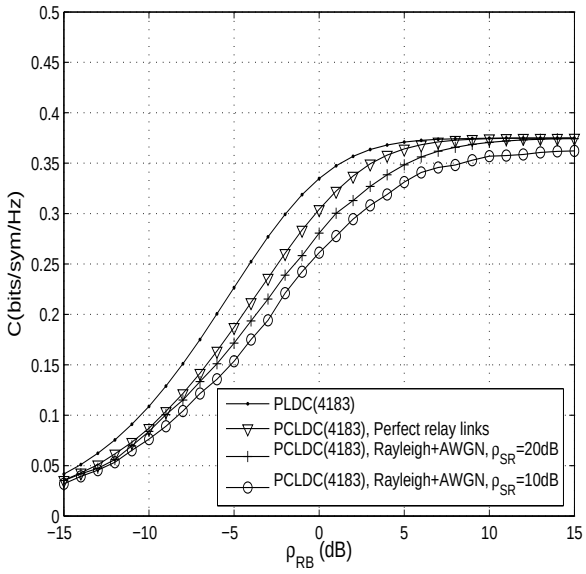

Figure 9.20: Maximum achievable rates of the PCLDC(4183) scheme of Table 9.5, when communicating over perfect channels, noisy media or Rayleigh-faded source-to-relay channels having an SNR of ρ_{SR}. All the system parameters were summarized in Table 9.7.

whereas the PLDC(4183) scheme is capable of exploring all the dimensions provided by the $T = 8$ time slots.

Observe in Figure 9.20 that when we have more realistic Rayleigh-faded source-to-relay channels having a finite SNR of $\rho_{SR} = 20$dB, a further maximum rate loss can be observed in Figure 9.20. Since each source-to-relay channel is independently faded and additionally corrupted by AWGN, each relay's received information inevitably becomes different, which implies that each relay will disperse potentially quite different information to the T_2 time slots, when relaying based on Equation (9.13). When the SNR of the source-to-relay links is reduced further to $\rho_{SR} = 10$dB, the associated maximum achievable rate suffers an additional loss compared to that recorded for $\rho_{SR} = 20$dB. Observe in Figure 9.20 that the associated rate reduction persists even in the high SNR region, owing to the inherent noise imposed during the broadcast interval.

9.3.2 Performance Results

For all the simulations, the first interleaver of Figure 9.16 is set to a length of 10^6 bits and all the simulation parameters are listed in Table 9.7. Again, we construct an identical IRCC-coded IR-PLDC scheme using Table 9.6 as the benchmarker to quantify the achievable performance.

Our design objective is to maximize the effective throughput across the widest possible SNR range, which can be achieved by adaptively adjusting the weighting coefficient vectors $\boldsymbol{\gamma} = [\gamma_1, \ldots, \gamma_{P_{out}}]$ of the IRCC scheme of Figure 7.46 and $\boldsymbol{\lambda} = [\lambda_1, \ldots, \lambda_{P_{in}}]$ of the IR-PCLDC scheme, respectively. More explicitly, an exhaustive search operation is carried out for all the possible combinations of $\boldsymbol{\gamma}$ and $\boldsymbol{\lambda}$ in order to maximize the throughput $C(\rho) = log_2(L) \cdot R_{in} \cdot R_{out}$ of Equation (9.23) under the following constraints:

- $\gamma_1 + \gamma_2 + \ldots + \gamma_{P_{out}} = 1$;
- $\lambda_1 + \lambda_2 + \ldots + \lambda_{P_{in}} = 1$;

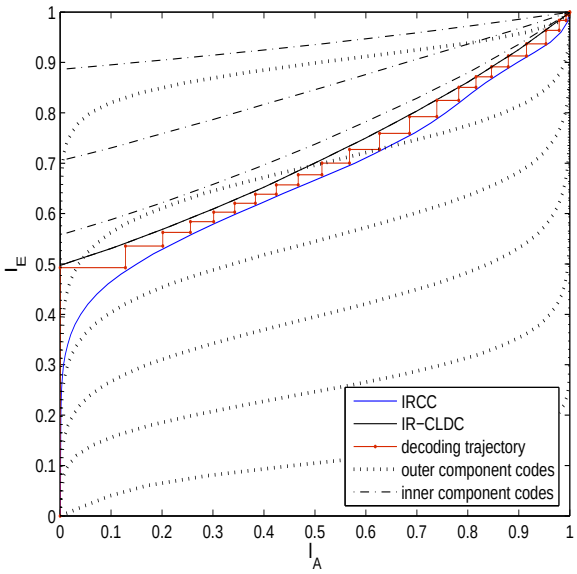

Figure 9.21: EXIT charts and the simulation-based decoding trajectory of the IRCC-coded IR-PCLDC scheme of Figure 9.16 recorded at ρ_{RB} = 0dB, when communicating over i.i.d. Rayleigh fading channels. All the system parameters were summarized in Table 9.7.

- An open convergence tunnel must exist in the EXIT chart, which enables the irregular system to achieve an infinitesimally low BER using iterative decoding;
- The open EXIT tunnel area is maximized, for the sake of minimizing the number *outer* iterations required.

Figure 9.21 presents the associated EXIT charts and the corresponding decoding trajectory of our IRCC-coded IR-PCLDC scheme designed for operating at ρ_{RB} = 0dB, when communicating over i.i.d. Rayleigh fading channels. The dashed lines represent the EXIT curves of the IR-PCLDC's component codes of Table 9.5, while the dotted lines denote the EXIT curves for the set of IRCC components. The solid lines represent the aggregate EXIT curves of the IRCC scheme having the weighting coefficient vector of $\boldsymbol{\gamma}$= $[0, 0, 0, 0.2374, 0.5036, 0.2590]$ and the IR-PCLDC scheme having the weighting coefficient vector of $\boldsymbol{\lambda} = [0, 0, 0, 1]$. By simultaneously maximizing the achievable rate and the open EXIT tunnel area at ρ_{RB} = 0dB, the proposed scheme becomes capable of achieving $C(0dB)$= 0.3475 (bits/sym/Hz) and the optimized EXIT curves of Figure 9.21 exhibit a narrow but still open tunnel, where the decoding trajectory shows that $k = 23$ *outer* iterations were required. The corresponding BER performance is portrayed in Figure 9.22.

By repeating the same design process as that used for ρ_{RB} = 0dB in Figures 9.21 and 9.22, we are able to design the IRCC-coded IR-PCLDC scheme of Figure 9.16 for other operating SNR values. Figure 9.23 portrays the maximum achievable rates attained by the IRCC-coded IR-PCLDC scheme of Figure 9.16. Each component of Figure 9.16 was designed to achieve the maximum effective throughput using specific weighting coefficient vectors $\boldsymbol{\lambda}$ and $\boldsymbol{\gamma}$ listed in Tables G.11 and G.12. Furthermore, we also plot the maximum rates achieved by the IRCC-coded IR-PLDC scheme of Figure 7.48 designed for co-located MIMO systems according to Tables G.13 and G.14. Observe in Figure 9.23 that there is an effective throughput discrepancy between the irregular system designed for the co-located MIMO system of Figure 9.3 and the corresponding irregular scheme designed for the cooperative MIMO arrangement of Figure 9.2. This phenomenon is also evidenced in Figure 9.19 and has been further explained in Figure 9.20. Finally, the LDC(4184) scheme's CCMC capacity obtained using Equation (7.9) is also provided in order to give us an idea as to how far

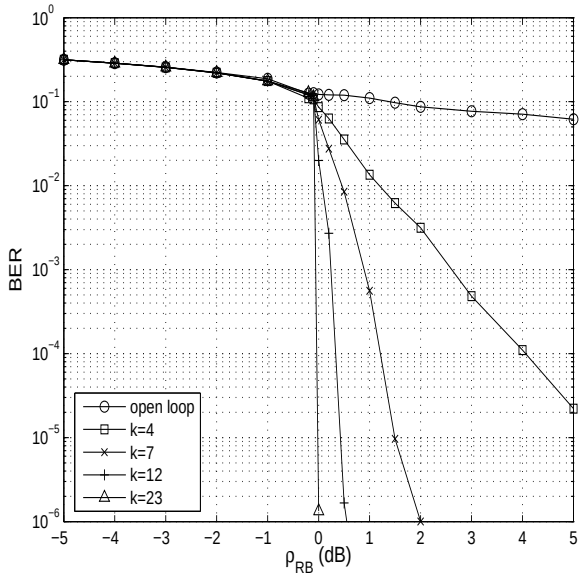

Figure 9.22: BER of the IRCC-coded IR-PCLDC scheme of Figure 9.16 designed for achieving an infinitesimally low BER at $\rho_{RB} = 0$dB, when communicating over i.i.d. Rayleigh fading channels. All the system parameters were summarized in Table 9.7.

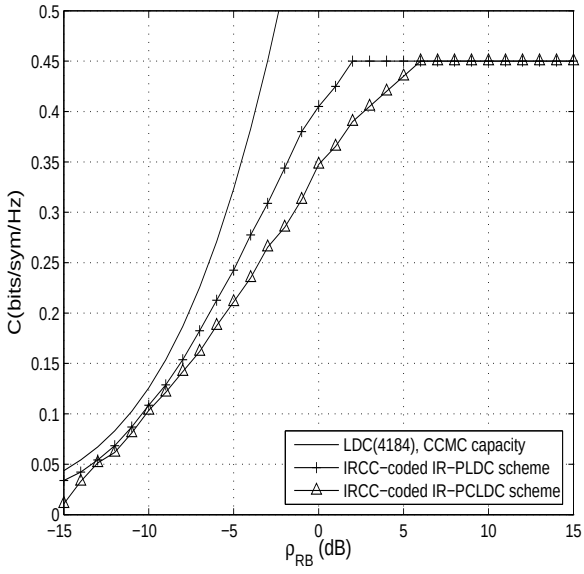

Figure 9.23: The maximum rates achieved by the IRCC-coded IR-PCLDC scheme of Figure 9.16 according to Tables G.11 and G.12 and the corresponding IRCC-coded IR-PLDC scheme of Figure 7.48 using Tables G.13 and G.14. All the system parameters were summarized in Table 9.7.

Table 9.8: Characteristics of Co-located MIMO systems using LDCs and Cooperative MIMO arrangements using CLDCs.

		Co-located MIMO	**Cooperative MIMO**
Similarity	$(MNTQ)$	arbitrary	arbitrary
	Modulation	arbitrary	arbitrary
	Diversity	$N \cdot \min(M, T)$	$\approx N \cdot \min(M, T_2)$
Uncoded	Small-scale fading	better than CLDCs	trends in Figure 9.7
	Large-scale fading	trends in Figure 9.8	better than LDCs
Coded	Small-scale fading	better than CLDCs	explained in Figure 9.20
	Throughput	compared in Figure 9.23	

we are operating from the capacity limit.

9.4 Conclusion

In this chapter, we extended the concept of LDCs designed for co-located MIMO systems in Chapter 7 to cooperative MIMO systems. Our key findings may be summarized as follows:

- In Sections 9.2.1 to 9.2.3, we established a general framework for the cooperative MIMO systems of Figure 9.2;
- Correspondingly, in Section 9.2.4, we have emphasized that the fundamental difference between co-located MIMO systems and cooperative MIMO systems is that the latter relies on a twin-phase transmission regime, which provides us with a high grade of freedom in terms of appropriately share the total number of slots between the broadcast- and cooperation-phase;
- In Section 9.2.5, we demonstrated the achievable BER performance of CLDC schemes having various parameter combinations. The effective throughput values achieved by the uncoded CLDCs have been summarized in Figures 9.14 and 9.15 and the achievable coding gains were listed in Table 9.4;
- In Section 9.3 we imposed irregularity on the relay-aided system based on the AF cooperation protocol, and demonstrated that the resultant IRCC-coded IR-PCLDC scheme of Figure 9.16 becomes capable of operating at a throughput, which is close to the corresponding IR-PLDC benchmarker as seen in Figure 9.23, while maintaining an infinitesimally low BER. The associated weighting coefficient vectors $\boldsymbol{\lambda}$ $\boldsymbol{\gamma}$ were listed in Tables G.11 and G.12, respectively.
- Finally, we summarized the characteristics of both co-located MIMO systems using LDCs and those of cooperative MIMO schemes using CLDCs in Table 9.8. Both of the schemes are capable of supporting arbitrary $(MNTQ)$ parameter combinations as well as employing arbitrary modulation schemes. Furthermore, the achievable total diversity order is jointly determined by the minimum spatial and temporal dimensions. For uncoded systems, the LDCs outperform the CLDCs, when encountering a small-scale fading environment. By contrast, the CLDCs tend to function more reliably than the LDCs in the context of large-scale fading, i.e. shadowing. The corresponding trends have been further explained in Figures 9.7 and 9.8. As far as near-capacity coded systems are concerned, which are implemented using IR-PLDCs/IR-PCLDCs, again, the effective throughput gap between co-located MIMO schemes and cooperative MIMO systems has been explicitly detailed in Figure 9.20.

Part III

Differential Turbo-Detection of Multi-Functional MIMO-Aided Multi-User and Cooperative Systems

Glossary

16-QAM	16-level Quadrature Amplitude Modulation
3G	Third generation
8-PSK	8-level Phase Shift Keying
AGM	Anti-Gray Mapping
APP	A Posteriori Probability
AWGN	Additive White Gaussian Noise
BEC	Binary Erasure Channel
BER	Bit error ratio, the number of the bits received incorrectly
BICM	Bit-Interleaved Coded Modulation
BICM-ID	Bit-Interleaved Coded Modulation with Iterative decoding
BPS	Bits per modulated symbol
BPSK	Binary Phase Shift Keying
BSA	Binary Switching Algorithm
CCMC	Continuous-input Continuous-output Memoryless Channel
CCSDS	Consultative Committee for Space Data Systems
CDMA	Code-Division Multiple-Access
CSI	Channel State Information
DCMC	Discrete-input Continuous-output Memoryless Channel
DMC	Discrete Memoryless Channel
DSTBC	Differential Space-Time Block Coding
D_4	The lattice corresponding to the sphere packing having the best minimum Euclidean distance in the four-dimensional real-valued Euclidean space R^4
EXIT	EXtrinsic Information Transfer

E_b/N_0	Ratio of bit energy to noise power spectral density
FFT	Fast Fourier Transform
GF	Galois Field
GM	Gray Mapping
i.i.d.	Independent and Identically Distributed
IRCC	Irregular Convolutional Code
ISI	Intersymbol Interference
LDPC	Low Density Parity Check
LLR	Log-Likelihood Ratio
MAP	Maximum A Posteriori
MED	Minimum Euclidean Distance
MI	Mutual Information
MIMO	Multiple-Input Multiple-Output
ML	Maximum Likelihood
PDF	Probability Density Function
PSK	Phase Shift Keying
QAM	Quadrature Amplitude Modulation
QAP	Quadratic Assignment Problem
QPSK	Quadrature Phase Shift Keying
RA	Repeat-Accumulate
RSC	Recursive Systematic Convolutional
RTS	Reactive Tabu Search
SISO	Soft-Input Soft-Output
SNR	Signal to Noise Ratio, noise energy compared to the signal energy
SP	Sphere Packing
SP-SER	Sphere Packing Symbol Error Ratio
SPSI	Sphere Packing Symbol Invariant
ST	Space-Time
ST-SER	Space-Time Symbol Error Rate
STBC	Space-Time Block Coding
STBC-SP	Space-Time Block Coding using Sphere Packing modulation
STC	Space-Time Coding
STP	Space-Time Processing

STTC	Space-Time Trellis Coding
TCM	Trellis Coded Modulation
V-BLAST	Vertical Bell Laboratories Layered Space-Time
WLAN	Wireless Local Area Network
ZF	Zero Forcing

Bibliography

[1] D. Gesbert, M. Shafi, D.-S. Shiu, P. J. Smith and A. Naguib , "From theory to practice: an overview of MIMO space-time coded wireless systems," *IEEE Journal on Selected Areas in Communications*, vol. 21, pp. 281–302, April 2003.

[2] FCC, "Third Generation Wireless Systems." http://www.fcc.gov/3G/#sec2, accessed September 2006.

[3] G. J. Foschini and M. Gans, "On limits of wireless communication in a fading environment when using multiple antennas," *Wireless Personal Communications*, vol. 6, pp. 311–335, March 1998.

[4] B. M. Hochwald, G. Caire, B. Hassibi and T. L. Marzetta, "The academic and industrial embrace of space-time methods," *IEEE Transactions on Information Theory*, vol. 49, pp. 2329–2331, October 2003.

[5] T. S. Rappaport, *Wireless Communications: Principles and Practice*. Prentice Hall, 1996.

[6] J.G. Proakis, *Digital communications*. McGraw-Hill, 2001.

[7] G. J. Pottie, "System design choices in personal communications," *IEEE Personal Communications*, vol. 2, pp. 50–67, October 1995.

[8] V. Tarokh, N. Seshardi and A. Calderbank, "Space-time codes for high data rate wireless communication: performance criterion and code construction," *IEEE Transactions on Information Theory*, vol. 44, pp. 744–765, March 1998.

[9] L. Hanzo, T.H. Liew and B.L. Yeap, *Turbo coding, turbo equalisation and space time coding for transmission over fading channels*. Chichester, UK: Wiley: IEEE Press, 2002.

[10] S.M. Alamouti, "A simple transmit diversity technique for wireless communications," *IEEE Journal on Selected Areas in Communications*, vol. 16, no. 8, pp. 1451–1458, 1998.

[11] V. Tarokh, H. Jafarkhani and A.R. Calderbank, "Space-time block codes from orthogonal designs," *IEEE Transactions on Information Theory*, vol. 45, no. 5, pp. 1456–1467, 1999.

[12] V. Tarokh, N. Seshadri and A.R. Calderbank, "Space-time codes for high data rate wireless communication: performance criterion and code construction," *IEEE Transactions on Information Theory*, vol. 44, pp. 744–765, March 1998.

[13] B. Hassibi and B.M. Hochwald, "High-rate codes that are linear in space and time," *IEEE Transactions on Information Theory*, vol. 48, pp. 1804–1824, July 2002.

[14] B. Hochwald, T.L. Marzetta and C.B. Papadias, "A transmitter diversity scheme for wideband CDMA systems based on space-time spreading," *IEEE Journal on Selected Areas in Communications*, vol. 19, no. 1, pp. 48–60, 2001.

[15] H. Jafarkhani, "A quasi-orthogonal space-time block code," *IEEE Transactions on Communications*, vol. 49, no. 1, pp. 1–4, 2001.

[16] P.W. Wolniansky, G.J. Foschini, G.D. Golden and R.A. Valenzuela, "V-BLAST: an architecture for realizing very high data rates over the rich-scattering wireless channel," in *International Symposium on Signals, Systems and Electronics*, (Pisa), pp. 295–300, September 1998.

[17] J. Blogh and L. Hanzo, *Third-generation systems and intelligent wireless networking: smart antennas and adaptive modulation*. John Wiley & Sons - IEEE Press, 2002.

[18] V. Tarokh, A. Naguib, N. Seshadri and A.R. Calderbank, "Combined array processing and space-time coding," *IEEE Transactions on Information Theory*, vol. 45, no. 4, pp. 1121–1128, 1999.

[19] M. Tao and R.S. Cheng, "Generalized layered space-time codes for high data rate wireless communications," *IEEE Transactions on Wireless Communications*, vol. 3, no. 4, pp. 1067–1075, 2004.

[20] E.N. Onggosanusi, A.G. Dabak and T.A. Schmidl, "High rate space-time block coded scheme: performance and improvement in correlated fading channels," in *IEEE Wireless Communications and Networking Conference*, vol. 1, pp. 194–199, March 2002.

[21] G. Jongren, M. Skoglund and B. Ottersten, "Combining beamforming and orthogonal space-time block coding," *IEEE Transactions on Information Theory*, vol. 48, pp. 611–627, March 2002.

[22] M. El-Hajjar, O. Alamri, J. Wang, S. Zummo and L. Hanzo, "Layered steered space-time codes using multi-dimensional sphere-packing modulation," *accepted for publication in IEEE Transactions on Wireless Communications*, 2008.

[23] L.-L. Yang and L. Hanzo, "Performance of generalized multicarrier DS-CDMA over Nakagami-m fading channels," *IEEE Transactions on Communications*, vol. 50, pp. 956–966, June 2002.

[24] L. Z. Zheng and D. Tse, "Diversity and multiplexing: a fundamental tradeoff in multiple-antenna channels," *IEEE Transactions on Information Theory*, vol. 49, pp. 1073–1096, May 2003.

[25] J.N. Laneman and G.W. Wornell, "Distributed space-time-coded protocols for exploiting cooperative diversity in wireless networks," *IEEE Transactions on Information Theory*, vol. 49, no. 10, pp. 2415–2425, 2003.

[26] V. Tarokh, H. Jafarkhani and A.R. Calderbank, "Space-time block coding for wireless communications: performance results," *IEEE Journal on Selected Areas in Communications*, vol. 17, no. 3, pp. 451–460, 1999.

[27] H. F. Lu and P. V. Kumar, "Rate-diversity tradeoff of space-time codes with fixed alphabet and optimal constructions for PSK modulation," *IEEE Transactions on Information Theory*, vol. 49, pp. 2747–2751, October 2003.

[28] R. W. J. Heath and A. Paulraj, "Linear dispersion codes for MIMO systems based on frame theory," *IEEE Transactions on Signal Processing*, vol. 50, pp. 2429–2441, October 2002.

[29] B. Hassibi and B. M. Hochwald, "High-rate codes that are linear in space and time," *IEEE Transactions on Information Theory*, vol. 48, pp. 1804–1824, July 2002.

[30] H. J. Chen, A. Haimovich, and J. A. Sjogren, "Turbo space-time codes with time varying linear transformations," *IEEE Transactions on Wireless Communications*, vol. 6, pp. 486–493, February 2007.

[31] H. E. Gamal and M. O. Damen, "Universal space-time coding," *IEEE Transactions on Information Theory*, vol. 49, pp. 1097–1119, May 2003.

[32] G. Ganesan and P. Stoica, "Differential modulation using space-time block codes," in *Conference Record of the Thirty-Fifth Asilomar Conference on Signals, Systems and Computers*, vol. 1, (Pacific Grove, CA), pp. 236–240, 2001.

[33] N. Wu and L. Hanzo, "Near-capacity irregular precoded linear dispersion codes," in *IEEE International Conference on Communications*, (Beijing, China), pp. 4501–4505, May 19–23, 2008.

[34] N. Wu and L. Hanzo, "Irregular precoder-aided differential linear dispersion codes," in *Vehicular Technology Conference*, (Marina Bay, Singapore), pp. 285–289, May 2008.

[35] D.G. Brennan, "Linear diversity combining techniques," in *Proceedings of the IRE*, vol. 47, pp. 1075–1102, June 1959.

[36] A. Wittneben, "Base station modulation diversity for digital simulcast," in *41st IEEE Vehicular Technology Conference Gateway to the Future Technology in Motion*, (St. Louis, MO), pp. 848–853, May 1991.

[37] A. Wittneben, "A new bandwidth efficient transmit antenna modulation diversity scheme for linear digital modulation," in *IEEE International Conference on Communications*, vol. 3, (Geneva), pp. 1630–1634, May 1993.

[38] N. Seshadri and J.H. Winters, "Two signaling schemes for improving the error performance of frequency-division-duplex transmission systems using transmitter antenna diversity," in *IEEE Vehicular Technology Conference*, (Secaucus, NJ), pp. 508–511, May 1993.

[39] J.H. Winters, "The diversity gain of transmit diversity in wireless systems with Rayleigh fading," in *IEEE International Conference on Communications*, (New Orleans, LA), pp. 1121–1125, May 1994.

[40] T. Eng, N. Kong and L.B. Milstein, "Comparison of diversity combining techniques for Rayleigh-fading channels," *IEEE Transactions on Communications*, vol. 44, pp. 1117–1129, September 1996.

[41] J.-C. Guey, M.P. Fitz, M.R. Bell and W.-Y. Kuo, "Signal design for transmitter diversity wireless communication systems over Rayleigh fading channels," *IEEE Transactions on Communications*, vol. 47, pp. 527–537, April 1999.

[42] P. Stoica and G. Ganesan, "Space-time block codes: trained, blind and semi-blind detection," in *IEEE International Conference on Acoustics, Speech and Signal Processing*, vol. 2, (Orlando, FL), pp. 1609–1612, 2002.

[43] D.G. Brennan, "Linear diversity combining techniques," *Proceedings of the IEEE*, vol. 91, pp. 331–356, February 2003.

[44] H. Wang and X.-G. Xia, "Upper bounds of rates of complex orthogonal space-time block codes," *IEEE Transactions on Information Theory*, vol. 49, pp. 2788–2796, October 2003.

[45] W. Su, Z. Safar and K.J.R. Liu, "Space-time signal design for time-correlated Rayleigh fading channels," in *IEEE International Conference on Communications*, vol. 5, pp. 3175–3179, 2003.

[46] H. Zhang and T.A Gulliver, "Capacity and error probability analysis for orthogonal space-time block codes over fading channels," *IEEE Transactions on Wireless Communications*, vol. 4, pp. 808–819, March 2005.

[47] T.-H. Liew and L. Hanzo, "Space-time trellis and space-time block coding versus adaptive modulation and coding aided OFDM for wideband channels," *IEEE Transactions on Vehicular Technology*, vol. 55, pp. 173–187, January 2006.

[48] O. Alamri, S. X. Ng, F. Guo, S. Zummo and L. Hanzo, "Sphere-packing modulation aided space-time coding using non-binary LDPC-coded iterative-detection," *submitted to IEEE Wireless Communications and Networking Conference (WCNC)*, (Hong Kong), March 2007.

[49] P. Luo and H. Leib, "Class of full-rank space-time codes combining orthogonal designs with delay diversity," *IEEE Transactions on Vehicular Technology*, vol. 57, pp. 260–272, January 2008.

[50] J.H. Winters, "The diversity gain of transmit diversity in wireless systems with Rayleigh fading," *IEEE Transactions on Vehicular Technology*, vol. 47, pp. 119–123, February 1998.

[51] H. Jafarkhani, *Space-time coding: Theory and practice*. Cambridge University Press, 2005.

[52] V. Tarokh, A. Naguib, N. Seshadri and A.R. Calderbank, "Space-time codes for high data rate wireless communication: performance criteria in the presence of channel estimation errors, mobility and multiple paths," *IEEE Transactions on Communications*, vol. 47, pp. 199–207, February 1999.

[53] L. Hanzo, L.-L. Yang, E.-L. Kuan and K. Yen, *Single and multi-carrier DS-CDMA: Multi-user detection, space-time spreading, synchronisation, networking and standards*. Chichester, England: John Wiley and Sons Ltd and IEEE Press, 2003.

[54] V. Tarokh, S.M. Alamouti and P. Poon, "New detection schemes for transmit diversity with no channel estimation," in *IEEE International Conference on Universal Personal Communications*, vol. 2, pp. 917–920, October 1998.

[55] V. Tarokh and H. Jafarkhani, "A differential detection scheme for transmit diversity," in *IEEE Wireless Communications and Networking Conference*, vol. 3, pp. 1043–1047, September 1999.

[56] B.M. Hochwald and W. Sweldens, "Differential unitary space-time modulation," *IEEE Transactions on Communications*, vol. 48, no. 12, pp. 2041–2052, 2000.

[57] B. L. Hughes, "Differential space-time modulation," *IEEE Transactions on Information Theory*, vol. 46, no. 7, pp. 2567–2578, 2000.

[58] H. Jafarkhani and V. Tarokh, "Multiple transmit antenna differential detection from generalized orthogonal designs," *IEEE Transactions on Information Theory*, vol. 47, no. 6, pp. 2626–2631, 2001.

[59] R. Schober and L. Lampe, "Noncoherent receivers for differential space-time modulation," *IEEE Transactions on Communications*, vol. 50, pp. 768–777, May 2002.

[60] C. S. Hwang, S. H. Nam, J. Chung, and V. Tarokh, "Differential space time block codes using nonconstant modulus constellations," *IEEE Transactions on Signal Processing*, vol. 51, no. 11, pp. 2955–2964, 2003.

[61] C.-S. Hwang, S.H. Nam, J. Chung and V. Tarokh, "Differential space time block codes using nonconstant modulus constellations," *IEEE Transactions on Signal Processing*, vol. 51, no. 11, pp. 2955–2964, 2003.

[62] S.H. Nam, C.-S. Hwang, J. Chung and V. Tarokh, "Differential space time block codes using QAM for four transmit antennas," in *IEEE International Conference on Communications*, vol. 2, pp. 952–956, 2004.

[63] Y. Zhu and H. Jafarkhani, "Differential modulation based on quasi-orthogonal codes," *IEEE Transactions on Wireless Communications*, vol. 4, no. 6, pp. 3005–3017, 2005.

[64] L.-Y. Song and A.G. Burr, "General differential modulation scheme for quasi-orthogonal space-time block codes with partial or full transmit diversity," *IET Communications*, vol. 1, pp. 256–266, April 2007.

[65] V. Tarokh and H. Jafarkhani, "A differential detection scheme for transmit diversity," *IEEE Journal on Selected Areas in Communications*, vol. 18, no. 7, pp. 1169–1174, 2000.

[66] B.M. Hochwald and T.L. Marzetta, "Unitary space-time modulation for multiple-antenna communications in Rayleigh flat fading," *IEEE Transactions on Information Theory*, vol. 46, pp. 543–564, March 2000.

[67] E. Biglieri, G. Taricco and A. Tulino, "Performance of space-time codes for a large number of antennas," *IEEE Transactions on Information Theory*, vol. 48, pp. 1794–1803, July 2002.

[68] A.J. Paulraj, D.A. Gore, R.U. Nabar and H. Bolcskei, "An overview of MIMO communications - a key to gigabit wireless," *Proceedings of the IEEE*, vol. 92, pp. 198–218, February 2004.

[69] J.G. Proakis, *Digital communications*. McGraw-Hill, 2001.

[70] Viterbo, E. and Boutros, J., "A universal lattice code decoder for fading channels," *IEEE Transactions on Information Theory*, vol. 45, pp. 1639–1642, July 1999.

[71] O. Damen, A. Chkeif and J.-C. Belfiore, "Lattice code decoder for space-time codes," *IEEE Communications Letters*, vol. 4, pp. 161–163, May 2000.

[72] E. Agrell, T. Eriksson, A. Vardy and K. Zeger, "Closest point search in lattices," *IEEE Transactions on Information Theory*, vol. 48, pp. 2201–2214, August 2002.

[73] G.J. Foschini, "Layered space-time architecture for wireless communication in a fading environment when using multiple antennas," *Bell Laboratories Technical Journal*, vol. 1, pp. 41–59, Autumn 1996.

[74] G.D. Golden, C.J. Foschini, R.A. Valenzuela and P.W. Wolniansky, "Detection algorithm and initial laboratory results using V-BLAST space-time communication architecture," *Electronics Letters*, vol. 35, pp. 14–16, January 1999.

[75] A. Benjebbour, H. Murata and S. Yoshida, "Comparison of ordered successive receivers for space-time transmission," in *IEEE Vehicular Technology Conference*, vol. 4, (Atlantic City, NJ), pp. 2053–2057, October 2001.

[76] M. Sellathurai and S. Haykin, "Turbo-BLAST for wireless communications: theory and experiments," *IEEE Transactions on Signal Processing*, vol. 50, pp. 2538–2546, October 2002.

[77] D. Wubben, R. Bohnke, V. Kuhn and K.-D. Kammeyer, "MMSE extension of V-BLAST based on sorted QR decomposition," in *IEEE Vehicular Technology Conference*, vol. 1, pp. 508–512, October 2003.

[78] H. Zhu, Z. Lei and F.P.S. Chin, "An improved square-root algorithm for BLAST," *IEEE Signal Processing Letters*, vol. 11, pp. 772–775, September 2004.

[79] Y. Huang, J. Zhang and P.M. Djuric, "Bayesian detection for BLAST," *IEEE Transactions on Signal Processing*, vol. 53, pp. 1086–1096, March 2005.

[80] S. Verdu, *Multiuser Detection.* Cambridge University Press, 2003.

[81] B. Hassibi, "An efficient square-root algorithm for BLAST," in *IEEE International Conference on Acoustics, Speech and Signal Processing*, vol. 2, (Istanbul), June 2000.

[82] D. Wubben, R. Bohnke, J. Rinas, V. Kuhn and K.D. Kammeyer, "Efficient algorithm for decoding layered space-time codes," *Electronics Letters*, vol. 37, pp. 1348–1350, October 2001.

[83] W. Zha and S.D. Blostein, "Modified decorrelating decision-feedback detection of BLAST space-time system," in *IEEE International Conference on Communications*, vol. 1, (New York), pp. 335–339, April/May 2002.

[84] T. Xiaofeng, Y. Zhuizhuan, Q. Haiyan, Z. Ping, H. Haas and E. Costa, "New sub-optimal detection algorithm of layered space-time code," in *IEEE Vehicular Technology Conference*, vol. 4, pp. 1791–1794, May 2002.

[85] J. Choi, "A bi-directional zero-forcing BLAST receiver," *IEEE Transactions on Signal Processing*, vol. 52, pp. 2670–2673, September 2004.

[86] H. Zhu, Z. Lei and F.P.S. Chin, "An improved square-root algorithm for BLAST," *IEEE Signal Processing Letters*, vol. 11, pp. 772–775, September 2004.

[87] W.-J. Choi, K.-W. Cheong and J.M. Cioffi, "Iterative soft interference cancellation for multiple antenna systems," in *IEEE Wireless Communications and Networking Conference*, vol. 1, (Chicago, IL), pp. 304–309, September 2000.

[88] S. Baro, G. Bauch, A. Pavlic and A. Semmler, "Improving BLAST performance using space-time block codes and turbo decoding," in *IEEE Global Telecommunications Conference (GLOBECOM)*, vol. 2, (San Francisco, CA), pp. 1067–1071, 2000.

[89] X. Jing, H. Wang, C. Ming and S. Cheng, "A novel BLAST detection algorithm based instantaneous error ordering," in *IEEE International Conference on Communications*, vol. 5, pp. 3056–3060, May 2003.

[90] C. Shen, H. Zhuang, L. Dai and S. Zhou, "Detection algorithm improving V-BLAST performance over error propagation," *Electronics Letters*, vol. 39, pp. 1007–1008, June 2003.

[91] H. Yao and G.W. Wornell, "Lattice-reduction-aided detectors for MIMO communication systems," in *IEEE Global Telecommunications Conference*, vol. 1, pp. 424–428, November 2002.

[92] D. Wubben, R. Bohnke, V. Kuhn and K.-D. Kammeyer, "Near-maximum-likelihood detection of MIMO systems using MMSE-based lattice reduction," in *IEEE International Conference on Communications*, vol. 2, pp. 798–802, June 2004.

[93] A. Elkhazin, K. Plataniotis and S. Pasupathy, "Group MAP BLAST detector," in *IEEE International Conference on Acoustics, Speech and Signal Processing*, vol. 4, pp. 785–788, May 2004.

[94] M. Sellathurai and S. Haykin, "T-BLAST for wireless communications: first experimental results," *IEEE Transactions on Vehicular Technology*, vol. 52, pp. 530–535, May 2003.

[95] R.T. Compton, *Adaptive antennas: concepts and performance.* Englewood Cliffs (NJ): Prentice-Hall, 1988.

[96] L.C. Godara, "Applications of antenna arrays to mobile communications I: Performance improvement, feasibility and system considerations," *Proceedings of the IEEE*, vol. 85, pp. 1031–1060, July 1997.

[97] L.C. Godara, "Application of antenna arrays to mobile communications II: Beam-forming and direction-of-arrival considerations," *Proceedings of the IEEE*, vol. 85, pp. 1195–1245, August 1997.

[98] M. Chryssomallis, "Smart antennas," *IEEE Antennas and Propagation Magazine*, vol. 42, pp. 129–136, June 2000.

[99] A.F. Naguib, N. Seshadri and A.R. Calderbank, "Applications of space-time block codes and interference suppression for high capacity and high data rate wireless systems," in *Conference Record of the Thirty-Second Asilomar Conference on Signals, Systems and Computers*, vol. 2, (Pacific Grove, CA), pp. 1803–1810, 1998.

[100] H. Huang and H. Viswanathan, "Multiple antennas and multiuser detection in high data rate CDMA systems," in *IEEE 51st Vehicular Technology Conference Proceedings*, vol. 1, (Tokyo), pp. 556–560, May 2000.

[101] A. Stamoulis, N. Al-Dhahir and A. Calderbank, "Further results on interference cancellation and space-time block codes," in *Conference Record of the Thirty-Fifth Asilomar Conference on Signals, Systems and Computers*, vol. 1, (Pacific Grove, CA), pp. 257–261, November 2001.

[102] H. Huang, H. Viswanathan and G.J. Foschini, "Multiple antennas in cellular CDMA systems: transmission, detection and spectral efficiency," *IEEE Transactions on Wireless Communications*, vol. 1, pp. 383–392, July 2002.

[103] R.A. Soni, R.M. Buehrer and R.D. Benning, "Intelligent antenna system for CDMA2000," *IEEE Signal Processing Magazine*, vol. 19, pp. 54–67, July 2002.

[104] J. Liu and E. Gunawan, "Combining ideal beamforming and Alamouti space-time block codes," *Electronics Letters*, vol. 39, pp. 1258–1259, August 2003.

[105] F. Zhu and M.S. Lim, "Combined beamforming with space-time block coding using double antenna array group," *Electronics Letters*, vol. 40, pp. 811–813, June 2004.

[106] L. Zhao and V.K. Dubey, "Detection schemes for space-time block code and spatial multiplexing combined system," *IEEE Communications Letters*, vol. 9, pp. 49–51, January 2005.

[107] H. Lee, E.J. Powers and J. Kang, "Low-complexity ZF detector for D-STTD systems in time-selective fading channels," in *IEEE 62nd Vehicular Technology Conference*, vol. 3, pp. 2043–2047, September 2005.

[108] M. Sellathurai, T. Ratnarajah and P. Guinand, "Multirate layered space-time coding and successive interference cancellation receivers in quasi-static fading channels," *IEEE Transactions on Wireless Communications*, vol. 6, pp. 4524–4533, December 2007.

[109] S. Ekbatani and H. Jafarkhani, "Combining beamforming and space-time coding using quantized feedback," *IEEE Transactions on Wireless Communications*, vol. 7, pp. 898–908, March 2008.

[110] A.F. Naguib, N. Seshadri and A.R. Calderbank, "Increasing data rate over wireless channels," *IEEE Signal Processing Magazine*, vol. 17, pp. 76–92, May 2000.

[111] N. Al-Dhahir, C. Fragouli, A. Stamoulis, W. Younis and R. Calderbank, "Space-time processing for broadband wireless access," *IEEE Communications Magazine*, vol. 40, pp. 136–142, September 2002.

[112] W. Meng, L. Gu and C. Li, "The combined beamforming and space-time block coding technique for downlink transmission," in *International Conference on Wireless Networks, Communications and Mobile Computing*, vol. 1, pp. 481–486, June 2005.

[113] X. Li, A. Chindapol and J. A. Ritcey, "Bit-interleaved coded modulation with iterative decoding and 8 PSK signaling," *IEEE Transactions on Communications*, vol. 50, pp. 1250–1257, August 2002.

[114] R. Negi, A.M. Tehrani and J.M. Cioffi, "Adaptive antennas for space-time codes in outdoor channels," *IEEE Transactions on Communications*, vol. 50, pp. 1918–1925, December 2002.

[115] R. Nabar, H. Bolcskei and A.J. Paulraj, "Transmit optimization for spatial multiplexing in the presence of spatial fading correlation," in *IEEE Global Telecommunications Conference (GLOBECOM)*, vol. 1, (San Antonio, TX), pp. 131–135, November 2001.

[116] Z. Hong, K. Liu, R.W. Jr. Heath and A.M. Sayeed, "Spatial multiplexing in correlated fading via the virtual channel representation," *IEEE Journal on Selected Areas in Communications*, vol. 21, pp. 856–866, June 2003.

[117] H. Kim and J. Chun, "MIMO structure which combines the spatial multiplexing and beamforming," in *IEEE Vehicular Technology Conference*, vol. 1, pp. 108–112, May 2004.

[118] A. Sendonaris, E. Erkip and B. Aazhang, "User cooperation diversity Part I: System description," *IEEE Transactions on Communications*, vol. 51, no. 11, pp. 1927–1938, 2003.

[119] A. Sendonaris, E. Erkip and B. Aazhang, "User cooperation diversity Part II: Implementation aspects and performance analysis," *IEEE Transactions on Communications*, vol. 51, no. 11, pp. 1939–1948, 2003.

[120] E.C. Van der Meulen, "Three-terminal communication channels," *Advanced Applied Probability*, vol. 3, no. 1, pp. 120–154, 1971.

[121] T. Cover and A. El Gamal, "Capacity theorems for the relay channel," *IEEE Transactions on Information Theory*, vol. 25, no. 5, pp. 572–584, 1979.

[122] F. Willems, "The discrete memoryless multiple access channel with partially cooperating encoders," *IEEE Transactions on Information Theory*, vol. 29, no. 3, pp. 441–445, 1983.

[123] A. Sendonaris and E. Erkip and B. Aazhang, "Increasing uplink capacity via user cooperation diversity," in *IEEE International Symposium on Information Theory*, (Cambridge, MA), August 1998.

[124] J.N. Laneman, G.W. Wornell and D.N.C. Tse, "An efficient protocol for realizing cooperative diversity in wireless networks," in *IEEE International Symposium on Information Theory*, (Washington, DC), 2001.

[125] T.E. Hunter and A. Nosratinia, "Cooperation diversity through coding," in *IEEE International Symposium on Information Theory*, 2002.

[126] M. Dohler, E. Lefranc and H. Aghvami, "Space-time block codes for virtual antenna arrays," in *The 13th IEEE International Symposium on Personal, Indoor and Mobile Radio Communications*, vol. 1, pp. 414–417, September 2002.

[127] M.C. Valenti and B. Zhao, "Distributed turbo codes: towards the capacity of the relay channel," in *IEEE Vehicular Technology Conference VTC-Fall*, vol. 1, pp. 322–326, October 2003.

[128] B. Zhao and M.C. Valenti, "Distributed turbo coded diversity for relay channel," *Electronics Letters*, vol. 39, pp. 786–787, May 2003.

[129] J.N. Laneman, D.N. Tse and G.W. Wornell, "Cooperative diversity in wireless networks: Efficient protocols and outage behavior," *IEEE Transactions on Information Theory*, vol. 50, pp. 3062–3080, December 2004.

[130] R.U. Nabar, H. Bolcskei and F.W. Kneubuhler, "Fading relay channels: performance limits and space-time signal design," *IEEE Journal on Selected Areas in Communications*, vol. 22, pp. 1099–1109, August 2004.

[131] M. Janani, A. Hedayat, T. Hunter and A. Nosratinia, "Coded cooperation in wireless communications: space-time transmission and iterative decoding," *IEEE Transactions on Signal Processing*, vol. 52, pp. 362–371, February 2004.

[132] A. Stefanov and E. Erkip, "Cooperative coding for wireless networks," *IEEE Transactions on Communications*, vol. 52, pp. 1470–1476, September 2004.

[133] K. Azarian, H. El Gamal and P. Schniter, "On the achievable diversity-multiplexing tradeoff in half-duplex cooperative channels," *IEEE Transactions on Information Theory*, vol. 51, pp. 4152–4172, December 2005.

[134] H. Sneessens and L. Vandendorpe, "Soft decode and forward improves cooperative communications," in *6th IEE International Conference on 3G and Beyond*, (Washington, DC), pp. 1–4, November 2005.

[135] R. Hu and J. Li, "Exploiting Slepian-Wolf codes in wireless user cooperation," in *IEEE 6th Workshop on Signal Processing Advances in Wireless Communications*, pp. 275–279, June 2005.

[136] M. Yu and J. Li, "Is amplify-and-forward practically better than decode-and-forward or vice versa?," in *IEEE International Conference on Acoustics, Speech and Signal Processing*, vol. 3, March 2005.

[137] T.E. Hunter and A. Nosratinia, "Diversity through coded cooperation," *IEEE Transactions on Wireless Communications*, vol. 5, pp. 283–289, February 2006.

[138] T.E. Hunter, S. Sanayei and A. Nosratinia, "Outage analysis of coded cooperation," *IEEE Transactions on Information Theory*, vol. 52, pp. 375–391, February 2006.

[139] Y. Li, B. Vucetic, T.F. Wong and M. Dohler, "Distributed turbo coding with soft information relaying in multihop relay networks," *IEEE Journal on Selected Areas in Communications*, vol. 24, pp. 2040–2050, November 2006.

[140] R. Hu and J. Li, "Practical compress-forward in user cooperation: Wyner-Ziv Cooperation," in *IEEE International Symposium on Information Theory*, (Seattle, WA), pp. 489–493, July 2006.

[141] A. Host-Madsen, "Capacity bounds for cooperative diversity," *IEEE Transactions on Information Theory*, vol. 52, pp. 1522–1544, April 2006.

[142] T. Bui and J. Yuan, "A decode and forward cooperation scheme with soft relaying in wireless communication," in *IEEE 8th Workshop on Signal Processing Advances in Wireless Communications (SPAWC)*, (Helsinki), pp. 1–5, June 2007.

[143] M.N. Khormuji and E.G. Larsson, "Improving collaborative transmit diversity by using constellation rearrangement," in *IEEE Wireless Communications and Networking Conference*, (Kowloon), pp. 803–807, March 2007.

[144] X. Bao and J. Li, "Efficient message relaying for wireless user cooperation: Decode-Amplify-Forward (DAF) and Hybrid DAF and coded-cooperation," *IEEE Transactions on Wireless Communications*, vol. 6, pp. 3975–3984, November 2007.

[145] L. Xiao, T. Fuja, J. Kliewer and D. Costello, "A network coding approach to cooperative diversity," *IEEE Transactions on Information Theory*, vol. 53, pp. 3714–3722, October 2007.

[146] G. Yue, X. Wang, Z. Yang and A. Host-Madsen, "Coding schemes for user cooperation in low-power regimes," *IEEE Transactions on Signal Processing*, vol. 56, pp. 2035–2049, May 2008.

[147] W. Zhang, Y. Li, X.-G. Xia, P.C. Ching and K. Ben Letaief, "Distributed space-frequency coding for cooperative diversity in broadband wireless Ad Hoc networks," *IEEE Transactions on Wireless Communications*, vol. 7, pp. 995–1003, March 2008.

[148] T. Wang and G.B. Giannakis, "Complex field network coding for multiuser cooperative communications," *IEEE Journal on Selected Areas in Communications*, vol. 26, pp. 561–571, April 2008.

[149] P. Mitran, H. Ochiai and V. Tarokh, "Space-time diversity enhancements using collaborative communications," *IEEE Transactions on Information Theory*, vol. 51, pp. 2041–2057, June 2005.

[150] G. Forney, *Concatenated codes*. Cambridge: MIT Press, 1966.

[151] C. Berrou, A. Glavieux and P. Thitimajshima, "Near Shannon limit error-correcting coding and decoding: Turbo-codes. 1," in *IEEE International Conference on Communications*, vol. 2, (Geneva), pp. 1064–1070, May 1993.

[152] D. Divsalar and F. Pollara, "Multiple turbo codes for deep-space communications," Telecommunications and Data Acquisition Progress Report 42-121, Jet Propulsion Laboratory, Pasadena, CA, May 1995.

[153] S. Benedetto and G. Montorsi, "Serial concatenation of block and convolutional codes," *IEE Electronics Letters*, vol. 32, pp. 887–888, May 1996.

[154] S. Benedetto, D. Divsalar, G. Montorsi and F. Pollara, "Analysis, design, and iterative decoding of double serially concatenated codes with interleavers," *IEEE Journal on Selected Areas in Communications*, vol. 16, pp. 231–244, February 1998.

[155] Raphaeli, D. and Zarai, Y., "Combined turbo equalization and turbo decoding," in *Proceedings of IEEE Global Telecommunications Conference (GLOBECOM)*, vol. 2, (Phoenix, AZ), pp. 639–643, November 1997.

[156] D. Raphaeli and Y. Zarai, "Combined turbo equalization and turbo decoding," *IEEE Communications Letters*, vol. 2, pp. 107–109, April 1998.

[157] M. Toegel, W. Pusch and H. Weinrichter, "Combined serially concatenated codes and turbo-equalization," in *2nd International Symposium on Turbo Codes*, (Brest, France), pp. 375–378, September 2000.

[158] R. Ramamurthy and W. E. Ryan, "Convolutional double accumulate codes (or double turbo DPSK)," *IEEE Communications Letters*, vol. 5, pp. 157–159, April 2001.

[159] C. Douillard, M. Jezequel, C. Berrou, A. Picart, P. Didier and A. Glavieux, "Iterative correction of intersymbol interference: turbo equalization," *European Transaction on Telecommunications*, vol. 6, pp. 507–511, September/October 1995.

[160] S. Benedetto, D. Divsalar, G. Montorsi and F. Pollara, "A soft-input soft-output APP module for iterative decoding of concatenated codes," *IEEE Communications Letters*, vol. 1, pp. 22–24, January 1997.

[161] G. Caire, G. Taricco and E. Biglieri, "Bit-interleaved coded modulation," in *Proceedings of IEEE International Symposium on Information Theory (ISIT)*, (Ulm, Germany), p. 96, June-July 1997.

[162] G. Caire, G. Taricco and E. Biglieri, "Bit-interleaved coded modulation," *IEEE Transactions on Information Theory*, vol. 44, pp. 927–946, May 1998.

[163] S. ten Brink, J. Speidel and R.-H. Yan, "Iterative demapping and decoding for multilevel modulation," in *IEEE Global Telecommunications Conference (GLOBCOM)*, vol. 1, (Sydney,NSW), pp. 579–584, 1998.

[164] X. Li and J. A. Ritcey, "Bit-interleaved coded modulation with iterative decoding," *IEEE Communications Letters*, vol. 1, pp. 169–171, November 1997.

[165] X. Li and J. A. Ritcey, "Bit-interleaved coded modulation with iterative decoding using soft feedback," *IEE Electronics Letters*, vol. 34, pp. 942–943, May 1998.

[166] X. Li and J. A. Ritcey, "Trellis-coded modulation with bit interleaving and iterative decoding," *IEEE Journal on Selected Areas in Communications*, vol. 17, pp. 715–724, April 1999.

[167] X. Wang and H. V. Poor, "Iterative (turbo) soft interference cancellation and decoding for coded CDMA," *IEEE Transactions on Communications*, vol. 47, pp. 1046–1061, July 1999.

[168] A. Sezgin, D. Wuebben and V. Kuehn, "Analysis of mapping strategies for turbo-coded space-time block codes," in *Proceedings of IEEE Information Theory Workshop*, (Paris, France), pp. 103–106, March/April 2003.

[169] L. Bahl, J. Cocke, F. Jelinek and J. Raviv, "Optimal decoding of linear codes for minimizing symbol error rate," *IEEE Transactions on Information Theory*, vol. 20, no. 2, pp. 284–287, 1974.

[170] P. Robertson, E. Villebrun and P. Hoeher, "A comparison of optimal and sub-optimal MAP decoding algorithms operating in the Log domain," in *Proceedings of International Conference on Communications*, (Seattle, USA), pp. 1009–1013, June 1995.

[171] S. Benedetto, D. Divsalar, G. Montorsi and F. Pollara, "Serial concatenation of interleaved codes: performance analysis, design, and iterative decoding," *IEEE Transactions on Information Theory*, vol. 44, pp. 909–926, May 1998.

[172] D. Divsalar, S. Dolinar and F. Pollara, "Low complexity turbo-like codes," in *2nd International Symposium on Turbo Codes and Related Topics*, (Brest, France), pp. 73–80, September 2000.

[173] D. Divsalar, S. Dolinar and F. Pollara, "Serial turbo trellis coded modulation with rate-1 inner code," in *Proceedings of IEEE International Symposium on Information Theory (ISIT)*, (Sorrento, Italy), p. 194, June 2000.

[174] S. ten Brink, "Designing iterative decoding schemes with the extrinsic information transfer chart," *AEÜ International Journal of Electronics and Communications*, vol. 54, pp. 389–398, November 2000.

[175] I. Lee, "The effect of a precoder on serially concatenated coding systems with an ISI channel," *IEEE Transactions on Communications*, vol. 49, pp. 1168–1175, July 2001.

[176] S. ten Brink, "Code characteristic matching for iterative decoding of serially concatenated codes," *Annals of Telecommunications*, vol. 56, pp. 394–408, July-August 2001.

[177] S. ten Brink, "Convergence behavior of iteratively decoded parallel concatenated codes," *IEEE Transactions on Communications*, vol. 49, no. 10, pp. 1727–1737, 2001.

[178] H. El Gamal and A.R. Hammons, "Analyzing the turbo decoder using the Gaussian approximation," *IEEE Journal on Selected Areas in Communications*, vol. 47, pp. 671–686, February 2001.

[179] M. Tüchler, "Convergence prediction for iterative decoding of threefold concatenated systems," in *Proceedings of IEEE Global Telecommunications Conference (GLOBECOM)*, vol. 2, (Taipei, Taiwan), pp. 1358–1362, November 2002.

[180] M. Tüchler, S. ten Brink and J. Hagenauer, "Measures for tracing convergence of iterative decoding algorithms," in *Proceedings of the 4th International ITG Conference on Source and Channel Coding*, (Berlin, Germany), pp. 53–60, January 2002.

[181] M. Tüchler, "Convergence prediction for iterative decoding of threefold concatenated systems," in *IEEE Global Telecommunications Conference (GLOBECOM)*, vol. 2, pp. 1358–1362, November 2002.

[182] M. Tüchler, "Design of serially concatenated systems depending on the block length," *IEEE Transactions on Communications*, vol. 52, pp. 209–218, February 2004.

[183] L. Lifang, D. Divsalar and S. Dolinar, "Iterative demodulation, demapping and decoding of coded non-square QAM," in *IEEE Transactions on Communications*, vol. 53, pp. 16–19, January 2005.

[184] F. Brännström, L. K. Rasmussen and A. Grant, "Convergence analysis and optimal scheduling for multiple concatenated codes," *IEEE Transactions on Information Theory*, vol. 51, pp. 3354–3364, September 2005.

[185] R.G. Maunder, J. Wang, S.X. Ng, L.-L. Yang and L. Hanzo, "On the performance and complexity of irregular variable length codes for near-capacity joint source and channel coding," *IEEE Transactions on Wireless Communications*, vol. 7, pp. 1338–1347, April 2008.

[186] S. Benedetto, D. Divsalar, G. Montorsi and F. Pollara, "Serial concatenation of interleaved codes: performance analysis, design and iterative decoding," *IEEE Transactions on Information Theory*, vol. 44, pp. 909–926, May 1998.

[187] K. R. Narayanan, "Effect of precoding on the convergence of turbo equalization for partial response channels," *IEEE Journal on Selected Areas in Communications*, vol. 19, pp. 686–698, April 2001.

[188] J. Hagenauer, "The EXIT chart - Introduction to extrinsic information transfer in iterative processing," in *European Signal Processing Conference*, (Vienna, Austria), pp. 1541–1548, September 2004.

[189] J. Kliewer, S.X. Ng and L. Hanzo, "Efficient computation of EXIT functions for non-binary iterative decoding," *IEEE Transactions on Communications*, vol. 54, pp. 2133–2136, December 2006.

[190] W. Su, Z. Safar and K. J. Liu, "Space-time signal design for time-correlated Rayleigh fading channels," in *Proceedigns of IEEE International Conference on Communications (ICC)*, vol. 5, (Anchorage, Alaska), pp. 3175–3179, May 2003.

[191] M. Tüchler and J. Hagenauer, "EXIT charts of irregular codes," in *Proceedings of the 36th Annual Conference on Information Science and Systems (CISS)*, (Princeton, NJ, USA), March 2002.

[192] B. Scanavino, G. Montorsi and S. Benedetto, "Convergence properties of iterative decoders working at bit and symbol level," in *Proceedings of IEEE Global Telecommunications Conference (GLOBECOM)*, vol. 2, (San Antonio, TX), pp. 1037–1041, November 2001.

[193] J. Kliewer, S. X. Ng and L. Hanzo, "On the computation of EXIT characteristics for symbol-based iterative decoding," in *4th International Symposium on Turbo Codes in connection with 6th International ITG-Conference on Source and Channel Coding*, (Munich, Germany), April 2006.

[194] N. Wu, O. Alamri, S. X. Ng, and L. Hanzo, "Precoded sphere packing aided bit-interleaved differential space-time coded modulation using iterative decoding," *IEEE Transactions on Vehicular Technology*, vol. 57, pp. 1311–1316, March 2008.

[195] O. Alamri, B. L. Yeap and L. Hanzo, "Turbo detection of channel-coded space-time signals using sphere packing modulation," in *Proceedings of IEEE Vehicular Technology Conference (VTC)*, vol. 4, (Los Angeles, USA), pp. 2498–2502, September 2004.

[196] O. Alamri, B. L. Yeap and L. Hanzo, "Turbo detection of channel-coded space-time signals using sphere packing modulation," in *3rd International Workshop on Signal Processing for Wireless Communications (SPWC)*, (King's College, London, UK), June 2005.

[197] O. Alamri, B. L. Yeap and L. Hanzo, "A turbo detection and sphere packing modulation aided space-time coding scheme," *to appear in IEEE Transactions on Vehicular Technology*, January 2007 (available at http://www.ecs.soton.ac.uk/∼ora02r/turbo-stbc-sp.pdf).

[198] O. Alamri, Nan Wu and L. Hanzo, "A differential turbo detection aided sphere packing modulated space-time coding scheme," in *Proceedings of IEEE Vehicular Technology Conference (VTC)*, (Melbourne, Australia), May 2006.

[199] O. Alamri, J. Wang, S. X. Ng, L. L. Yang and L. Hanzo, "Near-capacity three-stage turbo detection of irregular convolutional coded joint sphere-packing modulation and space-time coding," *submitted to IEEE Transactions on Communications*, 2006.

[200] O. Alamri, J. Wang, S. X. Ng, L. L. Yang and L. Hanzo, "Near-capacity transceiver design using EXIT-curve fitting: three-stage turbo detection of irregular convolutional coded joint sphere-packing modulation and space-time coding," *submitted to IEEE International Conference on Communications (ICC)*, (Glasgow, Scotland), June 2007.

[201] O. Alamri, F. Guo, M. Jiang and L. Hanzo, "Turbo detection of symbol-based non-binary LDPC-coded space-time signals using sphere packing modulation," in *Proceedings of IEEE Vehicular Technology Conference (VTC)*, vol. 1, (Dallas, USA), pp. 540–544, September 2005.

[202] O. Alamri, S. X. Ng, F. Guo and L. Hanzo, "Non-binary LDPC-coded sphere-packed transmit diversity," *submitted to IEEE Transactions on Vehicular Technology*, 2006.

[203] O. Alamri, S. X. Ng, F. Guo and L. Hanzo, "A purely symbol-based precoded and LDPC-coded iterative-detection assisted sphere-packing modulated space-time coding scheme," in *Proceedings of IEEE Wireless Communications and Networking Conference (WCNC)*, vol. 3, (Las Vegas, USA), pp. 1201–1206, April 2006.

[204] M. Tüchler and J. Hagenauer, "Exit charts of irregular codes," in *36th Conference on Information Sciences and Systems (CISS)*, (Princeton, NJ), pp. 748–753, March 2002.

[205] M. El-Hajjar, O. Alamri, S. X. Ng and L. Hanzo, "Turbo detection of precoded sphere packing modulation using four transmit antennas for differential space-time spreading," *IEEE Transactions on Wireless Communications*, vol. 7, pp. 943–952, March 2008.

[206] M. El-Hajjar, O. Alamri and L. Hanzo, "Differential space-time spreading using four transmit antennas and iteratively detected sphere packing modulation," in *9th International Symposium on Spread Spectrum Techniques and Applications (ISSSTA)*, (Manaus-Amazon, Brazil), August 2006.

[207] M. El-Hajjar, O. Alamri and L. Hanzo, "Differential space-time spreading using four transmit antennas and iteratively detected sphere packing modulation," in *IEEE Ninth International Symposium on Spread Spectrum Techniques and Applications*, (Manaus-Amazon), pp. 322–326, August 2006.

[208] N. Othman, M. El-Hajjar, O. Alamri and L. Hanzo, "Iterative AMR-WB source and channel-decoding of differential space-time spreading assisted sphere packing modulation," *accepted for publication in IEEE Transactions on Vehicular Technology*, 2008.

[209] N. Othman, M. El-Hajjar, O. Alamri and L. Hanzo, "Soft-bit assisted iterative AMR-WB source-decoding and turbo-detection of channel-coded differential space-time spreading using sphere packing modulation," in *IEEE Vehicular Technology Conference (VTC)*, pp. 2010–2014, April 2007.

[210] N.S. Othman, M. El-Hajjar, A.Q. Pham, O. Alamri, S.X. Ng and L. Hanzo, "Over-complete source-mapping aided AMR-WB MIMO transceiver using three-stage iterative detection," in *IEEE International Conference on Communications*, (Beijing, China), pp. 751–755, May 2008.

[211] M. El-Hajjar, O. Alamri and L. Hanzo, "Adaptive differential space-time-spreading-assisted turbo-detected sphere packing modulation," in *IEEE Wireless Communications and Networking Conference*, pp. 645–649, March 2007.

[212] M. El-Hajjar and L. Hanzo, "Layered steered space-time codes and their capacity," *Electronics Letters*, vol. 43, pp. 680–682, June 2007.

[213] M. El-Hajjar, O. Alamri and L. Hanzo, "Layered steered space-time codes using iterative detection," in *IEEE Workshop on Signal Processing Systems*, (Shanghai, China), pp. 35–39, October 2007.

[214] M. El-Hajjar, O. Alamri, R.G. Maunder and L. Hanzo, "Layered steered space-time spreading using generalised MC DS-CDMA," *submitted to IEEE Signal Processing Letters*, April 2008.

[215] S. Alamouti, "A simple transmit diversity technique for wireless communications," *IEEE Journal on Selected Areas in Communications*, vol. 16, pp. 1451–1458, October 1998.

[216] V. Tarokh, H. Jafarkhani and A. R. Calderbank, "Space-time block codes from orthogonal designs," *IEEE Transactions on Information Theory*, vol. 45, pp. 1456–1467, July 1999.

[217] J. G. Guey, M. P. Fitz, M. R. Bell and W. Y. Kuo, "Signal design for transmitter diversity wireless communication systems over Rayleigh fading channels," *IEEE Transactions on Communications*, vol. 47, pp. 527–537, April 1999.

[218] V. Tarokh, A. Naguib, N. Seshadri and A. R. Calderbank, "Space-time codes for high data rate wireless communication: performance criteria in the presence of channel estimation errors, mobility, and multiple paths," *IEEE Transactions on Communications*, vol. 47, pp. 199–207, February 1999.

[219] G. Ganesan and P. Stoica, "Space-time block codes: a maximum SNR approach," *IEEE Transactions on Information Theory*, vol. 47, pp. 1650–1656, May 2001.

[220] O. Tirkkonen and A. Hottinen, "Square-matrix embeddable space-time block codes for complex signal constellations," *IEEE Transactions on Information Theory*, vol. 48, pp. 384–395, February 2002.

[221] W. Su and X. G. Xia, "On space-time block codes from complex orthogonal designs," *Wireless Personal Communications, (Kluwer Academic Publishers)*, vol. 25, pp. 1–26, April 2003.

[222] B. M. Hochwald and W. Sweldens, "Differential unitary space-time modulation," *IEEE Transactions on Communications*, vol. 48, pp. 2041–2052, December 2000.

[223] A. Shokrollahi, B. Hassibi, B. M. Hochwald and W. Sweldens, "Representaion theory for high-rate multiple-antenna code design," *IEEE Transactions on Information theory*, vol. 47, pp. 2335–2367, September 2001.

[224] B. Hassibi and B. M. Hochwald, "Cayley differential unitary space-time codes," *IEEE Transactions on Information Theory*, vol. 48, pp. 1485–1503, June 2002.

[225] X.-B. Liang and X.-G. Xia, "Unitary signal constellations for differential space-time modulation with two transmit antennas: parametric codes, optimal designs, and bounds," *IEEE Transactions on Information Theory*, vol. 48, pp. 2291–2322, August 2002.

[226] J. Grimm, M. Fitz and J. Krogmeier, "Further results on space-time coding for Rayleigh fading," in *Proceedings of the 36th Allerton Conference on Communications,Control and Computing*, (Illinois, USA), pp. 391–400, 1998.

[227] A. R. Hammons Jr and H. El Gamal, "On the theory of space-time codes for PSK modulation," *IEEE Transactions on Information Theory*, vol. 46, pp. 524–542, March 2000.

[228] Z. Safar and K. J. Liu, "Systematic design of space-time trellis codes for diversity and coding advantages," *EURASIP Journal on Applied Signal Processing, Special Issue on Space-Time Coding and Its Applications*, pp. 221–235, March 2002.

[229] Q. Yan and R. Blum, "Robust space-time block coding for rapid fading channels," in *Proceedings of IEEE Global Telecommunications Conference (GLOBECOM)*, vol. 1, (San Antonio, Texas), pp. 460–464, November 2001.

[230] S. Zummo and S. Al-Semari, "Space-time coded QPSK for rapid fading channels," in *Proceedings of IEEE International Symposium on Personal, Indoor and Mobile Radio Communications (PIMRC)*, vol. 1, (London, UK), pp. 504–508, 2000.

[231] W. Firmanto, B. Vucetic and J. Yuan, "Space-time TCM with improved performance on fast fading channels," *IEEE Communications Letters*, vol. 5, pp. 154–156, April 2001.

[232] G. H. Golub and C. F. Van-Loan, *Matrix Computations*. Baltimore, MD: Johns Hopkins, 1996.

[233] M. Fitz, J. Grimm and S. Siwamogsatham, "A new view of performance analysis techniques in correlated Rayleigh fading," in *Proceedings of IEEE Wireless Communications and Networking Conference (WCNC)*, vol. 1, (New Orleans, USA), pp. 139–144, September 1999.

[234] S. Siwamogsatham, M. P. Fitz and J. Grimm, "A new view of performance analysis of transmit diversity schemes in correlated Rayleigh fading," *IEEE Transactions on Information Theory*, vol. 48, pp. 950–956, April 2002.

[235] W. C. Jakes, *Microwave Mobile Communications*. New York: Wiley, 1974.

[236] J. H. Conway and N. J. Sloane, *Sphere Packings, Lattices and Groups*. Springer-Verlag, 1999.

[237] T. C. Hales, "Cannonballs and honeycombs," *Notices of the American Mathematical Society*, vol. 47, pp. 440–449, 2000.

[238] T. C. Hales, "A proof of the Kepler conjecture," *Annals of Mathematics*, vol. 162, p. 10651185, 2005.

[239] H. J. S. Smith, "On the Orders and Genera of Quadratic Forms Containing More than Three Indeterminates," *Royal Society of London Proceedings Series I*, vol. 16, pp. 197–208, 1867.

[240] A. Korkine and G. Zolotare, "Sur les formes quadratiques," *Math. Ann. 6*, pp. 366–389, 1873.

[241] V. I. Levenshtein, "On bounds for packing in n-dimensional euclidean space," *Soviet Mathematics Doklady*, vol. 20, pp. 417–421, 1979.

[242] A. M. Odlyzko and N. J. A. Sloane, "New bounds on the number of unit spheres that can touch a unit sphere in n dimensions," *Journal of Combinatorial Theory A26*, pp. 210–214, 1979.

[243] D. Hilbert, "Mathematische Probleme," *Archiv der Mathematik und Physik*, vol. 3, pp. 44–63, 1901.

[244] J. Milnor, "Hilbert's problem 18: on crystallographic groups, fundamental domains and on sphere packing," *Proceedings Symposium Pure Mathematics*, vol. 28, pp. 491–506, 1976.

[245] E. P. Baranovskii, "Packings, coverings, partitionings and certain other distributions in spaces of constant curvature," *Progress in Mathematics*, vol. 9, p. 209253, 1971.

[246] H. S. M. Coxeter, *Twelve Geometric Essays*. Carbondsale, IL: Southern Illinois University Press, 1968.

[247] G. F. Tóth, *Regular Figures*. Oxford: Pergamon, 1964.

[248] T. Hahn, *International tables for crystallography*. Dortrech: Kluwer Academic Publishers, 2002.

[249] J. Hammer, *Unsolved Problems Concerning Lattice Points*. San Francisco, CA: Pitman, 1977.

[250] R. L. E. Schwarzenberger, *N-Dimensional Crystallography*. San Francisco, CA: Pitman, 1980.

[251] J. W. S. Cassels, *An Introduction to the Geometry of Numbers*. Germany: Springer-Verlag, 1971.

[252] H. Hancock, *Development of the Minkowski Geometry of Numbers*. NY: Dover, 1964.

[253] O. H. Keller, *Geometrie der Zahlen*. Germany: Springer-Verlag, 1954.

[254] T. J. Aird and J. R. Rice, "Systematic Search in High Dimensional Sets," *SIAM Journal on Numerical Analysis*, vol. 14, pp. 296–312, April 1977.

[255] I. M. Sobol, "On the Systematic Search in a Hypercube," *SIAM Journal on Numerical Analysis*, vol. 16, pp. 790–793, October 1979.

[256] R. J. Renka, "Interpolation on the Surface of a Sphere," *ACM Transactions on Mathematical Software*, vol. 10, pp. 437–439, December 1984.

[257] D. Dobkin and R. J. Lipton, "Multidimensional Searching Problems," *SIAM Journal on Computing*, vol. 5, pp. 181–186, 1976.

[258] U. Fincke and M. Pohst, "Improved methods for calculating vectors of short length in a lattice, including a complexity analysis," *Mathematics of Computation*, vol. 44, pp. 463–471, April 1985.

[259] O. Damen, A. Chkeif and J.-C. Belfiore, "Lattice code decoder for space-time codes," *IEEE Communications Letters* , vol. 4, pp. 161–163, May 2000.

[260] B. M. Hochwald, G. Caire, B. Hassibi and T. L. Marzetta, Eds., "Special issue on space-time transmission, reception, coding and signal processing," *IEEE Transactions on Information Theory*, vol. 49, pp. 2329–2806, October 2003.

[261] L. Hanzo, T. H. Liew and B. L. Yeap, *Turbo Coding, Turbo Equalisation and Space-Time Coding: for Transmission over Fading Channels*. Chichester, England: John Wiley and Sons Ltd and IEEE Press, NY, USA, 2002.

[262] B. Vucetic and J. Yuan, *Space-Time Coding*. Wiley, 2003.

[263] S. X. Ng and L. Hanzo, "On the MIMO channel capacity of multidimensional signal sets," *IEEE Transactions on Vehicular Technology*, vol. 55, no. 2, pp. 528–536, 2006.

[264] S. X. Ng and L. Hanzo, "Space-time IQ-interleaved TCM and TTCM for AWGN and Rayleigh fading channels," *IEE Electronics Letters*, vol. 38, pp. 1553–1555, November 2002.

[265] L. Hanzo, S. X. Ng, T. Keller and W. T Webb, *Quadrature Amplitude Modulation: From Basics to Adaptive Trellis-Coded, Turbo-Equalised and Space-Time Coded OFDM, CDMA and MC-CDMA Systems*. John Wiley and Sons Ltd, 2 ed., September 2004.

[266] R. Gallager, *Information Theory and Reliable Communication*. New York: Wiley, 1968.

[267] P. E. McIllree, "Channel capacity calculations for M-ary N-dimensional signal sets." M.S. thesis, School of Electronic Engineering, University of South Australia, Adelaide, Australia, 1995.

[268] E. Telatar, "Capacity of multi-antenna Gaussian channels," *European Transactions on Telecommunication*, vol. 10, pp. 585–595, Nov–Dec 1999.

[269] S. L. Goff, A. Glavieux and C. Berrou, "Turbo-codes and high spectral efficiency modulation," in *Proceedings of IEEE International Conference on Communications (ICC)*, (New Orleans, USA), pp. 645–649, May 1994.

[270] T. Mittelholzer, X. Lin and J. Massey, "Multilevel turbo coding for M-ary quadrature and amplitude modulation," in *International Symposium on Turbo Codes and Related Topics*, (Brest, France), pp. 127–134, September 1997.

[271] P. Robertson, "An overview of bandwidth efficient turbo coding schemes," in *International Symposium on Turbo Codes and Related Topics*, (Brest, France), pp. 103–110, September 1997.

[272] S. ten Brink, J. Speidel and R.-H. Yan, "Iterative demappping and decoding for multilevel modulation," in *Procedings of IEEE Global Telecommunications Conference (GLOBECOM)*, vol. 1, (Sydney, Australia), pp. 579–584, November 1998.

[273] A. Sezgin, D. Wuebben and V. Kuehn, "Analysis of mapping strategies for turbo-coded space-time block codes," in *Proceedings of IEEE Information Theory Workshop*, (Paris, France), pp. 103–106, March-April 2003.

[274] T. J. Richardson and R. Urbanke, "The capacity of low-density parity-check codes under message-passing decoding," *IEEE Transactions on Information Theory*, vol. 47, pp. 599–618, February 2001.

[275] T. J. Richardson, A. Shokrollahi and R. Urbanke, "Design of capacity-approaching low-density parity-check codes," *IEEE Transactions on Information Theory*, vol. 47, pp. 619–637, February 2001.

[276] S. Y. Chung, G. D. Forney, T. J. Richardson and R. Urbanke, "On the design of low-density parity-check codes within 0.0045 dB of the Shannon limit," *IEEE Communication Letter*, vol. 5, pp. 58–60, February 2001.

[277] H. El Gamal and A. R. Hammons, "Analyzing the turbo decoder using the Gaussian approximation," *IEEE Journal on Selected Areas in Communications*, vol. 47, pp. 671–686, February 2001.

[278] D. Divsalar, S. Dolinar and F. Pollara, "Low complexity turbo-like codes," in *2nd International Symposium on Turbo Codes and Related Topics*, (Brest, France), pp. 73–80, September 2000.

[279] M. Peleg, I. Sason, S. Shamai and A. Elia, "On interleaved differentially encoded convolutional codes," *IEEE Transactions on Information Theory*, vol. 45, pp. 2572–2582, November 1999.

[280] S. ten Brink, "Designing iterative decoding schemes with the extrinsic information transfer chart," *AEÜ International Journal of Electronics and Communications*, vol. 54, pp. 389–398, November 2000.

[281] S. ten Brink, "Convergence behaviour of iteratively decoded parallel concatenated codes," *IEEE Transactions on Communications*, vol. 49, pp. 1727–1737, October 2001.

[282] M. Tüchler, S. ten Brink and J. Hagenauer, "Measures for tracing convergence of iterative decoding algorithms," in *Proceedings of the 4th International ITG Conference on Source and Channel Coding*, (Berlin, Germany), pp. 53–60, January 2002.

[283] J. Hagenauer, "The EXIT chart - introduction to extrinsic information transfer in iterative processing," in *European Signal Processing Conference*, (Vienna, Austria), pp. 1541–1548, September 2004.

[284] P. Robertson, E. Villebrun and P. Höher, "A comparison of optimal and sub-optimal MAP decoding algorithms operating in the log domain," in *Proceedings of IEEE International Conference on Communications (ICC)*, (Seattle, USA), pp. 1009–1013, June 1995.

[285] A. Leon-Garcia, *Probability and Random Processes for Electrical Engineering*. New York: Addison-Wesley Publishing Company, 2 ed., 1994.

[286] J. Hagenauer, E. Offer and L. Papke, "Iterative decoding of binary block and convolutional codes," *IEEE Transactions on Information Theory*, vol. 42, pp. 429–445, March 1996.

[287] T. M. Cover and J. A. Thomas, *Elements of Information Theory*. New York: Wiley, 1991.

[288] G. Ungerboeck, "Channel coding with multilevel/phase signals," *IEEE Transactions on Information Theory*, vol. 28, pp. 55–67, January 1982.

[289] V. Tarokh, S. M. Alamouti and P. Poon, "New detection schemes for transmit diversity with no channel estimation," in *Proceedings of IEEE International Conference on Universal Personal Communications*, vol. 2, (Florence, Italy), pp. 917–920, October 1998.

[290] V. Tarokh and H. Jafarkhani, "A differential detection scheme for transmit diversity," in *Proceedings of IEEE Wireless Communications and Networking Conference (WCNC)*, vol. 3, (New Orleans, USA), pp. 1043–1047, September 1999.

[291] V. Tarokh and H. Jafarkhani, "A differential detection scheme for transmit diversity," *IEEE Journal on Selected Areas in Communications*, vol. 18, pp. 1169–1174, July 2000.

[292] C.-S. Hwang, S. H. Nam, J. Chung and V. Tarokh, "Differential space time block codes using QAM constellations," in *Proceedings of IEEE International Symposium on Personal, Indoor and Mobile Radio Communications, (PIMRC)*, vol. 2, (Beijing, China), pp. 1693–1697, September 2003.

[293] C.-S. Hwang, S. H. Nam, J. Chung and V. Tarokh, "Differential space time block codes using nonconstant modulus constellations," *IEEE Transactions on Signal Processing*, vol. 51, pp. 2955–2964, November 2003.

[294] B. M. Hochwald and T. L. Marzetta, "Unitary space-time modulation for multiple-antenna communications in Rayleigh flat fading," *IEEE Transactions on Information Theory*, vol. 46, pp. 543–564, March 2000.

[295] B. L. Hughes, "Differential space-time modulation," *IEEE Transactions on Information Theory*, vol. 46, pp. 2567–2578, November 2000.

[296] C. Berrou, A. Glavieux and P. Thitimajshima, "Near Shannon Limit Error-Correcting Coding and Decoding: Turbo Codes," in *IEEE International Confrence on Communications*, (Geneva, Switzerland), pp. 1064–1070, May 1993.

[297] M. Breiling and L. Hanzo, "The super-trellis structure of turbo codes," *IEEE Transactions on Information Theory*, vol. 46, pp. 2212–2228, September 2000.

[298] D. Divsalar, S. Dolinar and F. Pollara, "Serial concatenated trellis coded modulation with rate-1 inner code," in *Preceedings of IEEE Global Telecommunications Conference (GLOBECOM)*, vol. 2, (San Francisco, USA), pp. 777–782, November-December 2000.

[299] H. M. Tullberg and P. H. Siegel, "Serial concatenated trellis coded modulation with inner rate-1 accumulate code," in *Proceedings of IEEE Global Telecommunications Conference (GLOBECOM)*, vol. 2, (San Antonio, TX), pp. 936–940, November 2001.

[300] Li. Lifang, D. Divsalar and S. Dolinar, "Iterative demodulation, demapping, and decoding of coded non-square QAM," *IEEE Transactions on Communications*, vol. 53, pp. 16–19, January 2005.

[301] S. ten Brink, "Convergence of multi-dimensional iterative decoding schemes," in *35th Asilomar Conference on Signals, Systems, and Computers*, vol. 1, (Pacific Grove, CA), pp. 270–274, November 2001.

[302] F. Brännström, L. K. Rasmussen and A. Grant, "Optimal scheduling for multiple serially concatenated codes," in *3rd International Symposium on Turbo Codes and Related Topics*, (Brest, France), pp. 383–386, September 2003.

[303] A. Ashikhmin, G. Kramer and S. ten Brink, "Extrinsic information transfer functions: model and erasure channel properties," *IEEE Transactions on Information Theory*, vol. 50, pp. 2657–2673, November 2004.

[304] D. Divsalar, H. Jin and R. J. McEliece, "Coding theorems for turbo-like codes," in *Proceedings of the 36th Allerton Conference on Communications, Control, and Computing*, (Illinois, USA), pp. 201–210, September 1998.

[305] C. E. Shannon, "A mathematical theory of communication," *Bell Systems Technical Journal*, vol. 27, pp. 379–423, July-October 1948.

[306] A. Ashikhmin, G. Kramer and S. ten Brink, "Extrinsic information transfer functions: A model and two properties," in *Proceedings of the 36th Annual Conference on Information Sciences and Systems (CISS)*, (Princeton, NJ, USA), March 2002.

[307] R. Gallager, "Low density parity check codes," *IEEE Transactions on Information Theory*, vol. 8, pp. 21–28, January 1962.

[308] T. Richardson and R. Urbanke, "The renaissance of Gallager's low-density parity-check codes," *IEEE Communications Magazine*, vol. 41, pp. 126–131, August 2003.

[309] D. J. MacKay and R. M. Neal, "Near Shannon limit performance of low density parity check codes," *IEE Electronics Letters*, vol. 32, August 1996.

[310] T. J. Richardson and R. Urbanke, "The capacity of low-density parity-check codes under message-passing decoding," *IEEE Transactions on Information Theory*, vol. 47, pp. 599–618, February 2001.

[311] M. C. Davey and D. J. MacKay, "Low density parity check codes over GF(q)," *IEEE Communications Letters*, vol. 2, pp. 165–167, June 1998.

[312] A. Grant, "Convergence of non-binary iterative decoding," in *Proceedings of IEEE Global Telecommunications Conference (GLOBECOM)*, vol. 2, (San Antonio, USA), pp. 1058–1062, November 2001.

[313] I. Land, P. Hoeher and S. Gligorevic, "Computation of symbol-wise mutual information in transmission systems with logAPP decoders and application to EXIT charts," in *Proceedings of the International ITG Conference on Source and Channel Coding (SCC)*, (Erlangen, Germany), pp. 195–202, January 2004.

[314] S. Benedetto, D. Divsalar, G. Montorsi and F. Pollara, "A soft-input soft-output APP module for iterative decoding of concatenated codes," *IEEE Communications Letters*, vol. 1, pp. 22–24, January 1997.

[315] L. Bahl, J. Cocke, F. Jelinek and J. Raviv, "Optimal decoding of linear codes for minimizing symbol error rate," *IEEE Transactions on Information Theory*, vol. 20, pp. 284–287, March 1974.

[316] H. Chen and A. Haimovich, "EXIT charts for turbo trellis-coded modulation," *IEEE Communications Letters*, vol. 8, pp. 668–670, November 2004.

[317] S. X. Ng, J. Y. Chung and L. Hanzo, "Turbo-detected unequal protection MPEG-4 wireless video telephony using multi level coding, trellis coded modulation and space-time trellis coding," *IEE Proceedings on Communications*, vol. 152, pp. 1116–1124, December 2005.

[318] S. X. Ng, J. Wang, M. Tao, L.-L. Yang and L. Hanzo, "Iteratively decoded variable length space-time coded modulation: code construction and convergence analysis," *accepted for publication in IEEE Transactions on Wireless Communications*, 2006.

[319] M. O. Damen, H. E. Gamal, and N. C. Beaulieu, "Linear threaded algebraic space-time constellations," *IEEE Transactions on Information Theory*, vol. 49, pp. 2372–2388, October 2003.

[320] X. L. Ma and G. B. Giannakis, "Full-diversity full-rate complex-field space-time coding," *IEEE Transactions on Signal Processing[see also IEEE Transactions on Acoustics, Speech, and Signal Processing]*, vol. 51, no. 11, pp. 2917–2930, 2003.

[321] G.J. Foschini and M.J. Gans, "On limits of wireless communications in a fading environment when using multiple antennas," *Kluwer Academic Publishers, Wireless Personal Communications*, pp. 311–335, 1998.

[322] R. H. Gohary and T. N. Davidson, "Design of linear dispersion codes: asymptotic guidelines and their implementation," *IEEE Transactions on Wireless Communications*, vol. 4, pp. 2892–2906, November 2005.

[323] J. G. Proakis, *Digital Communications*. McGraw-Hill, 2nd ed., 1989.

[324] I. Daubechies, *Ten Lectures on Wavelets*. SAIM, Philadelphia, PA, 1992.

[325] J. C. Belfiore, G. Rekaya, and E. Viterbo, "The golden code: a 2×2 full-rate space-time code with nonvanishing determinants," *IEEE Transactions on Information Theory*, vol. 51, pp. 1432–1436, April 2005.

[326] Y. Hong, E. Viterbo, and J. C. Belfiore, "Golden space-time trellis coded modulation," *IEEE Transactions on Information Theory*, vol. 53, pp. 1689–1705, May 2007.

[327] L. Hanzo, T. H. Liew, and B. L. Yeap, *Turbo Coding, Turbo Equalisation, and Space-Time Coding: For Transmission over Fading Channels*. Wiley-IEEE Press, July 2002.

[328] N. Wu and L. Hanzo, "Near-capacity irregular convolutional-coding aided irregular precoded linear dispersion codes," *IEEE Transactions on Vehicular Technology*, submiteed March 2008.

[329] M. O. Damen, H. E. Gamal, and G. Caire, "On maximum-likelihood detection and the search for the closest lattice point," *IEEE Transactions on Information Theory*, vol. 49, pp. 2389–2402, October 2003.

[330] J. B. Wang, X. D. Wang, and M. Madihian, "On the optimum design of space-time linear-dispersion codes," *IEEE Transactions on Wireless Communications*, vol. 4, pp. 2928–2938, November 2005.

[331] S. X. Ng, Jörg Kliewer, O. Alamri and L. Hanzo, "On the design of turbo trellis coded modulation schemes using symbol-based EXIT charts," in *Proceedings of IEEE Vehicular Technology Conference (VTC)*, (Montreal, Canada), September 2006.

[332] R. A. Horn and C. R. Johnson, *Matrix Analysis*. Cambridge University Press, 1985.

[333] H. F. Lu and P. V. Kumar, "A unified construction of space-time codes with optimal rate-diversity tradeoff," *IEEE Transactions on Information Theory*, vol. 51, pp. 1709–1730, May 2005.

[334] M. O. Damen and N. C. Beaulieu, "On diagonal algebraic space-time block codes," *IEEE Transactions on Communications*, vol. 51, pp. 911–919, January 2003.

[335] N. Sharma and C. B. Papadias, "Improved quasi-orthogonal codes through constellation rotation," *IEEE Transactions on Communications*, vol. 51, no. 3, pp. 332–335, 2003.

[336] W. F. Su and X. G. Xia, "Quasi-orthogonal space-time block codes with full diversity," in *IEEE Global Telecommunications Conference*, vol. 2, pp. 1098–1102, November 2002.

[337] W. F. Su and X. G. Xia, "Signal constellations for quasi-orthogonal space-time block codes with full diversity," *IEEE Transactions on Information Theory*, vol. 50, no. 10, pp. 2331 – 2347, 2004.

[338] G. Ganesan and P. Stoica, "Space-time diversity using orthogonal and amicable orthogonal designs," in *IEEE International Conference on Acoustics, Speech, and Signal Processing*, vol. 5, (Istanbul), pp. 2561–2564, June 2000.

[339] S. Sandhu and A. Paulraj, "Space-time block codes: a capacity perspective," *IEEE Communications Letters*, vol. 4, no. 12, pp. 384–386, 2000.

[340] S. Sandhu and A. Paulraj, "Unified design of linear space-time block codes," in *IEEE Global Telecommunications Conference*, vol. 2, (San Antonio), pp. 1073–1077, November 2001.

[341] C. Yuen, Y. L. Guan, and T. T. Tjhung, "Algebraic relationship between amicable orthogonal designs and quasi-orthogonal STBC with minimum decoding complexity," in *IEEE International Conference on Communications*, vol. 11, (Istanbul), pp. 4882–4887, June 2006.

[342] C. Yuen, Y. L. Guan, and T. T. Tjhung, "Quasi-orthogonal STBC with minimum decoding complexity," *IEEE Transactions on Wireless Communications*, vol. 4, pp. 2089–2094, September 2005.

[343] O. Alamri, N. Wu, and L. Hanzo, "A differential turbo detection aided sphere packing modulated space-time coding scheme," in *Vehicular Technology Conference*, vol. 5, (Melbourne), pp. 2474–2478, May 2006.

[344] S. ten Brink, "Designing iterative decoding schemes with the extrinsic information transfer chart," *AEÜ International Journal of Electronics and Communications*, vol. 54, pp. 389–398, 2000.

[345] J. Wang, S.X. Ng, A. Wolfgang, L.-L. Yang, S. Chen and L. Hanzo, "Near-capacity three-stage MMSE turbo equalisation using irregular convolutional codes," in *International Symposium on Turbo Codes*, (Munich, Germany), April 2006.

[346] A. Ashikhmin, G. Kramer, and S. ten Brink, "Extrinsic information transfer functions:a model and two properties," *36th Conference on Information Sciences and Systems (CISS), (Princeton University)*, vol. 1, pp. 742–747, March 2002.

[347] R. G. Maunder, J. Wang, S. X. Ng, L. L. Yang, and L. Hanzo, "Iteratively decoded irregular variable length coding and trellis coded modulation," in *IEEE Workshop on Signal Processing Systems*, (Shanghai), pp. 222–227, October 2007.

[348] B. M. Hochwald and W. Sweldens, "Differential unitary space-time modulation," *IEEE Transactions on Communications*, vol. 48, no. 12, pp. 2041–2052, 2000.

[349] S. Cheng, A. Nallanathan, and P. Y. Kam, "A new class of signal constellations for differential unitary space-time modulation (DUSTM)," *IEEE Communications Letters*, vol. 8, pp. 1–3, January 2004.

[350] T. P. Soh, C. S. Ng, and P. Y. Kam, "Improved signal constellations for differential unitary space-time modulations with more than two transmit antennas," *IEEE Communications Letters*, vol. 9, pp. 7–9, January 2005.

[351] T. Himsoon, W. F. Su, and K. J. R. Liu, "Differential unitary space-time signal design using matrix rotation structure," *IEEE Signal Processing Letters*, vol. 12, pp. 45–48, January 2005.

[352] L. Hanzo, S. X. Ng, T. Keller, and W. Webb, *Quadrature Amplitude Modulation: From Basics to Adaptive Trellis-Coded, Turbo-Equalised and Space-Time Coded OFDM, CDMA and MC-CDMA Systems*. Wiley-IEEE Press, September 2004.

[353] L. Zheng and D.N.C. Tse, "Communication on the Grassmann manifold: a geometric approach to the noncoherent multiple-antenna channel," *IEEE Transactions on Information Theory*, vol. 48, no. 2, pp. 359–383, 2002.

[354] A. L. Moustakas., S. H. Simon, and T. L. Marzetta, "Capacity of differential versus nondifferential unitary space-time modulation for MIMO channels," *IEEE Transactions on Information Theory*, vol. 52, pp. 3622–3634, August 2006.

[355] S. H. Nam, C. S. Hwang, J. Chung, and V. Tarokh, "Differential space time block codes using QAM for four transmit antennas," in *IEEE International Conference on Communications*, vol. 2, pp. 952–956, June 2004.

[356] G. Ganesan and P. Stoica, "Differential modulation using space-time block codes," *IEEE Signal Processing Letters*, vol. 9, no. 2, pp. 57–60, 2002.

[357] C. Yuen, Y. L. Guan, and T. T. Tjhung, "Single-symbol-decodable differential space-time modulation based on QO-STBC," *IEEE Transactions on Wireless Communications*, vol. 5, no. 12, pp. 3329–3334, 2006.

[358] R. Ertel and J. H. Reed, "Generation of two equal power correlated Rayleigh fading envelopes," *IEEE Communications Letters*, vol. 2, no. 10, pp. 276–278, 1998.

[359] A. Shokrollahi, B. Hassibi, B.M. Hochwald and W. Sweldens, "Representaion theory for high-rate multiple-antenna code design," *IEEE Transactions on Information theory*, vol. 47, pp. 2335–2367, September 2001.

[360] M. Hajiaghayi and C. Tellambura, "Unitary signal constellations for differential space-time modulation," *IEEE Communications Letters*, vol. 11, pp. 25–27, January 2007.

[361] F. Oggier and B. Hassibi, "Algebraic Cayley differential space-time codes," *IEEE Transactions on Information Theory*, vol. 53, pp. 1911–1919, May 2007.

[362] J. B. Wang, X. D. Wang, and M. Madihian, "Design of minimum error-rate Cayley differential unitary space-time codes," *IEEE Journal on Selected Areas in Communications*, vol. 23, pp. 1779–1787, September 2005.

[363] A. Chindapol and J. A. Ritcey, "Design, analysis, and performance evaluation for BICM-ID with square QAM constellations in Rayleigh fading channels," *IEEE Journal on Selected Areas in Communications*, vol. 19, no. 5, pp. 944–957, 2001.

[364] Y. B. Li and X. G. Xia, "Constellation mapping for space-time matrix modulation with iterative demodulation/decoding," *IEEE Transactions on Communications*, vol. 53, no. 5, pp. 764–768, 2005.

[365] K. R. Narayanan and G. L. Stüber, "A serial concatenation approach to iterative demodulation and decoding," *IEEE Transactions on Communications*, vol. 47, no. 7, pp. 956–961, 1999.

[366] P. Hoeher and J. Lodge, "Turbo DPSK: iterative differential PSK demodulation and channel decoding," *IEEE Transactions on Communications*, vol. 47, no. 6, pp. 837–843, 1999.

[367] W. F. Su, Z. Safar, and K. J. R. Liu, "Space-time signal design for time-correlated Rayleigh fading channels," in *IEEE International Conference on Communications*, vol. 5, pp. 3175–3179, May 2003.

[368] J. H. Conway and N. J. A. Sloane, *Sphere Packings, Lattices and Groups*. Springer-Verlag, 1998.

[369] Y. Huang and J. A. Ritcey, "Improved 16-QAM constellation labeling for BI-STCM-ID with the Alamouti scheme," *IEEE Communications Letters*, vol. 9, pp. 157–159, February 2005.

[370] L. Hanzo, J. Blogh, and S. Ni, *3G, HSPA and FDD versus TDD Networking: Smart Antennas and Adaptive Modulation*. Wiley-IEEE Press, 2 ed., February 2008.

[371] Y. Fan and J. Thompson, "MIMO configurations for relay channels: Theory and practice," *IEEE Transactions on Wireless Communications*, vol. 6, pp. 1774–1786, May 2007.

[372] M. Dohler, Y. Li, B. Vucetic, A. H. Aghvami, M. Arndt, and D. Barthel, "Performance analysis of distributed space-time block-encoded sensor networks," *IEEE Transactions on Vehicular Technology*, vol. 55, pp. 1776–1789, November 2006.

[373] G. Kramer, M. Gastpar, and P. Gupta, "Cooperative strategies and capacity theorems for relay networks," *IEEE Transactions on Information Theory*, vol. 51, pp. 3037–3063, September 2005.

[374] K. C. Liang, X. D. Wang, and I. Berenguer, "Minimum error-rate linear dispersion codes for cooperative relays," *IEEE Transactions on Vehicular Technology*, vol. 56, pp. 2143–2157, July 2007.

[375] Y. D. Jing and B. Hassibi, "Distributed space-time coding in wireless relay networks," *IEEE Transactions on Wireless Communications*, vol. 5, no. 12, pp. 3524–3536, 2006.

[376] S. Yiu, R. Schober, and L. Lampe, "Distributed space-time block coding," *IEEE Transactions on Communications*, vol. 54, pp. 1195–1206, July 2006.

[377] E. Stauffer, O. Oyman, R. Narasimhan, and A. Paulraj, "Finite-SNR diversity-multiplexing tradeoffs in fading relay channels," *IEEE Journal on Selected Areas in Communications*, vol. 25, pp. 245–257, February 2007.

[378] S. Yang and J. C. Belfiore, "Optimal space-time codes for the MIMO amplify-and-forward cooperative channel," *IEEE Transactions on Information Theory*, vol. 53, pp. 647–663, February 2007.

[379] T. Y. Bui and J. H. Yuan, "A decode and forward cooperation scheme with soft relaying in wireless communication," in *IEEE 8th Workshop on Signal Processing Advances in Wireless Communications*, (Helsinki), pp. 1–5, June 2007.

[380] S. ten Brink, J. Speidel, and R. H. Yan, "Iterative demapping and decoding for multilevel modulation," in *IEEE Global Telecommunications Conference*, vol. 1, (Sydney), pp. 579–584, November 8–12, 1998.

[381] S. Wei, "Diversity-multiplexing tradeoff of asynchronous cooperative diversity in wireless networks," *IEEE Transactions on Information Theory*, vol. 53, pp. 4150–4172, November 2007.

[382] Y. Shang and X. G. Xia, "Shift-full-rank matrices and applications in space-time trellis codes for relay networks with asynchronous cooperative diversity," *IEEE Transactions on Information Theory*, vol. 52, pp. 3153–3167, July 2006.

[383] W. C. Jakes, *Microwave Mobile Communications*. John Wiley & Sons, 1974.

[384] J. Liu, J. Li and E.G. Larsson, "Differential space-time block code modulation for DS-CDMA systems," *EURASIP Journal on Applied Signal Processing*, vol. 3, pp. 289–296, 2002.

[385] N. Seshadri, V. Tarokh and A.R. Calderbank, "Space-time codes for wireless communication: code construction," in *IEEE Vehicular Technology Conference*, vol. 2, (Phoenix, AZ), pp. 637–641, 1997.

[386] G.J. Foschini, D. Chizhik, M.J. Gans, C. Papadias and R.A. Valenzuela, "Analysis and performance of some basic space-time architectures," *IEEE Journal on Selected Areas in Communications*, vol. 21, no. 3, pp. 303–320, 2003.

[387] B.M. Hochwald, G. Caire, B. Hassibi and T.L. Marzetta, "The academic and industrial embrace of space-time methods," in *IEEE Transactions on Information Theory*, vol. 49, pp. 2329–2331, October 2003.

[388] B.M. Hochwald, G. Caire, B. Hassibi and T.L. Marzetta, "Special Issue on Space-Time Transmission, Reception, Coding and Signal Processing," *IEEE Transactions on Information Theory*, pp. 2329–2806, October 2003.

[389] G. Ganesan and P. Stoica, "Utilizing space-time diversity for wireless communications," *Wireless Personal Communications*, vol. 18, pp. 149–163, 2001.

[390] G. Ganesan and P. Stoica, "Space-time diversity using orthogonal and amicable orthogonal designs," *Wireless Personal Communications*, vol. 18, pp. 165–178, 2001.

[391] G. Ganesan, P. Stoica and E. Larsson, "Orthogonal space-time block codes with feedback," *Wireless Personal Communications*, vol. 28, pp. 287–312, 2004.

[392] L. Hanzo, S.X. Ng, T. Keller and W. Webb, *Quadrature amplitude modulation: From basics to adaptive trellis-coded, turbo equalised and space-time coded OFDM, CDMA and MC-CDMA systems, 2nd Edition*. Chichester, England: John Wiley and Sons Ltd and IEEE Press, 2004.

[393] L. Hanzo, M. Münster, B.J. Choi and T. Keller, *OFDM and MC-CDMA for broadband multi-user communications, WLANs and broadcasting*. Chichester, UK: Wiley, 2003.

[394] J.H. Conway and N.J. Sloane, *Sphere packings, lattices and groups*. Springer-Verlag, 1999.

[395] C. E. Shannon, "A mathematical theory of communication," *Bell Systems Technical Journal*, vol. 27, pp. 379–423, July 1948.

[396] H. Shin and J.H. Lee, "Capacity of multiple-antenna fading channels: spatial fading correlation, double scattering and keyhole," *IEEE Transactions on Information Theory*, vol. 49, no. 10, pp. 2636–2647, 2003.

[397] J.M. Wozencraft and I. M. Jacobs, *Pinciples of communication engineering*. John Wiley & Sons, NY, USA, 1965.

[398] T.J. Richardson and R. Urbanke, "The capacity of low-density parity-check codes under message-passing decoding," *IEEE Transactions on Information Theory*, vol. 47, pp. 599–618, February 2001.

[399] T.J. Richardson, A. Shokrollahi and R. Urbanke, "Design of capacity-approaching low-density parity-check codes," *IEEE Transactions on Information Theory*, vol. 47, pp. 619–637, February 2001.

[400] Sae-Young Chung and Richardson, T.J. and Urbanke, R.L., "Analysis of sum-product decoding of low-density parity-check codes using a Gaussian approximation," *IEEE Transactions on Information Theory*, vol. 47, pp. 657–670, February 2001.

[401] M. Peleg, I. Sason, S. Shamai and A. Elia, "On interleaved differentially encoded convolutional codes," *IEEE Transactions on Information Theory*, vol. 45, pp. 2572–2582, November 1999.

[402] S. ten Brink, J. Speidel and R.-H. Han, "Iterative demapping for QPSK modulation," *Electronics Letters*, vol. 34, no. 15, pp. 1459–1460, 1998.

[403] V.B. Balakirsky, "Joint source-channel coding with variable length codes," in *IEEE International Symposium on Information Theory*, (Ulm, Germany), p. 419 , June 1997.

[404] J. Hagenauer, E. Offer and L. Papke, "Iterative decoding of binary block and convolutional codes," *IEEE Transactions on Information Theory*, vol. 42, no. 2, pp. 429–445, 1996.

[405] S. Benedetto, G. Montorsi, "Serial concatenation of block and convolutional codes," *Electronics Letters*, vol. 32, pp. 887–888, May 1996.

[406] T.M. Cover and J.A. Thomas, *Elements of information theory*. New York: Wiley, 1991.

[407] L. Hanzo, F.C. Somerville and J. P. Woodard, *Voice compression and communications: Principles and applications for fixed wireless channels*. IEEE Press-John Wiley & Sons, 2001.

[408] L. Hanzo, P.J. Cherriman and J. Streit, *Wireless video communications: second to third generation and beyond*. IEEE Press-John Wiley & Sons, 2001.

[409] T. Fingscheidt and P. Vary, "Speech decoding with error concealment using residual source redundancy," *IEEE Workshop on Speech Coding for Telecommunication*, pp. 91–92, September 1997.

[410] T. Fingscheidt and P. Vary, "Softbit speech decoding: A new approach to error concealment," *IEEE Transactions on Speech and Audio Processing*, vol. 9, pp. 240–251, March 2001.

[411] M. Adrat, P. Vary and J. Spittka, "Iterative source-channel decoder using extrinsic information from softbit-source decoding," *IEEE International Conference on Acoustics, Speech and Signal Processing*, pp. 2653–2656, May 2001.

[412] T. Clevorn, J. Brauers, M. Adrat and P. Vary, "Turbo decodulation: Iterative combined demodulation and source-channel decoding," *IEEE Communications Letters*, vol. 9, pp. 820–822, September 2005.

[413] B. Bessette, R. Salami, R. Lefebvre, M. Jelinek, J. Rotola-Pukkila, J. Vainio, H. Mikkola, K. Jarvinen, "The adaptive multirate wideband speech codec (AMR-WB)," *IEEE Transactions on Speech and Audio Processing*, vol. 10, pp. 620–636, November 2002.

[414] T. Hindelang, T. Fingscheidt, N. Seshadri and R.V. Cox, "Combined source/channel (de-)coding: can a priori information be used twice?," *IEEE International Conference on Communications*, pp. 1208–1212, June 2000.

[415] S. Lloyd, "Least squares quantization in PCM," *IEEE Transaction on Information Theory*, vol. 28, pp. 129–137, March 1982.

[416] V. Buttigieg and P.G. Farrell, "Variable-length error-correcting codes," *IEE Proceedings-Communications*, vol. 147, pp. 211–215, August 2000.

[417] N. Dimitriou, R. Tafazolli and G. Sfikas, "Quality of service for multimedia CDMA," *IEEE Communications Magazine*, vol. 38, pp. 88–94, July 2000.

[418] K.S. Gilhousen, I.M. Jacobs, R. Padovani, A.J. Viterbi, L.A. Jr. Weaver and C.E. Wheatley, "On the capacity of a cellular CDMA system," *IEEE Transactions on Vehicular Technology*, vol. 40, pp. 303–312, May 1991.

[419] L. Hanzo, C.H. Wong and M.S. Yee, *Adaptive wireless transceivers: turbo-coded, turbo-equalized and space-time coded TDMA, CDMA and OFDM systems*. Chichester, UK: John Wiley and Sons, 2002.

[420] P.A. Bello, "Sample size required in error-rate measurement on fading channels," *Proceedings of the IEEE*, vol. 86, pp. 1435–1441, July 1998.

[421] L.-L. Yang and L. Hanzo, "Adaptive space-time-spreading-assisted wideband CDMA systems communicating over dispersive Nakagami-m fading channels," *EURASIP Journal on Wireless Communications and Networking*, vol. 2, pp. 216–230, April 2005.

[422] W.T. Webb and R. Steele, "Variable rate QAM for mobile radio," *IEEE Transactions on Communications*, vol. 43, no. 7, pp. 2223–2230, 1995.

[423] A.J. Goldsmith and S.-G. Chua, "Variable-rate variable-power MQAM for fading channels," *IEEE Transactions on Communications*, vol. 45, pp. 1218–1230, 1997.

[424] J. Hayes, "Adaptive feedback communications," *IEEE Transactions on Communications*, vol. 16, pp. 29–34, 1968.

[425] J. Cavers, "Variable-rate transmission for Rayleigh fading channels," *IEEE Transactions on Communications*, vol. 20, no. 1, pp. 15–22, 1972.

[426] B.-J. Choi and L. Hanzo, "Optimum mode-switching-assisted constant-power single- and multi-carrier adaptive modulation," *IEEE Transactions on Vehicular Technology*, vol. 52, no. 3, pp. 536–560, 2003.

[427] L.-L. Yang and L. Hanzo, "Adaptive rate DS-CDMA systems using variable spreading factors," *IEEE Transactions on Vehicular Technology*, vol. 53, no. 1, pp. 72–81, 2004.

[428] T. Ottosson and A. Svensson, "On schemes for multirate support in DS-CDMA systems," *Wireless Personal Communications, Kluwer Academic Publisher*, vol. 6, pp. 265–287, March 1998.

[429] T. Ojanpera and R. Prasad, *Wideband CDMA for third generation mobile communications*. Artech House Publishers, 1998.

[430] S.W. Kim, "Adaptive rate and power DS-CDMA communications in fading channels," *IEEE Communications Letters*, vol. 3, pp. 85–87, April 1999.

[431] S. Abeta, S. Sampei and N. Morinaga, "Channel activation with adaptive coding rate and processing gain control for cellular DS-CDMA systems," in *IEEE 46th Vehicular Technology Conference*, vol. 2, (Atlanta, GA), pp. 1115–1119, April/May 1996.

[432] G. Ungerboeck, "Channel coding with multilevel/phase signals," *IEEE Transactions on Information Theory*, vol. 28, no. 1, pp. 55–67, 1982.

[433] L. Linnan, K. Jingming and F. Zesong, "Combining Eigen-beamforming and space-time block coding with equal power allocation," in *International Conference on Communication Technology (ICCT)*, (Guilin, China), pp. 1–4, November 2006.

[434] L. Hanzo and T. Keller, *OFDM and MC-CDMA: A Primer*. IEEE Press-John Wiley & Sons, April 2006.

[435] L. Vandendorpe, "Multitone spread spectrum multiple access communications system in a multipath Rician fading channel," *IEEE Transactions on Vehicular Technology*, vol. 44, pp. 327–337, May 1995.

[436] E.A. Sourour and M. Nakagawa, "Performance of orthogonal multicarrier CDMA in a multipath fading channel," *IEEE Transactions on Communications*, vol. 44, pp. 356–367, March 1996.

[437] M. El-Hajjar, B. Hu, L.-L. Yang and L. Hanzo, "Coherent and differential downlink space-time steering aided generalised multicarrier DS-CDMA," *IEEE Transactions on Wireless Communications*, vol. 6, pp. 3857–3863, November 2007.

[438] M. El-Hajjar, R.Y.S. Tee, H. Bin, L.-L. Yang and L. Hanzo, "Downlink steered space-time spreading assisted generalised Multicarrier DS-CDMA using sphere packing aided multilevel coding," in *IEEE 66th Vehicular Technology Conference*, (Baltimore, MD, USA), pp. 472–476, September 2007.

[439] Bin Hu, *Multicarrier DS-CDMA communication systems using smart antennas*. PhD thesis, School of Electronics and Computer Science, University of Southampton, April 2006.

[440] X. Gui and T.S. Ng, "Performance of asynchronous orthogonal multicarrier CDMA system in frequency selective fading channel," *IEEE Transactions on Communications*, vol. 47, pp. 1084–1091, July 1999.

[441] S. Hara and R. Prasad, "Overview of multicarrier CDMA," *IEEE Communications Magazine*, vol. 35, pp. 126–133, December 1997.

[442] L.-L. Yang and L. Hanzo, "Performance of broadband multicarrier DS-CDMA using space-time spreading-assisted transmit diversity," *IEEE Transactions on Wireless Communications*, vol. 4, no. 3, pp. 885–894, 2005.

[443] S. ten Brink, "Convergence of iterative decoding," *Electronics Letters*, vol. 35, no. 13, pp. 1117–1119, 1999.

[444] G. Scutari and S. Barbarossa, "Distributed space-time coding for regenerative relay networks," *IEEE Transactions on Wireless Communications*, vol. 4, pp. 2387–2399, September 2005.

[445] A. Nosratinia, T.E. Hunter and A. Hedayat, "Cooperative communication in wireless networks," *IEEE Communications Magazine*, vol. 42, no. 10, pp. 74–80, 2004.

[446] Y. Jing and B. Hassibi, "Wireless networks, diversity and space-time codes," in *IEEE Information Theory Workshop*, pp. 463–468, October 2004.

[447] C. Berrou and A. Glavieux, "Near optimum error correcting coding and decoding: turbo-codes," *IEEE Transactions on Communications*, vol. 44, pp. 1261–1271, October 1996.

[448] O. Alamri, *Turbo detection of sphere packing modulation aided space-time coding schemes*. PhD thesis, School of Electronics and Computer Science, University of Southampton, September 2006.

[449] L.-F. Wei, "Trellis-coded modulation with multidimensional constellations," *IEEE Transactions on Information Theory*, vol. 33, pp. 483–501, July 1987.

[450] L.-F. Wei, "Rotationally invariant trellis-coded modulations with multidimensional M-PSK," *IEEE Journal on Selected Areas in Communications*, vol. 7, pp. 1281–1295, December 1989.

[451] R. H. Deng and D. J. Costello-Jr., "High rate concatenated coding systems using multidimensional bandwidth-efficient trellis inner codes," *IEEE Transactions on Communications*, vol. 37, pp. 1091–1096, October 1989.

[452] S. S. Pietrobon, R. H. Deng, A. Lafanechere, G. Ungerboeck and D. J. Costello-Jr., "Trellis-coded multidimensional phase modulation," *IEEE Transactions on Information Theory*, vol. 36, pp. 63–89, January 1990.

[453] N. H. Tran and H. H. Nguyen, "Improving the performance of QPSK BICM-ID by mapping on the hypercube," in *Proceedings of IEEE Vehicular Technology Conference (VTC)*, vol. 2, (Los Angeles, USA), pp. 1299–1303, September 2004.

[454] N. H. Tran and H. H. Nguyen, "Design and performance of BICM-ID systems with hypercube constellations," *IEEE Transactions on Wireless Communications*, vol. 5, pp. 1169–1179, May 2006.

[455] S. Bäro, "turbo-detection in MIMO systems: bit labeling and pre-coding," in *5th International ITG Conference on Source and Channel Coding*, (Erlangen, Germany), January 2004.

[456] F. Simoens, H. Wymeersch and M. Moeneclaey, "Spatial mapping for MIMO systems," in *Proceedings of IEEE Information Theory Workshop*, (San Antonio, Texas), pp. 187–192, October 2004.

[457] F. Simoens, H. Wymeersch, H. Bruneel and M. Moeneclaey, "Multidimensional mapping for bit-interleaved coded modulation with BPSK/QPSK signaling," *IEEE Communications Letters*, vol. 9, pp. 453–455, May 2005.

[458] H. Wymeersch, F. Simoens, H. Bruneel and M. Moeneclaey, "Multi-dimensional modulation for UWB communications," in *Proceedings of IEEE Workshop on Signal Processing Advances in Wireless Communications (SPAWC)*, (New York, USA), pp. 42–46, June 2005.

[459] A. S. Mohammed, W. Hidayat and M. Bossert, "Multidimensional 16-QAM constellation labeling of BI-STCM-ID with the Alamouti scheme," in *Proceedings of IEEE Wireless Communications and Networking Conference (WCNC)*, (Las Vegas, USA), April 2006.

[460] R. Battiti and G. Tecchiolli, "Reactive search: toward self-tuning heuristics," *Operations Research Society of America (ORSA) journal on computing*, vol. 6, no. 2, pp. 126–140, 1994.

[461] M. Tüchler, "Design of serially concatenated systems for long or short block lengths," in *Proceedings of IEEE International Conference on Communications (ICC)*, vol. 4, (Anchorage Alaska, USA), pp. 2948–2952, May 2003.

[462] V. Tarokh, H. Jafarkhani and A. R. Calderbank, "Space-time block coding for wireless communications: performance results," *IEEE Journal on Selected Areas in Communications*, vol. 17, pp. 451–460, March 1999.

[463] G. J. Foschini, "Layered space-time architecture for wireless communication in a fading environment when using multiple antennas," *Bell Labs Technical Journal*, vol. 1, pp. 41–59, Autumn 1996.

[464] J. Akhtman and L. Hanzo, "Reduced-complexity near-optimum detection for MIMO-OFDM: Parts I and II," *submitted to IEEE Transactions on Wireless Communications*, 2005.

[465] A. Maaref and S. Aissa, "Capacity of space-time block codes in MIMO Rayleigh fading channels with adaptive transmission and estimation errors," *IEEE Transactions on Wireless Communications*, vol. 4, pp. 2568–2578, September 2005.

[466] K. K. Wong, A. Paulraj, and R. D. Murch, "Efficient high-performance decoding for overloaded MIMO antenna systems," *IEEE Transactions on Wireless Communications*, vol. 6, pp. 1833–1843, May 2007.

[467] L. Zhang, H. P. Lei, X. Zhang, and D. C. Yang, "Efficient complex sphere decoding framework for linear dispersion space-time block codes," in *IEEE International Symposium on Personal, Indoor and Mobile Radio Communications*, (Greece), pp. 1–4, September 2007.

[468] D. Deng, M. Zhao, and J. K. Zhu, "Transmit antenna selection for linear dispersion codes based on linear receiver," in *Vehicular Technology Conference*, vol. 6, (Melbourne), pp. 2927–2931, May 2006.

[469] M. Luby, "LT codes," in *IEEE Symposium on Foundations of Computer Science*, (Vancouver, Canada), pp. 271–280, November 2002.

[470] C. Y. Wei, T. Nguyen, N. Wu, J. Akhtman, L. L. Yang, and L. Hanzo, "Luby transform coding aided iterative detection for downlink SDMA systems," in *IEEE Workshop on Signal Processing Systems*, (Shanghai, China), pp. 397–402, October 2007.

[471] N. Wu, T. D. Nguyen, C. Y. Wei, L. L. Yang, and L. Hanzo, "Integrated LT coding, bit interleaved differential space time coding and sphere packing modulation for the wireless internet," in *Vehicular Technology Conference*, (Marina Bay, Singapore), pp. 344–348, May 2008.

[472] T. Kiran and B. S. Rajan, "Partially-coherent distributed space-time codes with differential encoder and decoder," *IEEE Journal on Selected Areas in Communications*, vol. 25, pp. 426–433, February 2007.

[473] G. Y. Wang, Y. M. Zhang, and M. Amin, "Differential distributed space-time modulation for cooperative networks," *IEEE Transactions on Wireless Communications*, vol. 5, pp. 3097–3108, November 2006.

[474] R. Mudumbai, G. Barriac, and U. Madhow, "On the feasibility of distributed beamforming in wireless networks," *IEEE Transactions on Wireless Communications*, vol. 6, pp. 1754–1763, May 2007.

[475] M. El-Hajjar, S. Zummo and L. Hanzo, "Near-instantaneously adaptive cooperative schemes based on space-time block codes and V-BLAST," in *IEEE Vehicular Technology Conference (VTC2007-Spring)*, pp. 2200–2204, April 2007.

Author Index

D

E

F

G

H

W

X

Y

Z